Università degli Studi di Padova

DIPARTIMENTO DI INGEGNERIA INDUSTRIALE

SCUOLA DI DOTTORATO DI RICERCA IN INGEGNERIA INDUSTRIALE

INDIRIZZO: Ingegneria Chimica, dei Materiali e Meccanica

CICLO XXVIII

Silicate ceramics from preceramic polymers and fillers

Direttore della Scuola
Ch.mo Prof. Paolo Colombo

Coordinatore d'indirizzo:
Ch.mo Prof. Enrico Savio

Supervisore:
Ch.mo Prof. Enrico Bernardo

Dottorando: ***Laura Fiocco***

To my family,
for all their love

"Some graduate students and I were using the electron microscope to examine phase separation in some semiconducting glass systems. The date was on or about February 14. A unique and distinctive structure appeared on the screen and was subsequently photographed.

In case there have been any doubters in the world, we feel this conclusively proves that ceramics is a field into which you can put your heart."

L. L. Hench

Glass microstructure

Ringraziamenti

Niente di tutto questo avrebbe potuto realizzarsi senza il supporto dei miei genitori. Per questo, innanzitutto, grazie mamma e papà per quanto avete sempre fatto per me, per la vostra generosità e per il vostro sostegno. Voi avete sempre creduto in me e avete sempre desiderato il meglio per me. Sappiate che è soprattutto grazie a voi se ho potuto realizzare me stessa fino a qui e per questo vi dedico questo lavoro. Ale, a te grazie per aver reso diciamo “meno noiosa” la vita in appartamento!

Vorrei poi esprimere la mia più sincera gratitudine al mio supervisore Prof. Enrico Bernardo. Gli sono immensamente grata per avermi sempre appoggiata e incoraggiata, per la sua fiducia in me, di cui vado orgogliosa, e per avermi permesso di fare tantissimi magnifici viaggi. Mi ha aiutata in mille occasioni con la sue enorme esperienza e la sua pazienza, sia durante questi anni di ricerca insieme, sia al momento della stesura di questa tesi. Sicuramente, tante idee e suggerimenti che mi ha dato mi hanno semplificato il lavoro in svariate occasioni e, per questo, ha la sua parte di merito nei miei risultati. Non scorderò mai la motivazione, l’entusiasmo e la devozione per il nostro lavoro che è sempre riuscito a trasmettermi. Lo ringrazio per tutto quello che mi ha insegnato da quando lo conosco, che è davvero molto, e per essere stato una guida e un esempio importante per me, ancor più che un maestro.

I miei sentiti ringraziamenti vanno anche al Prof. Paolo Colombo, per la sua disponibilità e umanità, oltre che per avermi concretamente aiutata a realizzare il mio sogno di volare a Londra e viverci da studentessa universitaria e non da semplice turista. E un grazie anche al Prof. Julian R. Jones, per avermi accolta nel suo incredibile gruppo di ricerca all’Imperial College London e avermi fatto sentire parte di esso, ma anche per avermi insegnato molto. Ricorderò per sempre quei sette mesi a Londra come una delle migliori opportunità che ho avuto nella mia vita, un sogno a occhi aperti.

Ringrazio anche tutti i miei amici e compagni di laboratorio, che con me hanno lavorato tre anni e in alcuni casi anche oltre: li ringrazio per il loro generoso aiuto in laboratorio, per la loro sincera amicizia e per aver condiviso insieme molti bei momenti. Abbiamo in comune una bellissima esperienza e sono sicura che senza di loro il mio dottorato non sarebbe stato altrettanto piacevole. Ricordo con gratitudine anche i miei colleghi e amici londinesi, per avermi fatto sentire a casa e per i tanti preziosi consigli. Spero di cuore che ognuno di loro abbia successo nella propria vita, ma anche nella propria futura carriera, e che si senta felice delle proprie scelte. Mi mancheranno tutti. Ringrazio anche Mauro, il miglior tecnico di sempre.

Per ultimo, ma non per importanza, un ringraziamento speciale va a Giulio: io e lui sappiamo perché. Tra mille cose per cui potrei ringraziarlo, ha sempre creduto in me, in noi, e sono convinta che sia la migliore persona là fuori per me.

Abstract

The topic of this research work deals with the synthesis, the characterization and the optimization of silicate ceramics, realized through the controlled pyrolysis of preceramic polymers filled with inorganic fillers.

According to this synthesis route, preceramic polymers can be used as silica precursors by virtue of their conversion from polymers to ceramics by thermal oxidative reactions. Besides the low cost, large availability and easy-handling of the preceramic polymers, a further advantage regards the fabrication of the final ceramic from the process point of view. In fact, the component can be easily shaped by means of the conventional plastic forming techniques, thanks to the polymeric nature of the system before cross-linking. These simple shaping techniques even include the realization of dense components, by warm/cold pressing, and of highly porous bodies, by direct 3-D printing or by foaming of preceramic slurries, before ceramization.

The incorporation of fillers, that generally can be passive or active, is considered one of the most effective strategies to decrease the shrinkage and the formation of macro-defects, that inevitably take place throughout the polymer-to-ceramic conversion, allowing the realization of relatively large components.

A novel approach concerning the use of reactive fillers consists, instead, in incorporating fillers as oxide precursors, that are intended to fully react with the ceramic residue of the polymeric precursors, rather than to compensate the shrinkage. As a result, these reactions between the preceramic polymers and the reactive fillers, occurring throughout the pyrolysis, lead to the formation of specific crystalline phases, that are generally not directly achievable by the simple pyrolysis of a preceramic polymer. Following this methodology, the present Ph.D. thesis has been devoted to an organic investigation of the applications that this strategy could offer, starting from silicone-based mixtures incorporating reactive fillers. By this route, the advantages connected with the presence of a polymeric phase, especially in the shaping step of the processing, can even be combined with the advantages related to the whole processing cycle of preceramic polymers, leading to the realization of ceramic components at relatively low temperatures (even below 1200 °C) and avoiding the conventional methodologies.

In this research work, the fillers incorporated in the preceramic mixtures have also been exploited as foaming agents or liquid phase formers, thus helping respectively the direct shaping in porous bodies or the obtainment of glass-ceramic components. However, as already mentioned, the main purpose of the fillers, here, is to serve as oxide precursors, in order to synthesize crystalline ceramics after pyrolysis of specific compositions, achievable by the reaction occurring between the ceramic residue of the polymeric precursor and the oxides coming from the thermal decomposition of reactive fillers. The type of fillers can be conveniently selected according to the desired final composition; therefore, a wide variety of ceramic systems can be achieved, simply by changing the proportions and composition of the starting polymers and fillers.

The first part of the following chapters will be focused on the realization of peculiar ceramic and glass-ceramic formulations, that are well known to have very pronounced biological properties, and in their shaping in suitable architectures for biomedical purposes, thus having applicability as bioceramics for bone regeneration implants. Besides bioglasses, other bioceramic formulations have recently received a growing interest in the field of bone ingrowth, according to their ability to stimulate body tissues to repair themselves. The formulations developed in this research work mainly belong to the $CaO-SiO_2$ or $CaO-MgO-SiO_2$ oxides systems, but some crystalline phases have also been combined to obtain composite formulations, or have been coated with other materials (hydroxyapatite) exhibiting the same properties as natural bone from a chemical and structural point

of view, to increase their bioactivity even more. In this framework, the developed materials have not only been characterized in terms of microstructure, mechanical and physical properties, but their biological behaviour has been assessed as well.

Then, exploiting the concept of multifunctionality characterizing some silicates, besides deep analogies in the crystal structure and in the processing route, it has been possible to establish a thread running between the above-discussed biosilicates and other silicates with further advanced functional applications. In accordance with this logic, the technology has been extended to dielectric, photoluminescent and refractory silicates.

Riassunto

L’attività di ricerca presentata in questa tesi ha riguardato la sintesi, la caratterizzazione e l’ottimizzazione di ceramici silicatici, realizzati a partire dalla pirolisi controllata di polimeri preceramici caricati con fillers inorganici.

Sulla base di tale metodo di sintesi, i polimeri preceramici possono essere utilizzati come precursori per l’ottenimento di silice in virtù della loro conversione da polimeri a ceramici tramite reazioni termo-ossidative. Oltre al basso costo, alla larga disponibilità e alla semplicità di utilizzo, un ulteriore vantaggio riguarda la fabbricazione del ceramico finale dal punto di vista del processo. Infatti, il componente può essere formato sfruttando le convenzionali tecniche di formatura per i materiali polimerici, grazie alla presenza di una componente polimerica nel sistema, prima di imporne la reticolazione. Tali semplici tecniche di formatura includono anche la realizzazione di componenti densi, tramite pressatura, o di corpi altamente porosi, tramite stampaggio 3-D diretto o schiumaggio delle miscele preceramiche, prima di ceramizzarle.

L’inserimento di fillers, che generalmente si suddividono in attivi e passivi, è considerata una delle più efficaci strategie per ridurre il ritiro dimensionale e la formazione di macrodifetti, che inevitabilmente ha luogo durante la conversione da materiale polimerico a ceramico, permettendo la realizzazione di componenti relativamente spessi.

Un approccio più innovativo relativo all’uso di fillers reattivi, invece, riguarda l’introduzione di fillers come precursori di ossidi che possano reagire completamente con il residuo ceramico dei precursori polimerici, piuttosto che finalizzati a compensare il ritiro dimensionale dei componenti. Dalle reazioni tra i precursori polimerici e i fillers reattivi durante la pirolisi, risulta la formazione di fasi cristalline specifiche, che generalmente non sono ottenibili in modo diretto dal semplice trattamento termico dei precursori polimerici. Seguendo tale processo di sintesi, la presente tesi di dottorato ha avuto come obiettivo lo studio delle applicazioni che tale tecnica potrebbe offrire, partendo da miscele a base di polimeri siliconici caricati con fillers reattivi. In questo modo, i vantaggi derivanti dalla presenza di una componente polimerica, sfruttati soprattutto in fase di formatura, possono anche essere combinati con i vantaggi offerti dall’intero ciclo produttivo dei ceramici da polimeri preceramici, portando alla realizzazione di componenti ceramici a temperature abbastanza basse (entro i 1200 °C) ed evitando i metodi di sintesi più convenzionali.

Nel presente lavoro di ricerca, i fillers incorporati nelle miscele preceramiche sono anche stati sfruttati come agenti schiumanti o formatori di fase liquida, permettendo, rispettivamente, lo schiumaggio diretto di componenti altamente porosi in un caso e l’ottenimento di vetro-ceramiche nel secondo. Ad ogni modo, come già spiegato, il fine principale dell’uso dei fillers, qui, è stato il loro utilizzo come precursori di ossidi, in modo da permettere, dopo ceramizzazione, la sintesi di fasi ceramiche cristalline di specifica composizione, direttamente ottenibili dalla reazione tra il residuo ceramico dei precursori polimerici e gli ossidi provenienti dalla decomposizione termica dei fillers reattivi. La tipologia dei fillers può essere adeguatamente modificata a seconda della composizione finale desiderata; di conseguenza, un’enorme varietà di sistemi ceramici può essere realizzata semplicemente modificando le proporzioni e la composizione dei polimeri e dei fillers di partenza.

La prima parte dei capitoli seguenti sarà imperniata sulla realizzazione di particolari ceramici e vetro-ceramiche molto conosciuti per le loro pronunciate proprietà biologiche, oltre che sulla loro formatura in strutture che risultino adeguate ad applicazioni biomedicali, come gli impianti per rigenerazione ossea. Parallelamente ai biovetri, altre formulazioni bioceramiche hanno ricevuto recentemente un interesse crescente nel campo biomedicale, in virtù della loro capacità di stimolare i tessuti biologici ad auto-ripararsi. Le formulazioni qui sviluppate appartengono prevalentemente ai sistemi di ossidi del tipo CaO-SiO_2 o CaO-MgO-SiO_2, ma alcune fasi cristalline sono anche state

combinate tra loro per ottenere formulazioni composite, oppure sono state rivestite con altri materiali, come l'idrossiapatite, esibenti proprietà simili a quelle dell'osso naturale, sia sotto il punto di vista chimico che strutturale, al fine di incrementarne ulteriormente la bioattività. In questo contesto, i materiali sviluppati sono stati caratterizzati non solo dal punto di vista microstrutturale, meccanico e fisico, ma è stato studiato anche il loro comportamento sotto il profilo biologico.

Inoltre, sfruttando il concetto di multifunzionalità che caratterizza alcuni silicati, oltre alle profonde analogie in termini di struttura cristallina e di caratteristiche di processo, è stato possibile stabilire un filo conduttore tra i biosilicati sopra menzionati e altri silicati con diverse applicazioni funzionali avanzate. In quest'ottica, la tecnologia è stata estesa ad altri silicati caratterizzati in particolare da proprietà dielettriche, luminescenti e refrattarie.

Contents

Introduction

1 Overview of polymer-derived ceramics

1.1 Introduction

Polymer-derived ceramics (PDCs), as the name suggests, refers to a synthesis process for the fabrication of ceramic materials through the controlled thermolysis of polymeric precursors. This methodology has gained substantial interest in the last decades, due to a series of advantages related to the use of preceramic polymers, such as the wide variety and availability of precursors, their low cost and easy-handling, besides the relatively low synthesis temperatures and the possibility to apply the conventional plastic shaping techniques, such as polymer infiltration pyrolysis, injection moulding, extrusion, resin transfer moulding. All these favourable aspects make PDCs an extremely promising route for the realization of a unique class of materials with extraordinary characteristics.

The first production of non-oxide ceramics from molecular precursors was reported in the early 1960s by Ainger and Herbert[1], Chantrell and Popper[2]. Ten years later, Verbeek, Winter and Mansmann[3-5] presented the first practical ceramic transformation of polyorganosilicon compounds (polysilazanes, polisiloxanes and polycarbonsilanes), primarily aimed at manufacturing small-diameter Si_3N_4/SiC ceramic fibers for high temperature use. Synthesis of SiC ceramic material from polycarbosilanes was developed by Fritz and Raabe[6] and, almost at the same time, by Yajima[7-8]. Since these first experiments, silicon-based polymers demonstrated to be promising precursors for the production of technologically important ceramic components, such as fibers, coatings, composites, infiltrated porous media or complex-shaped bulk parts, which cannot be easily obtained using the powder technology, that is the traditional method to prepare ceramics and, however, requires the addition of sintering additives and significantly constrains technical applications.

In recent years, the growing interest for PDCs led to further significant improvements of their chemistry, synthesis, processing and properties. To be competitive with traditional ceramics, PDCs have to be either cheap or their synthesis has to be selective to give the desired product with novel composition and exceptional properties. Nowadays, many classes of preceramic polymers are available, the most important of which are polysiloxanes, polycarbosilanes and polysilazanes. Many efforts have been made not only for the synthesis of classical binary ceramics, such as Si_3N_4 or SiC, but also to produce ternary systems, like SiOC and SiCN. Depending on the degree of complexity of the starting polymers, the final ceramic composition can also be further extended. Indeed, the incorporation of boron can lead to produce ceramics in the quaternary SiBCN system, or modification of polymeric precursors with metallic elements like Al, Ti, Zr can allow the realization of several multinary systems, as it has been reported in recent years.

PDCs in general exhibit enhanced thermo-mechanical properties with respect to creep and oxidation, crystallization or phase separation up to 1500 °C, or even up to 2200 °C if the preceramic polymer incorporates some amount of boron. Moreover, their synthesis process requires less energy consumption, having a relatively low synthesis temperature of 1000-1300 °C, that is of economical interest in comparison with conventional ceramic powder processing technology, which requires 1700-2000 °C to sinter covalent Si_3N_4- and SiC-based ceramics. Besides the applications as high-temperature-resistant materials (energy materials, automotive, aerospace, etc.), other key engineering fields are suitable for PDCs, including hard materials, chemical engineering, electrical engineering, micro/nanoelectronics, demonstrating that the science and technological development of PDCs are highly interdisciplinary due to the high flexibility of this methodology.

In the next sections, the most significant aspects of the PDCs route will be described, with particular attention to the chemistry of preceramic polymers, their processing and the properties of the final ceramics.

1.2 Preceramic polymers chemistry

1.2.1 General aspects

Preceramic polymers can be represented by the following oversimplified general formula (Fig. 1.1), consisting of a Si-based polymeric chain and side functionalities.

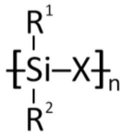

$$\left[\underset{R^2}{\overset{R^1}{\mathrm{Si}}}-X\right]_n$$

Fig. 1.1 General simplified formula of Si-based preceramic polymers.

The main backbone is constituted by Si atoms bonded to a generic X group, which probably is the most important parameter to modify the preceramic compound and which determines the class of the final polymer, as summarized in Tab. 1.1: polysilanes with X=Si, polysiloxanes with X=O, polycarbosilanes with $X=CH_2$, polysilazanes with X=NH, polyborosilanes with X=BR and polysilylcarbodiimides with X=[N=C=N].

Tab. 1.1 Principal classes of Si-based preceramic polymers, based on the nature of the X group in the polymer backbone.

X group	Polymer class
Si	Polysilanes
O	Polysiloxanes, Polysilsesquixanes
C	Polycarbosilanes
N	Polysilazanes, polysilsesquiazanes
B	Polyborosilanes

R_1 and R_2 substituents, instead, can be changed to modify the thermal and chemical stability, as well as the solubility of the polymer, the electronic, optical and rheological properties. These side functional groups are generally C-based (e.g. H, aromatic, aliphatic). In particular, the solubility, the thermal stability and the viscosity as a function of temperature are important features for the processing of the polymers[9-10]. Moreover, suitable functionalities are necessary to achieve the polymer setting through cross-linking reactions before the pyrolysis step, the nature of which is strictly related to the nature of the side groups involved (e.g. condensation reactions in the case of –OH functionalities, addition reactions in the case of –vynil groups). Upon pyrolysis, instead, the nature and the quantity of the different side groups are well known to determine the residual C content in the final ceramics (if a non-oxidizing atmosphere is used during pyrolysis).

Combining different X, R_1 and R_2 groups, a wide range of potential polymer compositions are achievable, also considering than more than one X group can be present at the same time inside the polymer backbone. For instance, polyborosilazanes are a class of hybrid polymers where both X=B and X=N are present in the main chain. Thus, the macroscopic chemical and physical properties of PDCs can be varied and adjusted to a huge extent by the design of the molecular precursor[9,11-12]. A more comprehensive description and graphical representation of Si-based preceramic polymers is reported in Fig. 1.2, as schematized by Colombo *et al.*[9]. As visible, an extremely wide variety of preceramic polymers is achievable, although not all of these classes have become equally common and widespread. This is mostly due to the fact that, besides the properties and performances of the final ceramics, there is a series of other factors affecting the selection of a preceramic polymer. The most important parameter to be considered, especially from an industrial point of view, is the cost of the precursors, but even the specific handling that every precursor requires is relevant (it is influenced by its chemical durability, thermal stability, toxicity and reactivity towards the atmosphere or other substances), since it inevitably influences all the aspects of its processing[13].

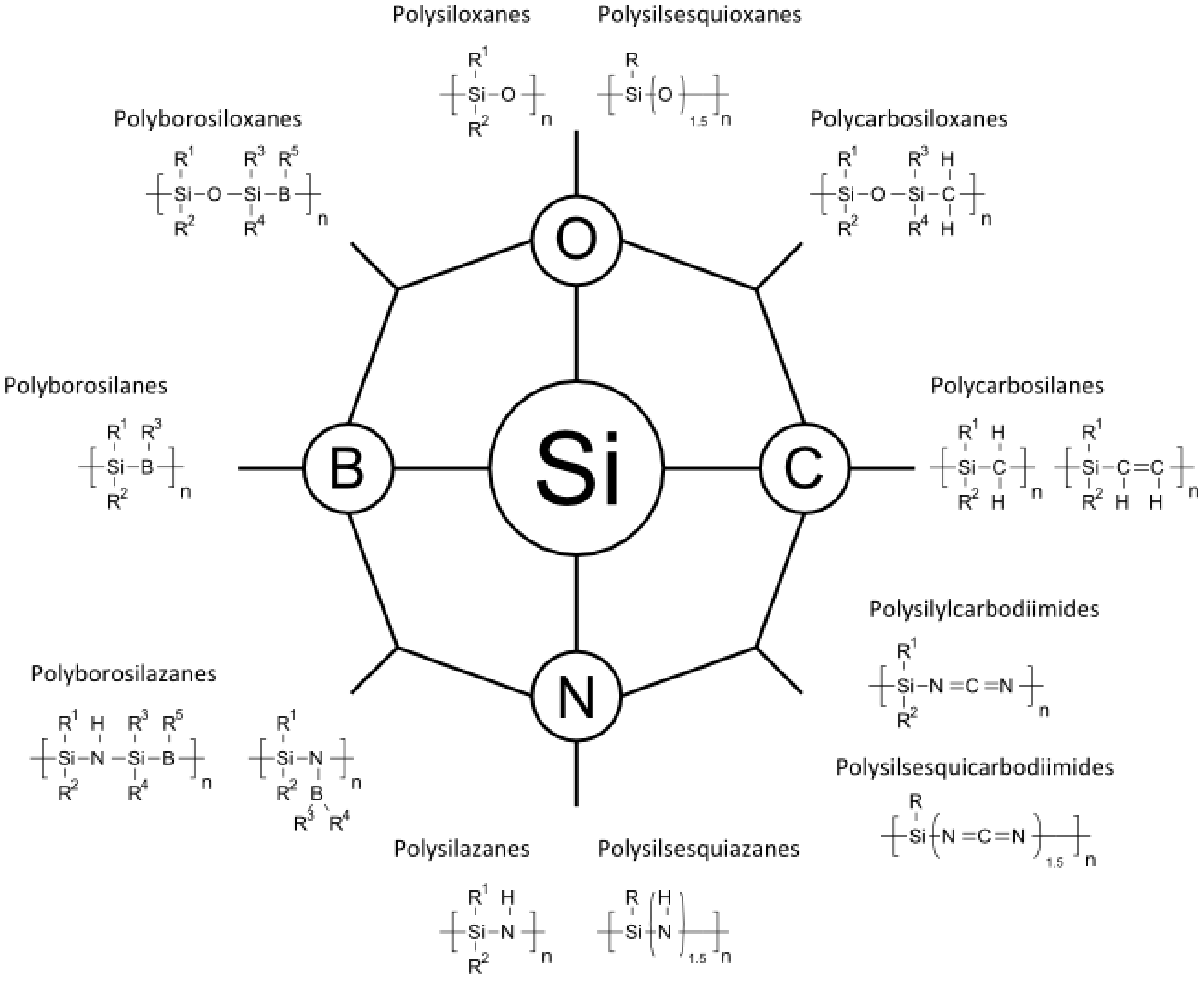

Fig. 1.2 Main classes of Si-based preceramic polymers in the Si-O-C-N-B system[9].

Among all the classes of preceramic polymers, the most studied class of preceramic polymers is represented by the polysiloxanes, being inexpensive, non-toxic and having high thermo-chemical stability[14-15]. They are the preferred choice for the realization of silicon oxycarbide glasses with interesting thermo-mechanical properties up to approximately 1200 °C. Instead, when higher thermal stability is required, polysilazanes and polyboronsilazanes are the best choice (for temperatures respectively up to 1400 and 1600 °C), but their higher performances are obviously accompanied by increased prices of the precursors, more complex synthesis routes, generally higher reactivity towards other substances (moisture and O) and toxicity, thus increasing processing complexity and hindering their applicability on an industrial scale.

1.2.2 Polysiloxanes

Polysiloxanes surely represent the most important and widespread class of preceramic polymers, due to a number of advantageous features, such as their general low cost (the lowest among all Si-based polymers), their easy and cheap synthesis route, their thermo-chemical stability, making this class of precursors very versatile, easy to handle and processable without particular precautions[16-20]. They are denoted as silicones and they are odourless, colourless, water resistant, chemical resistant, stable at high temperatures and electrical insulating. By virtue of all these favourable characteristics, they have been involved in all the formulations investigated in the present thesis.

Millions of modern products rely in some way on silicones for performance and reliability. They have many uses in several industrial applications, not only as lubricants, adhesives, sealants, gaskets, coolants in transformers, but also as foam-control agents in laundry detergents or protective coatings for facades and historical monuments. They are widely used even in hi-tech fields, like in the aerospace industry to increase the lifespan of vital components, in the semiconductor industry as protective materials, in the railway industry as long-lasting motor insulation and lubricants for bearings, or in the electronics and telecommunications industry for the processing of products like optical glass fibers, silicon wafers and chips. Moreover, due to their extremely low reactivity and non-toxicity, they have biomedical applications, like in breast implants, or they can be used in the personal care products industry or as food additives.

Besides the above-mentioned characteristics, other attractive technological properties are the low surface tension, the low glass transition temperature, the low hydrophobicity, the high melting and boiling points, they are liquid even with high molecular weights, etc. Due to all these interesting properties and to the continuous development of this family of precursors, a further growth of the polysiloxanes market is expected, as well as the discovery of new applications, beyond the present claims as synthetic fabric, high oxygen permeable contact lenses, adhesive foams, waterproof membranes, process aids, self lubricants, improved toughness, lithographic applications[21].

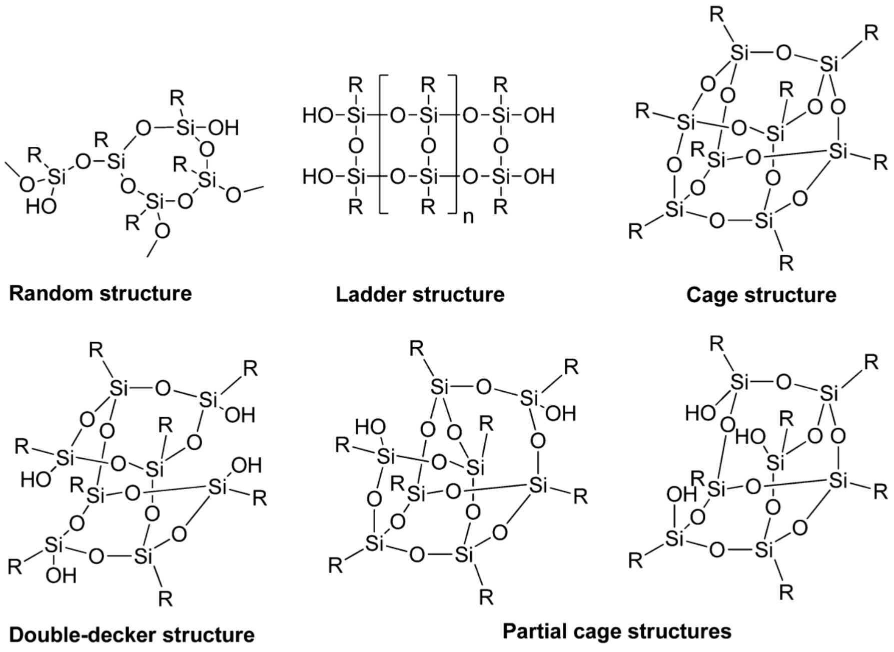

Random structure

Ladder structure

Cage structure

Double-decker structure

Partial cage structures

Fig. 1.3 General types of polysilsesquioxanes[9].

The general synthesis method for the preparation of polysiloxanes comprises the reaction of chloro(organo)silanes with water, but other synthesis routes have also been proposed, such as the polycondensation reaction of functionalized linear silanes and ring-opening polymerization of cyclic silaethers, leading to hybrid materials combining the properties of polysilanes with those of polysiloxanes.

In non-oxidizing atmosphere, the pyrolysis of polysiloxanes gives the formation of a silicon oxycarbide amorphous residue, consisting of both Si-O and Si-C bonds, impossible to be obtained with more traditional processing techniques. The presence of both covalent bonds is the basis for all the distinguishing properties of PDCs, like enhanced thermal stability and creep, oxidation and corrosion resistance. They are black in aspect, due to the residual “free” C present inside the material.

Besides linear and cyclical polymers, another important subclass is represented by polysilsesquioxanes, characterized by the general formula $–[RSi–O_{1.5}]_n–$ and for having a highly-branched molecular structure, that can have very different possible configurations, such as random, ladder or cage, as reported in Fig. 1.3. Due to their high branching level, this class of polymers is often referred to as siliconic resins , they are generally solid at room temperature and they have very high ceramic yields upon pyrolysis[13].

Tab. 1.2 reports the main characteristics of the two preceramic polymers used in the present research work.

Tab. 1.2 Characteristics of the preceramic polymers used in the experiments[22].

Commercial name of preceramic polymer	Main ceramic phase 1000 °C in N_2	Physical form T_{room}	Tg (°C)	Ceramic yield N_2/air 1000 °C (wt%)	Class	Composition 1000 °C in N_2 (at%)
Silres® MK	SiOC	Powder	35-55	84/84	Methyl-polysilsesquioxane	$SiO_{1.52}C_{0.64}$
Silres® H62C	SiOC	Liquid	–	n.a./58	Methylphenylvinyl-hydrogen-polysiloxane	n.a.

1.3 Preceramic polymers processing

1.3.1 Shaping

One of the most advantageous aspects of PDC route is that the preceramic precursors have the specific characteristic of having polymeric nature at the temperature at which they are shaped into components. Therefore, they can be subjected to a large variety of forming methods, some of which are reported in Fig. 1.4. All the common and well-known plastic forming technologies can be applied to preceramic polymers: besides the quite standard compaction method by uniaxial, isostatic and warm pressing[23 - 25], other possibilities for the shaping of preceramic polymers may include extrusion[26-28], injection moulding[29-30] or coating of substrates by spraying, dip coating, spin coating or chemical vapour deposition (CVD)[31-33]. Coupling the PDC route with special forming technologies gives the possibility to realize some special components, generally not easy, if not impossible, to achieve with powders processing: some representative examples include fiber drawing[34 - 35], infiltration of pre-formed scaffolds for ceramic matrix composites (CMCs)[36 - 38], ceramic joining/bonding[39 - 41], micro-component production through selective curing of substrates by lithographic techniques[42-44] and easy realization of highly porous bodies by direct foaming or other techniques such as negative replica[45].

Having a fully polymeric system allows an easy fabrication of green compacts with no need for additional binders, that exhibit a suitable mechanical consistency for further handling and, if required, machining (after cross-linking). The possibility of machining before ceramization is a remarkable advantage compared to common powder processing routes, since it allows a more precise shape control and avoids the problems connected to tool wear and ceramic brittleness[46]. Also, when using preceramic polymers for joining, the precursor effectively binds together the parts at low temperature, making handling before treatment much simpler[39]. The rheological characteristics of the precursors can be tailored by modifying their molecular architecture, thus allowing for example the fiber spinning[47]. In fact, preceramic polymers can be liquid or solid: if solid, they can also be dissolved in several organic solvents or can be molten at low temperatures (<150 °C), usually leading to components possessing finer details, in comparison with powder-based systems[9].

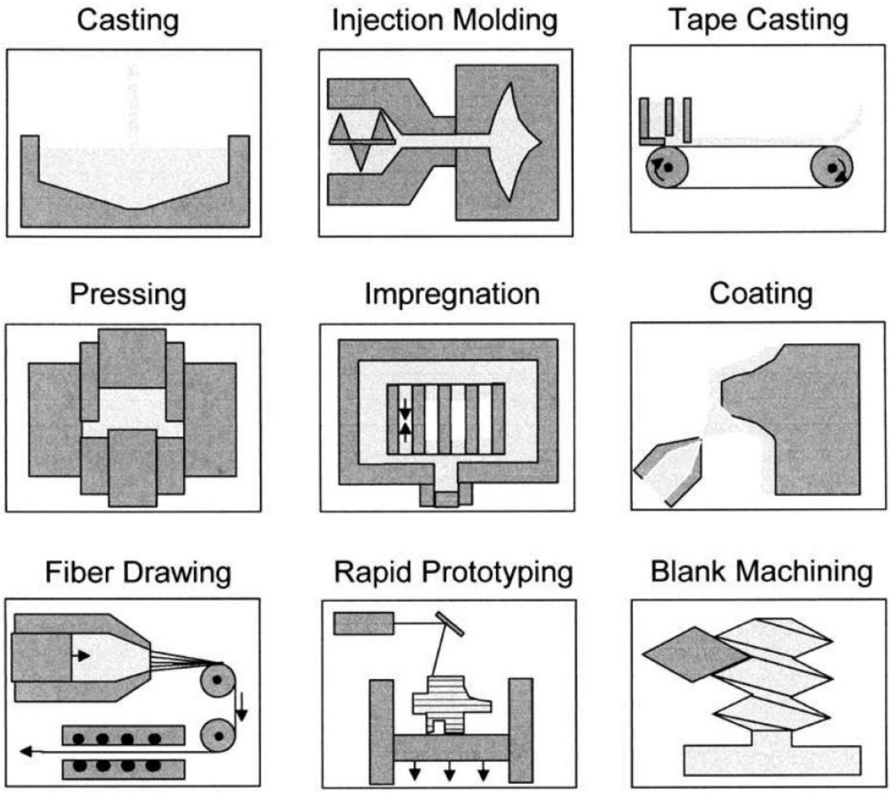

Fig. 1.4 Shaping technologies for polymer-derived ceramics manufacturing[11].

Concerning the fiber production, ultra-high performance SiC-based ceramic fibers for polymer, metal or ceramic matrix composites have been produced in the last decades by Nippon Carbon Co. (NICALON™) and by UBE Industries (Tyranno®) starting from polycarbosilanes[7,8]. Another example are the non-oxide Si-C-N fibers, that have been successfully produced at ITCF (Denkendorf) from a polycarbosilazane precursor[48]. Polyacrylonitrile (PAN), although not silicon-based, is one last significant example of the application of the PDCs route for the industrial realization of ceramic components. Since first investigation during World War II by Union Carbide Corporation, it has been used extensively for the realization of high-strength carbon fibers for polymer and ceramic matrix composites. Nowadays, the PAN process is the most important production process for carbon fibers[10].

As a final remark, it should be pointed out that this approach has important technological advantages over the use of other molecular precursors as well, such as sol-gel ones, as preceramic polymers do not have any drying problems that hamper the possibility of fabricating bulk components, do not need long processing times for gelation and drying, do not require flammable solvents, can be processed in the molten state, their solutions are stable in time and, at least for cheap, commercially available polysiloxanes, they do not require any specialized handling procedures[9].

1.3.2 Cross-linking

A specific requirement for processing components using preceramic polymers is that, after shaping, the part needs to be converted into a thermoset, capable of retaining the shape during ceramization. The most common methodology to achieve the setting of the polymeric phase is the thermal curing below 250 °C, that can be easily obtained by incorporating suitable functionalities (e.g. -H, -OH, -vynil groups) in the polymer structure, thus enabling the cross-linking by addition or condensation reactions. Thermal curing temperatures might also be lowered by using catalysts or radical initiator, with the further advantage of an increased ceramic yield due to the lowering of oligomers evaporation[49-50].

Curing can be achieved using other different strategies, such us UV-radiation (if proper photo-sensitive groups are present), γ-rays, electron-beams, and the use of reactive substances, gases or plasma[51-53]. Selective laser curing can be also applied, especially when a high degree of morphological complexity is required[54].

A release of gaseous by-products (e.g. water or ethanol) could take place during the curing step, depending on the curing mechanism. The consequence of this gas release is the generation of bubbles that may remain trapped inside the polymeric medium: this phenomenon could either be exploited for producing porous bodies by self-foaming processes, or be detrimental if a dense pore-free ceramic is desired.

It should be remarked that the extent of cross-linking strongly affects the rheological behaviour of a preceramic polymer, therefore it has to be carefully controlled especially when plastic forming technologies are used[55]. Moreover, it has to be noted that, when a preceramic polymer is filled with higher amounts of fillers, the curing step might not be necessary, as the solid additives may offer sufficient support to the polymeric matrix to retain the shape upon heating, by limiting the flow. In fact, the incorporation of fillers usually strongly affects the rheological behaviour of the preceramic polymers[56].

As will be more extensively discussed later, polymer cross-linking is also of fundamental importance for the obtainment of high ceramic yields upon pyrolysis: effective cross-linking reactions lead to highly branched/higher molecular weight polymeric molecules and thus to a lower content of oligomers and low molecular weight chains, that could volatilize at higher temperatures, thus increasing the final ceramic yield.

1.3.3 Polymer-to-ceramic conversion

After shaping and cross-linking, the preceramic part has to be converted into a ceramic. This conversion (above 400 °C) leads to a totally inorganic, non-volatile ceramic residue. The most widely process is oven pyrolysis[57], in which the flowing gas continuously removes the decomposition gases from the system and can be carried out in oxidizing or non-oxidizing atmosphere[58]. However, non-thermal processes can also be applied, such as ion irradiation[59-60], which might be applied to preceramic layers.

The pyrolysis mechanism involved in the polymer-to-ceramic conversion is generally quite complex. The final result is the formation of an inorganic network, as a consequence of a reactions sequence, involving structural rearrangements and radical reactions. The process leads to the cleavage of chemical bonds (e.g. Si–H, Si–C and C–H), to the release of organic moieties (e.g. methyl, phenyl, vynil groups) and elimination of Si-H, Si-OH or Si-NH_x groups[9,11-12]. In the case of polysiloxane resins, for example, it has been verified that in the 600–800 °C range methane is the main volatile species released, while at higher temperature (600–1100 °C) the release of hydrogen is observed[61]. At temperatures above 400 °C, an open-pore channel network is formed, that, upon further heating to 800-100 °C, can diminish (transient porosity)[11-12].

A fundamental parameter to be considered concerning preceramic polymers is their ceramic yield, which is defined as the ratio between the mass of the starting polymer and the mass of the ceramic residue upon pyrolysis. Typical ceramic yields are in the 70-90 wt% range, although even higher have been reported when reactive atmospheres are use[62]. The polymer-to-ceramic conversion terminates at 800-1000 °C and is associated with a weight loss of typically 10-30 %, which has several contributions, each having its characteristic temperature range. A simplified representation of the weight loss (TG curve) and structural rearrangements of a preceramic polymer (polycarbosilane) during heat treatment in inert (Ar) atmosphere is reported in Fig. 1.5, as schematized by Greil[12].

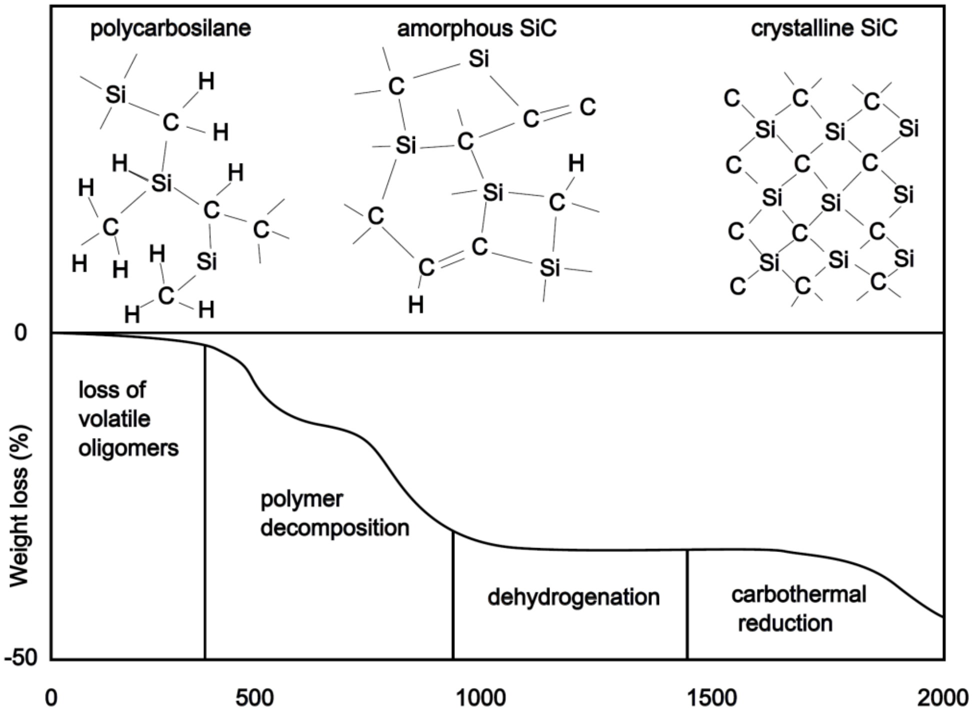

Fig. 1.5 Typical structural transformation during thermal decomposition of a polycarbonsilane and TG curve[12].

The nature of the polymeric precursors and their chemistry play an essential role in determining the final ceramic yield. Therefore, in the last decades, the continuous development of preceramic polymers chemistry and processing has been of fundamental importance for increasing the ceramic yield, in order to obtain valuable precursors with potential practical applications[21]. For example, low molecular weight polymers, as well as the presence of oligomers, could dramatically decrease the ceramic yield upon pyrolysis, due to volatilization and de-polymerization reactions. A proper cross-linking step thus acquires a fundamental importance, not only for the obtainment of an infusible compact, but also to increase the final ceramic yield.

However, there are other factors affecting the ceramic yield of preceramic polymers. First of all, the presence of organic side chain groups is crucial in determining both the cross-linking and thermolysis chemistry[21]. Then, higher branching levels have generally a positive influence on the final ceramic yield. Another relevant factor is the thermal decomposition occurring during pyrolysis, since it represents the step when most of the weight loss is observed, deriving from the cleavage of chemical bonds and release of gaseous by-products. Finally, dehydrogenation and carbothermal reduction reactions at higher temperatures could give an additional contribution to the global weight loss, although these phenomena are generally less significant[61].

The most serious drawback of PDCs is associated with the thermal decomposition and rearrangements, that are a distinctive characteristic of the ceramic conversion. In fact, the gases release is inevitably accompanied not only by a mass loss, but also by the formation of cracks and porosity inside the material and by a more or less pronounced shrinkage, which lead to a deterioration of the mechanical properties. Moreover, the density of the material is generally observed to increase by a factor of 2-3, passing from the polymeric phase (density ≈ 1 g/cm^3) to the final ceramic (density ≈ 2.2-2.6 for SiO_2, 3-3.2 for SiC and Si_3N_4)[12]. If the material structural changes cannot be relaxed by viscous flow or diffusion processes, the internal tensions combined with pores and cracks can lead to the destruction of the component integrity, especially in presence of external constraints (e.g. coatings). Therefore, crack-free large components are impossible to realize, even from preceramic polymers with high ceramic yields, because of the issues in obtaining an easy conversion of polymers into dense ceramics. Few exceptions are represented by components characterized by dimensions below a few hundred micrometers, like fibers, thin films and foams[9].

In the last 25 years, much concentration has been devoted to the scaling up of ceramic components dimensions, in order to widen the applicability of PDCs, especially in the field of structural ceramics. To prevent cracking, the thermolysis can be influenced by use of additional fillers, as later discussed[11-12], and this is the solution which has been so far more widely explored. Anyway, other solutions have been proposed, such as the infiltration of scaffolds by a liquid polymer[63] or the compaction of partially pre-cured powders[64-65].

When the polymer-to-ceramic conversion is carried to completion, the obtained ceramics are typically amorphous up to 1000-1800 °C, mainly depending on the molecular structure and composition of the precursors used. This amorphous network is constituted by a mixture of covalent bonds, the most important being Si-C, Si-O, Si-N and C-C, but also other bonds may be present with atoms like B, Al, Zr, Ti, depending on the composition of the precursor. This amorphous structure, that is fundamental in determining the distinguishing properties of PDCs (e.g. thermal stability, creep, oxidation and chemical resistance), is distinctive of PDCs and so far has been impossible to be obtained through traditional reactive sintering[9].

At elevated temperatures, PDCs usually undergo further structural rearrangements, that can take place both during processing or during service, leading to the evolution from the amorphous state to the partially crystalline state. The devitrification of the initial amorphous network starts with a progressive redistribution of the chemical bonds, causing phase separation and the eventual crystallization of different crystalline phases, such as SiC, SiO_2, Si_3N_4, depending again on the nature of the precursors, and “free” C (turbostratic or graphitic). In particular, “free” C is defined, with respect to stoichiometry, as the amount of C not bonded to Si in ceramic. An equilibrium between these phases can be achieved, if sufficient temperatures/times are applied. Moreover, in many cases decompositions and subsequent eventual crystallization are accompanied by the releasing of gaseous products, such as CO_2, SiO_2, NO_x and others[9].

Anyway, the nucleation and growth of crystals is a generally undesired phenomenon, since it usually degrades most of the beneficial properties of PDCs, that are often connected with the retention of their amorphous structure[13]. As mentioned, the type of covalent bonds present in the ceramic are strictly dependent on the type of precursor used. This has a role in determining the characteristic maximum service temperature of the final ceramic before the occurrence of the devitrification process, usually taking place in the 1000-1800 °C range. SiOC glasses, surely the most common type of PDCs, are considered to be stable up to 1200 °C, being resistant to creep, oxidation and chemical attack. Above this temperature, their properties begin to deteriorate, due to the phase separation/crystallization located around 1300 °C[66-67]. SiCN amorphous ceramics, instead, are able to maintain their properties up to 1400 °C. Concerning oxynitride glasses, the presence of N atoms have beneficial effects on the viscosity, micro-hardness, elastic modulus and fracture toughness in comparison to pure oxide glasses[68].

Finally, the introduction of further elements, such as B or Al, into the preceramic polymers can increase the high-temperature stability, creep and oxidation resistance, which are features directly correlated to the nanostructure of the ceramics and some of them can persist even at temperatures as high as 1800-2000 °C. For instance, SiBCN glasses can increase their crystallization temperature up to above 1800 °C[21], making them competitive with more traditional nitrides and carbides.

A final schematization of the whole processing cycle of preceramic polymers used in the present research work is represented in Fig. 1.6. The further mixing step at room temperature regards more complex systems, consisting of preceramic polymers filled with oxide precursors as reactive fillers. The benefit of this procedure will be examined in detail in §2.

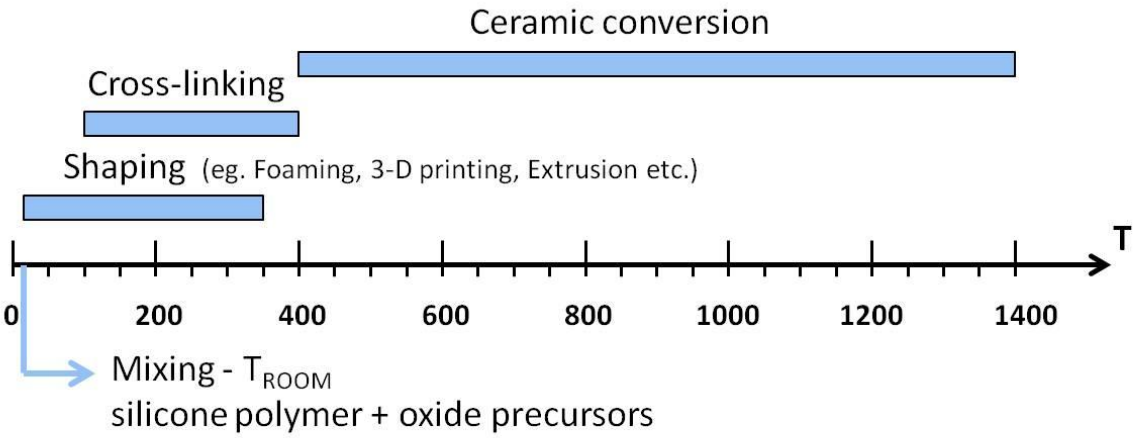

Fig. 1.6 Schematic representation of the whole preceramic polymers used in this research work.

1.4 Properties of polymer-derived ceramics

1.4.1 Microstructure

As mentioned above, the class of preceramic polymers selected as a silica source during pyrolysis in air, for all the formulations investigated in the present thesis, is represented by silicones, due to a series of advantageous features already described in §1.2.2. The chemical composition of the final ceramics is strictly related to the chemistry of the polymeric precursors, as well as to other processing factors (temperature and atmosphere) and to the addition of fillers (see §2).

The pyrolysis of silicones, characterized by a Si-O backbone, carried out in inert atmosphere gives the formation of amorphous $Si_xO_yC_z$, in which Si is simultaneously bonded to C and O[9,21]. The presence of “free” C is also observed, the content of which may vary by changes of the organic substituents to silicon (e.g. an increase in the phenyl group concentration leads to an increase in the C content). The separation of “free” C is responsible for the black colour of SiOC, often referred to as “black glass”, and for electrical properties[21]. Microstructural analysis performed by Raman spectroscopy on SiOC glasses demonstrated the presence of absorption bands located at 1360 and 1600 cm^{-1}, which can be assigned to the D- and G-band characteristic for *sp*^{3}- and *sp*^{2}-carbon, respectively.

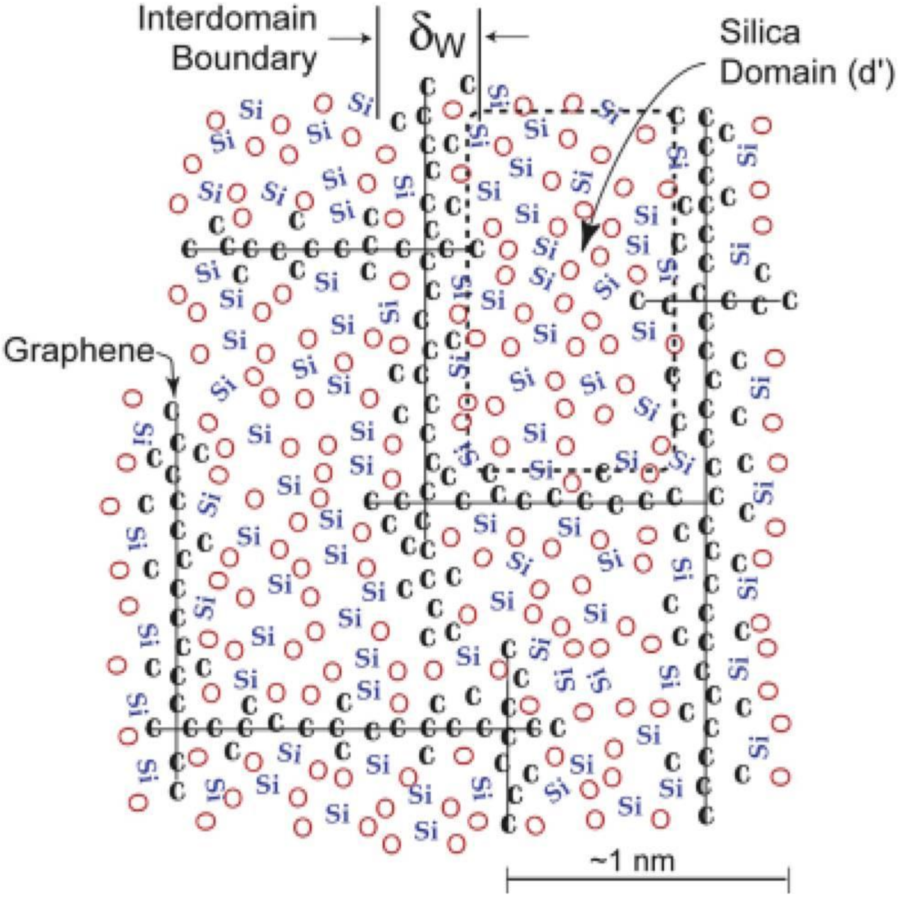

Fig. 1.7 Proposed model for the nanodomain structures in polymer-derived SiOC[69].

In 2006, Saha *et al.*[69] showed the evidence that SiOC made from the preceramic polymer route contains nanodomains that persist up to very high temperatures and they proposed a simple geometrical model reported in Fig. 1.7, constructed from three constituents: clusters of SiO_2 tetrahedra, that form the heart of the domain, the surrounding monolayer of mixed bonds of the type SiC_nO_{4-n}, where “n” gives the fourfold coordination of Si to C and O, and the graphene cage-like network that encases the domains. The C bonded to Si is called *sp*^{3} or carbidic carbon, while the carbon in graphene is *sp*^{2} or graphitic carbon. In their work, they explain that it is conceivable that these domains evolve from the organic state because of two main reasons: i) the pyrolysis of organic leaves behind significant amounts of C in the ceramic and ii) the C in essentially insoluble in SiO_2. So they postulate that, as the SiO_2 tetrahedra coarsen during pyrolysis, they reject C to their outer surfaces and, when these surfaces form continuous structure of mixed bonds and graphene, the coarsening stops and the nanodomains remain stable. Whether such nanodomains are kinetically and thermodynamically stable is still an open question, anyway, the presence of nanodomains is one of the most intriguing characteristics of PDCs, being responsible for their resistance to crystallization even at high temperatures. Reports in literature confirm that SiOC contains nanodomains with 1-5 nm in size (d' in Fig. 1.7) and interdomain boundaries with 300-1000 pm in width (δ_W in Fig. 1.7).

These observations are specific for the ceramic conversion in inert atmosphere of polysiloxanes, but other classes of preceramic polymers can lead to different ceramic compositions, depending on their starting chemistry. A simplified scheme of the thermal decomposition of Si-based polymers in inert atmosphere is reported in Fig. 1.8.

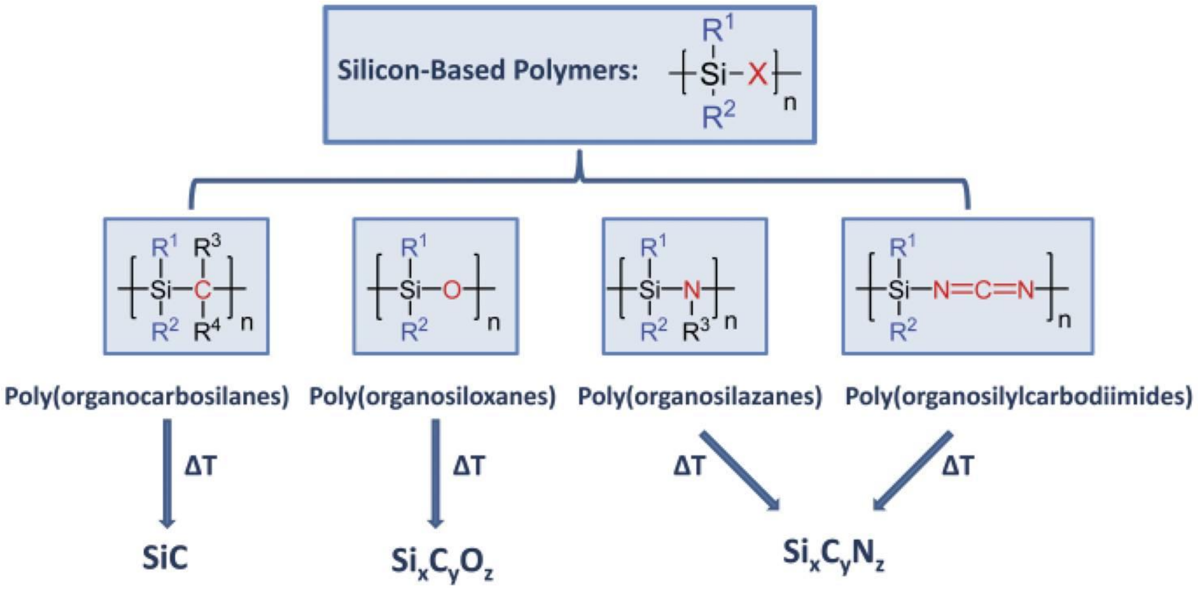

Fig. 1.8 Thermal decomposition of Si-based polymers in inert atmosphere[9].

Conversely, an oxidizing atmosphere leads to the formation of an amorphous SiO_2 matrix, regardless of the chemistry of the precursors. This is due to the removal of all the C-based moieties by oxidation reactions, as well as cleavage of Si-C and Si-N bonds of the main chain (if present, they are less stable than Si-O bonds), with intake of further O from the atmosphere.

A further remark should be made on the pyrolysis temperature, since it plays an important role in determining the final microstructure of PDCs. At low temperatures (600-800 °C), immediately after the end of the decomposition of the polymeric phase, the microstructure is mainly homogeneous and amorphous, formed by amorphous SiO_2, if the pyrolysis is led in air, and by a random mixture of covalent bonds (Si-O and Si-C in case of polysiloxanes), if the pyrolysis is carried out in inert atmosphere. This microstructure is directly derived from the polymeric precursor deprived of all the organic moieties that were removed during the decomposition phase. At this stage, the amorphous microstructure is characterized by an open-pore channel network. In oxidizing atmosphere, all the C content is eliminated, while in inert atmosphere the excessive C, not linked to Si atoms, is present as C clusters[9].

Increased temperatures lead to the devitrification process and in this phase the formation of the above-described nanodomains can be ascribed, with the generation of turbostratic C network (see again Fig. 1.7). The porosity previously mentioned can diminish, due to viscous flow mechanisms that start to be significant. For this reason, porosity is often defined as "transient"[13]. In this phase, although a certain degree of phase separation is achieved, a clear nucleation of crystallites has still to be observed[9].

Finally, at higher temperatures, an extensive formation of crystals is exhibited (SiC and SiO_2 for silicones), which can further increase their size by a further increase of temperature or dwell time[13].

1.4.2 Mechanical properties

The mechanical properties of SiOC have been investigated at different pyrolysis temperatures, although the difficulties arising from the limitation in the fabrication of sufficiently large components. Two methods have been used to process small bulk PDC samples: by the pyrolysis of warm-pressed[64-65], partially cross-linked polymer powders, or by casting a sol-gel solution[70] or a liquid polymer[50] (a silicone expressly for SiOC, or a polysilazane for SiCN, reported for comparison).

Elastic modulus for SiOC falls in the broad range of ≈ 80-155 GPa (≈ 57-113 GPa for SiCN): they are well below the values of the crystalline counterparts, because of their much more open structure. Densities are in the 1.85-2.35 g/cm^3 range for both SiCO and SiCN systems and they are an evidence of a rather open structure. Both the elastic modulus and the density generally are found to increase with increasing treatment temperature[50,70-71].

Poisson's ratio is generally low, SiOC exhibiting the lowest reported value for glasses and polycrystalline ceramics, only 0.11, and it is explained by the low atomic packing density and high cross-linking degree of SiOC (for the SiCN system, it is in the 0.21-0.24 range)[72].

Vickers hardness ranges from ≈ 5 to 9 GPa[70,72-73] and increases by increasing i) the pyrolysis temperature, ii) the amount of C incorporated; while fracture toughness is in the 0.56-3 MPa·m$^{0.5}$ range[71,73].

Creep resistance is surely one of the most remarkable characteristics of PDCs in general: creep is very limited up to 1300 °C for SiOC (1550 °C instead for SiCN) and it has been proposed that the relaxation occurs via viscous flow involving the O-rich regions[9].

1.4.3 Chemical properties

As already mentioned for other properties, chemical stability of PDCs is correlated with their microstructure: the phase separation observed at high temperatures in fact can negatively affect their chemical behaviour.

The chemical durability of SiOC glasses with different amounts of "free" C has been studied by Soraràu *et al.*[67] in highly basic and acidic (HF) conditions: the SiOC network exhibits higher durability than the pure silica glass (SiO_2) in both basic and acidic media, because of the presence of Si-C bonds. Moreover, amorphous siloxane-derived SiOC exhibits better properties than the sol-gel derived one. It was also observed that the chemical durability starts to decrease at temperatures higher than 1200 °C, due to the phase separation into SiO_2-based, SiC and C regions, since the SiO_2 species can easily be extracted.

The oxidation resistance is another important parameter that has been widely studied, since PDCs have been initially developed for high-temperature applications in oxidizing environments. For PDCs belonging to the SiOC, SiCN, SiC and SiBCN systems, a parabolic oxidation rate has been observed in several studies, showing the formation of a dense and continuous oxide layer, without cracks or bubbles[74-77]. Moreover, oxidation kinetic seems to increase with an increase of "free" C[9].

1.4.4 Electromagnetic properties

Depending on the polymeric precursor, composition, pyrolysis temperature and atmosphere, the room temperature electrical conductivity of PDCs can vary up to 15 orders of magnitude, typically in the range 10^{-10}-10^{-8} to 1 $(\Omega\cdot\text{cm})^{-1}$. Generally, for pyrolysis temperatures below 600 °C, PDCs can be better described as insulators, while, for amorphous PDCs obtained at pyrolysis temperatures above 800 °C, the conductivity increases with the temperature at which it is measured, showing a typical semiconducting behaviour[9].

Metallic-like (electron) conduction as high as 0.2-1 $(\Omega\cdot\text{cm})^{-1}$ has been found in polysilsesquioxanes-derived SiOC, pyrolyzed at temperatures above 1400 °C, when a percolation network of “free” C is formed. For high-C SiOC, such as that obtained from a phenyl-containing polysiloxane, the development of a continuous C network occurs at a lower temperature (1100 °C)[78].

A similar trend of the electrical conductivity with the pyrolysis temperature is found for SiCN.

The conductivity of PDCs can also be modified by addition of filler particles to the preceramic matrix, such as $MoSi_2$[78], C nanotubes[79] or graphene layers, due to the formation of percolation.

A rather new finding is the ultrahigh piezoresistivity, i.e. the change of the electrical resistivity due to an applied stress, shown by amorphous PDCs[80]. Piezoresistivity has also been found in SiOC ceramic derived from a commercial methyl-containing polysiloxane pyrolyzed at 1400 °C[81].

The tunable electrical properties, high piezoresistivity, together with the micro fabrication capability and excellent high-temperature thermal and mechanical properties, make the polymer-derived SiCN and SiOC excellent candidate materials for high-temperature sensors and ceramic MEMS for high temperature/corrosive-environment application[82], micro glow plugs[83] and electrode materials for Li-ion batteries[84].

Concerning the magnetic properties, they can be imparted to PDCs by the simple introduction of fillers exhibiting magnetic properties. For instance, ceramic foams of SiOC have been magnetically functionalized from a preceramic polymer containing Fe_3Si[85]. Another option is represented by the incorporation of α-iron or Fe_3O_4. A more elegant approach to produce PDCs with magnetic functionalities comprises the incorporation of the metallic iron atoms in the backbone of the polymer precursor, by a chemical modification with organometallic compounds, such as ferrocene[86].

1.4.5 Optical properties

Optical properties of PDCs are scarcely exploited if treated in inert atmosphere, because they are black: the reason for their colour has been generally ascribed to the presence, in the ceramic structure, of sp^2 C atoms, which form graphene layers that are responsible for the absorption of visible light, thus hindering the capability of PDCs for the production of optical devices.

A careful control of the chemical composition of the starting precursors, however, can lead to transparent SiOC glasses, as demonstrated by Soraràu et *al.*[87]. The most transparent SiOC glasses exhibit an optical absorption edge at 500-550 nm, and a broad luminescence band around 500 nm, attributable to the presence of sp^2 C clusters. The concentration of these clusters seems high enough to give an intense luminescence, but at the same time sufficiently low to allow a good transparency of the resulting glass.

Finally, SiOC glasses doped with Eu or Er have also been proposed[88]. Eu^{3+}-based luminescence was observed up to 400 °C. At higher pyrolysis temperatures, a broad blue emission band, centred at 450 nm, was formed due to *in situ* reduction of Eu^{3+} into Eu^{2+}.

Other examples regard the *in situ* formation of Si nanocrystals[89], producing a typical luminescence in the 600-800 nm range, or C and Au ion irradiation[90] of preceramic polymers.

2 Preceramic polymers containing fillers

2.1 Introduction

The polymer-to-ceramic conversion is a crucial phase of the whole processing of preceramic polymers, carried out above 400 °C in a selected atmosphere (e.g. inert/reactive, oxidizing/non-oxidizing) and consisting, as already discussed in §1.3.3, in a series of reactions/rearrangements that progressively eliminate all the organic groups of the starting precursor and generate a ceramic component. It has also been highlighted that it is usually accompanied by gas release, (isotropic) volume shrinkage (10-30 %, linear), weight loss (not lower than 15 %) and formation of porosity.

The main issue, which makes the direct conversion of a preceramic component to a dense ceramic virtually unachievable (unless its dimension is typically below a few hundred micrometers, as in the case of foams, fibers and coatings), is the generation of large defects, such as cracks and pores, that inevitably lead to the destruction of the whole component or to the deterioration of the mechanical properties, besides lower densities than expected. These defects arise from the fact that, during the pyrolysis, all the tensions related to the shrinkage, to the release of gaseous products and to the structural rearrangements cannot be relaxed by viscous flow or other mechanisms. Anyway, it should be also mentioned that some porosity could be eliminated at higher temperatures, often referred to as “transient” porosity.

As a direct consequence, a lot of effort has been put in the last years into developing novel methods to eliminate, or at least limit, the material shrinkage and the generation of cracks. In this context, a valid option can be represented by the direct pyrolysis of specifically-made scaffolds infiltrated by a liquid preceramic polymer[63]; otherwise the warm-pressing of partially cross-linked polymer powders[64,65]. Above all, the introduction of fillers has been so far the main strategy followed, enabling the fabrication of bulk components of size restricted only by the dimension of the pyrolysis furnace[9].

Fillers to be added before shaping can serve multiple purposes and have several effects. Their insertion in preceramic polymers demonstrated to be extremely effective in limiting the global shrinkage, maintaining at the same time all the advantages connected to the presence of a polymeric phase, above all, the easy shaping possibilities. They do not only reduce the shrinkage and the generation of defects, but they can also be used to obtain a composite material, to achieve higher densities or to tailor mechanical/electrical/magnetic properties. They can be of various nature (polymeric, metallic, ceramic), shape (equiaxed particles, elongate grains, whiskers, platelets, nanotubes, chopped/long/nano- fibers) and dimension (from nanoparticles to fibers of several centimetres). A further important distinction should be drawn between “passive” and “active” fillers, that will be more extensively discussed in §2.2 and §2.3: passive fillers do not react at all, at any stage, with the preceramic matrix, the ceramic residue or the heating atmosphere (SiC or Si_3N_4 powders), while active fillers can react mainly with the gaseous products, but also with the ceramic residue or the heating gas, generating carbides, nitrides, oxides (metallic/intermetallic fillers)[9].

The content of fillers introduced is another variable, in fact they can be added in small amount or they can even constitute the majority of the volume of the final part, and therefore in this case the polymeric precursor merely acts as a binder, allowing the achievement of high densities[9]. Anyway, the introduction of fillers modifies the final properties of the ceramic component, which becomes, in practice, a composite material constituted by a phase derived from the pyrolysis of the preceramic polymer and one or more secondary phases related to the incorporation of fillers.

2.2 Passive fillers

The incorporation of passive fillers is the most simple solution to effectively reduce the shrinkage and the defect generation arising from the polymer-to-ceramic conversion. They do not undergo any transformation or evolution during the pyrolysis and do not react with the ceramic residue, nor with the gaseous products released during the conversion into ceramic or with the heating gas. They remain totally inert during the whole processing of the preceramic polymer, as the name suggests, and they mainly serve the purpose of reducing the percentage of the whole transforming mass during the pyrolysis, thus diminishing the total weight loss, the shrinkage of the component and the presence of macrodefects, as well as the purpose of favouring the escape of gaseous species by the creation of an easier means of escape. Typical examples of passive fillers are SiC or Si_3N_4 powders, but Al_2O_3, B_4C and BN powders have been used as well[11]. Fig. 2.1 reports a schematic representation of passive fillers action[13].

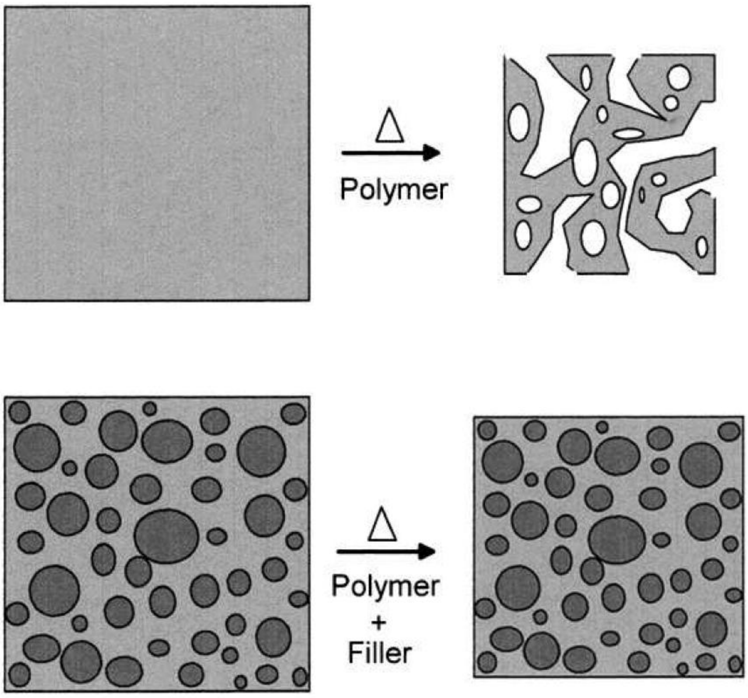

Fig. 2.1 Reduction of shrinkage of a PDC bulk component by the addition of a passive filler[13].

Concerning the amount of fillers to be incorporated, the added filler can even be predominant over the amount of polymer. In this case, the polymer act as a low-loss binder allowing the achievement of higher densities in the final ceramic, if compared to analogous parts produced using conventional binders, that are completely eliminated after green shaping. The advantageous effects of using preceramic polymers as binders are greatest for powders with the lowest packing densities (ultrafine powders), while a less pronounced effect is obtained with coarser powders[11]. Preceramic polymers can also be used as sintering additives for enhanced pressureless or pressure-aided sintering (e.g. hot-pressing, hot isostatic pressing, spark plasma sintering) of advances ceramics, such as Si_3N_4[91] or ZrB_2[92]. The intergranular phase provided by preceramic polymers, besides acting as a sintering aid during sintering and densification, could also offer enhanced creep resistance at high temperature, due to its higher viscosity (if compared to the intergranular glassy phase that is usually generated when more traditional sintering aids are used, e.g. Y_2O_3). In addition, they can provide an improved corrosion resistance and higher mechanical properties[13]. These features are always connected with the characteristic amorphous network of PDCs, which is constituted by a mixture of Si–O, Si–C, Si–N and other covalent bonds (depending on the nature of the starting precursor).

A further remark concerns the use of preceramic polymers as reactive binders for metallic powders, in fact the preceramic polymer can afford useful properties to the metal components, such as increased wear or corrosion resistance[93]. Functional fillers such as $MoSi_2$[78], although still classifiable as "passive", can impart new specific functional properties to the final ceramic, such as electrical conductivity or magnetic properties. In these cases, the content of filler introduced is crucial: as an example, electrical conductivity does not depend linearly on the percentage of electrically conductive filler introduced, but is subjected to an abrupt increase only when a critical concentration of filler is exceeded (Fig. 2.2 right). This critical value is often referred to as the "percolation threshold" and coincides with the transition from dispersed/isolated particles to an interconnected particles network. Similar results could also be obtained by introducing C nanotubes, graphene sheets or C nanofibers, to impart electrical conductivity and/or to enhance mechanical properties[79].

By use of fillers, the resulting mechanical properties of the final ceramics can be tailored and improved. As an example, toughness could be effectively enhanced even at very low (<10 vol%) filler concentrations, thanks to crack-tip bridging phenomena. Generally, the mechanical properties increase with increasing fillers volume fraction up to about 40–50 vol%, followed by a pronounced decrease at higher filler fractions, due to enhanced porosity formation[11] (Fig. 2.2 left).

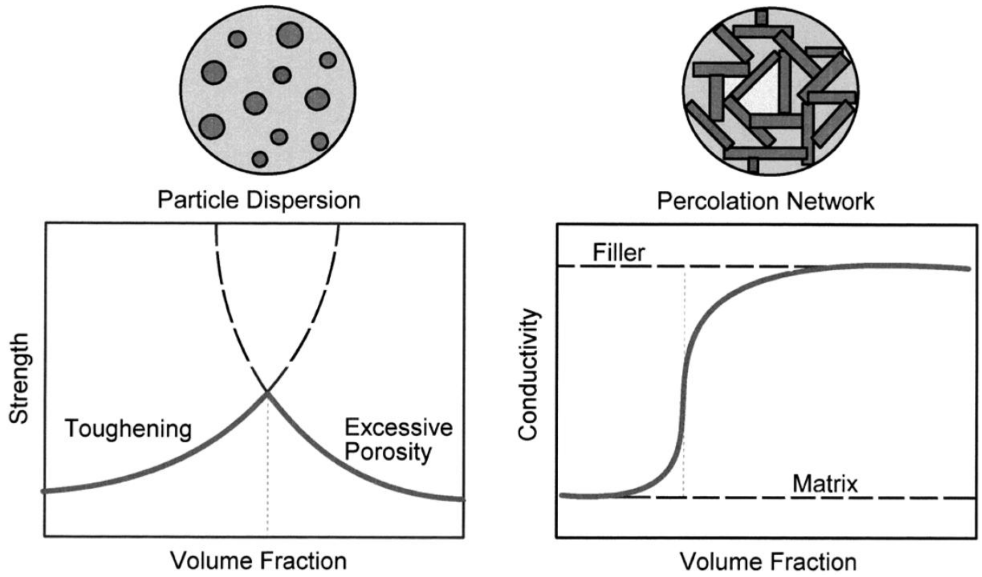

Fig. 2.2 Effect of filler loading on the mechanical properties (left) and field properties (electrical conductivity) of PDCs[11].

Finally, the coefficient of thermal expansion (CTE) of ceramic components can be tailored, with many advantages especially in the field of coatings (e.g. on metals) or for sealing applications[9]. The CTE of the filler phase is of fundamental importance, because it contributes in determining the global CTE of the final composite. However, it should be highlighted that a high CTE mismatch between the ceramic residue and the filler phase could cause the formation of micro-cracks, that could negatively affect the final mechanical properties.

One last remark should be done concerning the economic point of view: the introduction of passive fillers may also represent a way of lowering the global cost of the final ceramic product.

2.3 Active fillers

The distinction between “active” and “passive” fillers was introduced in the early 90s, as a result of the investigations of Prof. Peter Greil and co-workers. Specific fillers, above all (but non only) metallics and intermetallic compounds, have been termed “active”, as they react either with the ceramic matrix, the thermolysis gaseous products and the heating gas during the polymer-to-ceramic conversion, generating carbides, nitrides, oxides or silicides. A large volume of work has been devoted to the implementation of this method to fabricate near-net-shape components from the conversion of preceramic polymers into bulk ceramic components with extremely limited (or event absent) global shrinkage. This is achievable thanks to the incorporation of metallic fillers, by virtue of the formation of metallic compounds by reaction of metallic fillers with gaseous species from the polymer decomposition, or alternatively with the furnace atmosphere. The formation of these compounds occurs with a volume expansion up to 50 %vol, thus compensating the polymer shrinkage[9]. Fig. 2.3 offers a schematic representation of active fillers action.

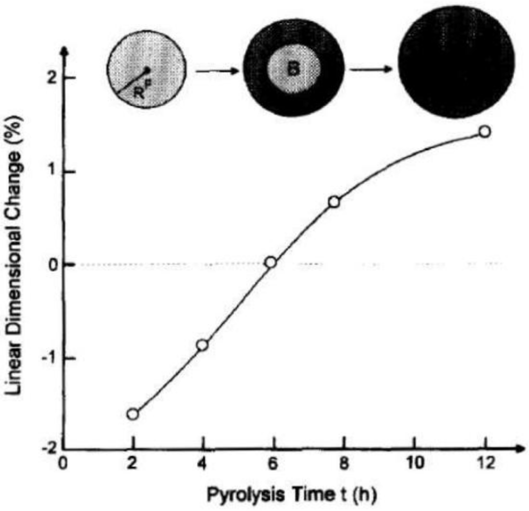

Fig. 2.3 Linear dimensional change of polysiloxane/40 vol% boron mixture pyrolyzed at 1480 °C in N_2, as a function of filler reaction time[94].

Especially when working with active fillers, the choice of polymers/fillers combinations could not be done arbitrarily, but must be based on thermodynamic stability criteria, filler expansion characteristics and reaction kinetic limitation (e.g. temperature dependent formation and elimination of transient open porosity, which govern material transport and the reaction process of filler particles)[12]. Linear dimensional changes of less than 0.1 % could be obtained with time-temperature controlled pyrolysis of the material, which allow a high precision manufacturing of complex shape components[11]. The resulting material is thus generated by the combination of the preceramic polymer, the active filler introduced, the gaseous by-products deriving from the decomposition of the preceramic polymer and the treatment atmosphere. As an example, if $CrSi_2$ is used as an active filler, at sufficiently high temperatures (around 750 °C) can react with C from the ceramic residue of the preceramic polymer (to give the formation of Cr_3C_2) and with the N_2 of the atmosphere (to give the formation of Si_3N_4). In this case, while the formation of carbides is observed also in Ar atmosphere, the formation of Si_3N_4 is strictly connected with the N_2 pressure in the furnace atmosphere. Moreover, the microstructure of the open-pores network (deriving from the pyrolysis of the preceramic polymer) is fundamental as well in determining the reaction of the fillers. For this reason, it is generally better to consider the ”effective” N_2 pressure in the open pore channel network, which depends on the nitrogen pressure and the porosity microstructure[13].

Still concerning the incorporation of metallic fillers, transition metal carbides can form, such as NbC, Mo_2C or WC, always depending on the polymer precursors/fillers combinations, greatly improving the hardness of the final ceramics. Graphite powder can be even added to siloxanes to exploit its carbothermal reduction reactions with the silica-based matrix, leading to the formation of SiC[9].

Oxides fillers can be both active or inert, depending on the heating atmosphere, firing temperature and their dimension. For instance, processing in inert atmosphere can lead to the formation of metallic particles, or silicides, carbides and nitrides, because of reduction reactions with the C present in the preceramic precursor. Another example is given by Al_2O_3 powders incorporated to obtain oxide ceramics to be processed in air: if micro-sized α-Al_2O_3 is incorporated in a polysiloxane, it remains unreacted up to 1400 °C, then the transformation into mullite starts at 1500 °C; however, if a nano-sized γ-Al_2O_3 powder is used, the reaction with the siloxane-derived silica matrix occurs at temperatures as low as 1250 °C, leading to a single phase ceramic at 1350 °C[95].

Polymeric fillers can also be added to preceramic polymers. They totally decompose during the pyrolysis and therefore act as sacrificial fillers, leading to the formation of porosity, whose size and amount depend on the characteristics of the filler itself. This approach is particularly interesting to create a large volume of porosity: in fact, expandable polymeric microbeads can be combined with siloxanes, then the mixture can be heated at temperatures below 150 °C, so that the microbeads undergo a four- to eightfold volume expansion within the molten silicone resin matrix[96].

A fundamental parameter in determining the effectiveness of the active fillers is time. This is due to the fact that the total time required for a complete conversion of a filler particle must consider the diffusion of gaseous reactants through the open porosity surrounding the particle, the time of penetration and diffusion of the reactants through the reaction product layer on the particle surface and finally the time of reaction with the unreacted core at the interface. Based on these considerations and on other thermodynamics parameters, numeric models have been obtained[12], from which some general trends could be derived. For example, with decreasing particle size, filler reaction time is reduced so that, within a given reaction time, a higher fraction of smaller filler particles is transformed compared to larger particles, and, hence, reduction of overall shrinkage is higher. A similar tendency should result if the concentration of gaseous reactants increases, as it is the case at higher ”effective” N_2 pressures in the pore channel network. With increasing N_2 pressure, diffusional transport in the porous compact is faster because of a reduction in mean free path length of the gaseous molecules, thus increasing the chemical driving force for filler reaction, and reducing the total shrinkage.

Finally, it should also be kept in mind that, since the active fillers react with gaseous by-products deriving from the decomposition of the polymeric phase, the final ceramic yield of the preceramic polymer is then higher than when no active fillers are present[9].

Although the use of active-filler-controlled pyrolysis of preceramic polymers has proven to be extremely effective in reducing the total amount of porosity in the final ceramics, with consequent improved mechanical properties, it must be said that this technique requires an extremely accurate control of all the pyrolysis conditions, as well as the characteristics of the raw materials. Although theoretical models have been derived for an *a priori* selection of processing conditions and fillers characteristics, small variations in particle environment, particle distribution and particle physical properties could finally result in significant variations in kinetic variables. For this reason, a trial and error procedure is still generally required to optimize the final properties of the material.

2.4 Final considerations

In this chapter, the incorporation of active/passive fillers has been described as the most successful strategy to reduce shrinkage, weight loss and formation of defects in the PDCs, leading to the formation of a sort of composite material, comprising the ceramic residue from the polymer and one or more phases due to the fillers. Anyway, besides active and passive fillers, a third option can be considered and has been exploited in the present thesis.

A distinction has been drawn between passive and active fillers. It has been explained that the use of passive fillers is surely the most simple strategy, consisting in the “dilution” of the total transforming mass during the pyrolysis, by the combination of the polymeric phase with an inert phase which does not evolve, at any pyrolysis stage. Besides being effective in reducing the shrinkage, this strategy can also impart additional features like electrical conductivity or other properties. Passive fillers can be added in large amount and no special precautions are required.

The second and more interesting option is represented by the addition of active filler (especially metallic and intermetallic), that have an active role in compensating the shrinkage of the preceramic polymer, expanding by reaction with the ceramic residue, the gaseous by-products or the furnace atmosphere. In this case, an extremely accurate control of the processing conditions (pyrolysis temperature, time and atmosphere) is required, as well as much concentration must be devoted to the selection of the precursors/fillers combination and to the choice of the filler amount, in order to obtain the final desired characteristics in the ceramic product. Again, a number of properties can be effectively tailored and improved using different types of active fillers.

A novel approach, besides these two strategies, consists in incorporating fillers that are intended to fully react only with the ceramic residue of the polymeric precursors, in order to obtain the formation of specific crystalline phases, that are generally not directly achievable by the simple pyrolysis of a preceramic polymer, rather than to compensate the shrinkage.

In the light of this third possibility, the present Ph.D. thesis has been devoted to an organic investigation of the applications that this strategy could offer, starting from silicone-based mixtures incorporating reactive fillers. By this route, the advantages connected with the presence of a polymeric phase, especially in the shaping step of the processing, can even be combined with the advantages related to the whole processing cycle of preceramic polymers, leading to the realization of ceramic components at relatively low temperatures (even below 1200 °C) and avoiding the conventional methodologies. The fillers incorporated in the preceramic mixtures can also be exploited as foaming agents or liquid phase formers, thus helping respectively the direct shaping in porous bodies or the obtainment of glass-ceramic components. However, the main purpose of the fillers, in this thesis, is to serve as oxide precursors, in order to synthesize crystalline ceramics after pyrolysis of specific compositions, achievable by the reaction occurring between the ceramic residue of the polymeric precursors and the oxides deriving from the thermal decomposition of reactive fillers. The type of fillers can be conveniently selected according to the desired final composition; therefore, a wide variety of ceramic systems can be achieved, simply by changing the proportions and composition of the starting polymers and fillers.

The first part of the following chapters is focused on the realization of peculiar ceramic and glass-ceramic formulations, that are well known to have very pronounced biological properties, thus having applicability in the biomedical fields as bioceramics for bone regeneration implants. In the second part, instead, there will be a technology transfer to other silicate formulations specifically designed for other functional applications.

References

[1] W. Ainger, J. M. Herbert, ”The Preparation of Phosphorus-Nitrogen Compounds as Non-Porous Solids”; pp. 168–82 in Special Ceramics, Edited by P. Popper. Academic press, New York, 1960

[2] P. G. Chantrell, P. Popper, ”Inorganic Polymers and Ceramics”; pp. 87–103 in Special Ceramics, Edited by P. Popper. Academic Press, New York, 1965.

[3] Verbeek, ”Production of Shaped Articles of Homogeneous Mixtures of Silicon Carbide and Nitride”; Ger. Offen., 2218960 (Bayer AG), November 8, U.S. Patent No. 3853567, 1973.

[4] W. Verbeek, G. Winter, ”Formkoerper aus Siliciumcarbid und Verfahren zu Ihrer Herstellung”; Ger. Offen., 2236078, 1974.

[5] G. Winter, W. Verbeek, M. Mansmann, ”Formkoerper aus Homogenen Mischungen von Siliciumcarbid und Siliciumnitrid und Verfahren zu Ihrer Herstellung”; Ger. Offen., 2243527, 1974.

[6] G. Fritz, B. Raabe, ”Bildung siliciumorganischer Verbindungen. V. Die Thermische Zersetzung von $Si(CH_3)_4$ und $Si(C_2H_5)_4$,” Z. Anorg. Allg. Chem., 286, 149–67 (1956).

[7] S. Yajima, J. Hayashi, M. Imori, ”Continuous Silicon Carbide Fiber of High Tensile Strength”, Chem. Lett., 4 [9] 931–4 (1975).

[8] S. Yajima, Y. Hasegawa, K. Okamura, I. Matsuzawa, ”Development of High Tensile Strength Silicon Carbide Fibre Using an Organosilicon Polymer Precursor”, Nature (London), 273, 525–7 (1978).

[9] P. Colombo, G. Mera, R. Riedel, G. D. Sorarù, “Polymer-Derived Ceramics: 40 Years of Research and Innovation in Advanced Ceramics”, J. Am. Ceram. Soc., 1837 1805–1837 (2010).

[10] W. Krenkel, “Ceramic matrix composites”, Springer (2003).

[11] P. Greil, “Polymer Derived Engineering Ceramics”, Adv. Eng. Mater., 2 [6] 339–348 (2000).

[12] P. Greil, “Active-Filler-Controlled Pyrolysis of Preceramic Polymers”, J. Am.Ceram. Soc., 78 [4] 835–848 (1995).

[13] G. Parcianello, “Advanced ceramics from precramic polymers and fillers”, Doctoral thesis (2012)

[14] Abe, Y., Gunji, T., Progress in polymer science, vol. 29 (3), p. 149 (2004).

[15] Jovanovic, J. D., Tehinika (Belgrade, Yugoslavia), vol. 58, p. 4 (2003).

[16] W. J. Noll, Chemistry and Technology of Silicones, Academic Press, San Diego, CA, 1968.

[17] M. Zeldin, ”An Overview of Inorganic and Organometallic Polymers”; pp. 151–64 in Improved Fire- and Smoke Resistant Materials for Commercial Aircraft Interiors, National Academy Press, Washington D.C., 1995.

[18] T. C. Kendrick, B. Parbhoo, J. W. White, ”Siloxane Polymers and Copolymers”; pp. 1289–361 in The Chemistry of Organic Silicon Compounds, Edited by S. Patai, and Z. Rappoport. John Wiley & Sons, Chichester, 1995.

[19] R. Corriu, P. Jutzi (eds). Tailor-Made Silicon–Oxygen Compounds from Molecules to Materials, Vieweg & Sohn, Braunschweig/Wiesbaden, Germany, 1996.

[20] Y. Abe, T. Gunji, ”Oligo- and Polysiloxanes”, Progress in Polymer Science, 29 [3] 149–82 (2004).

[21] R. Riedel, G. Mera, R. Hauser, A. Klonczynski, “Silicon-based polymer-derived ceramics: synthesis, properties and applications - a review”, J. Ceram. Soc. Jpn., 114 [6] 425–444 (2006).

[22] Colombo, P., Bernardo, E., Parcianello, G. (2013). Multifunctional advanced ceramics from preceramic polymers and nano-sized active fillers. Journal of the European Ceramic Society, 33(3), 453-469.

[23] R. Haug, M. Weinmann, J. Bill, F. Aldinger, ”Plastic Forming of Preceramic Polymers,” J. Eur. Ceram. Soc., 19, 1–6 (1999).

[24] D. Galusek, J. Sedlacek, R. Riedel, ”Al_2O_3–SiC Composites Prepared by Warm Pressing and Sintering of an Organosilicon Polymer-Coated Alumina Powder,” J. Eur. Ceram. Soc., 27, 2385–92 (2007).

[25] R. Kumar, Y. Cai, P. Gerstel, G. Rixecker, F. Aldinger, ”Processing, Crystallization and Characterization of Polymer Derived Nano-Crystalline Si–B– C–N Ceramics,” J. Mater. Sci., 41, 7088–95 (2006).

[26] B. C. Mutsuddy, ”Use of Organometallic Polymer for Making Ceramic Parts by Plastic Forming Techniques,” Ceram. Inter., 13, 41–53 (1987).

[27] Y.-W. Kim, J.-H. Eom, C. Wang, C. B. Park, ”Processing of Porous Silicon Carbide Ceramics from Carbon-Filled Polysiloxane by Extrusion and Carbothermal Reduction,” J. Am. Ceram. Soc., 91, 1361–4 (2008)

[28] G. Perale, C. Giordano, F. Daniele, M. Masi, P. Colombo, L. Gottardo, S. Maccagnan, ”A Novel Process for the Manufacture of Ceramic Microelectrodes for Biomedical Applications,” Int. J. Appl. Ceram. Technol., 5, 37–43 (2008).

[29] T. Zhang, J. R.G. Evans, J. Woodthorpe, ”Injection Moulding of Silicon Carbide Using an Organic Vehicle Based on a Preceramic Polymer,” J. Eur. Ceram. Soc., 15, 729–34 (1995).

[30] S. Walter, D. Suttor, T. Erny, B. Hahn, P. Greil, ”Injection Moulding of Polysiloxane/FillerMixtures for Oxycarbide Ceramic Composites,” J. Eur. Ceram. Soc., 16, 387–93 (1996).

[31] O. Goerke, E. Feike, T. Heine, A. Trampert, H. Schubert, ”Ceramic Coatings Processed by Spraying of Siloxane Precursors (Polymer-Spraying),” J. Eur. Ceram. Soc., 24, 2141–7 (2004).

[32] P. Colombo, T. E. Paulson, C. G. Pantano, ”Synthesis of Silicon Carbide Thin Films With Polycarbosilane (PCS),” J. Am. Ceram. Soc., 80, 2333–40 (1997).

[33] T. P. Smirnova, A. M. Badalian, L. V. Yakovkina, V. V. Kaichev, V. I. Bukhtiyarov, A. N. Shmakov, I. P. Asanov, V. I. Rachlin, A. N. Fomina, ”SiCN Alloys Obtained by Remote Plasma Chemical Vapour Deposition from Novel Precursors,” Thin Solid Films, 429, 144–51 (2003).

[34] A. R. Bunsell, A. Piant, ”A Review of the Development of Three Generations of Small Diameter Silicon Carbide Fibres,” J. Mater. Sci., 41, 823–39 (2006).

[35] K. Okamura, T. Shimoo, K. Suzuya, K. Suzuki, ”SiC-Based Ceramic Fibers Prepared via Organic-to-Inorganic Conversion Process–A Review,” J. Jpn. Ceram. Soc., 114, 445–54 (2006).

[36] K. Satoa, A. Tezuka, O. Funayama, T. Isoda, Y. Terada, S. Kato, M. Iwata, ”Fabrication and Pressure Testing of a Gas-Turbine Component Manufactured by a Preceramic-Polymer-Impregnation Method,” Comp. Sci. Tech., 59, 853–9 (1999).

[37] M. Erdal, S. I. Güçeri, S. C. Danforth, ”Impregnation Molding of Particle-Filled Preceramic Polymers: Process Modeling,” J. Am. Ceram. Soc., 82, 2017–28 (1999).

[38] I.-K. Sung, S.-B. Yoon, J.-S. Yu, D.-P. Kim, ”Fabrication of Macroporous SiC from Templated Preceramic Polymers,” Chem. Comm., 1480–1 (2002).

[39] P. Colombo, V. Sglavo, E. Pippel, J. Woltersdorf, ”Joining of Reaction-Bonded Silicon Carbide Using a Preceramic Polymer,” J. Mater. Sci., 33, 2409–16 (1998).

[40] C. A. Lewinsohn, P. Colombo, I. Riemanis, O. Unal, ”Stresses Arising During Joining of Ceramics Using Preceramic Polymers,” J. Am. Ceram. Soc., 84, 2240–4 (2001).

[41] C. A. Lewinsohn and S. Elangovan, ”Development of Amorphous, Non- Oxide Seals for Solid Oxide Fuel Cells,” Ceram. Eng. Sci. Proc., 24 [3] 317–22 (2003).

[42] M. Schulz, M. Borner, J. HauXelt, R. Heldele, ”Polymer Derived Ceramic Microparts from X-Ray Lithography/Cross-Linking Behavior and Process Optimization,” J. Eur. Ceram. Soc., 25, 199–204 (2005).

[43] H.-J. Lee, T.-H. Yoon, D.-P. Kim, ”Fabrication of Microfluidic Channels Derived from a UV/Thermally Cured Preceramic Polymer via a Soft Lithographic Technique,” Microelect. Eng., 84, 2892–5 (2007).

[44] T.-H. Yoon, H.-J. Lee, J. Yan, D.-P. Kim, ”Fabrication of SiCBased Ceramic Microstructures from Preceramic Polymers With Sacrificial Templates and Lithographic Techniques–A Review,” J. Jpn. Ceram. Soc., 114, 473–9 (2006).

[45] C. Vakifahmetoglu, I. Menapace, A. Hirsch, L. Biasetto, R. Hauser, R. Riedel, P. Colombo, “Highly porous macro- and micro-cellular ceramics from a polysilazane precursor”, Ceram. Int., 35 [8] 3281–3290 (2009).

[46] R. M. da Rocha, P. Greil, J. C. Bressiani, A. H. de Almeida Bressiani, ”Complex-Shaped Ceramic Composites Obtained by Machining Compact Polymer- Filler Mixtures,” Mater. Res., 8, 191–6 (2005).

[47] S. Duperrier, C. Gervais, S. Bernard, D. Cornu, F. Babonneau, C. Balan, P. Miele, ‘‘Design of a Series of Preceramic B-Tri(methylamino)borazine-Based Polymers as Fiber Precursors: Architecture, Thermal Behavior, and Melt-Spinnability,’’ Macromolecules, 40, 1018–27 (2007).

[48] B. Clauss, D. Schawaller, “Modern Aspects of Ceramic Fiber Development”, Advances in Science and Technology, 50 1–8 (2006).

[49] R. Harshe, C. Balan, R. Riedel, ”Amorphous Si(Al)OC Ceramic from Polysiloxanes: Bulk Ceramic Processing, Crystallization Behavior and Applications,” J. Eur. Ceram. Soc., 24, 3471–82 (2004).

[50] N. Janakiraman F. Aldinger, ”Fabrication and Characterization of Fully Dense Si–C–N Ceramics from a Poly(ureamethylvinyl)Silazane Precursor,” J. Eur. Ceram. Soc., 29, 163–73 (2009).

[51] M. Narisawa, A. Idesaki, S. Kitano, K. Okamura,M. Sugimoto, T. Seguchi, M. Itoh, ”Use of Blended Precursors of Poly(vinylsilane) in Polycarbosilane for Silicon Carbide Fiber Synthesis With Radiation Curing,” J. Am. Ceram. Soc., 82, 1045–51 (1999).

[52] A. Idesaki, M. Narisawa, K. Okamura, M. Sugimoto, Y. Morita, T. Seguchi M. Itoh, ”Application of Electron Beam Curing for Silicon Carbide Fiber Synthesis from Blend Polymer of Polycarbosilane and Polyvinylsilane,” Radiat. Phys. Chem., 60, 483–7 (2001).

[53] M. Schulz, M. Borner, J. Gottert, T. Hanemann, J. Hausselt, G. Motz, ”Cross-Linking Behaviour of Preceramic Polymers Effected by UV- and Synchrotron Radiation,” Adv. Eng. Mater., 6, 676–80 (2004).

[54] T. Friedel, N. Travitzky, F. Niebling,M. Scheffler, P. Greil, ‘‘Fabrication of Polymer Derived Ceramic Parts by Selective Laser Curing,’’ J. Eur. Ceram. Soc., 25, 193–7 (2005).

[55] C. Wang, J. Wang, C. B. Park, Y.-W. Kim, ‘‘Cross-Linking Behavior of a Polysiloxane in Preceramic Foam Processing,’’ J.Mater. Sci. Lett., 39, 4913–5 (2004).

[56] C. Balan, R. Riedel, ‘‘Rheological Investigations of a Polymeric Precursor for Ceramic Materials: Experiments and Theoretical Modeling,’’ J. Optoelectr. Adv. Mater., 8, 561–7 (2006).

[57] Y. D. Blum, K. B. Schwartz, R. M. Laine, ‘‘Preceramic Polymer Pyrolysis. Part 1 Pyrolytic Properties of Polysilazanes,’’ J. Mater. Sci., 24, 1707–18 (1989).

[58] M. N. Rahaman, “Ceramic processing and sintering”, CRC (2003).

[59] J. C. Pivin, P. Colombo, ‘‘Ceramic Coatings by Ion Irradiation of Polycarbosilanes and Polysiloxanes. Part I: Conversion Mechanism,’’ J. Mater. Sci., 32, 6163–73 (1997).

[60] J. C. Pivin, P. Colombo, ‘‘Ceramic Coatings by Ion Irradiation of Polycarbosilanes and Polysiloxanes. Part II: Hardness and Thermochemical Stability,’’ J. Mater. Sci., 32, 6175–82 (1997).

[61] F. I. Hurwitz, P. Heimann, S. C. Farmer and D. M. Hembree, “Characterization of the pyrolytic conversion of polysilsesquioxanes to silicon oxycarbides”, Journal of Materials Science, 28 [24] 6622–6630 (1993).

[62] T. Isoda, H. Kaya, H. Nishii, O. Funayama, T. Suzuki, Y. Tashiro, “Perhydropolysilazane precursors to silicon nitride ceramics”, J. Inorg. Organomet. P., 2 [1] 151–160 (1992).

[63] Available at http://www.ceramicore.com

[64] R. Riedel, G. Passing, H. Schönfelder, R. J. Brook, ”Synthesis of Dense Silicon-Based Ceramics at Low Temperatures,” Nature (London), 355, 714–7 (1992).

[65] G. D. Sorarù , V.M. Sglavo, F. Vulcan, F. Babonneau, ”Fabrication and Characterization of β’-sialon Components from Polymeric Precursors,” Mater. Res. Soc. Symp. Proc., 287, 245–50 (1993).

[66] G. D. Sorarù, D. Suttor, “High temperature stability of sol-gel-derived SiOC glasses”, J. Sol-gel Sci. Techn., 14 69-74 (1999).

[67] G. D. Sorarù, S. Modena, E. Guadagnino, P. Colombo, J. Egan, C. Pantano, “Chemical Durability of Silicon Oxycarbide Glasses”, J. Am. Ceram. Soc., 85 [6] 1529–1536 (2002).

[68] R. E. Loehman, ”Oxynitride Glasses”; pp. 119–49 in Treatise on Materials Science and Technology, Vol. 26, Glass IV. Edited by M. Tomozawa and R. H. Doremus. Academic Press, New York, 1985.

[69] Saha, A., Raj, R., Williamson, D. L. (2006). A Model for the Nanodomains in Polymer-Derived SiCO. Journal of the American Ceramic Society, 89(7), 2188-2195.

[70] G. D. Sorarù, E. Dallapiccola, G. D’Andrea, ”Mechanical Characterization of Sol–Gel-Derived Silicon Oxycarbide Glasses,” J. Am. Ceram. Soc., 79, 2074–80 (1996).

[71] V. Moraes, L. V. Interrante, ”Processing, Fracture Toughness, and Vickers Hardness of Allylhydridopolycarbosilane-Derived Silicon Carbide,” J. Am. Ceram. Soc., 86, 342–6 (2003).

[72] C. Moysan, R. Riedel, R. Harshe, T. Rouxel, F. Augereau, ”Mechanical Characterization of a Polysiloxane-Derived SiOC Glass,” J. Eur. Ceram. Soc., 27, 397–403 (2007).

[73] G. M. Renlund, S. Prochazka, R. H. Doremus, ”Silicon Oxycarbide Glasses: Part II. Structure and Properties,” J. Mater. Res., 6, 2723– 34 (1991).

[74] G. Chollon, ”Oxidation Behaviour of Ceramic Fibres from the Si–C–N–O System and Related Sub-Systems,” J. Eur. Ceram. Soc., 20, 1959–74 (2000).

[75] S. Modena, G. D. Sorarù, Y. Blum, R. Raj, ”Passive Oxidation of an Effluent System: The Case of Polymer-Derived SiCO,” J. Am. Ceram. Soc., 88, 339–45 (2005).

[76] L. Bharadwaj, Y. Fan, L. Zhang, D. Jiang, L. An, ”Oxidation Behavior of a Fully Dense Polymer-Derived Amorphous Silicon Carbonitride Ceramic,” J. Am. Ceram. Soc., 87, 483–6 (2004).

[77] P. Baldus, M. Jansen, D. Sporn, ”Ceramic Fibers for Matrix Composites in High-Temperature Engine Applications,” Science, 285, 699–703 (1999).

[78] J. Cordelair P. Greil, ”Electrical Characterization of Polymethylsiloxane/$MoSi_2$-Derived Composite Ceramics”, J. Am. Ceram. Soc., 84, 2256–9 (2001).

[79] E. Ionescu, A. Francis, R. Riedel, ”Dispersion Assessment and Studies on AC Percolative Conductivity in Polymer-Derived Si–C–N/CNT Ceramic Nanocomposites,” J. Mater. Sci., 44, 2055–62 (2009)

[80] L. G. Zhang, Y. S. Wang, Y.Wei, W. X. Xu, D. J. Fang, L. Zhai, K. C. Lin, L. N. An, ”A Silicon Carbonitride Ceramic With Anomalously High Piezoresistivity,” J. Am. Ceram. Soc., 91 [4] 1346–9 (2008).

[81] R. Riedel, L. Toma, E. Janssen, J. Nuffer, T. Melz, H. Hanselka, ‘‘Piezoresistive Effect in SiOC Ceramics for Integrated Pressure Sensors,’’ J. Am. Ceram. Soc., 93 [4] 920–4 (2010).

[82] L.-A. Liew, R. A. Saravanan, V. M. Bright, M. L. Dunn, J. W. Daily, R. Raj, ”Processing and Characterization of Silicon Carbon-Nitride Ceramics: Application of Electrical Properties Towards MEMS Thermal Actuators,” Sens. Act. A: Phys., 103 [1–2] 171–81 (2003).

[83] L. A. Liew, V.M. Bright, R. Raj, ”A Novel Micro Glow Plug Fabricated from Polymer-Derived Ceramics: In Situ Measurement of High-Temperature Properties and Application to Ultrahigh-Temperature Ignition,” Sensors Actuators A: Phys., 104 [3] 246–62 (2003).

[84] W. Xing, A. M. Wilson, K. Eguchi, G. Zank, J. R. Dahn, ”Pyrolyzed Polysiloxanes for Use as Anode Materials in Lithium-Ion Batteries,” J. Electrochem. Soc., 144 [7] 2410–6 (1997).

[85] L. Biasetto, A. Francis, P. Palade, G. Principi, P. Colombo, ”Polymer-DerivedMicrocellular SiOC Foams With Magnetic Functionality,” J. Mater. Sci., 43, 4119–26 (2008).

[86] B.-Z. Tang, R. Petersen, D. A. Foucher, A. J. Lough, N. Coombs, R. Sodhi, I. Manners, ”Novel Ceramic and Organometallic Depolymerization Products from Poly(Ferrocenylsilanes) via Pyrolysis,” J. Chem. Soc., Chem. Commun., 523–5 (1993).

[87] G. D. Sorarù , ”Silicon Oxycarbide Glasses from Gels,” J. Sol–Gel Sci. Technol., 2, 843–8 (1994).

[88] Y. Zhang, A. Quaranta, G. D. Sorarù , ”Synthesis and Luminescent Properties of Novel Eu^{2+}-Doped Silicon Oxycarbide Glasses,” Opt. Mater., 24, 601–5 (2004).

[89] G. D. Sorarù , S. Modena, P. Bettotti, G. Das, G. Mariotto, L. Pavesi, ”Si nanocrystals Obtained Through Polymer Pyrolysis,” Appl. Phys. Lett., 83, 749–51 (2003).

[90] J. C. Pivin, P. Colombo, G. D. Soraru‘ , ”Comparison of Ion Irradiation Effects in Silicon-Based Preceramic Thin Films,” J. Am. Ceram. Soc., 83, 713–20 (2000).

[91] S. T. Schwab, C. R. Blanchard, R. C. Graef, ‘‘The Influence of Preceramic Binders on the Microstructural Development of Silicon Nitride,’’ J. Mater. Sci., 29, 6320–8 (1994).

[92] S. Zhu, W. G. Fahrenholtz, G. E. Hilmas, ‘‘Enhanced Densification and Mechanical Properties of ZrB_2–SiC Processed by a Preceramic Polymer Coating Route,’’ Scripta Mater., 59, 123–6 (2008).

[93] S. Yajima, ‘‘Special Heat-Resisting Materials from Organometallic Polymers,’’ Am. Ceram. Soc. Bull., 62 [8] 893–915 (1983).

[94] P. Greil, “Near Net Shape Manufacturing of Polymer Derived Ceramics”, J. Eur. Ceram. Soc., 132-136 1981–1984 (1997).

[95] F. Griggio, E. Bernardo, P. Colombo, G. L. Messing, ‘‘Kinetic Studies of Mullite Synthesis from Alumina Nanoparticles and a Preceramic Polymer,’’ J. Am. Ceram. Soc., 91, 2529–33 (2008).

[96] Y.-W. Kim, S.-H. Kim, H.-D. Kim, C. B. Park, ‘‘Processing of Closed-Cell Silicon from a Preceramic Polymer,’’ J. Mater. Sci., 39, 5647–52 (2004).

Part I

Biosilicates from preceramic polymers and reactive fillers

3 Bioglasses

3.1 Introduction

Bioglasses, like all bioactive materials, stimulate a biological response from the body at the interface with the material, i.e. they are able to bond with living tissues, thanks to the formation of a hydroxyapatite-like layer on their surface when they are in contact with body fluids. In particular, 45S5 (45 wt% SiO_2, 26.4 wt% CaO, 26.4 wt% Na_2O, 6 wt% P_2O_5) and 58S (58.2 wt% SiO_2, 32.6 wt% CaO, 9.2 wt% P_2O_5) compositions are “Class A” bioactive materials, so they are not simply osteoconductive (they stimulate bone growth along the surface of the bioactive material) and capable of bonding to hard tissue, but they are also osteoproductive (they stimulate the growth of new bone on the material away from the interface with bone) and capable of bonding to soft tissue. In addition, these two compositions of bioglass are bioresorbable, that is they dissolve in contact with body fluids and their dissolution products are not toxic[1,2].

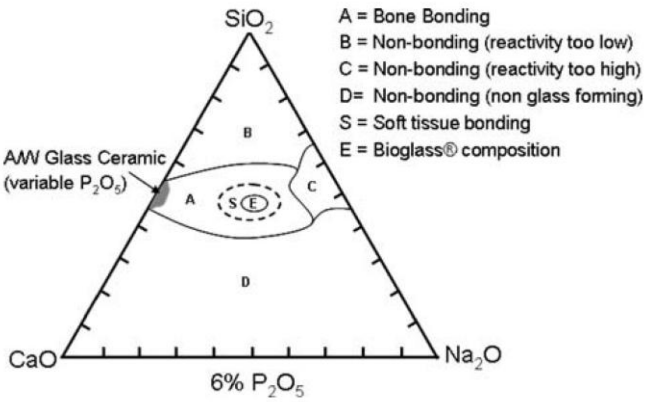

Fig. 3.1 Compositional dependence (wt%) of bone bonding and soft tissue bonding of bioactive glasses and glass-ceramics[2].

Fig. 3.1 shows the compositional diagram for bone-bonding referring to Na_2O-CaO-P_2O_5-SiO_2 glasses, with a constant 6 wt% of P_2O_5. Compositions in the middle (region A) form a bond with bone and in the region S form a bond with soft tissues, such as 45S5 Bioglass. Silica glasses in region B (such as windows, bottles, microscope slide glasses) behave as nearly inert materials, with a very low reactivity) and elicit a fibrous capsule at the implant-tissue interface. Glasses within region C are resorbable and disappear within 10-30 days of implantation because of their too high reactivity. Glasses in region D are not technically practical and therefore have not been tested as implants[3].

The mechanism at the basis of the bone bonding ability exhibited by bioglass consists of a rapid sequence of chemical reactions occurring at the surface of the implant when inserted into living tissues, involving chemical degradation with release of ions such as Na, Si, Ca, and causing the conversion of the surface into a carbonated-substituted hydroxyapatite-like layer[1-5].

There are 11 stages in process of complete bonding of bioactive glass to bone, five of which are chemical and six are the biological response[4].

1. Rapid exchange of Na^+ and Ca^{2+} of glass with H^+ or H_3O^+ from the solution, with subsequent hydrolysis of the silica groups, creation of silanol (Si-OH) and increase of pH.
2. The increase in the hydroxyl concentration of the solution leads to an attack on the silica glass network, causing dissolution of silica in the form of silicic acid $Si(OH)_4$ into the solution and the continued formation of Si-OH groups.

3. Condensation and repolymerization of an amorphous SiO_2-rich layer (1-2 µm thick) on the surface of the glass depleted in Na^+ and Ca^{2+}.
4. Further dissolution of the glass, coupled with migration of Ca^{2+} and PO_4^{3-} ions from the glass to the surface through the SiO_2-rich layer, forming an amorphous calcium phosphate layer on top of the SiO_2-rich layer.
5. Crystallization of the amorphous calcium phosphate film as an hydroxyapatite (HCA) layer, by incorporation of OH^- and CO_3^{2-} from the solution.
6. Adsorption and desorption of biological growth factors in the HCA layers to activate differentiation of stem cells (it continues throughout the process).
7. Action of macrophages to remove debris from the site allowing cells to occupy the space.
8. Attachment of stem cells on the bioactive surface.
9. Differentiation of stem cells to form bone growing cells, such as osteoblasts.
10. Generation of extra cellular matrix by the osteoblasts to form bone.
11. Crystallization of inorganic calcium phosphate matrix to enclose bone cells in a living composite structure.

For bone, interfacial bonding occurs because of the biological equivalence of the inorganic portion of bones and the HCA layer on the bioactive implant. While for soft tissues, the collagen fibrils are chemisorbed on the porous SiO_2 film via electrostatic, ionic, hydrogen bonding, and the HCA is precipitated and crystallized on the collagen fibrils and glass surfaces[4].

It should be remarked that the accumulation of dissolution products is strictly related to the composition and the pH of the solution and this can be detrimental to cells. For this reason, it is necessary to be able to control the solubility (dissolution rate) of the material. This can also allow to obtain bioactive implants with different life: for example, a HCA coating on orthopaedic metals needs to have a long life, while a high solubility implant is required if designed to aid bone formation, such as bioglasses. Therefore, a fundamental understanding of factors affecting the dissolution on bioactive glasses and bioreactivity is required to develop new materials for in situ tissue regeneration and tissue engineering[4]. In summary, they are:

- the dissolution medium (initial pH, ionic concentration, temperature);
- the geometry of the material (surface area to solution volume ratio);
- the structure of the glass (network connectivity and crystallization);
- the composition of the glass (silica content).

The controlled release of ionic dissolution products from bioactive glasses also provides some stimulation of cell genes towards a path of regeneration and self-repair, allowing the use of bioglass scaffolds in tissue engineering applications, aimed at regenerating diseased or damaged tissues, rather than simply in artificial prosthesis[6,7]. Glass solubility increases as network connectivity is reduced, while crystallization inhibits the ion exchange, so that it is recognized that bioactive properties are enhanced by an amorphous structure[4].

At present, the commercial use of bioactive glasses is mainly restricted to melt-derived components, such as powder, granules or small monoliths. 45S5 Bioglass is used in the clinic as a treatment for periodontal disease (Perioglas), as a bone filling material (Novabone) and as an additive in mineralizing toothpastes (Novamin). Bioglass implants have also been used to replace damaged middle ear bones, restoring hearing to thounsands of patients. Complex shapes, such as three-dimensional scaffolds, may be obtained by viscous flow sintering; however, it must be noted that, since sintering is accompanied by partial crystallization, the bioactivity is somewhat degraded, as discussed above.

Revised formulations (e.g. 13-93 bioglass, with a more complex chemical formulation) lead to limited crystallization, but compare negatively in terms of bioactivity with 45S5 and 58S. In this sense, in vitro cell culture showed no marked difference in the proliferation and differentiated function of osteoblastic cells between dense disks of 45S5 and 13-93; however 13-93 degrades and converts to an HA-like material more slowly than 45S5 glass[4]. Non-crystallized porous scaffolds may be actually obtained by a different strategy, i.e. by application of the sol-gel technique, but they have not yet been approved for clinical use[1]. Furthermore, sol-gel techniques are difficult to scale-up in the industrial system for several reasons, such as the high cost of the raw materials, the use of large amounts of flammable solvents, the associated drying problems, the complexity and the long duration of the process[8,9].

The research work presented in this chapter, published in 2014 by Fiocco *et al.*[10], aims at exploring a novel route to produce highly amorphous bioceramic foams, resembling the compositions of 45S5 and 58S bioglasses, as an alternative to both conventional melting techniques (with subsequent sintering) and sol-gel. The adopted formulations, containing more than one oxide (in addition to silica) and not corresponding to the stoichiometry of any crystalline silicate phase, were reputed to favor the amorphous state, as observed for common glass compositions.

Although partially successful (only foams of 58S composition were not highly crystalline), the approach here reported is reputed to be significant, due to its simplicity, its limited processing temperature (not exceeding 1000 °C), the microstructural homogeneity of selected samples and the promising results of the preliminary in vitro tests.

3.2 Experimental

3.2.1 Preparation of samples

Several combinations of silicone resins and fillers were tested in order to obtain the final composition of 45S5 and 58S bioactive glasses. Two commercial silicones, solid (Silres® H44, Wacker-Chemie GmbH, München, Germany) and liquid (Silres® H62C, Wacker-Chemie, and PDMS PS340.5, United Chemical Technologies, Inc., PA), were used as silica precursors, while the other oxides were introduced in the form of micro- and nano-sized fillers. Micro-sized fillers (reagent grade chemicals, all from Sigma Aldrich Ltd, Gillingham, UK, average diameter estimated using microscopy as not exceeding 10 μm) comprised calcium carbonate ($CaCO_3$), sodium carbonate (Na_2CO_3) and sodium phosphate dibasic heptahydrate ($Na_2HPO_4 \cdot 7H_2O$, later referred to as NaP7H). Nano-sized fillers consisted of calcium carbonate (average diameter of d_{50}=90 nm, specific surface of 20 m^2/g, PlasmaChem GmbH, Berlin, Germany) and as synthesized tri-calcium phosphate ($Ca_3(PO_4)_2$) precursor (later referred to as TCP-p). The latter was synthesized according to a previously presented procedure, and it was used in form of agglomerates with a maximum diameter of about 10 μm, as determined by microscopy[11].

The calculations of the required quantity of precursors were made on the basis of the desired final composition, the ceramic yield of the precursors and the stoichiometry of the employed fillers. Silicones and fillers were mixed with or without solvents. In the former case, the silicones were first dissolved in isopropyl alcohol, then fillers were added under magnetic stirring, and the mixture was ultrasonicated for 10 min. A thick paste was obtained after evaporation of the solvent (at 60 °C, overnight). In the latter case, the mixing procedure changed depending on the nature of the polymer: solid H44 was manually mixed with the fillers, by pestle and mortar, whereas liquid H62C incorporated the fillers under magnetic stirring, helped by the addition of low-viscosity polydimethylsiloxane (PDMS). Pastes were obtained without any drying step. For most formulations, dicarbamoylhydrazine (DCH, Alfa Aesar GmbH, Germany) powder was added to act as a foaming agent (2.5 wt% related to the overall ceramic residue), as it decomposes at around 250 °C releasing a large volume of gas.

The silicone-based mixtures, in form of both powders and pastes, were poured in small aluminum containers and subjected to a low temperature treatment, at 250-300 °C, aimed at both cross-linking the polymers (occurring through the functionalities present in the polymer structure, such as –OH or vinyl groups) and foaming, thanks to the release of gaseous products from the decomposition of some of the fillers or of DCH.

Samples from all formulations were fired at 1000 °C for 1 h in air, with a heating rate of 2 °C/min; in some cases the samples were heated with a rate of 5 °C/min and subjected to an intermediate holding stage at 550 °C for 4 h, aimed at optimizing the gas evolution and the polymer-to-ceramic transformation.

3.2.2 Characterization of samples

The resulting ceramic components were characterized by optical stereomicroscopy, scanning electron microscopy (JEOL, JSM-6300F), X-ray diffraction (Bruker AXS D8 Advance, Germany). The Match! software package (crystal Impact GbR, Bonn, Germany) was used for phase identification, supported by data from PDF-2 database (ICDD-International Centre for Diffraction Data, Newton Square, PA, USA).

The bulk density was obtained by considering the mass to volume ratio for 3 to 6 selected ceramic blocks with dimensions of 9 mm × 9 mm × 8 mm, while the total porosity was computed by considering the true density measured by gas picnometry (AccuPyc 1330, Micromeritics, Norcross, GA). The same blocks were subjected to compression testing at room temperature, operating with a cross-head speed of 1 mm/min. At least 5 samples were tested for each formulation.

The biocompatibility and bioactivity of samples C, D1 and D2 were assessed by in vitro tests through immersion in a Simulated Body Fluid (SBF) solution, according to the procedure proposed by Kokubo *et al.*[12]. Each sample was immersed in 25 ml of SBF in flasks, which were then placed in a controlled environmental chamber at a constant temperature of 37 °C. The solution was refreshed three times a week (after 2, 4, 7, 9, 11 days) to reproduce dynamic conditions. The pH variation induced by the samples was also monitored. The scaffolds were extracted from the SBF solution after given times of 1, 3, 7 and 14 days. Once removed from the incubation medium, all samples were gently rinsed using distilled water, and finally left to dry at room temperature for 24 h.

SEM (Quanta 2000; FEI, Eindhoven, the Netherlands) analyses were performed on the samples after in vitro studies. The SEM was operated in low-vacuum mode with a pressure of 0.53 Torr. In addition, a local chemical analysis was carried out by X-ray Energy Dispersion Spectroscopy (Inca; Oxford Instruments, Buckinghamshire, U.K.). Raman spectroscopy was performed by means of a Jobin-Yvon Raman Microscope spectrometer (Horiba Jobin-Yvon, Edison, NJ).

The biological tests were performed thanks to a collaboration with Prof. V. Cannillo's group (University of Modena and Reggio Emilia, Italy).

3.3 Results

3.3.1 Characterization of scaffolds

The formulations aimed at obtaining materials with the composition of 45S5 and 58S bioglasses are summarized in Tab. 3.1. All formulations led to highly foamed bodies, as illustrated by Fig. 3.2. The relatively dense surface of the samples derives from the contact of the slurries with the Al container into which they were poured.

Sample A allows to observe the effect of fillers, such as NaP7H, which accomplish two distinct functions. Besides yielding oxides (Na_2O, P_2O_5), the filler features a remarkable water release (corresponding to ~50 wt% of the starting compound, in accordance with its stoichiometry) associated to dehydration occurring in the temperature range 150 °C to 350 °C (as inferred from DTA analysis), leading to the observed significant foaming. In fact, bubbles generated by water release, upon dehydration of NaP7H, were retained within the body by the setting of the H62C polymer (occurring rapidly above 250 °C) [8]. However, foaming in sample A was not associated to the production of the desired amorphous phase; on the contrary, as testified by Fig. 3.3, a glass-ceramic formed, featuring the presence of sodium-calcium silicate phases (Na_2CaSiO_4, PDF#731726, referred to as N_2CS; $Na_2Ca_2Si_2O7$, PDF#100016, referred to as NCS) and tri-calcium phosphate ($Ca_3(PO_4)_2$, PDF#290359, referred to as TCP). Although interesting (N_2CS is bioactive)[13], sample A was not further investigated, since the basic goal of the present research was the achievement of mainly amorphous scaffolds.

Tab. 3.1 Summary of formulations for ceramics based on the 45S5 and 58S compositions (n.a.= data not available due to excessively weak samples)

Sample	*Silica precursor*	*Fillers*	*Foaming agent*	*Bulk density (g/cm^3)*	*Distinctive features*
A (45S5)	H62C	m-$CaCO_3$ Na_2CO_3 NaP7H	None	0.54 ± 0.03	- Solvent added (isopropyl alcohol) - Foaming at 300 °C - Intermediate stage at 550 °C - Highly crystallized ceramic
B1 (45S5)	H62C 20% PDMS 80%	m-$CaCO_3$ Na_2CO_3 NaP7H	DCH (2.5 wt.%)	n.a.	- No solvent added - Foaming at 280 °C - Highly crystallized ceramic product - Undesirable crystal phases
B2 (45S5)	H62C 20% PDMS 80%	TCP-p m-$CaCO_3$ Na_2SO_4	DCH (2.5 wt.%)	n.a.	- No solvent added - Foaming at 280 °C - Highly crystallized ceramic product - Undesirable crystal phases
C (58S)	H44	TCP-p m-$CaCO_3$	DCH (2.5 wt.%)	0.60 ± 0.06	- No solvent added - Dry powder mixing - Foaming at 270 °C
D1 (58S)	H62C 80% PDMS 20%	TCP-p m-$CaCO_3$	DCH (2.5 wt.%)	0.57 ± 0.11	- No solvent added - Foaming at 270 °C
D2 (58S)	H62C 80% PDMS 20%	TCP-p n-$CaCO_3$	DCH (2.5 wt.%)	1.48 ± 0.07	- No solvent added - Foaming at 270 °C

Accordingly, the alternative formulations for ceramics based on 45S5 were essentially aimed at obtaining more amorphous materials and simplifying the process. Low viscosity suspensions were achieved by mixing H62C with PDMS, without the addition of isopropyl alcohol. This choice, if advantageous in avoiding the drying step, involved some additional problems in the selection of fillers. As an example, NaP7H and Na_2CO_3 led to large agglomerates, resulting in poorly homogeneous dispersions (no subsequent ceramization of these samples was therefore carried out). The poor homogeneity was attributed to the interaction of the fillers with the chemical structure of PDMS. As reported in Tab.1, alternative fillers, such as sodium sulphate and TCP-p, were found to lead to more homogeneous dispersions and therefore they were considered for further processing (sample B2).

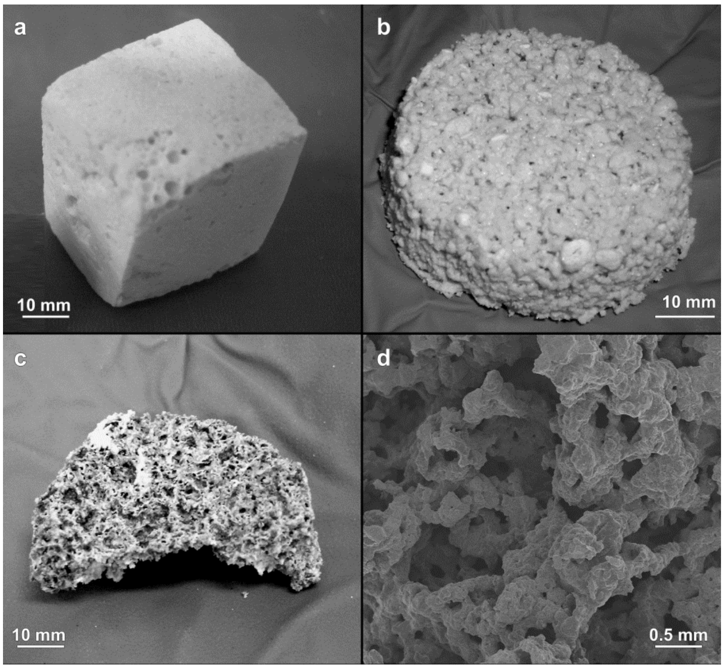

Fig. 3.2 Porous glass ceramics based on the 45S5 composition: a) sample A (low magnification); b) sample B1 (low magnification); c) sample B2 (low magnification); d) sample B2 (high magnification).

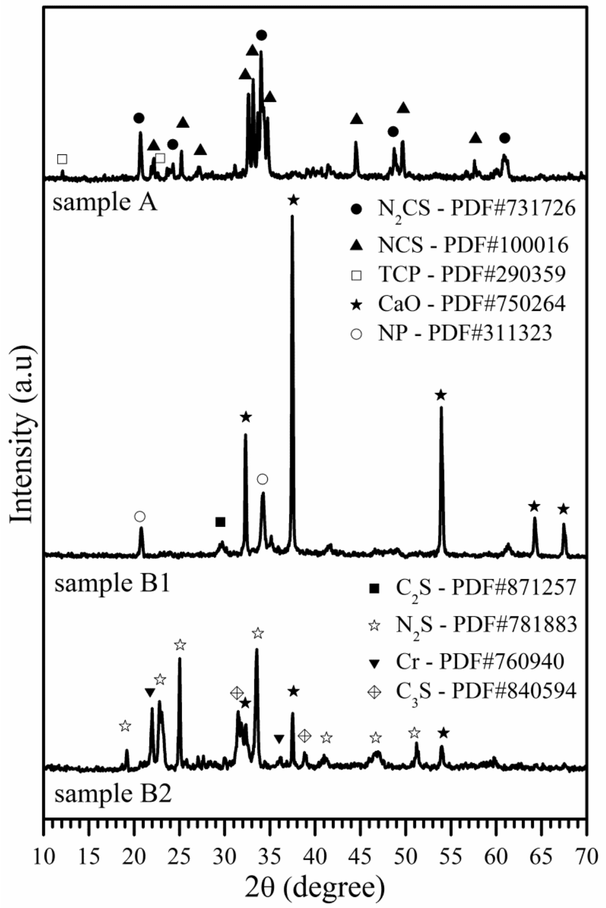

Fig. 3.3 Diffraction patterns of selected ceramics based on 45S5 composition.

Fig. 3.2b-c testify the foaming of samples from the new formulations (B1 and B2). In this case, a significant contribution to porosity was given, in addition to that of the foaming agent (DCH present in a low amount), by the same nature of PDMS. In fact, this silicone has a low ceramic yield, i.e. it is known to transform into silica with a remarkable gas release occurring in the 300 to 500 °C range. In fact, considering its ceramic yield of only 23 %, nearly 4/5 of the starting weight of the polymer is lost as gaseous species, while H62C and H44 possess ceramic yields of 58 % and 84 %, respectively[8].

Fig. 3.2c-d clearly show that the porosity in sample B2 is uniformly distributed and well interconnected, as required for bioceramic scaffolds. The favorable morphology, however, contrasts again with the phase assemblage. The diffraction pattern in Fig. 3.3 show the formation of a potentially bioactive phase, i.e. calcium silicate oxide (Ca_3SiO_5, PDF#840594, referred to as C_3S)[14] together with undesirable phases, such as unreacted sodium sulphate (of not proven biocompatibility; Na_2SO_4, PDF#781883, referred to as N_2S), unreacted CaO (not suitable for medical use; PDF#750264, referred to as CaO) and cristobalite (that could be responsible for the microcracks observed in the sample; SiO_2, PDF#760940, referred to as Cr)[15].

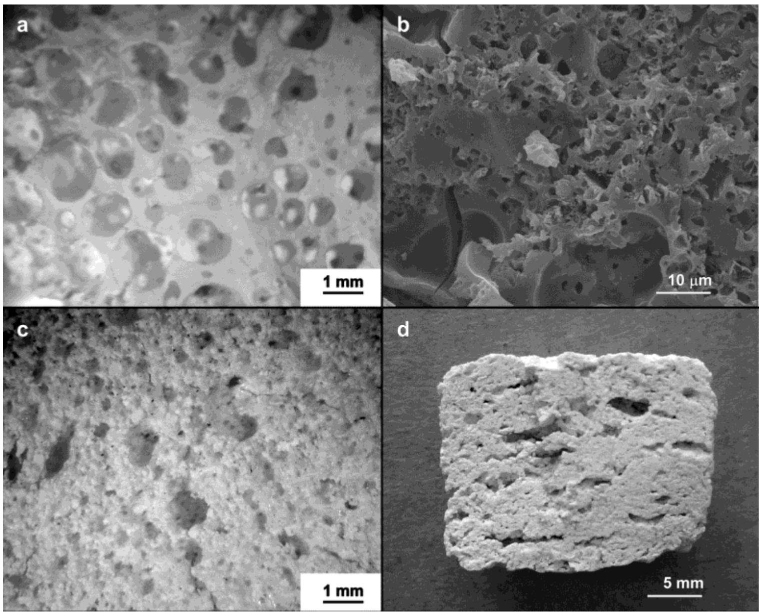

Fig. 3.4 Microstructural details of ceramic samples based on composition 58S: a,b) sample C; c) sample D1; d) sample D2.

Tab. 3.2 Properties and distribution of crystal phases in glass ceramic materials of 58S composition.

Sample	C	D1	D2
Properties			
Bulk density (g/cm^3)	0.60 ± 0.06	0.57 ± 0.11	1.48 ± 0.07
True density (g/cm^3)	2.88 ± 0.01	2.62 ± 0.01	2.19 ± 0.02
Porosity (vol%)	79	78	33
Crushing strength (MPa)	0.57 ± 0.35	0.28 ± 0.20	6.82 ± 0.68
Crystallinity (wt%)	50	30	43
Distribution of crystal phases (semi-quantitative)			
para-wollastonite (wt%)	25	12	19
C_2S (wt%)	5	2	2
TCP (wt%)	20	16	20

The problems found with Na-containing fillers forced us to consider the composition 58S, featuring only CaO, SiO_2 and P_2O_5, as reported in Tab. 3.1. Also in this case, the foaming was substantial, as illustrated by Fig. 3.4 and Tab. 3.2. In sample C, the pore diameter was estimated to be between 500 µm and 2 mm, according to the analysis of optical microscope images (see Fig. 3.4a; many interconnections are clearly visible). Scanning electron microscopy (Fig. 3.4b) revealed also the presence of finer pores, with a diameter below 2 µm. Sample D1, on the other hand, exhibited pores with diameter between 100 µm and 1 mm (Fig. 3.4c). Both types of ceramic foams feature a nearly identical amount of total porosity (~80 %), with at least a significant fraction of pores with a dimension in the optimal range for scaffolds for tissue engineering (100-300 µm)[16,17]. The high porosity reflects in a quite poor crushing strength, well below 1 MPa (see Tab. 3.2), which is known to be a threshold limit for scaffolds operating *in vivo*. However, lower strength values could be accepted in case the scaffolds should be used for tissue regeneration *ex vivo* (in this case only the mechanical properties of the final tissue-engineered implant are critical)[1,5,18-20].

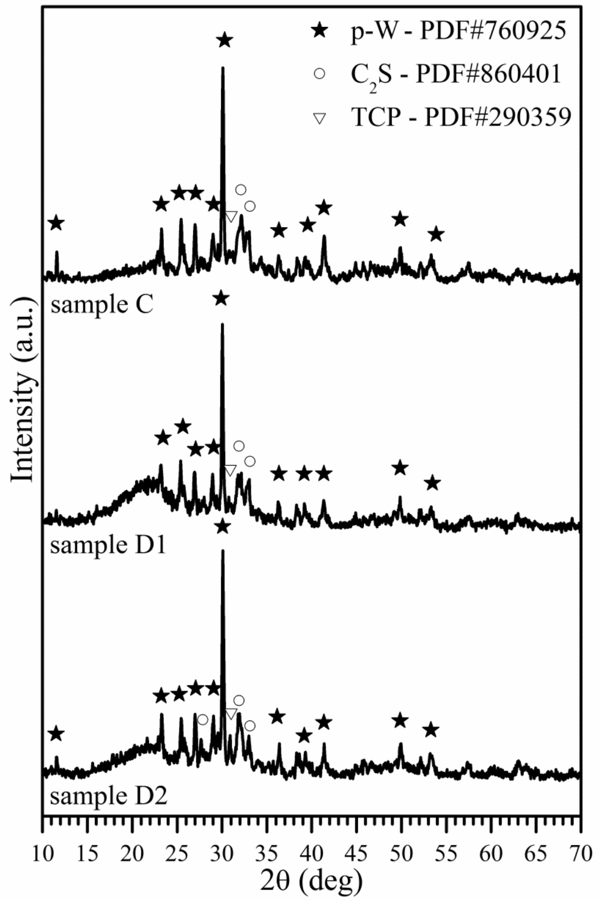

Fig. 3.5 Diffraction patterns of selected glass ceramics based on the 58S composition.

Differently from the other cases, sample D2 (Fig. 3.4d) was produced starting from nano-sized $CaCO_3$. This choice derived from the observation, based on very recent experiences, that nano-sized fillers usually enable a superior chemical homogeneity in the component after ceramic conversion[8]. It may be noted that the porosity was not uniform and practically comprised only large voids, probably due to air bubbles trapped upon mixing (the total porosity did not exceed 35 %): the entrapment was likely favored by the fact that nano-sized particles considerably increased the viscosity of the suspension, limiting the possibility of achieving a significant foaming and leading to a poor homogenization of the slurry.

The last samples were found to be less crystalline than the previous ones. In fact, the diffraction patterns, as shown in Fig. 3.5, contain an amorphous halo, located in the region typical of silicate glasses (i.e. ~21°), especially for samples D1 and D2, below the main crystal peaks. The crystal phases consisted of calcium silicates (para-wollastonite $CaSiO_3$, PDF#760925, referred to as p-w; Ca_2SiO_4, PDF#860401, referred to as C_2S,) and TCP (PDF#290359). Interestingly, there was no difference in the crystalline phases present: this means that the choice of the silica precursors (H44 or H62C-PDMS) and the granulometry of the $CaCO_3$ (nano- or micro-sized) had no influence on the type of crystalline phases formed. On the other hand, differences were observed in terms of the overall crystallinity and distribution of phases, as reported in Tab. 3.2. According to the semi-quantitative analysis provided by the Match! program package, para-wollastonite was dominant in sample C (25 wt% of the crystal phase), whereas TCP was the main phase in samples D1 and D2 (respectively 16 wt% and 20 wt% of crystal phase). C_2S was present in an amount of ~5 wt% in sample C; ~2 wt% in samples D1 and D2.

3.3.2 Bioactivity tests

The bioactive behavior of samples C, D1 and D2 was investigated by means of immersion tests in SBF, which claims to *mimic* the acellular human blood plasma. In particular, since the bone bonding ability of a biomaterial, also termed osseointegration,[21] is associated with the formation of an apatite layer on its surface, the ability to bond to bone can be preliminarily assessed by monitoring the formation of such apatite layer *in vitro* in SBF. In the present research activity, it was observed that, for all samples, the deposition of an apatite layer promptly began after 1 day in SBF, as shown in Fig. 3.6a for scaffold C, where white globular precipitates with the typical apatite morphology can be observed on the surface. This fact is further confirmed by the results of the EDS analysis performed on the globular precipitates which were substantially larger after 3 days (see in Fig. 3.6c the data for sample D2). The EDS spectrum revealed the presence of Na, O, Ca, Si, P, Cl; in particular, apart from local fluctuations, the Ca/P ratio was about 1.67, which is similar to that of stoichiometric apatite[22]. Analogous results were obtained for samples C and D1 (data not reported for the sake of brevity). The presence of Cl can be ascribed to chloride compounds precipitated from SBF, as widely reported in the literature,[23] while Si is due to a silica gel formed underneath the apatite precipitates[24]. The dissolution of the sample in SBF resulted in the formation of highly corroded areas and surface roughness (Fig. Fig. 3.6b), which are expected to favour cell adhesion, proliferation, differentiation and detachment strength,[25] thus promoting an adequate osseointegration of the material.

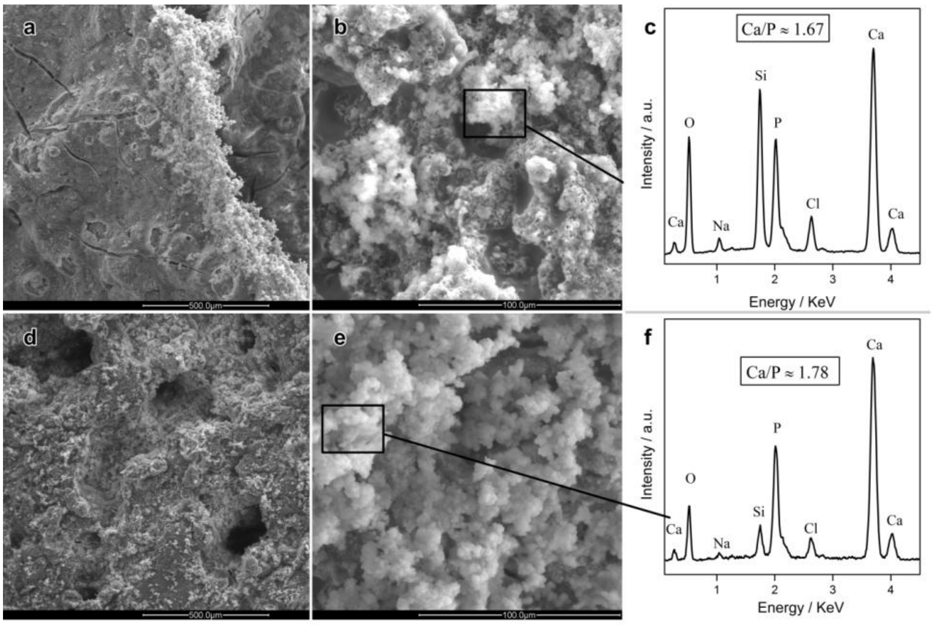

Fig. 3.6 Formation of an apatite layer on the surface of samples C, D1 and D2 after immersion in SBF for different lengths of time: a) sample C - 1 day; b) sample D2 – 3 days; c) sample D2 - results of the EDS analysis performed on the spot indicated in (b); d) D2 samples – 7 days; e) sample D2 – 7 days; f) sample D2 – results of the EDS analysis performed on the spot indicated in (e).

After 7 days in SBF, the surface of the samples was completely covered by apatite (Fig. 3.6d) and, at the same time, it appeared to be further altered by the SBF action. In particular, the internal pore structure of the samples was also coated with apatite precipitates. The EDS analysis carried out on the precipitates covering the surface of sample D2 after 7 days in SBF (Fig. 3.6e-f) suggests the presence of a particularly thick apatite layer covering the silica gel, since the spectrum shows a lower Si amount with respect to the analysis performed after 3 days in SBF (Fig. 3.6c). A prolonged soaking in SBF (14 days, data not reported for the sake of brevity) led to further apatite deposition. The cauliflower-like precipitates progressively grew and completely covered the surface of the scaffold struts (Fig. 3.6e).

Thanks to the particularly high intensity of the Raman peaks associated to P–O vibration modes, the development of an apatite film on the surface of samples could be confirmed by Raman spectroscopy. The Raman spectra acquired on the spherical precipitates covering the samples after 7 days in SBF are shown in Fig. 3.7. Vibration bands characteristic of apatite were observed at about 430 cm^{-1} ($\nu_2PO_4^{3-}$), 590 cm^{-1} ($\nu_4PO_4^{3-}$), 960 cm^{-1} ($\nu_1PO_4^{3-}$, the most intense band) and 1005 cm^{-1} ($\nu_3PO_4^{3-}$).[26,27] Raman spectroscopy is particularly important for the analysis of the apatite deposited *in vitro* because it emphasizes the C–O vibrations, since the *in vitro* grown apatite is usually carbonated[28]. In this respect, it is possible to observe a peak located at about 1070 cm^{-1} in the spectra reported in Fig. 3.7, which can be ascribed to the stretching of carbonate groups, thus confirming that the apatite film on samples C, D1 and D2 is carbonated.

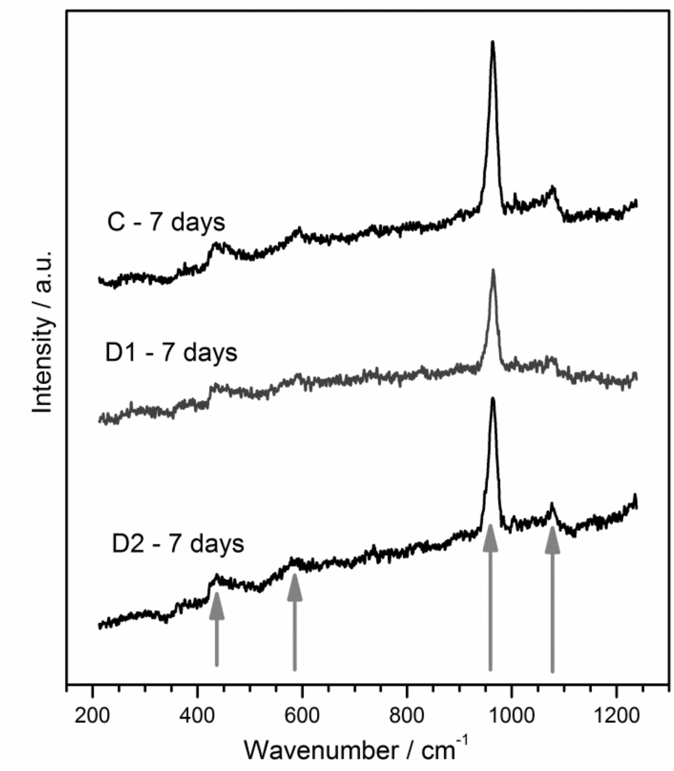

Fig. 3.7 Raman spectra acquired on samples C, D1 and D2 immersed in SBF for 7 days. The main peaks of apatite are indicated by arrows.

The obtained samples were particularly interesting also in terms of the pH variation induced in the SBF, as shown in Fig. 3.8. This issue is extremely important for the biocompatibility of glasses, glass-ceramics, and bioceramic coatings in general. In fact, when these systems are soaked in physiological fluids, the rate and amount of ion release can engender an excessive rise in the pH level or abrupt changes in pH, which are incompatible with life. Moreover, it has been reported in literature that the pH value influences the protein adsorption on the surfaces of biomaterials[29], which is a fundamental step among the biological reactions taking place at the interface between biological environment and medical implant. For example, Chen *et al.* reported high pH values (between 8.5 and 9) for 45S5 Bioglass® scaffolds soaked in SBF and observed that the attachment and stability of collagen on these systems was reduced.[30] A dramatic increase in pH (between 9 and 9.5) during the first days of exposure to SBF for 45S5 Bioglass® samples was also reported by Bellucci *et al.*, who observed that the pH value of the SBF stabilized near to physiological values only after three weeks of immersion[31]. A rapid pH increase was also observed for the treatment of 45S5 Bioglass® in DMEM tissue culture medium (pH~9 after 24 h) and in phosphate-buttered saline solution (pH~11)[32,33]. In this regard, stable pH values close to 7.8 can be considered optimal for osteoblast adhesion and proliferation[34] and many investigations have been reported in literature in order to develop new compositions tailored to avoid too high pH levels in SBF[35,36]. Fig. 3.8 shows the pH trend as a function of the immersion time in SBF for samples C, D1 and D2. All samples induced lower pH values compared to those commonly reported for 45S5 Bioglass®-derived glass ceramics. This fact is attributable to a slower ion leaching in our samples. In particular, D1 and D2 samples appear particularly promising, since the pH stabilizes near to physiological values already after a few hours.

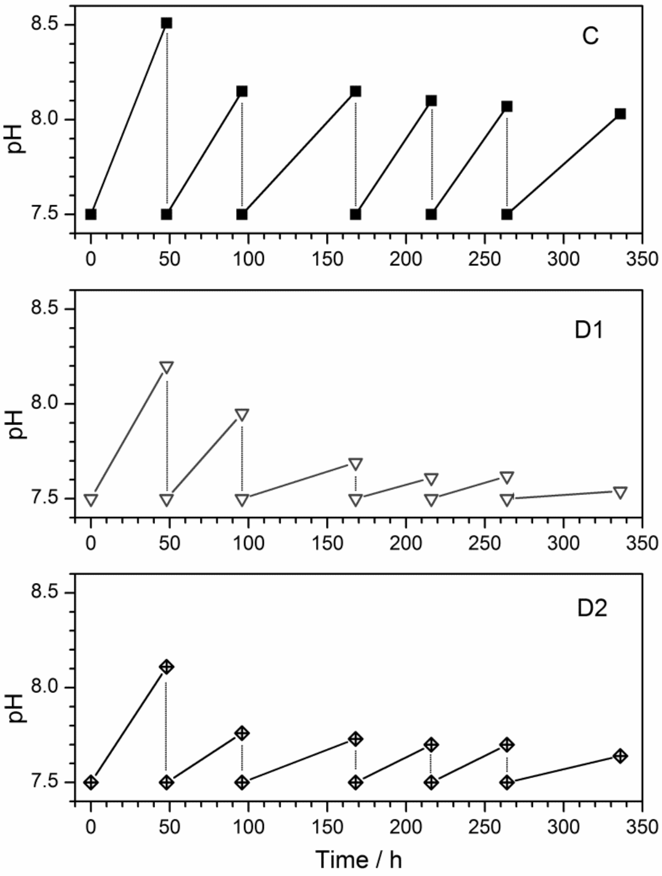

Fig. 3.8 pH variation induced by samples in SBF, refreshing the solution every 48 h.

The simulated body fluid (SBF) proposed by Kokubo *et al.* is an acellular solution and, as such, it is not able to simulate the real complexity of a biological environment, which also includes proteins, cells, etc.[12,37]. Therefore, SBF tests mainly offer an insight into the inorganic reactions which are expected to occur after the material is implanted into the human body, whereas the assessment of the biological response of cells needs further experimental trials, such as cytotoxicity tests[38]. Nevertheless the immersion of a new material in SBF is extremely useful to estimate its attitude to stimulate the formation of a surface layer of hydroxyapatite, which is similar to the mineral component of bone[37]. Even if it is known from the literature that the apatite-forming ability *in-vitro* does not always imply the bone-bonding ability *in vivo*[39], it is interesting to observe that all the scaffolds tested in SBF were able to support the development of a surface layer of hydroxyapatite. Moreover it is worth noting that samples C, D1 and D2 were produced without the addition of solvents and were processed to obtain a silicate amorphous matrix with some crystalline phases (calcium silicates, tri-calcium phosphate, Fig. 3.5) that are by no means dangerous to the human body[40-42]. Moreover no anomalous compounds (possibly deriving from the materials themselves or from unwanted reactions between the scaffolds and the liquid medium) were detected by SEM, X-EDS analysis and micro-Raman spectroscopy. In addition, the pH of the SBF never exceeded the value of 8.5 (Fig. 3.8), which represents an interesting result, since, as already mentioned, the reaction mechanisms of bioactive glasses (also sintered ones) usually induce very basic pH conditions, potentially harmful for cells[33-40]. For these reasons, the new scaffolds are suitable candidates for tissue engineering applications and further investigations on the cytotoxicity and other biological performance will be the target of future work.

3.4 Conclusions

Mixtures of silicones and fillers enabled to produce highly porous glass ceramic products, using a simple processing procedure. The synthesis cycle was composed of only two steps: foaming at 200-300°C followed by heating at 1000°C. Despite all, completely amorphous microstructures were not enabled by this methodology, so it should be remarked that the obtained samples were not “glasses”, but only resembled some bioglass compositions in terms of oxide amounts.

All samples of nominal composition corresponding to that of 45S5 bioglass were highly crystalline and led to difficulties concerning the selection of a suitable sodium oxide precursor. For a selected combination of silicones and fillers (formulation A) the homogeneity of foaming was accompanied by the formation of potentially bioactive phases.

Concerning silicone/fillers mixtures of nominal composition corresponding to that of 58S bioactive glass, they yielded partially amorphous components. It was observed that porosity and mechanical properties could be adjusted by modifying the starting precursors (micro- or nano-sized powders and silicones). Samples with 58S composition exhibited a quite low compressive strength, but they effectively promoted the development of a surface layer of hydroxyapatite when immersed in a simulated body fluid (SBF). The reactions occurring between the scaffolds and the soaking medium did not cause large changes of the pH, as frequently observed for conventional bioglass-derived materials and scaffolds. This is advantageous, since basic values of the pH or abrupt changes are known to be dangerous for cells.

A further important observation is related to the multifunctionality of some fillers. In particular, if we look at sodium phosphate dibasic heptahydrate, it had a double role: on the one hand, it was used as a precursor for P_2O_5 and Na_2O; on the other hand, its thermal decomposition reaction was exploited for its foaming capacity, thanks to the water release occurring.

References

[1] Jones JR, Boccaccini AR. Biomedical Applications: Tissue Engineering, in Colombo P, Scheffler M. Cellular Ceramics: Structure, Manufacturing, Properties and Applications. Wiley-VCH Verlag GmbH &Co. KGaA, Weinheim, Germany 2005;547-570.

[2] Hench LL. The story of Bioglass®. J Mater Sci: Mater Med 2006;17:967-978.

[3] Hench LL. Bioceramics: From Concept to Clinic. *J Am Ceram Soc 1991;74:*1487-1510.

[4] Jones JR, Hench LL. Biomedical Materials for new millennium: perspective on the future. Materials Science and Technology 2001; 17:891-90.

[5] Rahaman MN, Day DE, Bal BS, Fu Q, Jung SB, Bonewald LF, Tomsia AP. Bioactive glass in tissue engineering. Acta Biomater 2011;7:2355-2373.

[6] Hench LL. Genetic design of bioactive glass. J Am Ceram Soc 2008;29:1257-1265.

[7] Gough JE, Jones JR, Hench LL. Nodule formation and mineralization of human primary osteoblasts cultured on a porous bioactive glass scaffold. Biomaterials 2004;25:2039-2046.

[8] Bernardo E, Colombo P, Dainese E, Lucchetta G, Bariani PF. Novel 3-D Wollastonite-Based Scaffolds from Preceramic Polymers Containing Micro- and Nano-Sized Reactive Particles. Adv Eng Mat 2012;14:269-274.

[9] Cacciotti I, Lombardi M, Bianco A, Ravaglioli A, Montanaro L. Sol-gel derived 45S5 bioglass: synthesis, microstructural evolution and thermal behavior. J Mater Sci: Mater Med 2012;23:1849-1866.

[10] Fiocco L, Bernardo E, Colombo P, Cacciotti I, Bianco A, Bellucci D, Sola A, Cannillo V. (2014). Novel processing of bioglass ceramics from silicone resins containing micro-and nano-sized oxide particle fillers. Journal of Biomedical Materials Research Part A, 102(8), 2502-2510.

[11] Cacciotti I, Bianco A. High thermally stable Mg-substituted tricalcium phosphate by precipitation. Ceramics International 2011;37:127–137.

[12] Kokubo T, Hata K, Nakamura T, Yamamura T. Apatite formation on ceramics, metals, and polymers induced by a CaO–SiO2-based glass in simulated body fluid. In: Bonfield W, Hastings GW, Tanner KE, editors. Bioceramics. London: Butterworth-Heinemainn 1991;4:113.

[13] Zhao Y, Ning C, Chang J. Sol–gel synthesis of Na_2CaSiO_4 and its in vitro biological behaviors. Journal of Sol-Gel Science and Technology 2009;52:69-74.

[14] Zhao W, Wang J, Zhai W, Wang Z, Chang J. The self-setting properties and in vitro bioactivity of tricalcium silicate. Biomaterials 2005;26:6113–6121.

[15] Şan O, Özgür C. Investigation of a high stable β-cristobalite ceramic powder from $CaO–Al_2O_3–SiO_2$ system. J Eur Ceram Soc 2009;29:2945-2949.

[16] Vitale-Brovarone C, Verné E, Robiglio L, Appendino P, Bassi F, Martinasso G, Munzio G, Canuto R. Development of glass-ceramic scaffolds for bone tissue engineering: characterization, proliferation of human osteoblasts and nodule formation. Acta Biomaterialia 2007;3:199-208.

[17] Dorozhkin SV. Medical application of calcium orthophosphate bioceramics. BIO 2011;1:1-51.

[18] Pereira MM, Jones JR, Hench LL. Bioactive glass and hybrid scaffolds prepared by sol-gel method for bone tissue engineering. Advances in Applied Ceramics 2005;104:35-42.

[19] Jones JR, Hench LL. Regeneration of trabecular bone using porous ceramics. Current Opinion in Solid State and Material Science 2003;7:301-307.

[20] Xynos ID, Hukkanen MVJ, Batten JJ, Buttery LD, Hench LL, Polak JM. Bioglass® 45S5 stimulates osteoblast turnover and enhances bone formation in vitro: implications and applications for bone tissue engineering. Calcif Tiss Int 2000;67:321-329.

[21] Mavrogenis AF, Dimitriou R, Parvizi J, Babis GC. Biology of implant osseointegration. J Musculoskelet Neuronal Interact 2009;9:61-7.

[22] Göller G, Demirkiran H, Oktar FN, Demirkesen E. Processing and characterization of bioglass reinforced hydroxyapatite composites. Ceram Int 2003;29:721-724.

[23] Padilla S, Román J, Sánchez-Salcedo S, Vallet-Regí M. Hydroxyapatite/SiO_2-CaO-P_2O_5 glass materials: In vitro bioactivity and biocompatibility. Acta Biomater 2006;2:331-342.

[24] Hench LL. Bioceramics, from concept to clinic. J Am Ceram Soc 1991;74:1487-1510.

[25] Deligianni DD, Katsala ND, Koutsoukus PG, Missirlis YF. Effect of surface roughness of hydroxyapatite on human bone marrow cell adhesion, proliferation, differentiation and detachment strength. Biomaterials 2001;22:87-96.

[26] Grossin D, Rollin-Martinet S, Estournès C, Rossignol F, Champion E, Combes C, Rey C, Geoffroy C, Drouet C. Biomimetic apatite sintered at very low temperature by spark plasma sintering: Physico-chemistry and microstructure aspects. Acta Biomater 2010;6:577-585.

[27] Bellucci D, Sola A, Cannillo V. Low temperature sintering of innovative bioactive glasses. J Am Ceram Soc 2012;95:1313-1319.

[28] Antonakosa A, Liarokapisa E, Leventouri T. Micro-Raman and FTIR Studies of Synthetic and Natural Apatites. Biomaterials 2007;28:3043-3054.

[29] Yang J, Cleland JL. Factors affecting the in vitro release of recombinant human interferon-gamma (rhIFN-gamma) from PLGA microspheres. J Pharm Sci 1997;86:908-914.

[30] Chen QZ, Ahmed I, Knowles JC, Nazhat AN, Boccaccini AR, Rezwan K. Collagen release kinetics of surface functionalized 45S5 Bioglass®-based porous scaffolds. J Biomed Mater Res A. 2008;86:987-995.

[31] Bellucci D, Cannillo V, Sola A, Chiellini F, Gazzarri N, Migone C. Macroporous Bioglass® Derived Scaffolds for Bone Tissue Regeneration. Ceramics Int 2011;37:1575-1585.

[32] Chen QZ, Li Y, Jin LY, Quinn JMW, Komesaroff PA. A new sol–gel process for producing Na2O-containing bioactive glass ceramics. Acta Biomater 2010;6:4143-4153.

[33] Chen QZ, Ahmed I, Knowles JC, Nazhat AN, Boccaccini AR, Rezwan K. Collagen release kinetics of surface functionalized 45S5 Bioglass®-based porous scaffolds. J Biomed Mater Res A 2008;86:987-995.

[34] Brandao-Burch A, Utting JC, Orriss IR, Arnett TR. Acidosis Inhibits Bone Formation by Osteoblasts in vitro by Preventing Mineralisation. Calcif. Tissue Int 2005;77:167-174.

[35] Bellucci D, Cannillo V, Sola A. Calcium and potassium addition to facilitate the sintering of bioactive glasses. Materials Letters 2011;65:1825–1827.

[36] Vitale-Brovarone C, Verné E , Robiglio L, Martinasso G, Canuto RA, Murzio G. Biocompatible Glass Ceramic Materials for Bone Substituition. J Mater Sci: Mater Med 2008;19:471-478.

[37] Kokubo T, Takadama H. How useful is SBF in predicting in vivo bone bioactivity? Biomaterials 2006;27:2907-2915.

[38] Bohner M, Lemaitre J. Can bioactivity be tested in vitro with SBF solution? Biomaterials 2009;30:2175-2179.

[39] Pan H, Zhao X, Darvell BW, Lu WW. Apatite-formation ability–predictor of "bioactivity"? Acta Biomater. 2010;6:4181-4188.

[40] Liu X, Ding C. Reactivity of plasma-sprayed wollastonite coating in simulated body fluid. J. Biomed. Mater. Res. 2002;59: 259-264.

[41] Boccaccini AR, Chen Q, Lefebvre L, Gremillard L, Chevalier J. Sintering, crystallisation and biodegradation behaviour of Bioglass®-derived glass–ceramics. Faraday Discuss. 2007;136:27-44.

[42] Kamitakahara M, Ohtsuki C, Miyazaki T. Review paper: behavior of ceramic biomaterials derived from tricalcium phosphate in physiological condition. J Biomater Appl. 2008;23: 197-212.

4 Ca-Mg silicates

4.1 Introduction

Nowadays, tissue engineering is a well-established alternative approach to the conventional use of permanent implants, with the purpose of allowing not only repair but also regeneration and remodelling of damaged or diseased tissues[1]. In tissue engineering and regenerative medicine, synthetic or natural porous scaffolds mimicking the extracellular matrix can be directly implanted into a defect to guide and stimulate the formation of native tissue *in situ*. Alternatively, they can be seeded with appropriate cells extracted from the patient (see an example in Fig. 4.1, realized at the Faculty of Dentistry, University of Oslo, Norway, in 2014), or be enriched with specific biochemical substances with the aim to promote the cellular recruitment, proliferation and/or differentiation. The scaffolds are used as templates for tissue growth and should be resorbed by dissolving at controlled rates and concentrations as the new tissue forms[2,3].

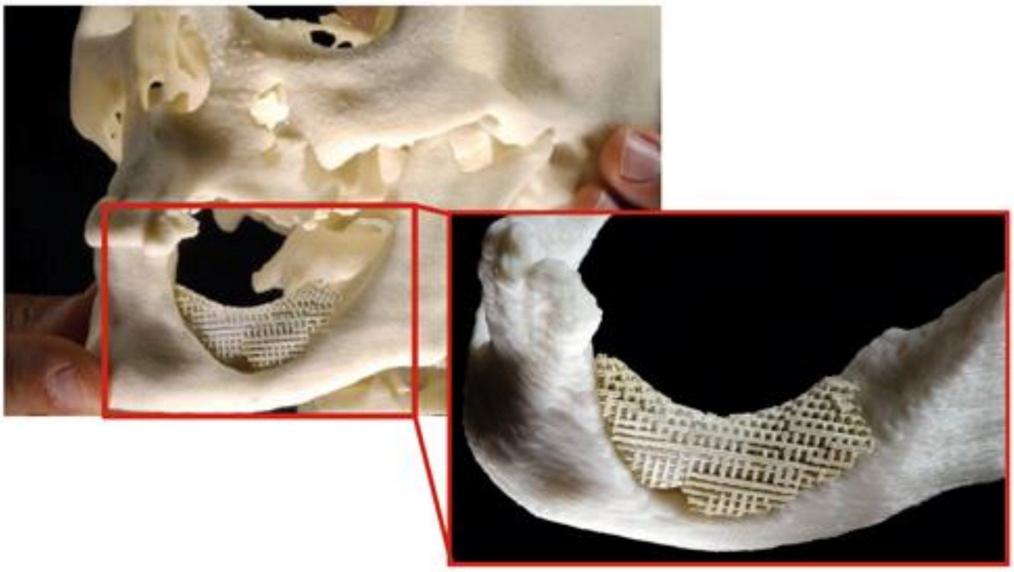

Fig. 4.1 Example[4] of artificial scaffold, containing bone progenitor cells from a patient, to remodel a mandible damaged by cancer, accident or infection. Realized in 2014 at the Faculty of Dentistry, University of Oslo, Norway.

Concerning bone regeneration, the scaffolds should ideally not only provide a passive structural support for cells with well defined mechanical and physical properties (in terms of compressive strength, porosity, pores interconnectivity), but they should stimulate osteoblastic cell proliferation and differentiation as well, thus favourably affecting the growth of new born tissue[5].

In the last decades, significant attention has been given to Ca-silicates, due to their excellent bioactivity and biodegradability. Silicon has a well established role in the bioactivity mechanism proposed by Hench[6,7,8], in the osteoblast proliferation[9] and bone mineralization[10]. Calcium is known to act in regulating osteogenisis[11, 12], positively affecting the osteoblasts proliferation and differentiation[13,14]. In particular, bioceramics with the composition of wollastonite have been widely investigated, due to the ability of this formulation to bond with living bone through the formation of an apatite interface layer both *in vitro* and *in vivo*[15,16]. The main drawbacks, however, are the low mechanical strength of porous bodies and the high degradation rate, which may lead to high pH values with detrimental effects on cells[17]. Wu *et al.* reported that a wollastonite scaffold of 80 % porosity exhibited a crushing strength of only 300 kPa[17].

Therefore, ion modifications of Ca-silicates have been proposed with the aim of tailoring both mechanical and biomedical properties. In this framework, the CaO-MgO-SiO_2 system has been receiving a growing interest in the field of bioactive materials. Zhai *et al*. have recently reported that this family of bioceramics possess a unique dual osteogenic/angiogenic stimulatory ability[18]. Many studies have examined the role of Mg, which is a trace element in the body, including bone and extracellular matrix. It was found that it has an important influence on osteoblasts adhesion[19], differentiation and proliferation[20], on mineralization of tissues and on mineral metabolism[21,22]. Further effects of the incorporation of Mg specifically in Ca-silicates involve the reduced degradation rate, as well as the improved mechanical properties. These positive consequences might be due to the higher complexity of the crystal structure after Mg incorporation: in particular, Mg-O bonds are stronger than Ca-O bonds[23,24].

In the present chapter, two Ca-Mg silicates will be shown: one, akermanite ($Ca_2MgSi_2O_7$), as the the only crystal phase; the other, diopside ($CaMgSi_2O_6$), coupled with wollastonite ($CaSiO_3$). Both akermanite and diopside are known to possess good bioactivity and great potential as bone tissue engineering materials[25,26]. The present study also explored the cellular response of MC3T3 osteoblast precursor cells to the two Ca-Mg-rich glass-ceramics. Cytotoxicity was tested in accordance to the ISO 10993 standard guidelines. Cell attachment, viability and osteogenic differentiation were also assessed. These investigations will be submitted soon for publication.

Part of this work was carried out at Imperial College London under the supervision of Prof. J. R. Jones, during a 1-month student exchange program in 2015.

4.2 Experimental

4.2.1 Preparation of samples

A commercially available silicone resin (Sikres® H62C, Wacker Chemie GmbH, Munich, Germany), liquid at room temperature, was considered as a silica precursor, with a yield of 58 wt%[27]. CaO and MgO precursors consisted of $CaCO_3$ (Industrie Bitossi, Vinci, Italy) and $Mg(OH)_2$ (Industrie Bitossi, Vinci, Italy) in the form of microparticles (< 10 µm). Borax (sodium borate decahydrate microparticles, $Na_2B_4O_7 \cdot 10H_2O$, Normapur Prolabo, France) was used as an additional foaming agent. All the other chemicals and reagents were purchased from Invitrogen/ Life Technologies Ltd. (Paisley, UK) and Sigma-Aldrich (Gillingham, UK).

The molar balance among the most important constituents (silicone:CaO precursor:MgO precursor) followed the stoichiometric SiO_2:CaO:MgO molar proportions of akermanite (i.e. CaO:MgO:SiO_2=2:1:2), or of a 50 mol% wollastonite-50% diopside mixture (i.e. CaO:MgO:SiO_2=2:1:3). Samples will be referred to as “Ak” and “WD” respectively.

H62C was first dissolved in isopropanol (10 g in 13 ml) and then mixed with micro-sized fillers, including sodium borate, in the as-received, hydrated form (the quantity of salt was 3 wt% of the theoretical ceramic yield of the other components). Stable and homogeneous dispersions in isopropanol were obtained by magnetic stirring and ultrasonication, then were left to dry overnight at 60 °C. After first drying, the mixtures were in the form of thick pastes, later manually transferred into cylindrical Al molds and then subjected to a heat treatment for foaming at 350 °C in air for 30 min. Cylindrical samples, 10 mm in diameter and 10 mm in height, were obtained from the foams. After polishing of the top surfaces, by means of abrasive paper, the samples were thermally treated at 1100 °C in air for 1 hour at a heating rate of 2 °C/min.

4.2.2 Characterization of samples

The bulk density (ρ_b) of the foams was determined using a caliper and a digital balance. The skeletal density (ρ_s) was measured on foams, using a He gas pycnometer (Micromeritics AccuPyc 1330, Norcross, GA). The percentage of open porosity (%P) was then calculated using the following equation: $\%P=1-(\rho_b/\rho_s)$.

Mercury intrusion porosimetry (PoreMaster 33, Quantachrome UK) was used to determine the pore interconnect size distribution. As the technique was destructive, it cannot be used to follow the change in pore sizes of the same scaffold as a function of sintering temperature.

Optical stereomicroscopy (AxioCam ERc 5s Microscope Camera, Carl Zeiss Microscopy, Thornwood, New York, US) on foams and scanning electron microscopy (JSM 6010 L, JEOL USA; LEO GEMINI 1525 FESEM, LEO electron microscopy, Thornwood, New York, USA) on chromium-coated specimens were used to examine the morphological and textural features of the samples.

The phase identification was performed by means of X-ray diffraction (Bruker AXS D8 Advance, Bruker, Germany; CuKα radiation, 0.15418 nm, 40 kV–40 mA, 2θ = 10°–70°, step size = 0.05°, 2 s counting time), supported by data from PDF-2 database (ICDD-International Centre for Diffraction Data, Newtown Square, PA) and Match! programme package (Crystal Impact GbR, Bonn, Germany).

The compressive strength of foams was measured at room temperature, using an Instron 1121 UTM (Instron Danvers, MA), equipped with a 10 kN load cell, with a crosshead speed of 1 mm/min. The mean value of 5 to 10 samples was used for each data point.

4.2.3 Bioactivity test

Foams with weight of 37.5 mg were immersed in 25 ml of simulated body fluid (SBF) at 37 °C and 120 rpm for 1, 2, 4, 8, 24, 72, 168, 336, 504 h. At each time point, the pH was measured and samples of 1 ml of the medium were taken and refreshed. After dilution with 9 ml of 2M HNO_3, the reacted medium was analyzed by inductive coupled plasma (ICP) spectroscopy (Thermo Scientific ICP Spectrometer, Model iCAP 6300 Series Duo, Thermo Fisher Scientific,Waltham, MA, USA) for Si, Ca, Mg, P concentration in solution. All the experiments were done in triplicate.

At the end of the test, the foams were washed in distilled water, dried and analysed by attenuated reflectance Fourier transform infrared spectroscopy (ATR-FTIR, Thermo Scientific Nicolet iS10) at room temperature, to monitor the growth of the hydroxycarbonate apatite layer, using a wavenumber resolution of 4 cm^{-1} for 32 scans from 4000 to 600 cm^{-1}.

4.2.4 ISO 10993 tests for in vitro cytotoxicity

Potential cytotoxicity effects of Ak and WD samples were assessed in accordance to ISO 10993-5 and ISO 10993-12. Briefly, dissolution products released by the samples (0.2 g/ml in α-MEM at 37°C) over a 72-hour period were prepared. Medical grade polyethylene (PE) was used as non-cytotoxic negative control and polyurethane (PU) containing 0.1% (w/w) zinc diethyldithiocarbamate (ZDEC) was used as toxic positive control. The dissolution products were filter sterilised and dilution series (25%, 50%, 75% and 100%) were prepared and supplemented with 10% (v/v) FCS prior to use.

Cell viability was assessed by a calorimetric cell metabolic activity assay based on the conversion of 3-(4,5-dimethylthiazol-2-yl)-2,5-diphenyltetrazolium bromide (MTT) into formazan. MC3T3-E1 cells were seeded on 96-well plates at 1×10^4 cells per well and left to grow in basal α-MEM for 24 hours prior to incubation in (1) fresh basal α-MEM, (2) the ceramic dissolution products or (3) controls for further 24 hours. Used culture media was removed and replaced with serum free MTT solution (1 mg/ml in α-MEM). Following an incubation period of 2 hours, the MTT solution was removed and each well was filled with 100 µl isopropanol and shaken briefly to dissolve the formazan derivatives. The optical density was measured spectrophotometrically at 570 nm using a microplate reader (SpectraMax M5).

4.2.5 Cell culture test

For cell attachment, proliferation and osteogenic differentiation studies, foams were cut to 37.5 mg of weight (the size was approximately 5×5×5 mm^3) and sterilised with 70% ethanol prior to washing in PBS.

Upon confluence, MC3T3 cells were harvested and suspended in basal media at a concentration of 1×10^6 cells in 25 ml. 25 ml of cell suspension was added to each sterile 50 ml Falcon tube containing one foam 3-D scaffold. The tubes were placed in an incubator (humidified atmosphere at 37 °C, 5% CO_2 and 21% O_2) for 2 hours with gentle agitation every 30 minutes to allow diffused cell adhesion. The solution was then replaced with osteogenic media (basal α-MEM supplemented with 100 μM ascorbate-2-phosphate, 10 nM dexamethasone and 10 mM of β-glycerophosphate). Cell-seeded foams were cultured in humidified atmosphere at 37 °C, 5% CO_2 and 21% O_2 for up to 21 days with media changes every 3-4 days. 1 ml of culture medium was collected prior to each media change for ICP analysis of Si, Ca, Mg and P concentrations. For gene expression analysis, cells were also seeded on Mg-free wollastonite-hydroxyapatite samples (CaO:SiO2=1.6), developed and discussed in a previous study[28], for comparison.

Viability of MC3T3 cells cultured on the 3-D foams at day 1, 3, 7 and 14 was determined by colorimetric WST-1 proliferation assay. At each time point, three cell-seeded foams were collected and each submerged in 5 ml of WST-1 reagent (1:10 dilution in α-MEM, Roche Diagnostic, West Sussex, UK). 100 μl was aspirated in triplicate from each sample following 2 hours incubation and, the optical density was measured spectrophotometrically at 440 nm using a SpectraMax M5 microplate reader.

Cell-seeded foams were fixed with 4% paraformaldehyde (PFA) and used for immunohistochemical analysis of cell attachment and osteogenic differentiation. After permeabilisation with buffered 0.5% Triton X-100 in PBS (300 mM sucrose, 50 mM NaCl, 3 mM $MgCl_2$, 20 mM Hepes and pH 7.2) and blocking with 10 mg/ml BSA in PBS, samples were incubated with relevant primary antisera (diluted appropriately using 10 mg/ml BSA in PBS) at 4 °C overnight. This was followed by hour-long incubation with Alexa Fluor® 488-conjugated secondary antibody.

The anti-Vimentin antibody (rabbit polyclonal, IgG, Abcam, Cambridge, UK), anti-Collagen Type I antibody (rabbit polyclonal, IgG, Abcam, Cambridge, UK), anti-Osteopontin antibody (rabbit polyclonal, IgG, Merck Millipore, Watford, UK) and anti-Osteocalcin antibody (rabbit polyclonal, IgG, Merck Millipore, Watford, UK) were used at dilutions of 1:500, 1:1000, 1:500 and 1:50 respectively. Alexa Fluor® 488-conjugated secondary antibody (goat anti-rabbit, IgG, Abcam, Cambridge, UK) was used at a dilution of 1:1000.

For analysis of cell attachment, F-actin was labelled using CytoPainter F-actin staining kit (Abcam, Cambridge, UK) following the manufacture's instruction. Briefly, Alexa Fluor® 568-conjugated phalloidin (1:1000 dilution in labelling buffer) was added simultaneously with the secondary antibody during the incubation period. All samples were counter-stained with DAPI (0.1 $\mu g\ ml^{-1}$ in PBS).

The samples were imaged under confocal microscopy (Leica SP5 MP laser scanning confocal microscope and software, Leica Microsystems, Wetzlar, Germany). The same samples were then dehydrated using an ascending series of ethanol and hexamethyldisilazane (HDMS) prior to sputter coating with gold and observation under scanning electron microscopy (JSM 6010 L, JEOL USA).

At day 21, two cell-seeded Ak or WD constructs were pooled and lysed for extraction of total RNA using Qiagen RNeasy kit (Qiagen, Manchester, UK) following manufacturer's instructions. The RNA samples were treated with DNase-1 reagent and reverse-transcribed using the SuperScript® VILO™ cDNA synthesis kit (Invitrogen, UK). SYBR green based qPCR assays were carried out using the QuantStudio™ 6 Flex system (Thermo Fisher, UK) for the analysis of osteogenic gene expression, including Runx2. The relative transcript levels of genes of interest were analysed using the comparative C_T method ($\Delta\Delta C_T$ method). Bar graphs were plotted and statistical analysis was performed at the level of ΔC_T.

Cytotoxicity and cell culture studies were performed by Dr. S. Li (Imperial College London).

4.2.6 Direct 3-D printing

Regarding exclusively wollastonite-diopside composition, it was also directly 3-D printed by means of a PowerWASP orienting extruder (Massa Lombarda, Italy), expressly equipped with a syringe to print preceramic inks consisting of silicone pastes incorporating fillers (see Fig. 4.2a). All the printing operations were done in collaboration with Mr. Hamada Elsayed (University of Padova).

The formulation was modified in terms of raw materials, replacing liquid silicone with a solid polymethylsiloxane (SILRES® MK, Wacker-Chemie GmbH, München, Germany), known to have a silica yield of 84 wt% after thermal decomposition in air. The required amount of silica (18 wt% of the final ceramic) was obtained from two contributions, that is 10 wt% from nano-sized silica (fumed silica, Aerosil R106, Evonik Germany) and 90 wt% from the above silicone, in order to positively modify the rheological properties of the slurry. No borax was added.

Fumed silica powders were wet mixed with MK in isopropanol (8 ml for 16 g of silica precursors) by means of a ball mill (60 min at 100 rpm, Pulverisette 7 planetary planetary ball mill, Fritsch, Idar-Oberstein, Germany). $CaCO_3$ and $Mg(OH)_2$ micro-sized powders (<10 µm, Industrie Bitossi, Italy) were subsequently incorporated into the polymer and again mixed (4 h at 400 rpm), to obtain a perfectly homogenous suspension with very fine fillers and no trace of powder aggregates. The achievement of such properties was extremely necessary for the direct ink writing, due to the need to avoid clogging throughout the printing step and to have continuity in the fluid flow through the nozzle.

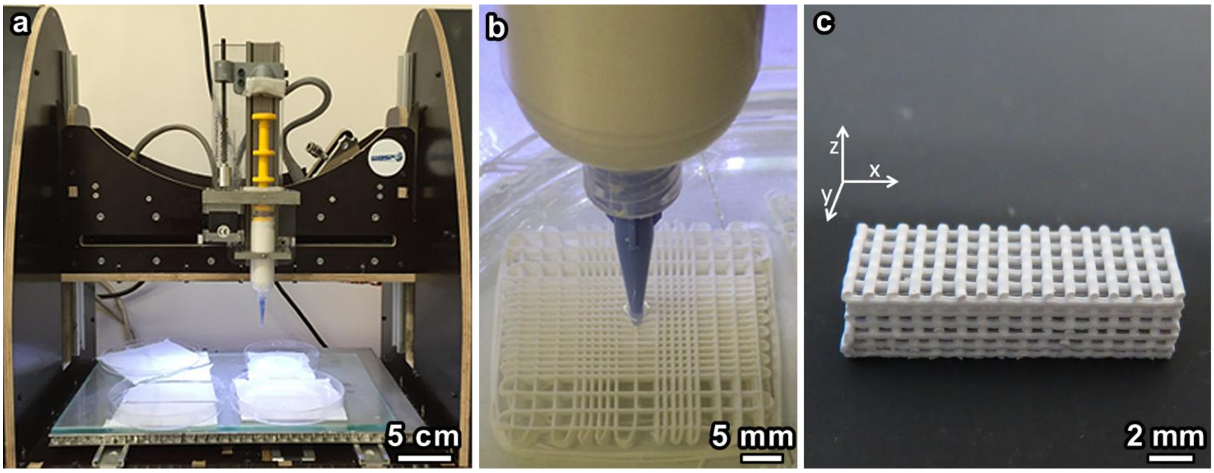

Fig. 4.2 Photographs of a) the 3-D printer equipped with syringe for silicone-based ink; b) detail of the printing process carried out in oil bath; c) overview of a 3-D printed scaffold with orientation of the axes.

The syringe of the printer feeding system was filled with the preceramic paste and scaffolds were later printed with conical nozzle (with a diameter of 0.41 mm, Nordson EFD, Westlake, Ohio) immersed in vegetal oil, thus preventing the premature drying of the solvent, that would have affected the viscosity of the ink (see Fig. 4.2b). Following the CAD file, scaffolds were in the form of prisms (see Fig. 4.2c) with dimensions 15 mm x 5 mm x 5 mm, as resulting from the overlapping of cylindrical rod, periodically arranged along x and y axes. The rods were in a stacking density of 11 rods/cm on the x-y plane and the distance between the longitudinal axes of adjacent rods was of 1 mm. The spacing between adjacent rods along the z axis was set at 350 µm.

After removal from the oil, printed scaffolds were cross-linked at 350 °C, with a heating rate of 0.5 °C/min and dwelling time of 1 h, prior to ceramization at 1100 °C (same heating rate and dwelling time as the cross-linking treatment) in air and nitrogen.

An example of a partial long bone replacement with a 3-D printed scaffold, found in literature, is given in Fig. 4.3. The implant was realized at the New Zealand Institute of Specialist Veterinary Surgeons and was received by a 8-year-older canine patient in 2013, in New Zealand[29].

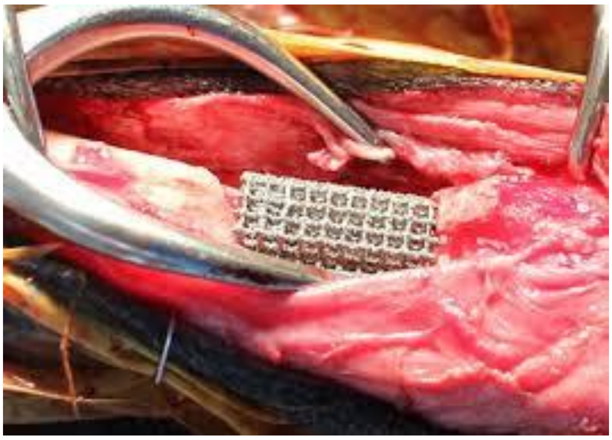

Fig. 4.3 Example[29] of a partial long bone replacement with a 3-D printed scaffold, realized at the New Zealand Institute of Specialist Veterinary Surgeons and received by a canine patient, in 2013.

4.3 Results

4.3.1 Characterization of scaffolds

Fig. 4.4a,b show that the ceramized samples of both formulations exhibited extensive porosity. Pores were derived from the water release occurred throughout the thermal decomposition of $Mg(OH)_2$ and borax. The simultaneous cross-linking of the polymer, which took place in the same temperature range as the dehydration of the fillers ($T<350°C$), allowed the porous shape to be maintained, without any viscous collapse. The foamed structure was maintained even after the subsequent ceramization at 1100 °C, implying the conversion of the silicone into silica and reaction with CaO and MgO, from the fillers.

It can be seen that the pore shape and size were more uniform in WD samples (Fig. 4.4b,d) in comparison to Ak ones (Fig. 4.4a,c). The pores in WD samples demonstrated near perfect spherical shape with diameters between 700 μm and 1 mm, which can be estimated from the image at higher magnification (Fig. 4.4c). In contrast, pores in Ak samples demonstrated a more random shape and had diameters of around 1 mm (Fig. 4.4d). One likely reason is represented by same composition of silicone-based mixtures. In fact, the overall molar balance for Ak samples was $CaO:MgO:SiO_2=2:1:2$, whereas WD samples had an overall molar balance of $CaO:MgO:SiO_2=2:1:3$. The higher content of silica in WD samples resulted in a higher silicone/fillers ratio and a consequently lower viscosity of pastes upon the foaming step.

The results from Hg intrusion porosimetry allowed a comparison between foams of different composition (Fig. 4.4e) in terms of the diameter of interconnections of adjacent pores. It is well known that an ideal scaffold should combine bioactive properties with a favourable structure, consisting of uniform pores with well-defined interconnections; in particular, interconnections with diameter exceeding 100 μm allow effective tissue ingrowth and eventually vascularisation, which is required for complete regeneration of bone[30]. The diameters of interconnections of Ak and WD samples are different (D_{mode} of 181 µm for Ak and 160 µm for WD foams, respectively), but both above the above-mentioned threshold.

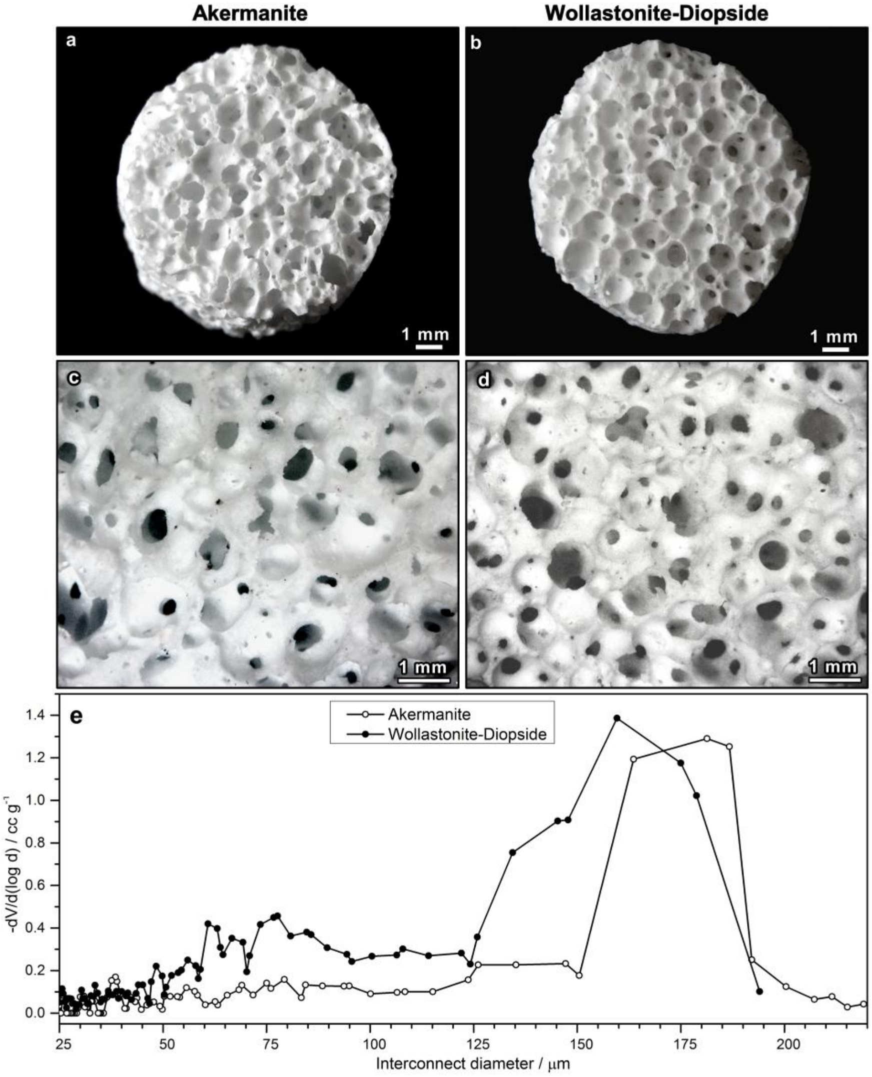

Fig. 4.4 a-b) Stereomicroscopy of the ceramized foam scaffolds; c-d) higher magnification; e) interconnect size distribution obtained by Hg porosimetry.

Fig. 4.5 confirmed the feasibility of Ca-Mg silicates by exploiting reactions between the ceramic residue from oxidative decomposition of H62C and the fillers. The upper pattern, for the Ak formulation, features the distinctive peaks of the desired phase ($Ca_2MgSi_2O_7$ - PDF#87-0046) with only minor peaks attributable to traces of monticellite ($CaMgSiO_4$ – PDF#84-1319). The lower pattern, again, testifies the obtainment of the desired phases ($CaSiO_3$ – PDF#75-1396, and $CaMgSi_2O_6$ – PDF#72-1497), with minor traces of akermanite. The presence of impurities was not considered as an issue, considering the reported bioactivity even of the "extra" monticellite crystal phase[31].

Mechanical and physical properties of the scaffolds are summarized in Tab. 4.1. Both Ak and WD scaffolds exhibited similar values of bulk and skeleton densities (ρ_{bulk} and $\rho_{skeleton}$ respectively). The average open porosities (P_{open}) for Ak and WD samples were 82 % and 83 % respectively. The average compressive strength (σ_{comp}) for Ak samples was 1.0 ± 0.2 MPa in comparison to 1.8 ± 0.3 MPa for WD. These values are superior compared to those reported in literature for analogous foams. For instance, Wu *et al.* have reported studies on akermanite-, diopside- and wollastonite-based foams with a compressive strength not exceeding 0.8 MPa, for a porosity of 81-82 %[17,24,25].

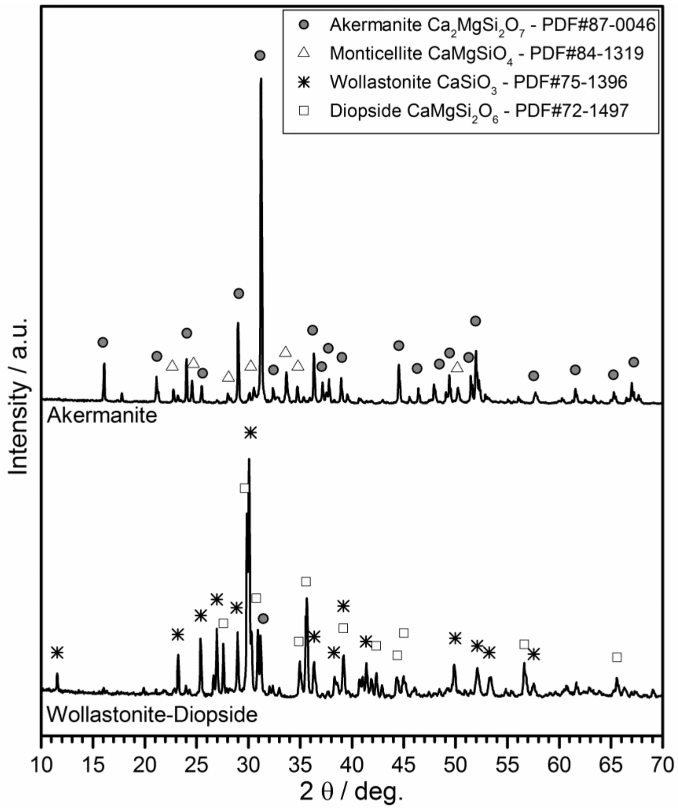

Fig. 4.5 XRD patterns of Ak and WD foam scaffolds.

Tab. 4.1 Physical and mechanical properties of Ak and WD samples.

	ρ_{bulk} (g cm^{-3})	$\rho_{skeleton}$ (g cm^{-3})	P_{open} (%)	σ_{comp} (MPa)
Ak	0.51 ± 0.06	3.08 ± 0.01	82	1.0 ± 0.2
WD	0.53 ± 0.04	3.28 ± 0.02	83	1.8 ± 0.3

4.3.2 Bioactivity test

Fig. 4.6 shows the dissolution profiles for the foam scaffolds, as functions of time, generated using both compositions. The dissolution profiles are the ionic concentrations in SBF as a function of contact time. They were determined by ICP for silicon (Si), calcium (Ca) and magnesium (Mg), i.e. the ions released by the scaffolds, as well as phosphorous (P), which was contained in SBF and involved in the formation of hydroxycarbonate apatite (HCA) on the samples. A control of pure SBF with no foams immersed was also included in the ICP analysis. The error bars are standard deviations calculated from triplicates.

SBF did not contain Si ions (Fig. 4.6a) and, following immersion of Ak samples, the Si concentration increased to 62 µg ml^{-1} over the first 24 h. From 24 h to 72 h, the concentration of Si species increased to 92 µg ml^{-1}, but with a slower rate of Si release, as the solution neared saturation. The amount of Si found in SBF was maintained at approximately 90 µg ml^{-1} from day 3 to day 7, followed by decrease to 70 µg ml^{-1}. Following the dissolution profile of WD samples, the Si concentration increased to 92 µg ml^{-1} over the first 72 h at an almost linear rate of release and then followed the same trend as Ak samples.

The Ca content of the control SBF was constant at approximately 90 µg ml^{-1} (Fig. 4.6b). Concerning the release profile of Ca^{2+} ions from the Ak foams, the concentration of Ca in SBF reached 255 µg ml^{-1} after 7 days and then was maintained constant up to day 21. The concentration of Ca released from WD samples in SBF reached approximately 190 µg ml^{-1} after 3 days, followed by a slow increase to 200 µg ml^{-1} from day 3 to 14. It should be remarked that the formulation for Ak samples was slighly richer in Ca compared to that of WD samples and this could explain the higher amount of Ca ions released by Ak samples (all the samples immersed in SBF at the same weight to volume ratio). The Ca concentration for WD, however, slightly decreased as the soaking time increased from 14 days to 21 days, reaching 180 µg ml^{-1}. This was likely caused by calcium phosphate deposition on the scaffold surface, even if weak, after 14 days of immersion.

The Ca release profiles of these two Ca-Mg silicates were also compared with those of the Mg-free wollastonite-hydroxyapatite bioceramics (WA) that we developed and discussed in a previous work[28]. WD samples exhibited a more controlled degradation, especially when comparing them with our previous WA scaffolds derived from a higher CaO/SiO_2 ratio.

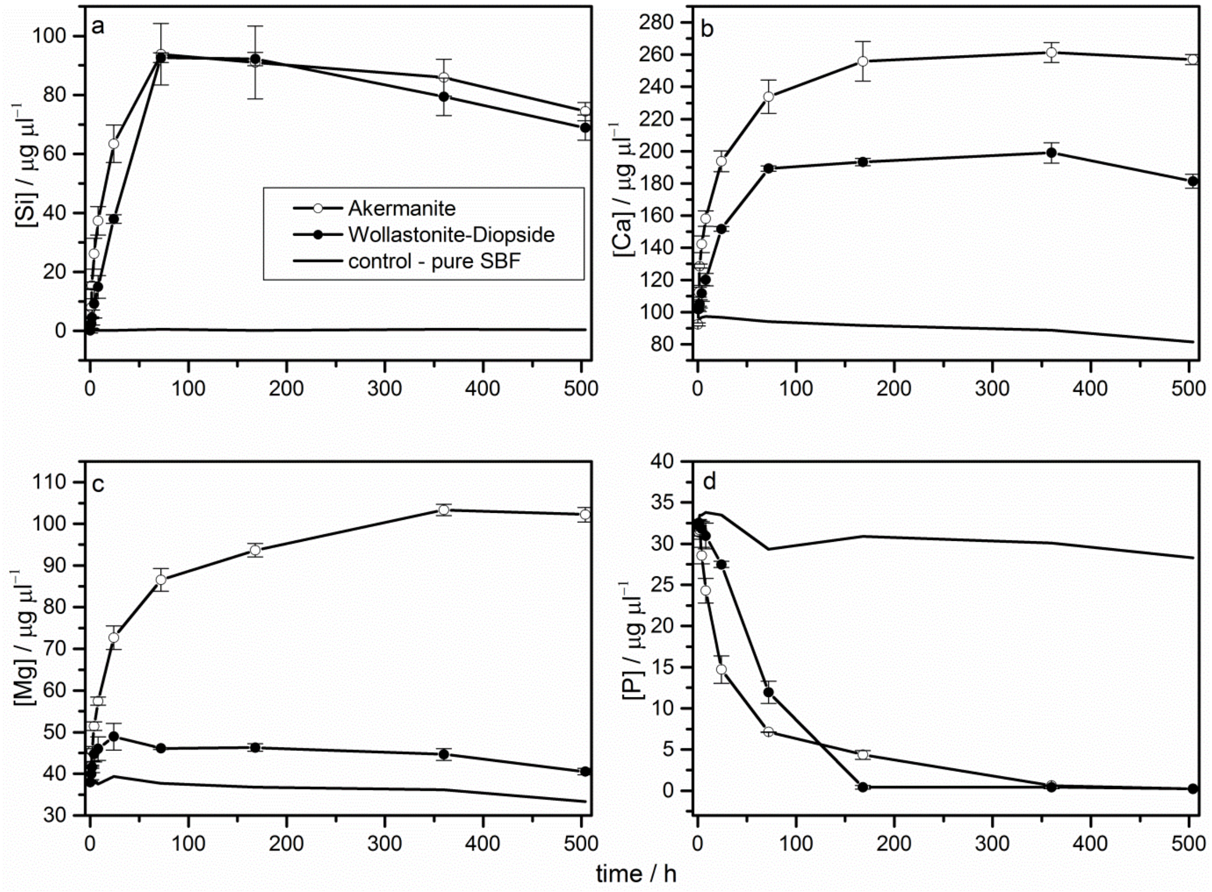

Fig. 4.6 Dissolutions profiles as a function of time for Ak and WD foams after soaking in SBF for 21 days. a) Si; b) Ca; c) Mg; d) P. Control is SBF without any samples immersed. [Results are presented as mean ± SD, n=3 per each time point].

Fig. 4.6c illustrates the release of Mg in SBF from Ak and WD samples. The control SBF showed levels of Mg between 32 and 38 µg ml^{-1} up to 21 days. After immersion of Ak samples in SBF for 24 h, the Mg species increased to 86 µg ml^{-1}. From 24 h to 14 days, the concentration of Mg ions kept increasing to 103 µg ml^{-1} at a slower rate of release and maintained at approximately 100 µg ml^{-1} to 21 days. The release of Mg was much lower for WD samples. Mg concentration in SBF reached 50 µg ml^{-1} after the first 24 h, then decreased and maintained at approximately 45 µg ml^{-1} to 14 days. There was a decrease to 40 µg ml^{-1} from 14 to 21 days. Similar to Ca release, the slow release of Mg in WD could be due to the smaller amount of Mg included in the formulation of WD compared to Ak formulation.

Both compositions did not contain P, so that there was no release of P species from the foams (Fig. 4.6d). The control SBF, however, showed levels of P between 32 and 28 µg ml^{-1} up to 21 days immersion. Following the immersion of both Ak and WD samples, there was a noticeable decrease in concentration of P species in SBF. The P concentration rapidly decreased to 7 µg ml^{-1} after 72 h for Ak and reached 0.5 µg ml^{-1} by day 14. The P concentration in SBF containing WD samples decreased to 12 µg ml^{-1} after 72 h and reached 0.5 µg ml^{-1} by day 7. The formation of a HCA layer on the surface of both scaffolds, as evidenced by FTIR spectra (Fig. 4.7a), was likely the reason for decreased P concentration in SBF.

The dissolution of the foams caused the pH of the medium to increase. Values were comprised between 7.4 and 8.2 for Ak samples and from 7.4 to 7.9 for WD samples.

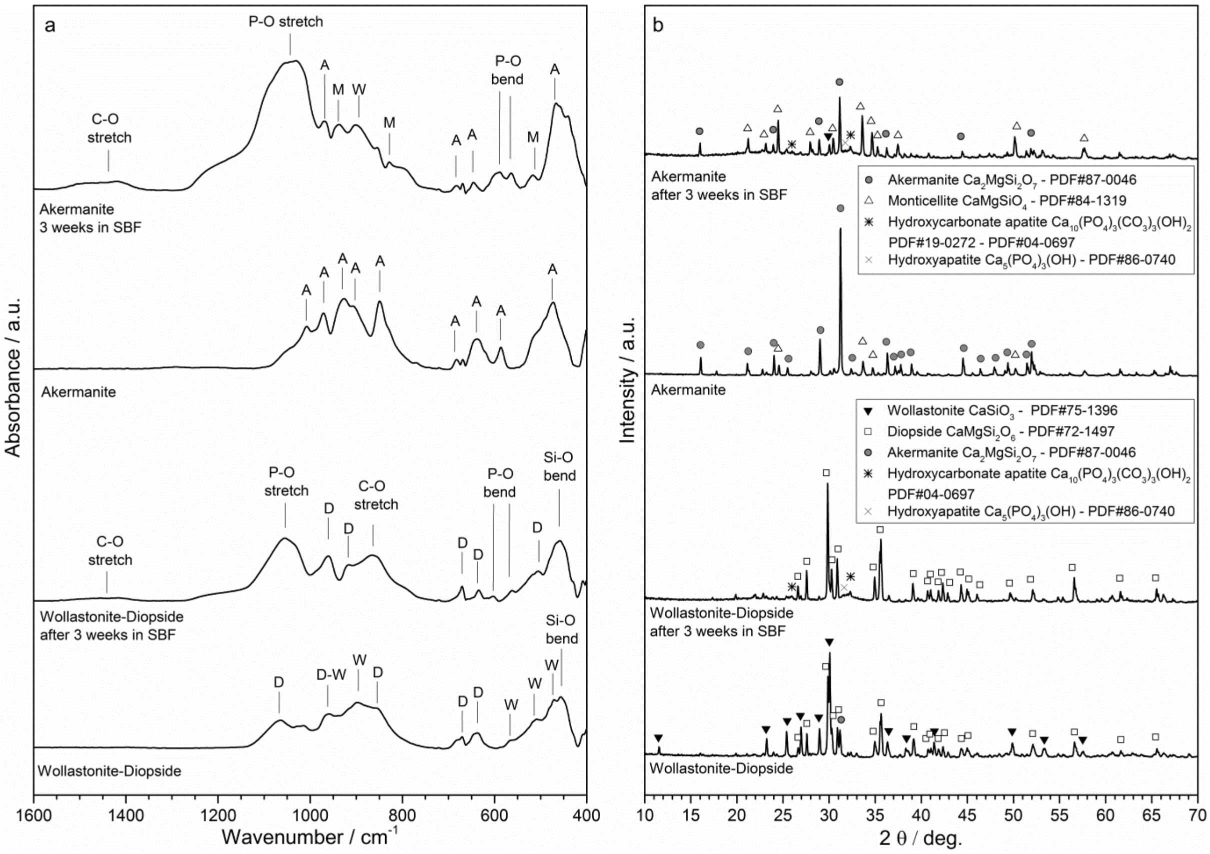

Fig. 4.7 FTIR and XRD spectra of Ak and WD foam scaffolds before and after soaking in SBF for 21 days.

FTIR spectroscopy was used to determine the growth of the HCA layer on the samples after soaking in SBF. Fig. 4.7 compares FTIR (panel "a") and XRD (panel "b") spectra of Ak and WD samples immersed in SBF for 21 days as well as unreacted samples. The FTIR spectrum of the unreacted Ak samples exhibited vibrational bands in the same positions as reported in literature for akermanite, that means 1009, 972, 928, 906, 852, 683, 638, 586, 475 cm^{-1} [32]. After soaking in SBF for 3 weeks, the XRD spectra suggested the conversion of most of the akermanite into monticellite, which has the same Ca/Si molar ratio compared to akermanite, but lower Ca/Mg and Si/Mg molar ratio. This was confirmed by the FTIR spectrum, showing only a few of the akermanite vibrational bands mentioned above and, instead, some at 942, 829 and 519 cm^{-1}, which can be attributed to monticellite[33]. A band at 896 cm^{-1} was likely due to wollastonite[34], as its presence was also confirmed by the XRD phase identification.

The FTIR spectrum of WD samples before soaking in SBF showed a vibrational band at 460 cm^{-1} which can be attributed to Si-O bending[35]. In addition, vibrational bands at 960, 896, 564, 509, 470 cm^{-1}, which are known from literature to be related to wollastonite[34], and at 1066, 960, 858, 673, 635 cm^{-1} due to diopside[36]. This phase assemblage is confirmed by the XRD pattern, showing mainly wollastonite. After soaking in SBF for 3 weeks, the XRD pattern of WD showed that the wollastonite was fully converted into diopside. Further evidence was given by the FTIR spectrum: indeed, the vibrational bands that were previously attributed to the presence of wollastonite were not present, maintaining only the vibrational bands related to diopside.

Concerning the growth of hydroxycarbonate apatite over the 21-day immersion in SBF, the FTIR spectra of both Ak and WD samples after soaking in SBF showed vibrational bands at 567 and 603 cm^{-1}, corresponding to the P-O υ_4 bending vibrations, and at 1050 cm^{-1}, corresponding to the P-O υ_3 stretching vibrations. Vibrational bands were observed as well for carbonate ions at approximately 1400-1500 cm^{-1}, corresponding to the carbonate υ_3 stretching vibrational mode, and, only for WD samples, at 870 cm^{-1}, corresponding to υ_2. All of them can be associated with the presence of crystalline hydroxycarbonate apatite[37].

It should be highlighted that hydroxycarbonate apatite formation on bioactive implants demonstrates superior bioactive response in comparison to non-carbonated hydroxyapatite[38]. This is due to the similarity in chemical and structural composition between hydroxycarbonate apatite and mineral phase in bone, which is responsible for interfacial bonding with tissues[6].

4.3.3 Cytotoxicity

The biocompatibility and ability of a biomaterial to support cell attachment and growth are important criteria for biological applications. In the present study, an MTT metabolic activity assay was performed in accordance to ISO 10993 (Biological evaluation of medical devices) to assess the potential cytotoxic effects of both Ak and WD materials. The ISO guidance stated that if the viability of cells is reduced to < 70 % of blank (i.e. non-cytotoxic controls), the test material will be deemed to have a cytotoxic potential. In addition, in a valid test, the 50 % dilution of the test sample should result in at least the same or a higher viability in comparison to the 100 % extract. As shown in Fig. 4.8, both Ak and WD demonstrated excellent biocompatibility with negligible reduction in metabolic activity.

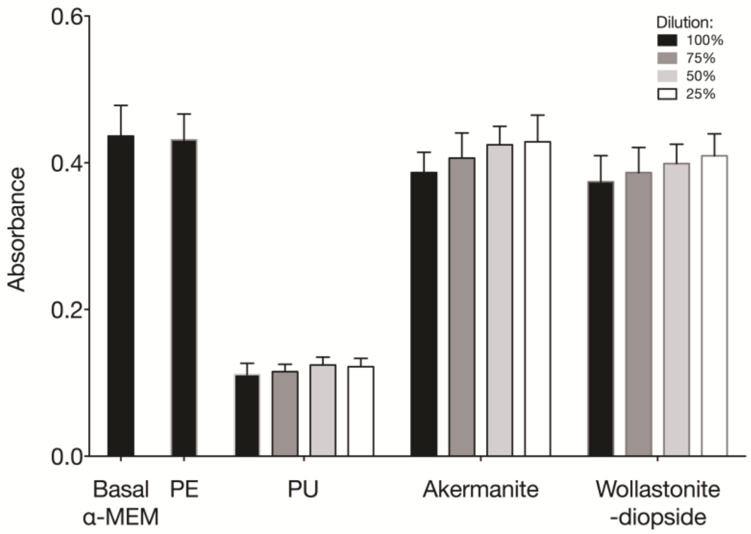

Fig. 4.8 In vitro cytotoxicity analysis by MTT metabolic activity assay performed in accordance to ISO 10993 standards.

4.3.4 Cell culture study

Following seeding into the foam scaffolds of Ak and WD, WST-1 cell proliferation assay was used as a quantitative measure to monitor viability of cells on the scaffold for up to 14 days. The optical density of WST-1 solution, incubated with cell-seeded constructs for 2 hours at each time point, indicated excellent gradual cell growth and on-going cell survival (Fig. 4.9). There was no significant difference in optical density (i.e. cell viability) between the 2 materials at each time point. We have also previously demonstrated that Mg-free wollastonite-hydroxyapatite was non-cytotoxic and thus, the excellent biocompatibility of polymer-derived silicate ceramics[28].

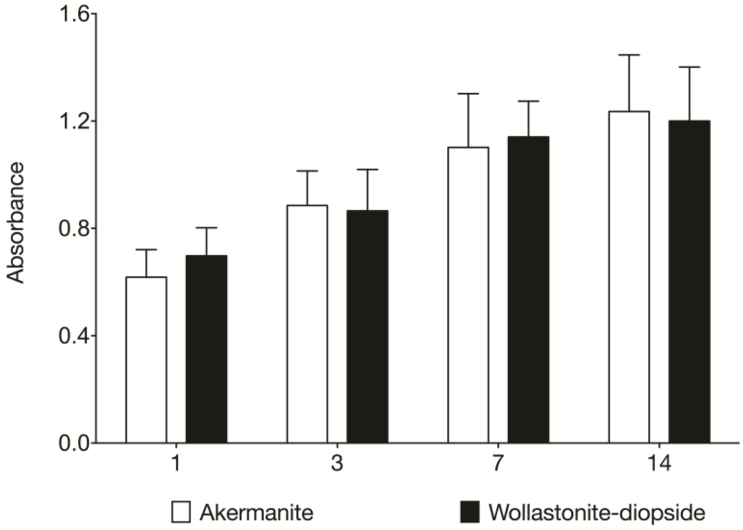

Fig. 4.9 WST-1 assay of MC3T3 cell seeded Ak and WD scaffolds, cultured for up to 15 days.

Furthermore, the results from cell attachment of the foams of Ak and WD materials was examined by immunohistochemical staining for up to 21 days. The expression of 2 of the major cytoskeletal constituents Vimentin (green stain), intermediate filament proteins, and F-actin (red stain), microfilaments, was evident in MC3T3 cells on both Ak and WD foam scaffolds (Fig. 4.10). More cell spreading can be observed on WD foams in comparison to Ak foams. Since cells are able to detect the mechanical properties of the adhesion substrate and subsequently regulate the integrin biding, focal adhesion assembly and cytoskeleton accordingly[39,40], the advanced cell spreading on WD foams was likely due to the superior mechanical property reported above in Tab. 1. It has been reported that when collagen was adsorbed or covalently bound on glass or hard polyacrylamide gel (PAG), cultured cells were more spread with streak-like focal adhesion site and rich in actin cytoskeleton. On the contrary, when soft PAG was used, the cells remained spherical without signs of spreading or adhesion apparatus and, subsequently underwent apoptosis[41].

The attachment of the cells to the scaffolds, the cell morphology and the formation of cell matrix were investigated by SEM imaging at different time points (Fig. 4.11). Fig. 4.11a-b make a comparison between Ak and WD samples after 7 days of cell culture. On the surface of both the formulations, the cells exhibited elongated filopodia, which serve as pioneers in protrusion and are used by the cells to probe the microenvironment and to promote their motility[42]. Besides, the cells seemed to have colonized the pores of the scaffolds.

Fig. 4.11c-d show the proliferation of the cells after 21 days of cell culture on the scaffolds Ak and WD respectively. In either case, the cells appeared to have formed mineralized bone nodules, in the form of white globular precipitates. In details, WD samples (Fig. 4.11d) seemed to have more mineralized bone nodules formed by the cells than Ak samples (Fig. 4.11c).

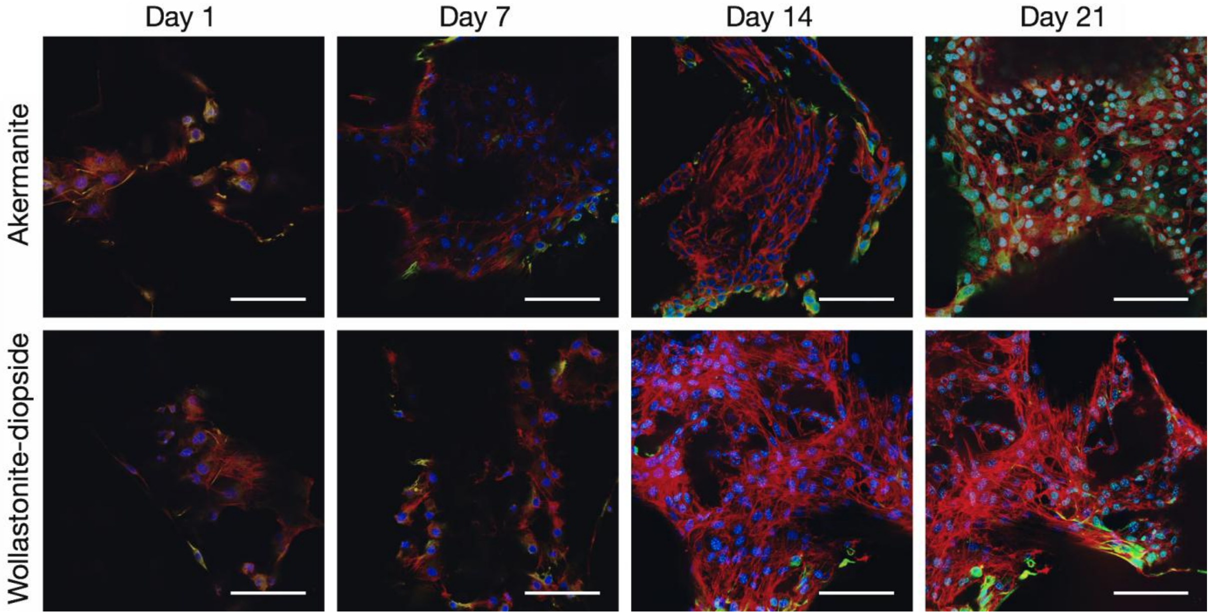

Fig. 4.10 Representative images of immunohistochemical staining of the cytoskeleton of MC3T3 cells cultured on Ak and WD foam scaffolds for up to 21 days. Stack images of cells expressing Vimentin (green fluorescence), F-actin (red fluorescence) and DAPI nuclei counter stain (blue fluorescence). Scale bar = 100 µm.

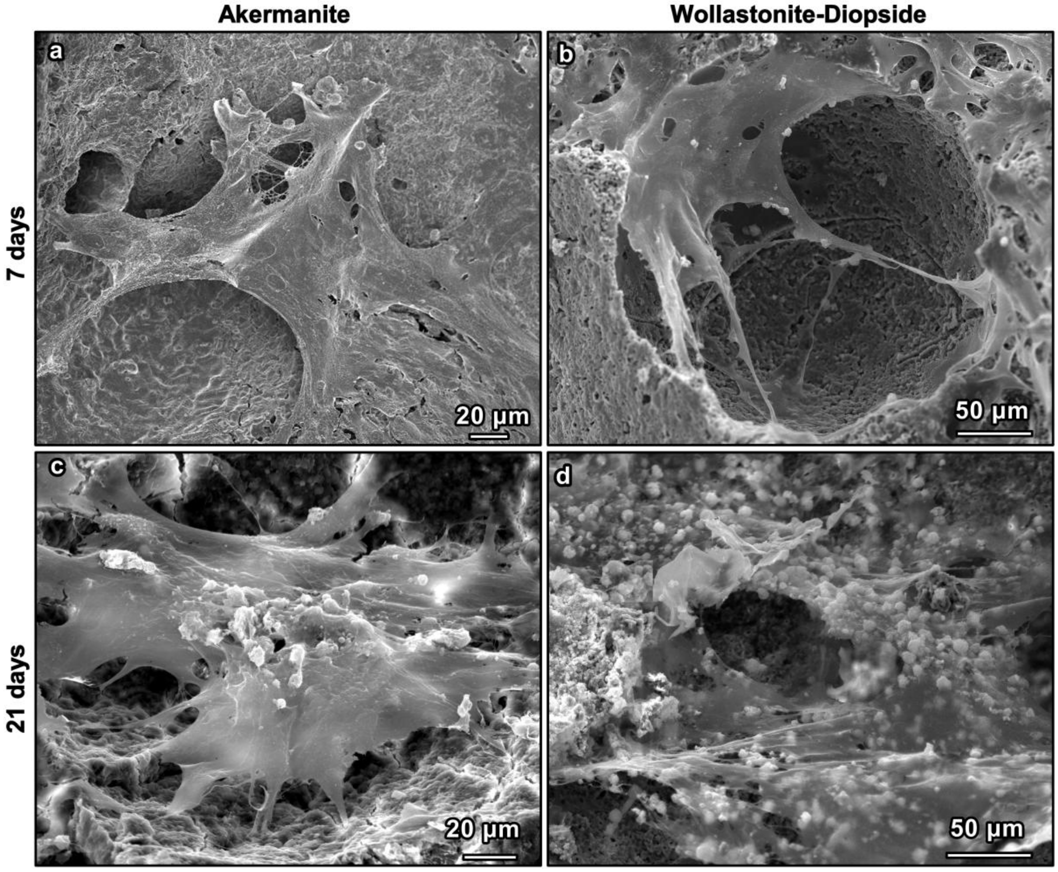

Fig. 4.11 SEM micrographs at different time points of the MC3T3 cells cultures on the scaffolds.

The EDS spectra reported in Fig. 4.12 were taken for both the sample formulations on the apparent mineralized bone nodules formed by the cells and on the scaffold surface adjacent to the cell groups, after coating the samples with chromium. All of them were normalized on the peak of Si at 1.74 keV with the aim of highlighting the differences in Ca/Si and Ca/P ratios (even though the content of Si in the bone nodules and in the adjacent surfaces are expected to be much different).

The spectra showed that Ca and P were present on the cellular deposits for both the samples Ak and WD, confirming that mineralization occurred; while the spectra taken on the scaffold surfaces adjacent to the cell groups showed that P and Ca contents were much lower when compared with Si content. It should be remarked that a very weak peak attributable to Na was detected. Na could be ascribed both to the borax fillers and the media used for the cell culture test.

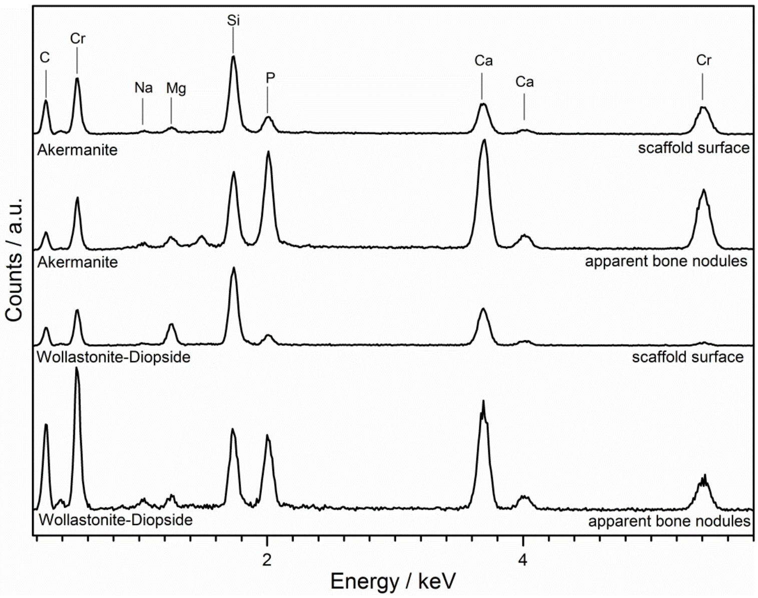

Fig. 4.12 spectra of the scaffold surface adjacent to the cells and of the apparent bone nodules formed by the cells on Ak and WD foams.

Concerning the growth of the cellular deposits mentioned above, SEM images of the samples seeded with cells after 21 days of cell culture were compared with those taken on the controls, that were the same Ak and WD samples immersed in the same culture medium, but not seeded with cells. The controls did not exhibit the formation of surface precipitates, that implies that the calcium phosphates observed on the seeded samples were not simply due to the reaction of the Ca ions released by the samples with the P provided by the culture medium, but they might be attributed to cellular osteogenic activities occurring throughout the cell culture test.

4.3.5 Osteogenic differentiation

For analysis of osteogenic differentiation and matrix formation, day-21 MC3T3 cell seeded Ak and WD constructs were first immunostained with antibodies against phenotypic osteogenic proteins (Fig. 4.13). The formation of bone-like matrix was evident. Osteoblastic activity was confirmed by the expression of Collagen Type I, a commonly used extracellular marker for early bone matrix formation. The expression of Collagen Type I appeared particularly robust and well organised on WD foam scaffolds. In turn, more robust expression of Osteopontin, an extracellular protein that regulate matrix mineralisation, as well as Osteocalcin, a late marker for bone formation and matrix mineralisation, was observed in WD foam scaffolds in comparison to Ak ones.

We have previously demonstrated promising osteogenic differentiation of MC3T3 cells on Mg-free wollastonite-hydroxyapatite (WA) foam scaffolds[28]. Real-time qPCR gene expression analysis was used in the present study as a quantitative measure to demonstrate the positive effects of Mg that were incorporated in the newly developed Ak and WD foams (Fig. 4.14).

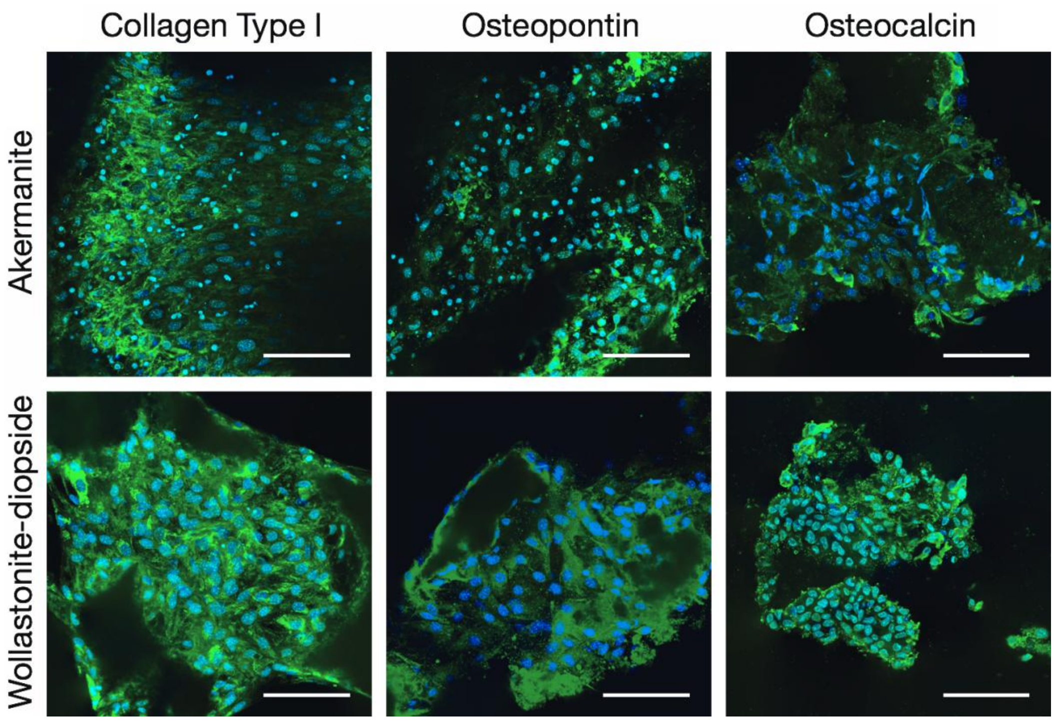

Fig. 4.13 Immunohistochemical examination (day-21) of MC3T3 seeded Ak and WD explants. Collagen Type I, Osteopotin and Osteocalcin (green fluorescence), nuclei (blue fluorescence). Scale bar = 100 µm.

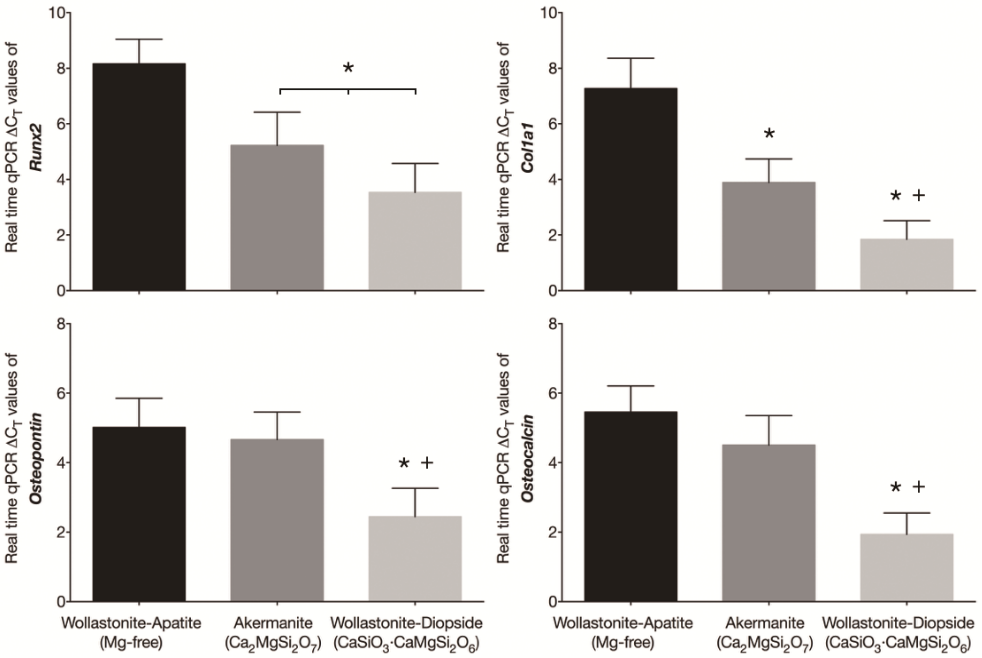

Fig. 4.14 Analysis of expression of Runx2, Col1a1, Osteopotin and Osteocalcin transcripts in day-21 MC3T3 cells cultured on Ak and WD scaffolds using real-time qPCR. * $p<0.05$ compared to Mg-free WA. + $p<0.05$ compared to both Ak and Mg-free WA.

Levels of Runx2, a key osteoblast differentiation transcription factor, were significantly higher in Ca-Mg silicate ceramics Ak and WD. The level of Runx2 detected in day-21 WD constructs appeared higher than Ak constructs, though this observation cannot be statistically proven. Interestingly, the transcription level of the three Runx target genes, Col1a1, Osteopontin and Osteocalcin, were all significantly higher in day-21 WD constructs compared to both Mg-free WA and Ak.

These observations confirmed the stimulatory effect of Mg in osteogenesis. In fact, previous studies have also demonstrated that Mg is a promising agent in skeletal tissue engineering applications due to its ability to stimulate new bone formation[19]. Mg was suggested to interact with integrins of osteoblasts that are responsibe for cell adhesion and stability[19,43]. The importance of Mg in bone metabolism was underlined by studies that demonstrated Mg depletion can result in impaired bone growth, increased bone resorption and loss in trabecular bone volume in animal models[21,44,45].

In addition to Mg, Ca^{2+} and soluble silica were also released by the bioactive Ca-Mg silicate ceramics. The stimulatory and dose-dependent osteogenic effects of these ionic products have been well-documented in a number of studies[46,47,48,49].

Although ICP analysis confirmed Ak foams released higher levels of Ca and Mg, the release of Si was significantly lower in comparison to WD foams. Si is a known essential element for metabolic processes associated with the formation and calcification of bone tissue. High Si contents have been detected in early stages of bone matrix calcification[50] and, aqueous Si has been shown to induce the precipitation of hydroxyapatite, the inorganic mineral phase that contributes to 70% of human bone mass[51]. Presence of Si in the form of orthosilicate acid has been shown to stimulate osteoblastic differentiation of human osteoblast cells and Collagen Type I formation[52]. Further, dietary Si intake has been shown to increase the bone mineral density in both men and premenopausal women[53,54].

Therefore, it is likely that the collective effects of Ca, Mg as well as Si released from WD foams played a significant role in the enhanced osteogenic differentiation and matrix formation observed in the present study. Further, the more controlled dissolution and consistent pore distribution in WD samples may also have contributed to the superior osteogenesis.

4.3.6 Direct 3-D printing

Regarding exclusively WD composition, the formulation was also 3-D printed by direct ink writing.

Mechanical properties of the samples are reported in Tab. 4.2 (courtesy of Mr. Hamada Elsayed, University of Padova). Reticulated WD scaffolds exhibited a remarkable compressive strength, ranging from 3.8 to 5.3 MPa, depending on the pyrolysis atmosphere, for a total porosity between 65 and 75 %.

Tab. 4.2 Compressive strength and open porosity of ceramized 3-D printed WD scaffolds.

Treatment	σ_{comp} (MPa)	P_{open} (%)
Air	5.3 ± 0.3	65
N_2	3.8 ± 0.4	75

As visible in Fig. 4.15 (courtesy of Mr. Hamada Elsayed, University of Padova), the obtained reticulated structures exhibited, after ceramization, the absence of macroscopic cracks. Moreover, it should be noted that the material was not dense, but extensively porous, as demonstrated by the high magnification detail of a rod surface (Fig. 4.15d).

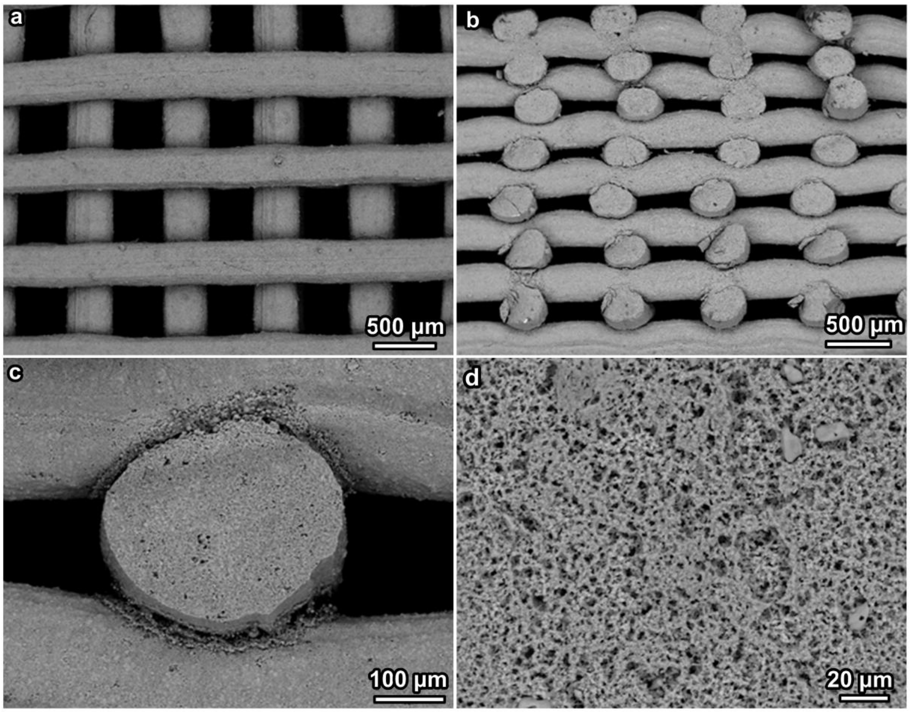

Fig. 4.15 Ceramized 3-D printed WD scaffolds: a) top view, b) cross-section, c) detail of a rod cross-section, d) high magnification detail of a rod surface.

4.4 Conclusions

Ca-Mg-rich glass-ceramics (based on akermanite and wollastonite-diopside) were successfully synthesized and shaped into highly porous foams, starting from silicone-based mixtures incorporating powdered oxide fillers.

Some fillers provided an extensive foaming, at 350 °C, simply by water release in the polymer before its ceramic conversion; this conversion was completed at 1100 °C, with the formation of the desired phases.

After ceramization, the foams exhibited an open porosity of 80 %, with interconnections of 160-180 μm and a compressive strength of 1-2 MPa.

Throughout a 21-day SBF dissolution test in SBF, the obtained glass-ceramics demonstrated suitable dissolution rates, pH and ionic concentrations. A cytotoxicity analysis, performed in accordance to ISO10993 standards, confirmed an excellent biocompatibility. MC3T3-E1 cells cultured on the foams demonstrated enhanced osteogenic differentiation and matrix formation in comparison to Mg-free counterparts.

The addition of Mg seemed to further enhance the bioactivity and the potential for bone regeneration applications of Ca-silicate materials.

Wollastonite-diopside formulation was also shaped by direct 3-D printing, obtaining crack-free reticulated structures.

Lastly, vascularisation is an important criterion for successful clinical translation of scaffold-based bone tissue engineering therapy. To assess the ability of the Ca-Mg silicate ceramic scaffolds to support vascular network formation, future studies will focus on the use of more clinically relevant cell population such as multipotent stem cells and, assess the survival and integration with host tissues in vivo in animal models.

References

[1] R.M. Nerem, A. Sambanis, “Tissue Engineering: From Biology to Biological Substitutes.” Tissue Eng. 1995 1 [1] 3-13.

[2] T.M. Freyman, I.V. Yannas, L.J. Gibson, ”Cellular materials as porous scaffolds for tissue engineering.” Prog Mater Sci. 2001;46:273–282.

[3] R.P. Lanza, R. Langer, J. Vacanti, “Principles of Tissue Engineering.” 2nd Ed., Ed. Academic Press, New York, 2000.

[4] http://medicalxpress.com

[5] A. Hoppe, N. S. Güldal, A. R. Boccaccini, A review of the biological response to ionic dissolution products from bioactive glasses and glass-ceramics. Biomaterials, 32 (2011) 2757-2774.

[6] L. L. Hench, “Bioceramics: From Concept to Clinic”, J. Am. Ceram. Soc., 74 [7] 1487-1510 (1991).

[7] L.L. Hench, and J.K. West. "Biological applications of bioactive glasses."Life Chem Rep 13 (1996): 187-241.

[8] L.L. Hench, J.M. Polak. "Third-generation biomedical materials."Science 295.5557 (2002): 1014-1017.

[9] E-J. Kim, S-Y. Bu, M-K. Sung, M-K- Choi. "Effects of silicon on osteoblast activity and bone mineralization of MC3T3-E1 cells." Biological trace element research 152.1 (2013): 105-112.

[10] M-Y. Shie, S-J. Ding, H-C. Chang, "The role of silicon in osteoblast-like cell proliferation and apoptosis." Acta biomaterialia 7.6 (2011): 2604-2614.

[11] F. Maehira, I. Miyagi, Y. Eguchi, "Effects of calcium sources and soluble silicate on bone metabolism and the related gene expression in mice." Nutrition 25.5 (2009): 581-589.

[12] E.M. Brown, R.J. MacLeod. "Extracellular calcium sensing and extracellular calcium signaling." Physiological reviews 81.1 (2001): 239-297.

[13] S. Maeno, Y. Niki, H. Matsumoto, H. Morioka, T. Yatabe, A. Funayama, Y. Toyama, T. Taguchi, J. Tanaka, “The effect of calcium ion concentration on osteoblast viability, proliferation and differentiation in monolayer and 3D culture,” Biomaterials. 26 [23] 4847-4855 (2005).

[14] M. Yamauchi, T. Yamaguchi, H. Kaji, T. Sugimoto, K. Chihara, “Involvement of calcium-sensing receptor in osteoblastic differentiation of mouse MC3T3-E1 cells,” Am. J. Physiol. Endocrinol. Metab. 288 [3] 608-616 (2005).

[15] P.N. De Aza, F. Guitan, S. De Aza, “Bioactivity of wollastonite ceramics: in vitro evaluation.” (Pergamon Press, 1994).

[16] W. Xue, X. Liu, X. Zheng, C. Ding, “In vivo evaluation of plasma-sprayed wollastonite coating.” Biomaterials, 26(17) (2005) 3455-3460.

[17] C. Wu, Y. Ramaswamy, P. Boughton, H. Zreiqat, “Improvement of mechanical and biological properties of porous CaSiO3 scaffolds by poly(D,L-lactic acid) modification.” Acta Biomater. 4(2) (2008) 343–53.

[18] W. Zhai, H. Lu, C. Wu, L. Chen, X. Lin, K. Naoki, J. Chang, “Stimulatory effects of the ionic products from Ca–Mg–Si bioceramics on both osteogenesis and angiogenesis in vitro.” Acta biomaterialia. 9(8) (2013) 8004-8014.

[19] H. Zreiqat, C.R. Howlett, A. Zannettino, P. Evans, G. Schulze-Tanzil, C. Knabe, M. Shakibaei, “Mechanisms of magnesium-stimulated adhesion of osteoblastic cells to commonly used orthopaedic implants.” Journal of biomedical materials research. 62(2) (2002) 175-184.

[20] F.I. Wolf, A. Cittadini, “Magnesium in cell proliferation and differentiation.” Front Biosci. 4 (1999) D607-D617.

[21] R.K. Rude, H.E. Gruber, H.J. Norton, L.Y. Wei, A. Frausto, J. Kilburn, “Reduction of dietary magnesium by only 50% in the rat disrupts bone and mineral metabolism.” Osteoporosis international. 17(7) (2006) 1022-1032.

[22] T. Okuma, “Magnesium and bone strength”. Nutrition. 17(7) (2001) 679-680.

[23] M. Vallet-Regi, A.J. Salinas, J. Roman, M. Gil, “Effect of magnesium content on the in vitro bioactivity of CaO-MgO-SiO_2-P_2O_5 sol-gel glasses”. Journal of Materials Chemistry. 9(2) (1999) 515-518.

[24] C. Wu, Y. Ramaswamy, H. Zreiqat, “Porous diopside ($CaMgSi_2O_6$) scaffold: a promising bioactive material for bone tissue engineering.” Acta Biomater. 6(6) (2010) 2237-2245.

[25] C. Wu, J. Chang, W. Zhai, S. Ni, J. Wang, “Porous akermanite scaffolds for bone tissue engineering: preparation, characterization, and in vitro studies.” Journal of Biomedical Materials Research Part B: Applied Biomaterials. 78(1) (2008) 47-55.

[26] M.A. Sainz, P. Pena, S. Serena, A. Caballero, “Influence of design on bioactivity of novel $CaSiO_3$–$CaMg(SiO_3)_2$ bioceramics: in vitro simulated body fluid test and thermodynamic simulation.” Acta Biomater. 6(7) (2010) 2797-2807.

[27] P. Colombo, E. Bernardo, G. Parcianello, Multifunctional advanced ceramics from preceramic polymers and nano-sized active fillers. J. Eur. Ceram. Soc. 33 (2013) 453–469.

[28] L. Fiocco, S. Li, M. M. Stevens, E. Bernardo, J. R. Jones, Highly porous polymer-derived wollastonite-hydroxyapatite ceramics for bone regeneration (submitted to Biomed. Mater., August 2015)

[29] http://www.nzva.org.nz

[30] J. R. Jones, L. L. Hench, Factors affecting the structure and properties of bioactive foam scaffolds for tissue engineering. J. Biomed. Mater. Res. Part B: App. Biomater. 68 (2004) 36-44.

[31] X. Chen, J. Ou, Y. Kang, Z. Huang, H. Zhu, G. Yin, H. Wen, Synthesis and characteristics of monticellite bioactive ceramic. J. Mater. Sci: Mater. Med. 19 (2008) 1257-1263.

[32] J. Hanuza, M. Ptak, M. Mączka, K. Hermanowicz, J. Lorenc, A.A. Kaminskii,Polarized IR and Raman spectra of $Ca_2MgSi_2O_7$, $Ca_2ZnSi_2O_7$ and $Sr_2MgSi_2O_7$ single crystals: temperature-dependent studies of commensurate to incommensurate and incommensurate to normal phase transitions, J. Solid State Chem., 191 (2012), pp. 90–101.

[33] R. T. Downs, (2006) The RRUFF Project: an integrated study of the chemistry, crystallography, Raman and infrared spectroscopy of minerals. Program and Abstracts of the 19th General Meeting of the International Mineralogical Association in Kobe, Japan. O03-13 (monticellite spectrum ID R040115).

[34] R. T. Downs, (2006) The RRUFF Project: an integrated study of the chemistry, crystallography, Raman and infrared spectroscopy of minerals. Program and Abstracts of the 19th General Meeting of the International Mineralogical Association in Kobe, Japan. O03-13 (wollastonite spectrum ID R040131).

[35] R. Morsy, R. Abuelkhair, T. Elnimr, Synthesis of Microcrystalline Wollastonite Bioceramics and Evolution of Bioactivity. Silicon. 2014.

[36] R. T. Downs, (2006) The RRUFF Project: an integrated study of the chemistry, crystallography, Raman and infrared spectroscopy of minerals. Program and Abstracts of the 19th General Meeting of the International Mineralogical Association in Kobe, Japan. O03-13 (diopside spectrum ID R040009).

[37] I. Rehman, W. Bonfield, Characterization of hydroxylapatite and carbonated apatite by photo acoustic FTIR spectroscopy. J. Mater. Sci.: Mat. in Med. 8 (1997) 1-4.

[38] J. C. Merry, I. R. Gibson, S. M. Best, W. Bonfield, Synthesis and characterization of carbonate hydroxyapatite. J. Mater. Sci. - Mater. Med. 9 (1998) 779-783.

[39] Ingber, D. E., Prusty, D., Sun, Z., Betensky, H. Wang, N. 1995. Cell shape, cytoskeletal mechanics, and cell cycle control in angiogenesis. J Biomech, 28, 1471-84.

[40] Bacakova, L., Filova, E., Rypacek, F., Svorcik, V. Stary, V. 2004. Cell adhesion on artificial materials for tissue engineering. Physiol Res, 53 Suppl 1, S35-45.

[41] Engler, A., Bacakova, L., Newman, C., Hategan, A., Griffin, M. Discher, D. 2004. Substrate compliance versus ligand density in cell on gel responses. Biophys J, 86, 617-28.

[42] P. K. Mattila, P. Lappalainen, Filopodia: molecular architecture and cellular functions. Nature Reviews Molecular Cell Biology 9 (2008) 446-454.

[43] Yamasaki, Y., Yoshida, Y., Okazaki, M., Shimazu, A., Uchida, T., Kubo, T., Akagawa, Y., Hamada, Y., Takahashi, J. Matsuura, N. 2002. Synthesis of functionally graded $MgCO_3$ apatite accelerating osteoblast adhesion. J Biomed Mater Res, 62, 99-105.

[44] R.K. Rude, H.E. Gruber, H.J. Norton, L.Y. Wei, A. Frausto, J. Kilburn, “Dietary magnesium reduction to 25% of nutrient requirement disrupts bone and mineral metabolism in the rat.” Bone. 37 (2015) 211-9.

[45] Rude, R. K., Gruber, H. E., Wei, L. Y., Frausto, A. Mills, B. G. 2003. Magnesium deficiency: effect on bone and mineral metabolism in the mouse. Calcif Tissue Int, 72, 32-41.

[46] Xynos, I. D., Edgar, A. J., Buttery, L. D., Hench, L. L. Polak, J. M. 2001. Gene-expression profiling of human osteoblasts following treatment with the ionic products of Bioglass 45S5 dissolution. J Biomed Mater Res, 55, 151-7.

[47] Xynos, I. D., Hukkanen, M. V., Batten, J. J., Buttery, L. D., Hench, L. L. Polak, J. M. 2000. Bioglass 45S5 stimulates osteoblast turnover and enhances bone formation In vitro: implications and applications for bone tissue engineering. Calcif Tissue Int, 67, 321-9.

[48] Tsigkou, O., Hench, L. L., Boccaccini, A. R., Polak, J. M. Stevens, M. M. 2007. Enhanced differentiation and mineralization of human fetal osteoblasts on PDLLA containing Bioglass composite films in the absence of osteogenic supplements. J Biomed Mater Res A, 80, 837-51.

[49] Tsigkou, O., Jones, J. R., Polak, J. M. Stevens, M. M. 2009. Differentiation of fetal osteoblasts and formation of mineralized bone nodules by 45S5 Bioglass conditioned medium in the absence of osteogenic supplements. Biomaterials, 30, 3542-50.

[50] Carlisle, E. M. 1970. Silicon: a possible factor in bone calcification. Science, 167, 279-80.

[51] Damen, J. J. Ten Cate, J. M. 1992. Silica-induced precipitation of calcium phosphate in the presence of inhibitors of hydroxyapatite formation. J Dent Res, 71, 453-7.

[52] Reffitt, D. M., Ogston, N., Jugdaohsingh, R., Cheung, H. F., Evans, B. A., Thompson, R. P., Powell, J. J. Hampson, G. N. 2003. Orthosilicic acid stimulates collagen type 1 synthesis and osteoblastic differentiation in human osteoblast-like cells in vitro. Bone, 32, 127-35.

[53] Jugdaohsingh, R., Tucker, K. L., Qiao, N., Cupples, L. A., Kiel, D. P. Powell, J. J. 2004. Dietary silicon intake is positively associated with bone mineral density in men and premenopausal women of the Framingham Offspring cohort. J Bone Miner Res, 19, 297-307.

[54] Jugdaohsingh, R., Watson, A. I., Bhattacharya, P., Van Lenthe, G. H. Powell, J. J. 2015. Positive association between serum silicon levels and bone mineral density in female rats following oral silicon supplementation with monomethylsilanetriol. Osteoporos Int, 26, 1405-15.

5 Ca-Mg silicates: engineering of the glass phase

5.1 Incorporation of a glass filler

5.1.1 Introduction

As discussed in §4, Ca-silicates[1-2] and Ca-Mg[3-6] silicates have recently received a growing interest for their bioactivity properties, according to their ability to stimulate body tissues to repair themselves. Silicone/fillers mixtures were found to be suitable for obtaining these peculiar bioactive formulations, but also for facilitating the shaping of the ceramic components in the form of highly porous bodies, which are extremely useful especially in the field of scaffolds for bone regeneration[7-8].

While a high phase purity is usually achievable in binary systems derived from preceramic polymers, such as Ca-silicates, ternary systems, like CaO-MgO-SiO_2, generally imply some difficulties, due to the potential formation of undesired binary compounds (e.g. calcium silicates mixed with magnesium silicates, mixed silicates with unreacted oxides) instead of ternary compounds, as expected from the balance among components[9-10].

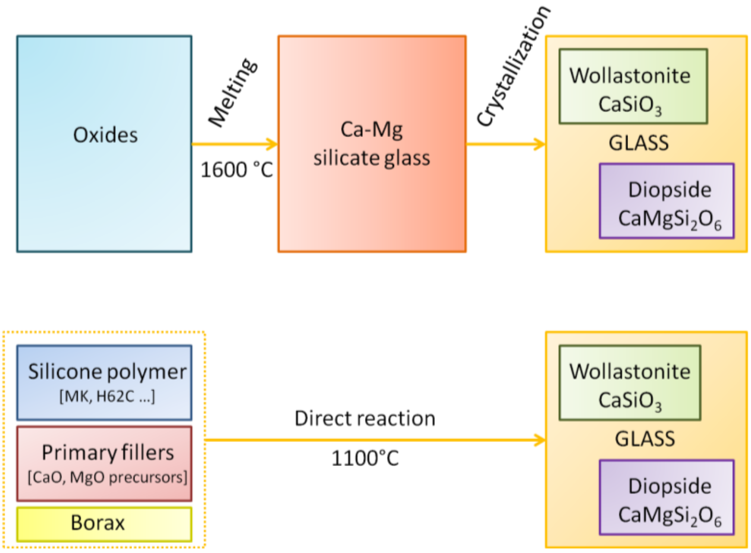

Fig. 5.1 Scheme for the obtainment of wollastonite-diopside ceramics according to conventional crystallization of a Ca/Mg-rich glass and to the reaction between silicones and fillers.

The solution may come from additional fillers, providing some liquid phase upon firing, and thus promoting the ionic interdiffusion: as an example, it is already known[11] that a borate liquid phase may effectively provide a "mineralizing effect", i.e. the catalysis of ionic interdiffusion. Taking into account this effect, hydrated sodium borate (borax, $Na_2O{\cdot}2B_2O_3{\cdot}10H_2O$), has already been shown as particularly significant for akermanite ($2CaO{\cdot}MgO{\cdot}2SiO_2$, or $Ca_2MgSi_2O_7$) ceramic foams. Besides providing a borate liquid phase, favorable, as explained, to the obtainment of the expected silicate, borax was used as a foaming agent for the silicone/resin mixtures, due to the water release associated with its dehydration reaction, occurring at only 350 °C (well below the ceramic transformation of silicone resins)[12]. For these reasons, borax could be seen actually as a multifunctional filler, playing a double role in the synthesis and shaping of silicates.

It must be noted that $Mg(OH)_2$, used as MgO precursor for Ca-Mg silicates, can also contribute to the foaming, but its impact is much lower than that of borax, which gave an extensive and uniform foaming of the liquid polymer[20]. The subsequent cross-linking of the polymer stabilized the porosity, even maintained after the conversion of the polymer into amorphous silica and the formation of silicates. Concerning the borate liquid phase, after cooling at room temperature, it remained as a glass phase. The resulting product (crystalline silicate+glass phase) is nominally identical to that from glasses undergoing some crystallization, i.e. glass-ceramics (parent glasses “ceramized” into silicate crystals mixed with residual glass phase).

The present chapter will evidence the similarities in the CaO-MgO-SiO_2 system, in terms of resulting phase assemblage, between products from conventional crystallization of a Ca/Mg-rich glass and from silicone/fillers mixtures, as illustrated by the scheme in Fig. 5.1, where. it is illustrated that these two technologies do not exclude each other, for the development of crack-free, highly porous diopside-wollastonite glass-ceramics. In particular, we will refer to the coupling of wollastonite and diopside ($CaO{\cdot}MgO{\cdot}2SiO_2$, $CaMgSi_2O_6$), already proved to be a highly attractive in terms of bioactivity and biocompatibility in recently developed ceramics [13] found in literature and also synthesized from preceramic polymers and discussed in §4. The results were published in 2015 by Fiocco *et al.*[14].

5.1.2 Experimental

5.1.2.1 Samples preparation

Two commercially available silicones, H62C and MK (Wacker-Chemie GmbH, Munich, Germany) were considered as silica precursors, with a yield of 58 and 84 wt%, respectively[9]. CaO and MgO precursors were $CaCO_3$ (Sigma Aldrich, Gillingham, UK) and $Mg(OH)_2$ (Industrie Bitossi, Vinci, Italy) respectively, with particle size diameter under 10 μm. Sodium borate ($Na_2O{\cdot}2B_2O_3{\cdot}10H_2O$, Sigma Aldrich, Gillingham, UK) was used as mineralizing agent[12]. Finally, a powdered Ca/Mg rich silicate glass with a particle size <60 μm (mean diameter ~5 μm), later referred to as G20CaII glass, was used in various amounts. The chemical composition of G20CaII glass is reported in Tab. 5.1.

Tab. 5.1 Chemical composition of G20CaII glass (%mol).

SiO_2	CaO	MgO	Na_2O	Li_2O
55.3	22.0	12.0	9.0	1.7

Viscous flow analysis of the glass was performed using a hot stage microscope (HSM) (Misura HSM ODHT – Expert system solutions) at a constant rate of 30 °C/min. The sample was initially cold pressed to cylindrical shape of 3 mm in both height and diameter from the glass powder. The temperature was measured with a Pt/Rh thermocouple placed under and in contact with the alumina support. The HSM projected the image of the sample through a quartz window and images of the sample were captured by a video camera every 2 °C. The temperatures corresponding to the characteristic viscosity points following Scholze’s definition[15,16] (η in dPa or Poise) were obtained from captured images taken in the following sequence: first shrinkage ($\log \eta=9.1$), maximum shrinkage ($\log \eta=7.8$), softening ($\log \eta=6.3$), half ball ($\log \eta=4.1$) and flow point ($\log \eta=3.4$).

The effective compatibility between silicone resins and G20CaII glass, in terms of phase assemblage of the developed ceramics, was tested before the processing of foams. This compatibility was tested starting from pellets obtained by uniaxial pressing. Monolithic pellets were prepared using $Mg(OH)_2$ and $CaCO_3$ micro-particles, mixed with MK, anhydrous borax (the same salt cited above, after preliminary dehydration at 350 °C, for 4 hours) and G20CaII glass (in an amount varying from 0 to 67 wt% of the theoretical ceramic yield of the other components). MK polymer was chosen instead of H62C for preliminary tests, for the easier processing (MK is solid, whereas H62C is liquid)[9].

MK was dissolved in isopropanol (15 ml for 10 g of final ceramic) and then mixed with micro-sized fillers, including sodium borate (1.6 wt% of the theoretical ceramic yield of the other components). The mixing was performed under magnetic stirring, followed by sonication for 10 min, which allowed to obtain stable and homogeneous dispersions. The mixtures were poured into large glass containers and dried at 80 °C overnight.

After drying, the silicone-based mixtures were in form of solid fragments, later converted into fine powders by ball milling at 350 rpm for 30 minutes. The powders were cold-pressed in a cylindrical steel die applying a pressure of 20 MPa for 1 min, without using any additive. Specimens of 0.5 g, having 16.6 mm in diameter and approximately 1.7 mm in thickness, were obtained. For comparison purposes, pellets of glass-free formulation were also prepared.

Concerning the preparation of foams, H62C was first dissolved in isopropanol (15 ml for 10 g of final ceramic) and then mixed with micro-sized fillers, including sodium borate, in the as-received, hydrated form (in order to provide the same amounts of Na_2O and B_2O_3 used with MK, the quantity of salt was 3 wt% of the theoretical ceramic yield of the other components). Stable and homogeneous dispersions in isopropanol were obtained using the same conditions applied for the MK-based mixtures, and left to dry overnight at 60 °C. After first drying, the mixtures were in the form of thick pastes, later manually transferred into cylindrical Al molds and then subjected to a heat treatment for foaming at 350 °C in air for 30 min. Cylindrical samples, 10 mm in diameter and 7-8 mm in height, were obtained from the foams. The top surfaces were polished with abrasive paper.

To investigate another processing route, the procedure described above was repeated for a second series of foams, including G20CaII glass powder (16.5 and 33 wt% of the theoretical ceramic yield of the other components) as further filler.

All the samples (monolithic or cellular, after removal from Al molds) were fired at 1100 °C for 1h, using a heating rate of 1 °C/min.

5.1.2.2 Characterization of samples

Microstructural characterizations were performed by optical stereomicroscopy and scanning electron microscopy (FEI Quanta 200 ESEM, Eindhoven, The Netherlands) equipped with energy dispersive spectroscopy (EDS).

The crystalline phases were identified by means of X-ray diffraction on powdered samples (XRD; Bruker AXS D8 Advance, Bruker, Germany), supported by data from PDF-2 database (ICDD-International Centre for Diffraction Data, Newtown Square, PA) and Match! program package (Crystal Impact GbR, Bonn, Germany).

The bulk density of foams was determined geometrically and by weighing using a digital balance. The true density of the various samples was measured by means of a gas pycnometer (Micromeritics AccuPyc 1330, Norcross, GA), operating with He gas on finely milled samples.

The crushing strength of foams was measured at room temperature, by means of an Instron 1121 UTM (Instron Danvers, MA) operating with a cross-head speed of 1 mm/min. Each data point represents the average value of 5 to 10 individual tests.

5.1.3 Results

5.1.3.1 Phase evolution

A first remark concerns the starting composition. With the main aim of obtaining ceramics with both wollastonite and diopside, operating with preceramic polymers and fillers, we adjusted the formulation adopted for akermanite ceramics, turning it from $CaO:MgO:SiO_2$=2:1:2 (by mol.) to

$CaO:MgO:SiO_2$=2:1:3. Such balance effectively corresponds to a diopside/wollastonite molar ratio equal to 1, as follows: $2\ CaO + MgO + 3\ SiO_2 \rightarrow CaO \cdot SiO_2 + CaO \cdot MgO \cdot 2SiO_2$.

The different oxides were provided by the same precursors used for akermanite porous ceramics with the highest phase purity, i.e. Ca carbonate, Mg hydroxide and H62C polymer. Borax was used, again, as both mineralizing and foaming agent[12].

With regard to preliminary tests of compatibility between polymer/fillers mixtures and G20CaII glass, relatively dense pellets were used. H62C was replaced by MK (the overall amount of polymer, owing to the higher silica yield of MK, compared to H62C, was obviously adjusted, in order to maintain the $CaO:MgO:SiO_2$ balance) and borax was used after dehydration (keeping the ratios between B_2O_3 and other oxides unchanged).

Fig. 5.2 (upper pattern, “a”) clearly shows wollastonite (PDF#75-1396) and diopside (PDF#75-1092) effectively formed from H62C and oxide precursors, in condition of high phase purity, with the exception of weak traces of akermanite (PDF#87-0046). The same figure (upper pattern, “b”), the crystalline phases developed after the heat treatment of the samples, are the same for both silica precursor used, i.e. MK and H62C.

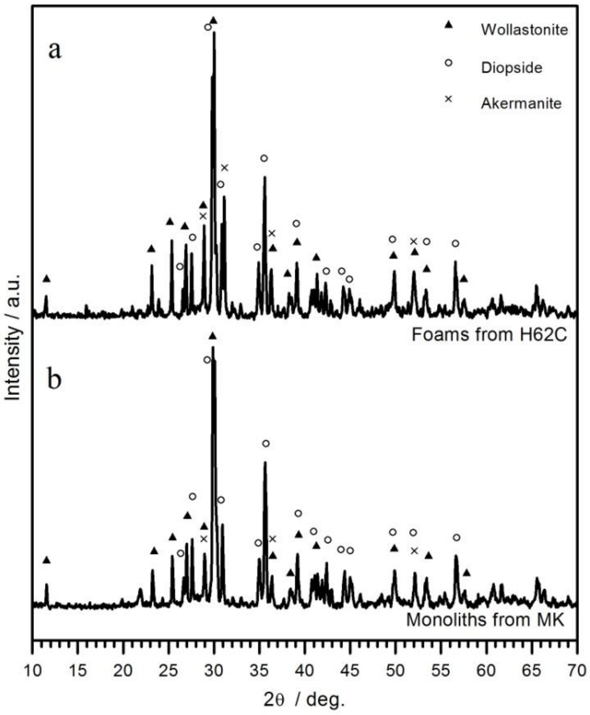

Fig. 5.2 Comparison of polymer-derived wollastonite-diopside ceramics obtained by using different silicones: a) H62C; b) MK.

The introduction of G20CaII glass particles as secondary filler, in substantial amounts (one or two thirds of the mass of ceramic product), as testified by Fig. 5.3, had a quite particular effect. We can see that the glass-free formulation had an evolution, with increasing firing temperature, from 900 to 1100 °C. At low temperature we can note that the two expected phases were accompanied by akermanite and silica (in form of cristobalite, PDF#76-0940); while akermanite remained as slight contamination at 1100 °C, crystalline silica practically disappeared, probably due to the progressive incorporation of silica, from the polymer, in the structure of the desired silicates. Contrary to the polymer-based formulation, G20CaII glass crystallized leading to very well-defined wollastonite and diopside peaks even at 900 °C; an increase in temperature, from 900 to 1100 °C had the only effect of reducing secondary phases, in form of other silicates: olivine (Mg_2SiO_4, PDF#87-2042), calcium silicate (Ca_2SiO_4, PDF#83-0463) and monticellite ($CaMgSiO_4$, PDF#87-2042).

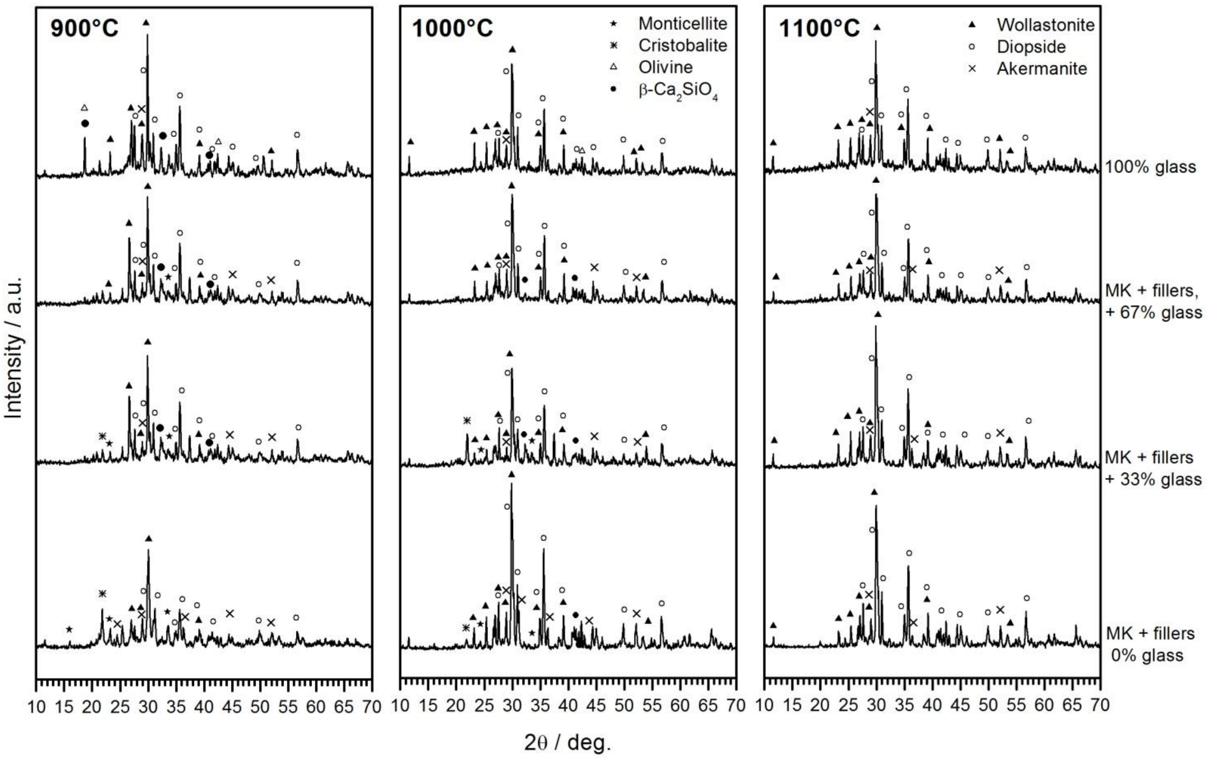

Fig. 5.3 X-ray diffraction patterns of wollastonite-diopside ceramics fired at different temperatures.

Interestingly, “intermediate” formulations, i.e. comprising both polymer and glass, were more similar to the glass-free formulation, in terms of phase assemblage. Intense wollastonite and diopside peaks were accompanied only by minor traces of Ca/Mg silicates, such as akermanite and monticellite. Finally, the main goal is that, independently from the formulation, except for minor traces of akermanite, all the formulations practically yielded the same phase assemblage, at 1100 °C. The glass evidently had the expected effect of promoting the ionic interdiffusion.

5.1.3.2 Development of foams

Fig. 5.4 presents the foams obtained from silicone/fillers mixtures. In particular, Fig. 5.4a shows that the first heat treatment at 350 °C led to very homogeneous rigid polymeric foams, owing to the release of water from both Mg hydroxide and hydrated borax, in good analogy with what happened for the formulation yielding akermanite; the stiffness of the foams is due to the crosslinking of H62C, when heated above 200 °C[12]. However, even if the homogeneity was maintained after ceramization at 1100 °C, as illustrated by Fig. 5.4b, the ceramic foams exhibited many microcracks (not found in previous akermanite foams), as visible from the SEM image in Fig. 5.4c.

The microcracks in wollastonite-diopside ceramic foams were likely caused by stresses, arising in the material, due to the volume changes associated to the crystallization of silicates (the crystallization implies an increase of density, and a decrease of volume, due to the regular packing of ions), within a rigid matrix (polymer-derived silica and fillers). Some stress relaxation was actually expected from the borate glass phase originating from borax; the quantity of additive was evidently too low to accommodate the volume changes. An increase of borax amount was not considered, owing to the risks of compromising the homogeneity of foams (an enhanced water release could determine some coarsening of the cellular structure). It was evident, however, that the enhancement of viscous flow could lead to crack-free samples.

In order to have some additional liquid phase, during ceramization at 1100 °C, we considered the addition of G20CaII glass powder, designed to yield wollastonite-diopside glass-ceramics by sinter-crystallization. Fig. 5.5 presents the linear shrinkage of G20CaII glass powder as a function of temperature, obtained from a hot stage microscopy. In this analysis some fixed points of viscosity can be determined. It can be seen that sintering starts at 645 °C (T_{sint}, corresponding to the first 1 % in linear shrinkage) and the temperature of sintering saturation (T_{sat}) is close to 760 °C for the G20CaII. In this temperature range, the glass particles sinter by viscous flow and this process is hindered by the superficial crystallization of the particles[17]. Above 930 °C, melting of the crystals starts, and therefore, the material begins to flow again. The softening point is around 1000 °C and the half ball point is around 1100 °C. The firing temperature of the foams correspond to the half ball point of the G20CaII glass, which shows $\log\eta=4.1$ at this temperature. This indicates that G20CaII glass powder can supply additional liquid phase to ceramization process of the foams and increase the viscous flow at 1100 °C. With this in mind, an alternative route to obtain crack-free foam samples was proposed using G20CaII powders.

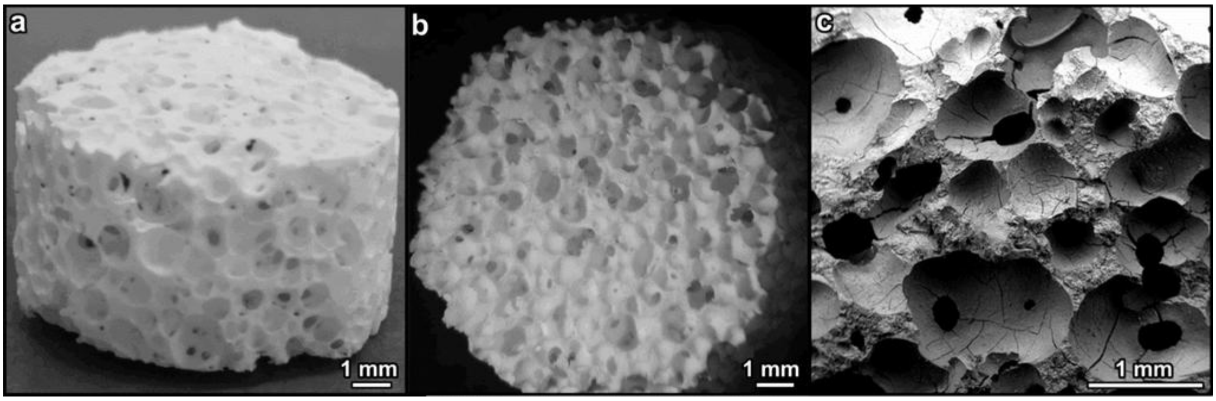

Fig. 5.4 Microstructural details of polymer-derived wollastonite-diopside foams: a) foam before ceramization; b) foam after ceramization; c) high magnification detail of cellular structure after ceramization.

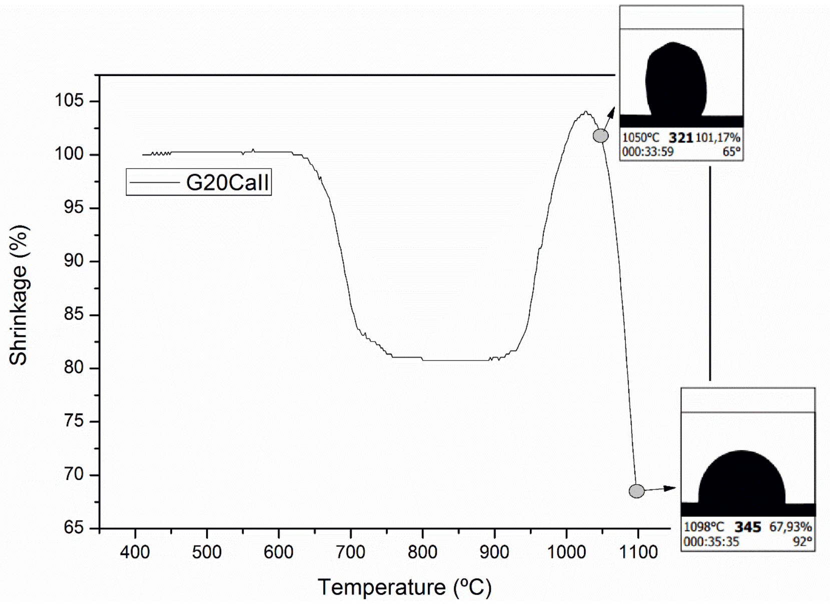

Fig. 5.5 Linear shrinkage as a function of temperature during the HSM measurement and images of the sample at 1050 °C and 1098 °C.

The success of the glass addition, in terms of confirmation of the phase assemblage, using MK, stimulated further investigations with H62C, with the manufacturing of a second series of foams (considering borax in hydrated form). Fig. 5.6 shows that the limited glass addition (16.5 % and 33 %, each value corresponding to one half of the amounts used with MK) still did not determine any practical change in the phase assemblage, after firing at 1100 °C.

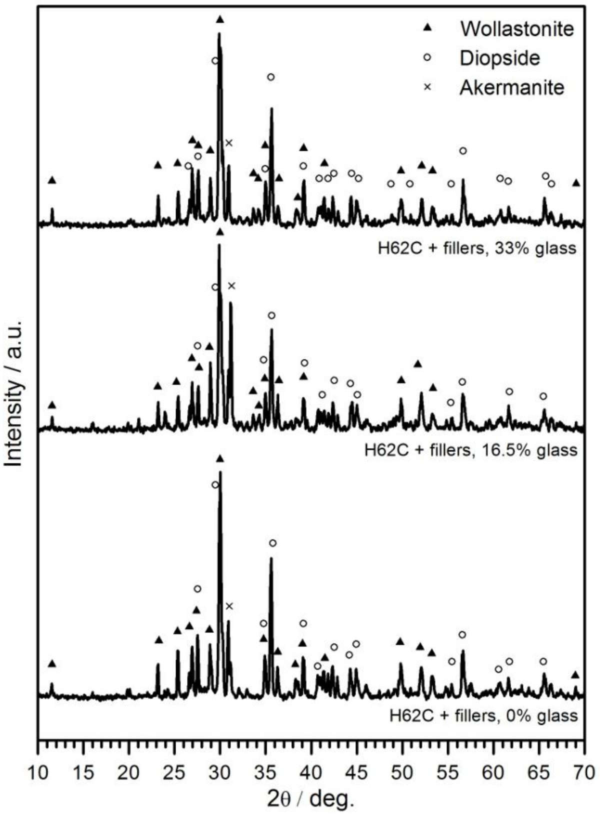

Fig. 5.6 X-ray diffraction patterns of wollastonite-diopside ceramic foams from H62C-based formulations.

Tab. 5.2 Physical and mechanical properties of foams with different amount of glass powders.

Foam formulation	ρ_b (g/cm^3)	P_{open} (%)	σ_{comp} (MPa)
H62C + fillers, 0 wt% glass	0.73 ± 0.02	77	1.8 ± 0.3
H62C + fillers, 16.5 wt% glass	0.75 ± 0.03	75	2.3 ± 0.2
H62C + fillers, 33 wt% glass	0.78 ± 0.04	72	6.1 ± 0.4

As shown in Tab. 5.2, the addition of GCa20II glass particles to H62C based formulations results in a slight increase of bulk density (ρ_b) of ceramic foams, with the concurrent slight decrease of open porosity (P_{open}). However, the crushing strength (σ_{comp}) increase significantly from 1.8 ± 0.3 MPa up to 6.1 ± 0.4 MPa, comparing the formulations containing 0 wt% of glass and 33 wt% of glass.

As previously discussed, the significant increment in crushing strength with glass addition is likely due to the enhancement of the viscous flow during ceramization. Fig. 5.7 clearly shows that microcracks, presented in the foams from glass-free formulation, were not visible at all in the glass-modified foams. The enhancement of viscous flow likely provided an adequate relaxation of stresses arising from crystallization-induced volume changes.

The optimized foams, from H62C and fillers (including glass) are going to be subjected to validation, in terms of biocompatibility and bioactivity. The phase assemblage, comprising silicates of well-documented biocompatibility and bioactivity, is obviously favorable. Further efforts will be probably dedicated to a progressive refinement of the matching between silicone/filler mixtures and G20CaII glass, also in terms of residual glass phase, e.g. replacing borax with sodium silicate. The replacement of borax, however, will not be trivial, owing to its double role (mineralizing and foaming agent).

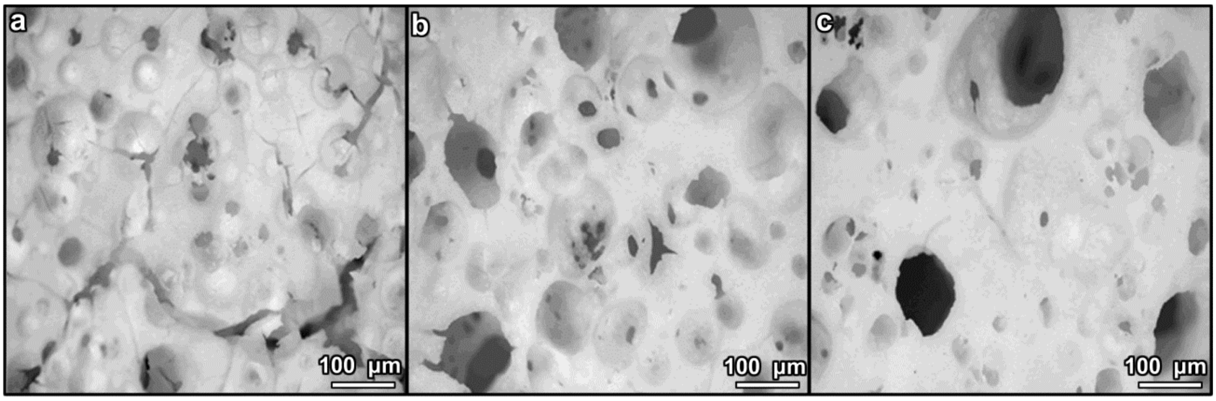

Fig. 5.7 Stereomicroscopy images of ceramic foams from H62C-based formulations:
a) glass-free formulation; b) 16.5 wt% glass; c) 33 wt% glass.

The "miscibility" of glass and silicone/oxide fillers, i.e. the possibility to develop wollastonite-diopside glass-ceramic materials, with the same phase assemblage (at 1100 °C), regardless of the proportion of glass particles, opens the way, in any case, for a number of possible experiments. We could consider the glass as an additional mineralizing agent, in a "low glass approach" (glass used in low amounts), like in the presented case, as well as silicone/fillers as binders for glass powders, in a "high glass approach" (glass used in high amounts, with silicone acting both as binder, at low temperature, and a crystallization promoter, by interaction with fillers, at high temperature). The latter hypothesis has been actually already exploited, for the development of 3-D scaffolds from indirect printing of bioglass powders, crystallizing into apatite and wollastonite, bound with MK silicone and fillers, in turn yielding calcium-zinc and zinc silicates[18]. The present findings may be seen as an advance, for the matching of crystal phases developed by different approaches.

5.1.4 Conclusions

This study showed that wollastonite-diopside ceramics can be obtained, in condition of high phase purity, starting from mixtures of silicone polymers and active fillers, which were later converted into a ceramic materials upon thermal treatment in oxidative atmosphere.

Operating with H62C polymer, extensive foaming could be obtained before ceramic conversion, by simple release of water from the fillers, at low temperature.

The two main phases started to develop at 900 °C; however, if a higher phase purity is desired, the firing temperature should be increased up to 1100 °C; at this temperature, the ceramic product is independent from the type of silicone resin used as silica precursor.

The ceramic product of silicone/fillers was practically identical to that from crystallization of Ca/Mg-rich silicate glass (G20CaII glass) and did not change when operating with silicone/fillers/glass mixtures, independently from the amount of glass.

H62C-based foams were significantly improved, in terms of structural integrity and compressive strength, by using G20CaII glass as additional filler, providing an enhanced viscous flow upon firing, with no change to the developed crystal phases.

5.2 Modification of the foaming agent

5.2.1 Introduction

As discussed in §4, Ca-silicates and Ca-Mg silicates have recently received a growing interest for their bioactivity properties, according to their ability to stimulate body tissues to repair themselves. Silicone/fillers mixtures were found to be particularly suitable for obtaining these peculiar bioactive formulations, but also for facilitating the shaping of the ceramic components in the form of highly porous bodies, which are extremely useful especially in the field of scaffolds for bone regeneration.

While a high phase purity is usually achievable in binary systems derived from preceramic polymers, such as Ca-silicates, ternary systems generally imply some difficulties, due to the potential formation of undesired binary compounds instead of the expected ternary compounds. As described in §5.1, the problem may be solved by providing a liquid phase upon firing, that could promote the ionic interdiffusion, operating with specific fillers[19]. A fundamental example is that of hydrated sodium borate, also known as borax ($Na_2B_4O_7{\cdot}10H_2O$), included in the formulations for akermanite ($Ca_2MgSi_2O_7$)[20] and wollastonite-diopside ceramics[14]. The additive formed a borate liquid phase upon firing and helped the crystallization of the desired phases. The borate liquid phase, after cooling at room temperature, remained as a glass phase, so that the resulting product could be seen as a sort of "polymer-derived glass-ceramic". Borax could be seen actually as a multifunctional filler, since its use in a liquid silicone could be exploited also for an extensive and uniform foaming, due to the water release associated with the dehydration reaction, occurring at only 350 °C. The cross-linking of the polymer stabilized the porosity, even maintained after the conversion of the polymer into amorphous silica and the formation of silicates. It must be noted that $Mg(OH)_2$, used as MgO precursor for Ca-Mg silicates, may contribute to the foaming, but its impact is much lower than that of borax[20].

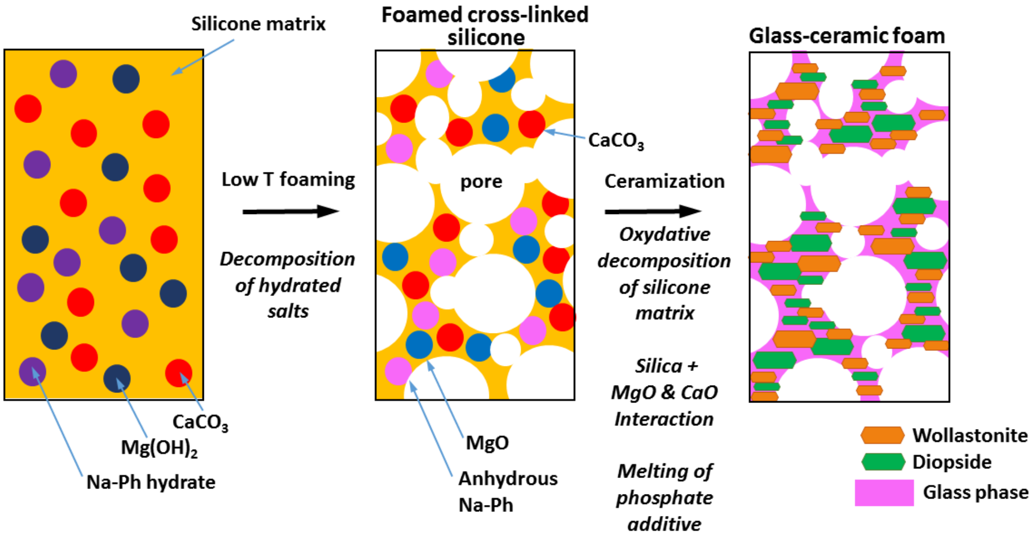

Fig. 5.8 Scheme for the obtainment of wollastonite-diopside "polymer-derived glass-ceramic" foams, according to the dual role of hydrated sodium phosphate filler (Na-Ph hydrate).

Being the addition of borax significant for the obtainment of glass-ceramic samples with a specific phase assemblage and with a homogeneous cellular structure, the same approach was used for the synthesis of akermanite and wollastonite-diopside shown in §4, but in that study the amount of borax was lowered from 5 to 3 wt%. This allowed a more controlled foaming step, leading to smaller and more ordered porosity in the scaffolds. A further reason for lowering the boron content was to avoid cytotoxicity phenomena. This choice was successful, in fact cell studies effectively confirmed the biocompatibility of the developed materials.

However, the effect of boron on the biocompatibility is still controversial. Several studies reported in literature highlighted a concern associated with borate bioactive glasses[21,22], due to the potential toxicity of boron released in the solution as borate ions $(BO_3)^{3-}$. As an example, the well-known borate bioglass 13-93B3 was found to be toxic to murine MLO-A5 osteogenic cells *in vitro*, above a boron threshold concentration of 0.65 mmol in the cell culture medium, while it supported the proliferation and growth of the cells below that concentration[23]. However, the same scaffolds did not show toxicity to cells *in vivo* and supported new tissue infiltration when implanted in rats[24,25,26,27]. Other boron containing glasses are reported to be biocompatible and bioactive[28,29].

Here, a further development concerning highly porous wollastonite-diopside "polymer-derived glass-ceramics" is discussed, based on the replacement of borax with sodium phosphate dibasic heptahydrate ($Na_2HPO_4 \cdot 7H_2O$), aimed at avoiding the above-described difficulties arising from the presence of boron. The selected filler, like borax, is multifunctional, i.e. it contributes to both foaming and forming a liquid phase upon firing, as illustrated by Fig. 5.8. The results obtained were published in 2015 by Fiocco *et al.* [30].

Like in the previously developed wollastonite-diopside ceramics[14], discussed in §5.1, the addition of a further filler, in form of powders of a glass crystallizing into wollastonite and diopside, will be discussed in order to optimize the integrity of samples. In fact, the ceramization step does not modify the macro-porosity formed in the low temperature foaming step, but it implies the formation of micro-cracks, caused by internal stresses. The glass addition is essentially conceived to reduce the cracks, enhancing the stress relaxation operated by the liquid phase, upon firing, with no impact on foaming and phase development.

Although preliminary, the results of a 5-day cell culture tests, on phosphate-modified wollastonite-diopside ceramics, indicated a good biocompatibility, independently from the glass addition.

5.2.2 Experimental

5.2.2.1 Preparation of samples

Two commercially available silicones, H62C and MK (Wacker-Chemie GmbH, Munich, Germany) were considered as silica precursors, with a yield of 58 and 84 wt%, respectively[9]. CaO and MgO precursors consisted of $CaCO_3$ (Sigma Aldrich, Gillingham, UK) and $Mg(OH)_2$ (Industrie Bitossi, Vinci, Italy) respectively, in form of powders with diameter below 10 μm. The amounts of silicones and precursors for CaO and MgO were calibrated in order to match the CaO-MgO-SiO_2 molar proportion of 2-1-3, corresponding to an equimolar mixture of wollastonite ($CaSiO_3$, or $CaO \cdot SiO_2$, CaO-MgO-SiO_2 molar proportion of 1-0-1) and diopside ($CaMgSi_2O_6$, or $CaO \cdot MgO \cdot 2SiO_2$, CaO-MgO-$SiO_2$ molar proportion of 1-1-2). Sodium phosphate dibasic heptahydrate ($Na_2HPO_4 \cdot 7H_2O$, Sigma Aldrich, Gillingham, UK) was used as additional filler. Finally, a powdered Ca/Mg rich silicate glass with a particle size < 60 μm (mean diameter ~ 5 μm), later referred as G20CaII glass[14], was added.

Tab. 5.3 Chemical composition of G20CaII glass.

SiO_2	CaO	MgO	Na_2O	Li_2O
55.3	22.0	12.0	9.0	1.7

The chemical composition of G20CaII glass is reported in Tab. 5.3. The molar proportions between CaO, MgO and SiO_2 roughly correspond to those of the desired mixture of wollastonite and diopside, with alkali oxides used as fluxes. The use of Li_2O, in addition to Na_2O, is in agreement with recent findings concerning the positive effect of this oxide added in formulations of bioglasses, previously involving only sodium oxide[31,32].

Concerning the preparation of foams, H62C was first dissolved in isopropanol (10 ml for 10 g of final ceramic) and then mixed with micro-sized fillers, including sodium phosphate, in the as-received, hydrated form (the quantity of salt was 10 wt.% of the theoretical ceramic yield of the other components, corresponding to 5 wt.% of anhydrous salt). Selected samples included also powders of G20CaII glass (10 wt.% of the theoretical ceramic yield of the other components). The mixing was performed under magnetic stirring, followed by sonication for 10 minutes, which allowed to obtain stable and homogeneous dispersions. The mixtures were poured into large glass containers and dried at 60 °C overnight.

After first drying, the mixtures were in the form of thick pastes, later manually transferred into cylindrical Al moulds and then subjected to a foaming treatment at 350 °C in air for 30 minutes. Cylindrical samples, 10 mm in diameter and 7-8 mm in height, were obtained from the foams. The top surfaces were polished with abrasive paper. The samples (after removal from Al moulds) were fired at 1100 °C for 1 hour, using a heating rate of 2 °/min.

Monolithic pellets were prepared using MK mixed with $Mg(OH)_2$ and $CaCO_3$ micro-particles, anhydrous sodium phosphate (the same salt cited above, after preliminary dehydration at 450 °C, with a heating rate of 5 °/min, for 1 hour) and G20CaII glass. MK was dissolved in isopropanol (10 ml for 10 g of final ceramic) and then mixed with the fillers. Stable and homogeneous dispersions in isopropanol were obtained using the same conditions applied for the H62C-based mixtures, and left to dry overnight at 60 °C.

After drying, the silicone-based mixtures were in the form of solid fragments, later converted into fine powders by ball milling at 350 rpm for 30 minutes. The powders were cold-pressed in a cylindrical steel die applying a pressure of 20 MPa for 1 minute, without using any additive. Specimens of 0.5 g, 16.6 mm in diameter and approximately 1.7 mm in thickness, were obtained. For comparison purposes, pellets of glass-free formulation were also prepared. The cold-pressed samples were fired at 1100 °C for 1 hour, using a heating rate of 2 °/min.

5.2.2.2 Characterization of samples

Microstructural characterizations were performed by optical stereomicroscopy (AxioCam ERc 5s Microscope Camera, Carl Zeiss Microscopy, Thornwood, NY, USA) and scanning electron microscopy (FEI Quanta 200 ESEM, Eindhoven, The Netherlands) equipped with energy dispersive spectroscopy (EDS).

The crystalline phases were identified by means of X-ray diffraction on powdered samples (XRD; Bruker AXS D8 Advance, Bruker, Germany—CuKα radiation, 0.15418 nm, 40 kV–40 mA, $2\theta = 15°–70°$, step size = 0.05°, 2 s counting time), supported by data from the PDF-2 database (Powder Diffraction File, ICDD-International Center for Diffraction Data, Newtown Square, PA, USA) and the Match! program package (Crystal Impact GbR, Bonn, Germany).

The bulk density of the foams was determined from the weight-to-volume ratio, using a caliper and a digital balance. The true density of the samples was measured by means of a gas pycnometer (Micromeritics AccuPyc 1330, Norcross, GA, USA), operating with He gas on finely-milled samples.

The crushing strength of foams was measured at room temperature, by means of an Instron 1121 UTM (Instron Danvers, MA, USA) operating with a cross-head speed of 1 mm/min. Each data pointrepresents the average value of 5–10 individual tests.

5.2.2.3 Cell culture

For cell culture studies, samples were cut to 10 mm x 10 mm x 5 mm and fixed to 48-well plates. The entire well plates where then sterilized. Human fibroblasts were seeded at a density of $4x10^5$ cells/piece in cDMEM, which consisted of Dulbecco's Modified Eagle Medium (DMEM) (Lonza S.r.l., Milano, Italy), supplemented with 10 vol% Fetal Bovine Serum (FBS) (Bidachem S.p.A., Milano, Italy) and 1 vol% Penicillin/Streptomycin (P/S) (EuroClone, Milano, Italy). The 3-D cultures were incubated at 37 °C and 5% CO_2 for 7 days, with media changes every 2 days.

Cell proliferation rate was evaluated after 3 and 7 days from seeding with the MTT (methylthiazolyl-tetrazolium) based proliferation assay, performed according to the method of Denizot and Lang with minor modifications[33]. Briefly, samples were incubated for 3 h at 37 °C in 1 mL of 0.5 mg/ml MTT solution prepared in Phosphate Buffered Saline (PBS) (Euroclone). After removal of the MTT solution by pipette, 0.5 ml of 10% DMSO in isopropanol was added to extract the formazan in the samples for 30 min at 37 °C. For each sample, absorbance values at 570 nm were recorded in duplicate on 200 µl aliquots deposited in microwell plates using a multilabel plate reader (Victor 3, Perkin Elmer, Milano, Italy).

LDH activity was measured using the Lactate Dehydrogenase Activity Assay Kit (Sigma Aldrich, St. Louis, MO, USA) according to the manufacturer's instructions. All conditions were tested in duplicate. The culture medium was reserved to determine extracellular LDH. The intracellular LDH was estimated after cells lysis with the assay buffer contained in the kit. All sampled were incubated with a supplied reaction mixture, resulting in a product whose absorbance was measured at 450 nm using Victor 3 multilabel plate reader.

For SEM imaging, fibroblasts grown on samples for 3 and 7 days were fixed in 2.5% glutaraldehyde in 0.1 M cacodylate buffer for 1 h, then progressively dehydrated in ethanol. Control and treated Ti discs without cells were also examined.

T-tests were used to determine significant differences ($p<0.05$). Repeatability was calculated as the standard deviation of the difference between measurements. All testing was performed in SPSS 16.0 software (SPSS Inc., Chicago, Illinois, USA) (license of the University of Padua, Italy).

Biological characterization was carried out thanks to a collaboration with Prof. B. Zavan (University of Padova).

5.2.3 Results

5.2.3.1 Foaming and development of foams

Fig. 5.9 testifies the very homogeneous foaming achieved, according to the approach described in Fig. 5.8. Many interconnections between adjacent pores were visible from both top and side views, as a proof of open porosity. The morphology of the newly obtained foams is comparable to that of previous wollastonite-diopside polymer-derived ceramics foamed by decomposition of borax, although the amount of foaming additive had to be drastically revised. The effect of 10 wt% hydrated Na-phosphate, in other words, roughly corresponded to that one of 3 wt% borax (samples with lower content of phosphate salt, exhibiting a much less abundant and uniform foaming, are not discussed here for the sake of brevity) in previous experiments (§4 and §5.1).

Like borax, the phosphate salt did not contribute to the formation of any crystal phase. In particular, Fig. 5.10 (upper pattern) shows that the expected silicate phases, i.e. wollastonite (PDF#42-0547) and diopside (PDF#86-0932), effectively formed at 1100 °C from H62C silicone and oxide precursors, with only minor traces of akermanite (PDF#83-1815) and merwinite ($Ca_3MgSi_2O_8$ - PDF#74-0382).

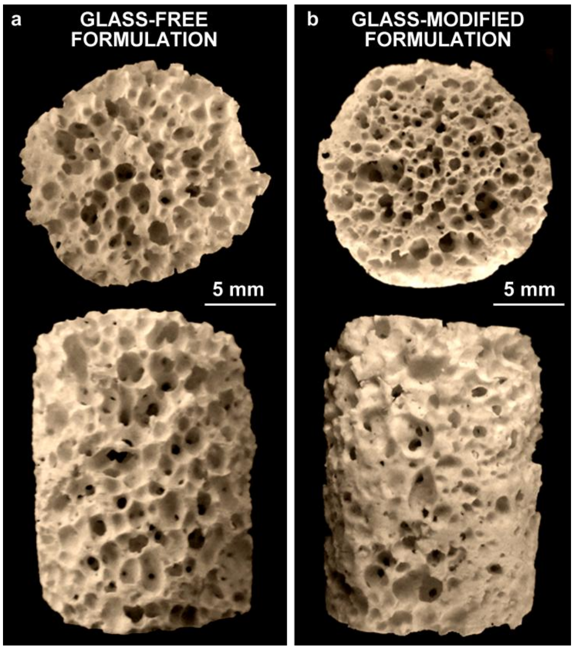

Fig. 5.9 Morphology of the foams (top and side views): a) Glass-free formulation; b) Glass-modified formulation (10 wt% glass).

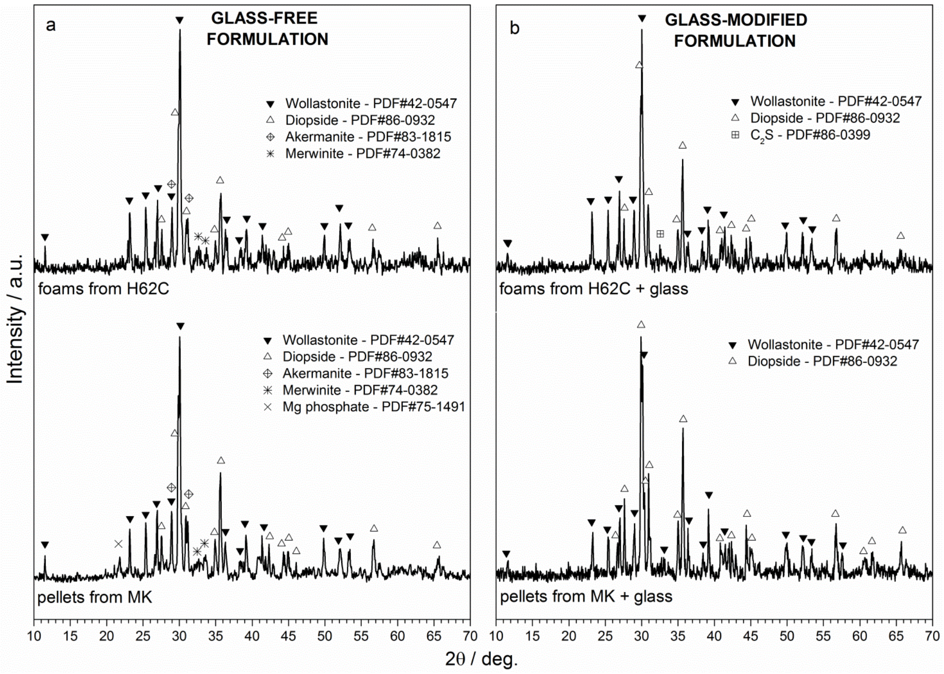

Fig. 5.10 X-Ray diffraction pattern of polymer-derived glass-ceramic samples (foams from H62C, pellets from MK): a) glass-free formulations; b) glass-modified formulations.

Tab. 5.4 Physical and mechanical properties of polymer-derived wollastonite-diopside foams. (* data from Fiocco et al.[14] and presented in §5.1).

Foam formulation	Bulk density (g/cm^3)	Open Porosity (%)	Crushing strength (MPa)
H62C + fillers [borax]*	0.73 ± 0.02*	77.0*	1.8 ± 0.3*
H62C + fillers [Na-phosphate]	0.70 ± 0.02	76.5	1.4 ± 0.1
H62C + fillers + 10 wt% glass [Na-phosphate]	0.63 ± 0.10	79.4	3.1 ± 0.7

The similarity with the previous wollastonite-diopside foams, developed with borax, was further confirmed by the physical and mechanical data reported in Tab. 5.4. Bulk density, open porosity and crushing strength were practically identical. The crushing strength (approximately 1.5 MPa), in particular, was quite low, considering the high crystallinity inferable from the diffraction pattern (the absence of "amorphous halo" suggested a limited amount of glass phase, mostly attributable to sodium phosphate).

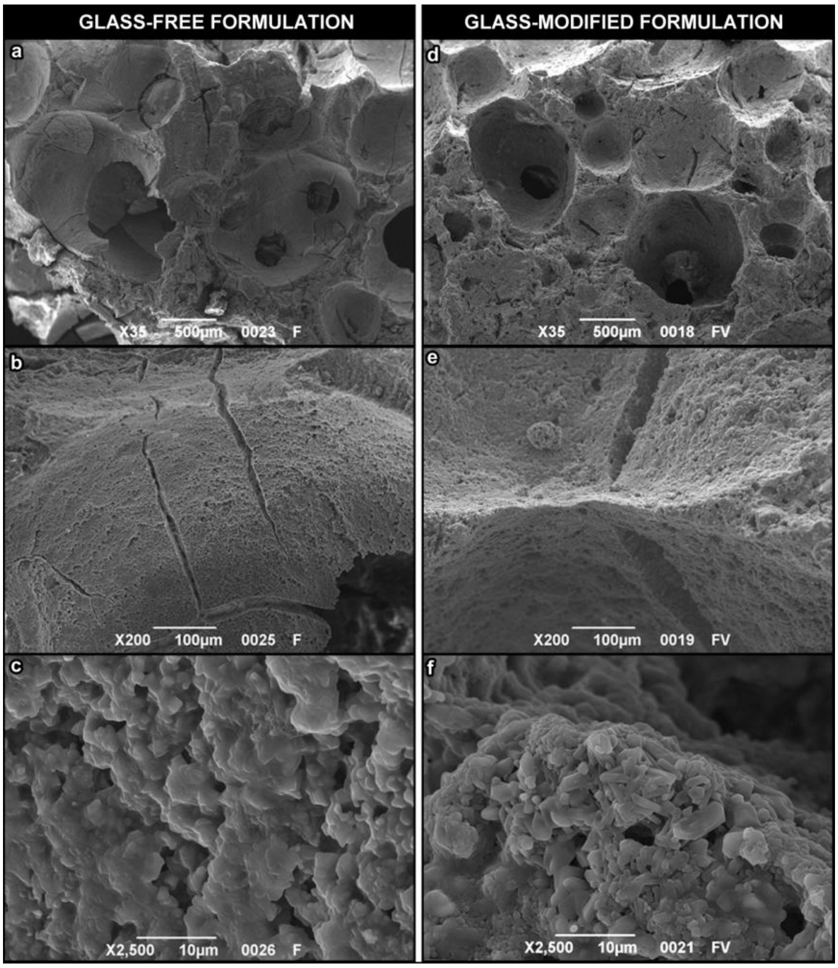

Fig. 5.11 Higher magnification details of the foams:
a-c) Glass-free formulation; d-f) Glass-modifed formulation (10 wt% glass)

As illustrated by Fig. 5.11, the foamed samples from glass-free formulation exhibited a large number of microcracks, that could be due the development of internal stresses upon ceramization. These stresses could be attributed to multiple factors, such as gas release from the polymer-to-ceramic conversion of silicones, decomposition of calcium carbonate (used as CaO precursor) and volume changes associated with the crystallization of silicates, visible as small granules in Fig. 5.11c.

Despite a slightly less homogeneously distributed macro-porosity and mean diameter Fig. 5.9b, with respect to the samples from glass-free formulation (Fig. 5.9a), foams developed with G20CaII glass as additional filler exhibited an improvement in the structural integrity (Fig. 5.11d-f). The viscous flow, due to the softening of glass particles, likely overlapped with that of the liquid phase offered by sodium phosphate, and caused some stress relaxation. The formation of elongated crystals, shown in Fig. 5.11f, might be seen as a proof of enhanced flow. The crystals can be practically attributed only to wollastonite and diopside, considering the upper pattern of Fig.1b, showing only very small traces of dicalcium silicate (C_2S, Ca_2SiO_4 or $2CaO\cdot SiO_2$, PDF#86-0399) in addition to well-defined peaks of the desired phases.

As reported in Tab. 5.4, both bulk density and open porosity were not affected by the glass addition. However, the glass addition was more effective, owing to the reduction of cracks, in the improvement of the mechanical strength, which increased from 1.4 ± 0.1 (for foams without glass) up to 3.1 ± 0.7 (for foams added with the 10 wt% of glass).

5.2.3.2 Impacts of preceramic polymer and glass on phase development

Cell culture tests are generally easier to be performed with flat samples, instead of foamed samples. For the specific purpose of preparing disc samples, H62C was replaced by MK. The solid silicone allowed an easy shaping of pellets by cold pressing of powdered silicone-fillers mixtures. The amount of MK was obviously calibrated, keeping the reference CaO-MgO-SiO_2 molar proportion, considering the different yield of silica, compared to H62C; since no foaming was expected, sodium phosphate was used in anhydrous form.

The lower pattern of Fig. 5.10a clearly shows that the change in the preceramic polymer had no practical impact on the phase development, except for the formation of traces of magnesium phosphate ($Mg_3P_2O_8$ – PDF#75-1491). This phosphate phase, together with akermanite and merwinite, completely disappeared in a MK-based formulation comprising G20CaII glass particles, as shown in the lower pattern of Fig. 5.10b. The “purifying” effect of the glass additive (an enhanced content of liquid phase promotes the interdiffusion) found for H62C was confirmed in the system based on MK.

Tab. 5.5 Wollastonite-diopside weight balances according to the semi-quantitative X-ray diffraction analysis provided by the Match! program package.

	Formulations	Wollastonite (wt%)	Diopside (wt%)
Theoretical	$CaO\cdot SiO_2 + CaO\cdot MgO\cdot 2SiO_2$	35	65
1	H62C + fillers	56	44
2	H62C + fillers + 10 wt% glass	40	60
3	MK + fillers	49	51
4	MK + fillers + 10 wt% glass	42	58

An additional discussion, concerning the phase development, can be done on the basis of semi-quantitative analysis provided by the Match! (Crystal Impact GbR, Bonn, Germany) program package, already employed for phase identification. Considering wollastonite and diopside, as a first approximation, as the only crystal phases, the program package can predict several weight ratios, reported in Tab. 5.5, corresponding to the best matching between experimental and theoretical diffraction patterns, depending on the formulation. In an ideal ceramic with wollastonite and diopside in equivalent molar amount (molar ratio equal to 1), the theoretical wollastonite/diopside weight balance would be equal to 35/65; from Tab. 5.5 we can easily note that the best agreement with the theoretical weight balance was provided by glass-modified formulation, based on both H62C and MK polymers.

As previously mentioned, the G20CaII glass proved to crystallize, alone, in wollastonite and diopside[14]. Considering the chemical composition (Tab. 5.3), we estimated a certain weight balance between crystalline and amorphous phase, in the hypothesis of CaO included only in wollastonite and diopside, in equivalent molar content, as reported in Tab. 5.6. Repeating the same calculation, on the basis of the weight balances reported in Tab. 5.5, for polymer-based mixtures (Tab. 5.6, again) we can note that: i) the amount of glass phase, in glass-free formulation, is only slightly above that expected from the sodium phosphate additive (5 wt%); ii) the addition of glass did not “dilute” the crystallization, wollastonite and diopside being formed not only by polymer-filler reactions, but also by glass devitrification.

Tab. 5.6 Semi-quantitative analysis of the weight balance between crystalline and amorphous phases.

	Formulations	Crystalline phase (wt%)	Amorphous phase (wt%)
0	Pure G20CaII	66	34
1	H62C + fillers	88	12
2	H62C + fillers + 10 wt% glass	98	2
3	MK + fillers	92	8
4	MK + fillers + 10 wt% glass	96	4

The calculations in Tab. 5.6 are only indicative (a more precise phase quantification, based on specific software packages, is in progress), but we can certainly say that silicone/fillers mixtures and G20CaII glass have an intrinsic, very significant “compatibility”; one system had a great potential in supporting the other. Going back to foams from H62C, the increase of liquid phase formed upon firing could be achieved by simple increase of the amount of sodium phosphate additive, but with risks of coarsening and/or viscous collapse of the cellular structure, upon firing, due to the dilution of the fraction leading to wollastonite and diopside. G20CaII glass represented a valid alternative, offering a “transient liquid phase”, mostly transformed in the desired crystal phases. The tests with MK, despite providing pellets for cell tests, are promising for the application of shaping techniques based on this specific polymer (foaming by release of CO_2, embedded upon supercritical CO_2-assisted extrusion[34]) or on MK/H62C mixtures (scaffolds from fused deposition of silicone-based pastes[35]).

5.2.3.3 In vitro biological characterization

As previously stated, a preliminary biological study, i.e. the MTT assay, was performed on MK-derived pellets. The graph in Fig. 5.12 shows that an increase in cell viability was observed passing from day 3 to day 7 for both the formulations (i.e. glass-free and glass-modified), implying that the fibroblast survived at day 3 might have duplicated and proliferated up to day 7. Interestingly, the incorporation of glass seemed to make the pellets generally even more biocompatible.

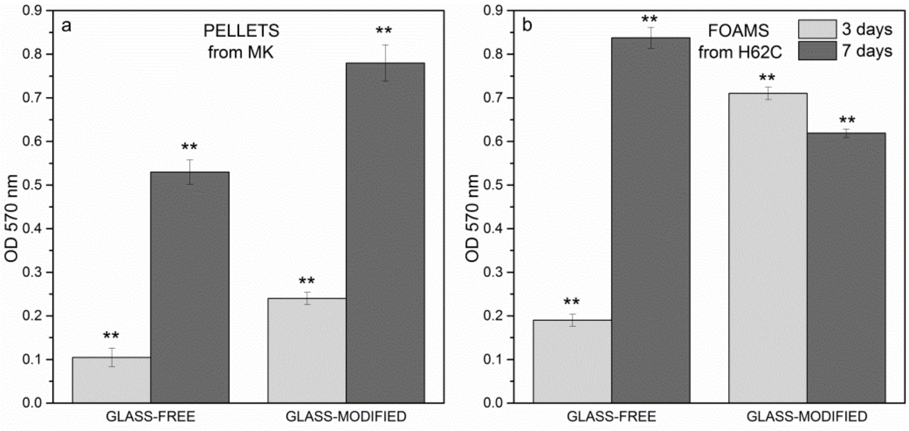

Fig. 5.12 MTT assay: a) pellets, 3-7 days; b) foams, 3-7 days.
*** indicates significant difference ($p<0.05$); ** ($p<0.01$); *** ($p<0.001$).**

The successful tests on pellets stimulated the application of MTT assay on H62C-derived foams, having a morphological organization closer to that of natural bones. As summarized in Fig. 5.12b, at day 3, cell viability looked higher in the glass-modified foams, as already seen in Fig. 5.12a, while at day 7, cells on the glass-free foams were more proliferated. From this observation, the addition of glass in the formulation of the foams did not lead to a clear improvement in cell viability at day 7, but only contributed to increase the biocompatibility at day 3. Comparing the behaviour of cells seeded on pellets and on foams, with regard to glass-free formulation, the foams allowed a more extensive cell viability; concerning the glass-modified formulation, the foams showed an improvement in viability only at day 3.

In order to overcome the controversial results of the MTT assay obtained for pellets and foams, LDH activity assay was also performed on the cells. Fig. 5.13a shows the intracellular LDH activity of the cells seeded on pellets: the graph proves that cells were able to produce metabolites, with improved results after 7 days from seeding. As reported in Fig. 5.13b, extracellular LDH activity was also measured on the culture medium: the graph confirms that metabolites were secreted by the same cells.

Even though the results of intracellular and extracellular LDH activity assays were not perfectly in agreement with each other, it can be observed that the incorporation of glass, which was effective in improving the mechanical behaviour of the foams and the phase assemblage, was not detrimental to cell survival and proliferation.

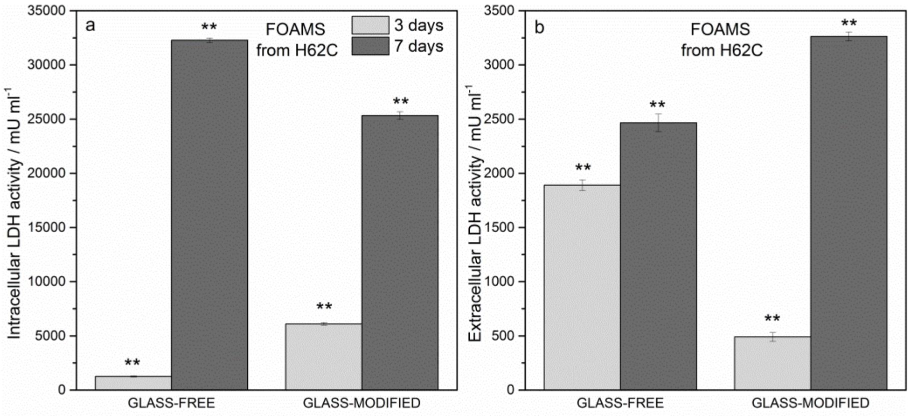

Fig. 5.13 LDH activity assay. (a) Intracellular LDH activity, foams, 3-7 days. (b) Extracellular LDH activity, foams, 3-7 days. * indicates significant difference ($p<0.05$); ** ($p<0.01$); * ($p<0.001$).**

SEM images of the foams, shown in Fig. 5.14, were taken after 3 and 7 days from fibroblast seeding. After 3 days (Fig. 5.14a, Fig. 5.14b), fibroblasts were found to be alive and spread on the surface of the samples, of both glass-free and glass-modified formulations; in particular they had a more elongated profile when seeding on glass-modified foams (Fig. 5.14b). After 7 days, cells had colonized the surface of the foams, still demonstrating elongated profiles, as shown in Fig. 5.14c and Fig. 5.14d for glass-modified samples. Moreover, the formation of hydroxyapatite precipitates (nodules in Fig. 5.14c,d) was observed, giving a further evidence of biocompatibility of the material.

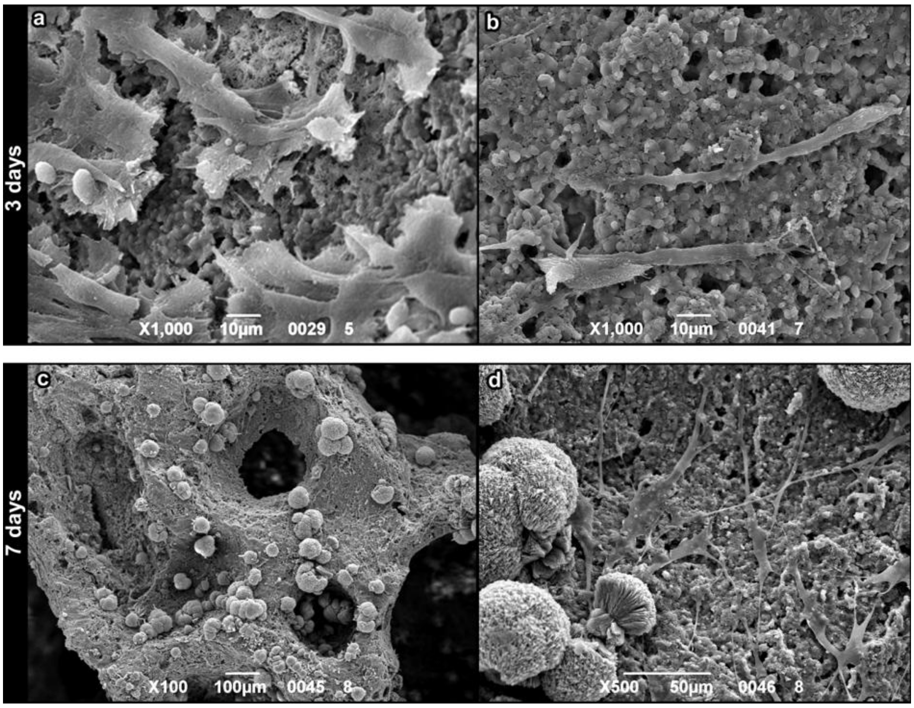

Fig. 5.14 SEM images after cell culture on foams: a) glass-free formulation – 3 days; b) glass-modified formulation – 3 days; c,d) glass-modified formulation – 7 days.

5.2.4 Conclusions

This study confirmed that wollastonite-diopside ceramics can be fabricated by firing mixtures based on preceramic polymers, in form of silicone resins (acting as silica sources), mixed with powdered metal oxide precursors. The use of preceramic polymers allowed the samples to be easily shaped both in form of pellets and foams.

Concerning the foaming step, hydrated sodium phosphate was found to be an efficient foaming agent, thanks to its thermal decomposition reaction, releasing water. The subsequent ceramic conversion of the foamed materials implied the transformation of the silicone foam into a glass-ceramic foam, incorporating silicate crystals embedded in glass phase provided by the same phosphate additive.

The liquid phase developed upon firing, due to the hydrated sodium phosphate, can be increased by introduction of a glass filler; the positive impact on the structural integrity of samples is not accompanied by any change in the phase assemblage, operating with a glass crystallizing itself in wollastonite and diopside.

A further observation concerns the fact that the choice of silicone polymers with different nature and chemistry (liquid H62C, solid MK) does not affect the ceramic product in terms of main phase assemblage.

With regard to the biological characterization of the materials, both dense and foamed wollastonite-diopside ceramic samples showed positive results in terms of cell viability, according to the MTT assay and LDH activity tests; the incorporation of glass in the formulations proved to be not detrimental to cell survival and proliferation. Although the addition of glass in the formulation was not crucial for viability at day 7, it was definitively effective in improving the biocompatibility of the samples throughout the cell culture period up to day 3.

References

[1] P. N. de Aza, F. Guitian, S. de Aza, Bioactivity of wollastonite ceramics: in vitro evaluation, Scr. Metall. Mater. 31 (1994) 1001–1005.

[2] K. Lin, W. Zhai, S. Ni, J Chang, Y. Zeng, W. Qian, Study of mechanical property and in vitro biocompatibility of $CaSiO_3$ ceramics, Ceram. Inter. 31(2005) 323–326.

[3] T. Nonami, S. Tsutsumi, Study of diopside ceramics for biomaterials, J. Mater. Sci. Mater. Med. 10 (1999) 475–479.

[4] J. M. G. Ventura, D. U. Tulyaganov, S. Agathopoulos, J. M. F. Ferreira, Sintering and crystallization of akermanite-based glass–ceramics, Mater. Lett. 60 (2006) 1488–1491.

[5] C. Wu, J.Chang, J. Wang, S. Ni, W. Zhai, Preparation and characteristics of a calcium magnesium silicate (bredigite) bioactive ceramic, Biomater. 26(2005) 2925–2931.

[6] C. Wu, J. Chang, Degradation, bioactivity and cytocompatibility of diopside, akermanite and bredigite ceramics, J. Biomed. Mater. Res-B Appl. Biomater. 83 (2007) 153–160.

[7] L. M. Rodríguez-Lorenzo, R.G. Carrodeguas, MA Rodríguez, S De Aza, J Parra, J. S. Román, Development of wollastonite-poly(ethylmethacrylate co-vinylpyrrolidone) based materials for multifunctional devices, J. Biomed. Mater. Res A. 1;81 (2007) 603-610.

[8] F. Barrera-Me´ndez, J. C. Escobedo-Bocardo, D. A. Corte´s-Herna´ndez, J. M. Almanza-Robles, E. M. Mu´zquiz-Ramos, Gentamicin sulphate release from lost foam wollastonite scaffolds using poly(DL-lactide-co-glycolide) acid, Ceram Int. 37 (2011) 2445–2451.

[9] P. Colombo, E. Bernardo, G. Parcianello, Multifunctional advanced ceramics from preceramic polymers and nano-sized active fillers, J. Eur. Ceram. Soc. 33 (2013) 453-469.

[10] E. Bernardo, L. Fiocco, G. Parcianello, E. Storti, P. Colombo, Advanced ceramics from preceramic polymers modified at the nano-scale: A review, Mater. 7 (2014) 1927-1956.

[11] G. Bhattacharya, S. Zhang, D. D. Jayaseelan, W. E. Lee, Mineralizing effect of $Li_2B_4O_7$ and $Na_2B_4O_7$ on magnesium aluminate spinel formation, J. Am. Ceram. Soc. 90 (2007) 97–106.

[12] E. Bernardo, J-F. Carlotti, P. M. Dias, L. Fiocco, P. Colombo, L. Treccani, U. Hess, K. Rezwan, Novel akermanite-based bioceramics from preceramic polymers and oxide fillers, Ceram. Int 40 (2014) 1029–1035.

[13] M.A. Sainz, O. Pena, S. Serena, A. Caballero, Influence of design on bioactivity of novel $CaSiO_3$-$CaMg(SiO_3)_2$ bioceramics: in vitro simulated body fluid test and thermodynamic simulation, Acta Biomater. 6 (2010) 2797-807

[14] Fiocco, L., Elsayed, H., Daguano, J. K. M. F., Soares, V. O., Bernardo, E. (2015). Silicone resins mixed with active oxide fillers and Ca–Mg Silicate glass as alternative/integrative precursors for wollastonite–diopside glass-ceramic foams. Journal of Non-Crystalline Solids, 416, 44-49.

[15] M. J. Pascual, A. Durán, M. O. Prado, A new method for determining fixed viscosity points of glasses, Phys. Chem. Glasses, 46 [5] (2005) 512-520.

[16] A. de Pablos-Martín, G.C. Mather, F. Muñoz, S. Bhattacharyya, Th. Höche, J. R. Jinschek, T. Heil, A. Durán, M. J. Pascual. Design of oxy-fluoride glass-ceramics containing NaLaF4 nano-crystals, J. Non-Cryst. Solids 356 (2010) 3071-3079.

[17] V. O. Soares, R.C.V.M. Reis, E. D. Zanotto, M. J. Pascual, A. Duran, Non-isothermal sinter-crystallization of jagged Li_2O-Al_2O_3-SiO_2 glass and simulation using a modified form of the Clusters model. J. Non-Cryst. Sol. 358 [23] (2012) 3234-3242.

[18] H. Elsayed, A. Zocca, E. Bernardo, C.M. Gomes, J. Günster, P. Colombo, Development of bioactive silicate-based glass-ceramics frompreceramic polymer and fillers, J. Eur. Ceram. Soc. 35 (2015) 731–739.

[19] Bhattacharya, G.; Zhang, S.; Jayaseelan, D.D.; Lee, W.E. Mineralizing effect of Li2B4O7 and Na2B4O7 on magnesium aluminate spinel formation. J. Am. Ceram. Soc. 2007, 90, 97–106.

[20] Bernardo, E.; Carlotti, J.-F.; Dias, P.M.; Fiocco, L.; Colombo, P.; Treccani, L.; Hess, U.; Rezwan, K. Novel akermanite-based bioceramics from preceramic polymers and oxide fillers, Ceram. Int. 2014, 40, 1029–1035.

[21] Rahaman, M.N.; Day, D.E.; Bal, B.S.; Fu, Q.; Jung, S.B.; Bonewald, L.F.; Tomsia, A.P. Bioactive glass in tissue engineering. Acta Biomater. 2001, 7, 2355–2373.

[22] Hoppe, A.; Güldal, N.S.; Boccaccini, A.R. A review of the biological response to ionic dissolution products from bioactive glasses and glass-ceramics. Biomaterials. 2011, 32, 2757-2774.

[23] Fu, Q.; Rahaman, M.N.; Bal, B.S.; Bonewald, L.F.; Kuroki, K., Brown, R.F. Silicate, borosilicate and borate bioactive glass scaffolds with controllable degradation rates for bone tissue engineering applications. II. In vitro and in vivo biological evaluation. J. Biomed. Mater. Res. A. 2010, 95, 172–9.

[24] Gorustovich, A.A.; Lopez, J.M.P.; Guglielmotti, M.B.; Cabrini, R.L. Biological performance of boron-modified bioactive glass particles implanted in rat tibia bone marrow. Biomed. Mater. 2006, 1, 100-105

[25] Jung, S.B.; Day, D.E.; Brown, R F.; Bonewald, L.F. Potential Toxicity of Bioactive Borate Glasses In-Vitro and In-Vivo. In Advances in Bioceramics and Porous Ceramics V. R. Narayan, R P. Colombo, M. Halbig, S. Mathur, Eds; Publisher: John Wiley & Sons, Inc., Hoboken, NJ, USA, 2012.

[26] Baino, F.; Brovarone, C.V. Three-dimensional glass-derived scaffolds for bone tissue engineering:Current trends and forecasts for the future, J. Biomed. Mater. Res. A 2010, 97A, 514-535.

[27] Kaur, G.; Pandey, O.P.; Singh, K.; Homa, D.; Scott, B.; Pickrell, G. A review of bioactive glasses: Their structure, properties, fabrication, and apatite formation. J. Biomed. Mater. Res. A 2013, 102, 254 – 274.

[28] Rahaman, M.N.; Liang, W.; Day D.E.; Marion, N.W.; Mao, J.J. Preparation and bioactive characteristics of porous borate glass substrates. Ceram. Eng. Sci. Proc. 2005, 26:3-10.

[29] Kaur, G.; Pickrell, G.; Kimsawatde, G.; Homa, D.; Allbe, H.A.; Sriranganathan, N. Synthesis, cytotoxicity and hydroxyapatite formation in 27-Tris-SBF for sol-gel based CaO-P2O5-SiO2-B2O3-ZnO bioactive glasses. Sci. Rep. 2014, 4, 1-14.

[30] Fiocco, L., Elsayed, H., Ferroni, L., Gardin, C., Zavan, B., Bernardo, E. (2015). Bioactive Wollastonite-Diopside Foams from Preceramic Polymers and Reactive Oxide Fillers. Materials, 8(5), 2480-2494.

[31] Khorami, M.; Hesaraki, S.; Behnamghader, A.; Nazarian, H.; Shahrabi, S. In vitro bioactivity and biocompatibility of lithium substituted 45S5 bioglass. Mat. Sci. Eng. C 2011; 31: 1584–1592.

[32] Miguez-Pacheco, V.; Büttner, T.; Maçon, A.L.B.; Jones, J.R.; Fey, T.; de Ligny, D.; Greil, P.; Chevalier, J.; Malchere, A.; Boccaccini, A.R. Development and characterization of lithium-releasing silicate bioactive glasses and their scaffolds for bone repair, J. Non-Cryst. Sol. 2015; in press - http://dx.doi.org/10.1016/j.jnoncrysol.2015.03.027.

[33] Denizot, F.; Lang, R. Rapid colorimetric assay for cell growth and survival. Modifications to the tetrazolium dye procedure giving improved sensitivity and reliability. J. Immunol. Methods. 1986, 89, 271-277.

[34] Bernardo, E.; Parcianello, G.; Colombo, P.; Matthews, S. Wollastonite foams from an extruded preceramic polymer mixed with $CaCO_3$ microparticles assisted by supercritical carbon dioxide. Adv. Eng. Mater. 2013, 5, 60–65.

[35] Bernardo, E.; Colombo, P.; Dainese, E.; Lucchetta, G.; Bariani, P.F. Novel 3-D wollastonite-based scaffolds from preceramic polymers containing micro- and nano-sized reactive particles. Adv. Eng. Mater. 2012, 14, 269–274.

6 Ca-Mg silicates: developments

6.1 Carbon-containing nanocomposites

6.1.1 Introduction

As already discussed, a fundamental advantage concerning the use of preceramic polymers is the possibility of combining synthesis and shaping of ceramics in a very easy and flexible way, thanks to the polymeric nature of the silicone precursors: components can be shaped by conventional plastic-forming techniques, such as spinning, blowing, warm/cold pressing, injection molding, extrusion, and later converted into ceramics by treatments above 800 °C[1-2].

The experiences included in the present thesis mainly refer to the introduction of fillers within solutions of silicone resins, based on solvents such as acetone or isopropyl alcohol, that need to be removed by drying before further processing (direct foaming by incorporation of hydrated fillers, cold/warm pressing, 3-D printing). Therefore, this approach has a limit, although definitely successful in terms of results: if it is simple at a laboratory scale, it is at the same time quite complicated from an industrial point of view, due to the risk in handling solvents and to the costs of the correct disposal of such hazardous substances.

A good way to make industrial applications of preceramic polymers feasible might be the extrusion of preceramic mixtures starting from a solid silicon (the same polymer already mentioned for preparing pellets or 3-D printable mixtures) mixed with powdered micro-sized inorganic fillers. In this case, no solvent would be used for dissolving polymers, but the homogeneity of the mixture would be provided mechanically by the extrusion process, due to the rotation of the screw inside the barrel. The heating during operation would enable the polymer to melt, being perfectly extrudable at the die. An enhanced mixing might be favoured by the incorporation in the molten mass of supercritical CO_2 (sc-CO_2) as a processing additive (see Fig. 6.1[3]).

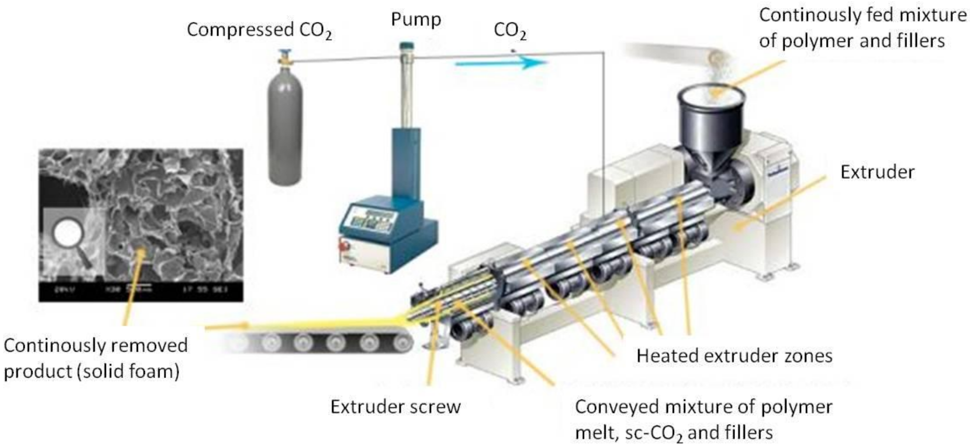

Fig. 6.1 Representation[3] of the extrusion process assisted by sc-CO_2.

In the present chapter, it will be shown that this processing technique is suitable for obtaining preceramic extrudates incorporating sc-CO_2, which can be later reprocessed in order to fabricate porous components. The selected composition for this processing route was again wollastonite-diopside, added with borax aimed at acting as a mineralizing filler, as already explained in §4 and §5.1. Extruded and reprocessed samples were later ceramized following different thermal treatment, both in air and nitrogen (N_2), and their biological properties were assessed by preliminary *in vitro* tests with fibroblasts. The results obtained will be submitted soon for publication.

A fundamental consequence of the treatment in inert atmosphere was the availability of a carbon phase; in fact, SiOC is known to be consisting of an “over-bridged” silica glass, including some Si-C bonds in the siloxanic network, mixed with turbostratic carbon nano-sheets[4], evolving into silica/SiC/C composite for treatments above 1200 °C. The formation of a carbon phase might be an interesting strategy for biomedical applications, given the recent developments concerning bioceramics incorporating carbon structures, from external sources. Xie *et al.*[5] have reported graphene-reinforced Ca-silicate coatings as a novel solution for load-bearing implants, owing to improvements in both wear resistance and cytocompatibility. A similar experience, on diopside, has been reported by Mehrali *et al.*[6], who developed a diopside-reduced graphene oxide composite with promising results for biomedical applications. Carbon nanotubes have also been used (up to 4 wt%), by Shuai *et al.*[7], as a reinforcement for diopside bone scaffolds, again with positive results on mechanical properties and cellular response after seeding. The present study, unlike the previous ones, represents, to our knowledge, the first example of formation of carbon phase directly *in situ*.

6.1.1.1 Supercritical CO_2 in extrusion processes

A supercritical fluid (SCF) is a substance that exists above its critical temperature and pressure (Fig. 6.2)[8]. It has properties intermediate between those of gases and liquids[9]. Thanks to this benefit of increased density, a SCF has the ability to dissolve, diffuse and carry materials.

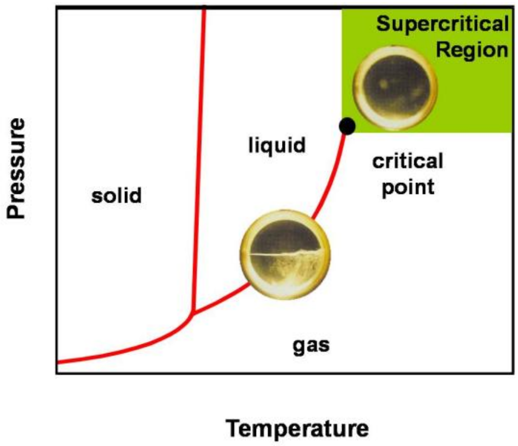

Fig. 6.2 Phase diagram[8] of CO_2.

In particular, sc-CO_2 is non-toxic, environmentally friendly, chemically inert, non-flammable and its critical conditions are easily reached (Tc=31 °C, Pc=7.38 MPa). Sc-CO_2 is often used as an additive in polymer processing, especially in extrusion process (Fig. 6.1)[10]. Its special combination of gas-like viscosity and liquid-like density makes it an excellent solvent or plasticizer. These reasons explain why sc-CO_2 is used in polymer processing in pharmaceutical and food industries as it is clean, efficient and environmentally friendly[11-14].

The diminution of viscosity will result in the limitation of mechanical stresses and a decrease in operating temperatures, so that introducing sc-CO_2 allows the processing of molecules which would be too fragile to withstand the mechanical stresses and the operating temperatures of a standard extrusion process. It can also allow handling molecules having a limited thermal stability. Moreover, its dissolution in the polymer under pressure will be accompanied by large volume expansion during the return to atmospheric pressure (at the die), so that sc-CO_2 can be also used as a foaming agent. It is therefore possible to control pore generation and growth by controlling the operating conditions[15].

6.1.2 Experimental

6.1.2.1 Extrusion and secondary processing

A commercial silicone resin (Silres MK, Wacker-Chemie GmbH, Munchen, Germany) was used to provide the polymeric matrix into which embed $CaCO_3$ and $Mg(OH)_2$ powders (<10 µm, Industrie Bitossi, Vinci, Italy). The balance among these constituents (silicones/MgO precursor/CaO precursor) followed the stoichiometric CaO/MgO/SiO_2 molar proportions of 2/1/3, corresponding to an equimolar mixture of wollastonite ($CaSiO_3$ or $CaO{\cdot}SiO_2$, CaO-MgO-SiO_2 molar proportion of 1/0/1) and diopside ($CaMgSi_2O_6$ or $CaO{\cdot}MgO{\cdot}2SiO_2$, CaO-MgO-$SiO_2$ molar proportion of 1/1/2). The effective weight balance of polymer and fillers was calculated assuming MK to be completely transformed into silica, like in the case of treatments in air ($CaCO_3$/$Mg(OH)_2$/MK=0.93/0.27/1). Sodium borate ($Na_2O{\cdot}2B_2O_3{\cdot}10H_2O$, Sigma Aldrich, Gillingham, UK) was used as mineralizing agent[16] in an amount of 3 wt% of the theoretical ceramic yield of the various components.

The precursors were first homogenized by means of a shaker-mixer (Turbula T2F, WAB, Switzerland), then inserted in a twin-screw extruder (24 mm screw diameter, length/diameter ratio equal to 40:1, Thermo Prism Ltd, Stone, United Kingdom) rotating at 250 rpm and operating at 75 °C at the die. The extrusion process was assisted by supercritical carbon dioxide (sc-CO_2), kept at a pressure of 8.3 MPa and a temperature of 35 °C. The sc-CO_2 was injected into the barrel of the extruder at a rate of 10 ml min^{-1}.

Extrusion led to almost round fragments (diameter of about 30 mm), later subjected to secondary processing. After grinding the extrudates by means of a ball mill (60 min at 450 rpm, Pulverisette 7 planetary ball mill, Fritsch, Idar-Oberstein, Germany), the powders were sieved to a dimension below 300 µm, gently hand pressed in Al moulds and then heat treated, thus causing both viscous flow sintering and foaming, at 350 °C in air for 30 min, with a heating rate of 5 °C/min. At this temperature, not only the remelting of the polymer was enabled, but also the release of the CO_2 previously entrapped in the material by extrusion and the release of water vapour from borax due to its thermal decomposition. At the same time, the polymeric component cross-linked, thus maintaining the porous structure given by the gas release. The obtained foams were 10 mm in diameter and 7-8 mm in height. After removal from the Al moulds, they were polished with abrasive paper and finally fired in nitrogen (N_2) at 1100 °C for 1 h, using a heating rate of 2 °C/min. Samples will be referred to as “W-D”.

The extrusions were performed at SCF Processing Ltd. (Drogheda, Ireland) during a 3-month student exchange in 2013.

6.1.2.2 Characterization of samples

Microstructural characterizations were performed by optical stereomicroscopy and scanning electron microscopy (FEI Quanta 200 ESEM, Eindhoven, The Netherlands) equipped with energy dispersive spectroscopy (EDS). The crystalline phases were identified by means of X-ray diffraction on powdered samples (XRD; Bruker AXS D8 Advance, Bruker, Germany), supported by data from PDF-2 database (ICDD-International Centre for Diffraction Data, Newtown Square, PA) and Match! program package (Crystal Impact GbR, Bonn, Germany). Quantitative phase analysis (QPA), based on the Rietveld method[17], was performed by Dr. Michele Secco (University of Padova) using TOPAS software (Bruker AXS, version 4.1, Karlsruhe, Germany), starting from XRD patterns collected on glass-ceramic powders, after mixing with zincite powders, operating as internal standard. The contents of crystalline and amorphous phases were determined using the combined Rietveld–RIR method[18].

Micro-Raman spectroscopy was carried out in collaboration with Prof. D. Pedron (Department of Chemical Sciences, University of Padova), using a homemade micro-Raman system, based on a single

320 mm focal length imaging spectrograph (Triax-320 Horiba Jobin Yvon), equipped with a holographic 1800 gr/mm grating and a liquid nitrogen cooled CCD detector. The excitation source was a Spectra Physics Ar^+ ion laser (Stabilite 2017) operating at 514.5 nm, an appropriate edge filter was used to reduce the stray-light level. An optical microscope (Olympus BX 40) equipped with a 20x objective optically coupled to the spectrograph was used to record the Raman spectra in micro configuration. The laser power on sample was 8 mW and the spectral interval was 1.5-2 cm^{-1}.

The bulk density (ρ_b) of the foams was determined using a caliper and a digital balance. The skeletal density (ρ_s) was measured on foams, using a He gas pycnometer (Micromeritics AccuPyc 1330, Norcross, GA).The percentage of open porosity (% P) was then calculated using the following equation: $\% P=1-(\rho_b/\rho_s)$.

The crushing strength of foams was measured at room temperature, by means of an Instron 1121 UTM (Instron Danvers, MA) operating with a cross-head speed of 1 mm/min. Each data point represents the average value of 5 to 10 individual tests.

6.1.2.3 Cell culture study

For cell culture studies, samples were cut to 10 mm x 10 mm x 5 mm and fixed to 48-well plates. The entire well plates where then sterilized. Human fibroblasts were seeded at a density of $4x10^5$ cells/piece in cDMEM, which consisted of Dulbecco's Modified Eagle Medium (DMEM) (Lonza S.r.l., Milano, Italy), supplemented with 10 vol% Fetal Bovine Serum (FBS) (Bidachem S.p.A., Milano, Italy) and 1 vol% Penicillin/Streptomycin (P/S) (EuroClone, Milano, Italy). The 3-D cultures were incubated at 37 °C and 5% CO_2 for 7 days, with media changes every 2 days.

For SEM imaging, fibroblasts grown on samples for 3 and 7 days were fixed in 2.5% glutaraldehyde in 0.1 M cacodylate buffer for 1 h, then progressively dehydrated in ethanol. Control and treated Ti discs without cells were also examined.

Biological characterizations were performed thanks to a collaboration with Prof. B. Zavan (University of Padova).

6.1.3 Results

The morphology of the W-D foams is shown in Fig. 6.3. The porosity was finely distributed and the size of the pores was quite homogenous. Besides the contribution of borax and Mg hydroxide in the foaming step, due to water release during the foaming treatment at 350 °C, the controlled pore size distribution was mostly due to the release of the CO_2, which was homogeneously dissolved within the polymeric chains through the $scCO_2$-assisted extrusion (it should be noted that very homogeneous foams were obtained, by $scCO_2$-assisted extrusion, even operating with $CaCO_3$, unable to provide any gas release at 350 °C, as the only filler[19]). In fact, the simultaneous presence of many sources of gas increased the number of gas evolution sites, thus allowing a well distributed porosity, which was even maintained after ceramization in N_2 at 1100 °C, as shown by Fig. 6.3b.

Fig. 6.4 reports a comparison between W-D samples subjected to exactly the same process, except for the ceramization atmosphere, N_2 for the foam in Fig. 6.4a, air for the one in Fig. 6.4b. It can be observed that the W-D sample treated in nitrogen is less micro-cracked than the one fired in air. The ceramization in air implies the complete removal of carbon, present in the starting silicone chains, in the form of gaseous products, with generally negative effects on the integrity of samples. In particular, the cracking may be favored by the oxidation of the $Si-CH_3$ groups in the silicone, starting above 350 °C[20], which is known for its strong exothermic effect[21,22]. When the ceramization is carried out in inert atmosphere, such as in N_2, carbon bonded to silicon in the silicon-based organic oligomers is partially retained, owing to the higher resistance of the silicon–carbon bonds, in non-oxidizing environment, compared to C–H bonds[4]. Up to 1200 °C, Si, C and O may coexist in a condition of great homogeneity[23], with nano-sized amorphous silica clusters encased within an interdomain wall constituted from mixed Si-C and Si-O bonds and from a network of graphitic carbon[21].

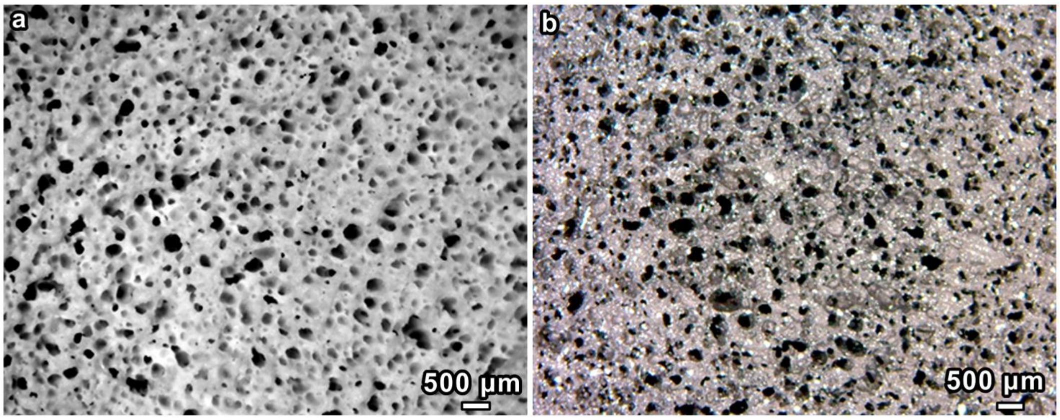

Fig. 6.3 Morphology of W-D samples: a) after foaming; b) after ceramization in N_2.

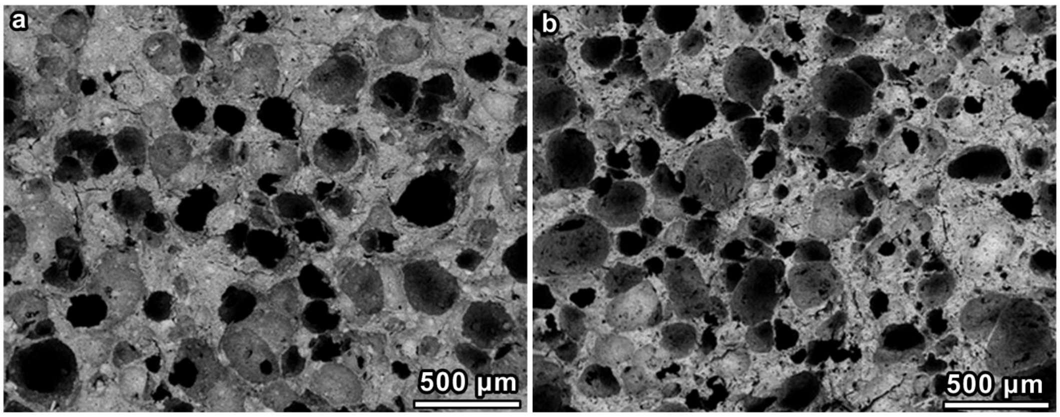

Fig. 6.4 SEM micrographs of W-D foams ceramized in a) N_2; b) air.

Tab. 6.1 Summary of physical and mechanical properties of W-D foams ceramized in N_2 (σ_c=compressive strength; ρ_{bulk}=bulk density; $\rho_{skeleton}$=skeleton density; ρ_{true}=true density; P_{open}=open porosity).

Firing Atmosphere	ρ_{bulk} (g/cm^3)	$\rho_{skeleton}$ (g/cm^3)	P_{open} (%)	σ_{comp} (MPa)
N_2	0.92 ± 0.09	2.61 ± 0.01	65	22.7 ± 4.2
Air	0.71 ± 0.04	3.06 ± 0.01	77	3.9 ± 0.3

The efficiency of the ceramization in N_2 atmosphere in reducing the number of cracks in the W-D samples is confirmed by the value of the compressive strength reported in Tab. 6.1, which exceeds 20 MPa. Compared to the case of samples fired in air, the compressive strength value is more than 4 times higher. The values obtained after the ceramization in N_2 are in agreement with the compressive strength of diopside scaffolds fabricated by selective laser sintering (SLS) and reinforced with graphene nanoplatelets, by Cijun *et al.*[24].

The strength enhancement (in the comparison with W-D samples fired in air) could be due also to the microstructure: as shown by Fig. 6.4a, there are interconnecting channels (with a diameter exceeding 100 µm, which is considered the minimum value for cell penetration and vascularization)[25], but also quite dense load-bearing cell walls. In other words, unlike in Ashby's ideal open-celled structure[26], the solid phase is not distributed only on cell edges in both types of samples. In the sample fired in air, the walls reasonably gave a limited contribution to the strength owing to the multitude of micro-pores, visible as small dots in the cell walls in Fig. 6.4b. The presence of denser walls, for the firing in N_2, justifies the lower amount of open porosity (65%), inferred from gas pycnometry, compared to the amount detected for the firing in air (77%), as an effect of gasses passing through both macro-pores and micro-pores, at cell walls.

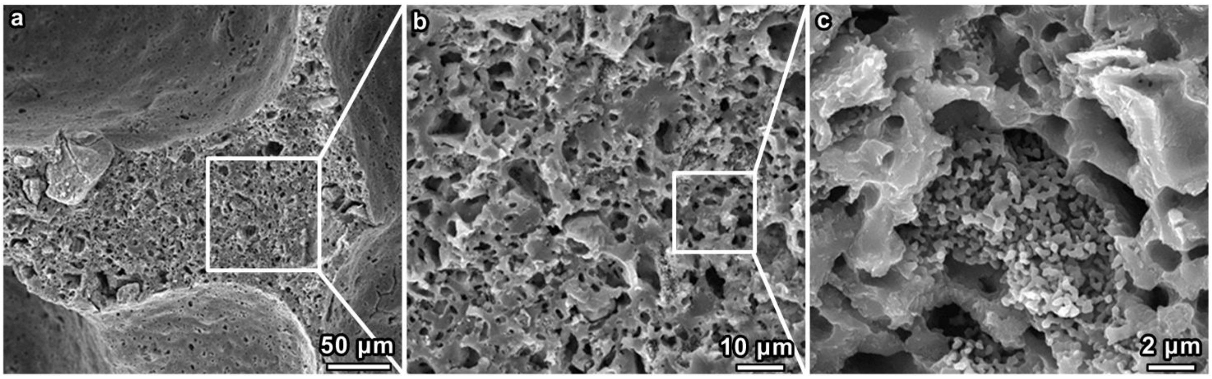

Fig. 6.5 Microporosity in W-D foams ceramized in N_2: a) detail of cell strut; b-c) cell wall.

As reported in Fig. 6.5, not only the cell walls are scattered with very small pores (≈1-2 µm), but also the struts are completely porous (Fig. 6.5a), showing a rather spongy microstructure, as visible at higher magnification in Fig. 6.5b. The micro-porosity is known to facilitates cell attachment and osteoinduction[27,28]. The high magnification detail of Fig. 6.5c illustrates the formation of groups of nano-crystals (with dimension in the order of 500 nm) mixed with relatively smooth glassy zones.

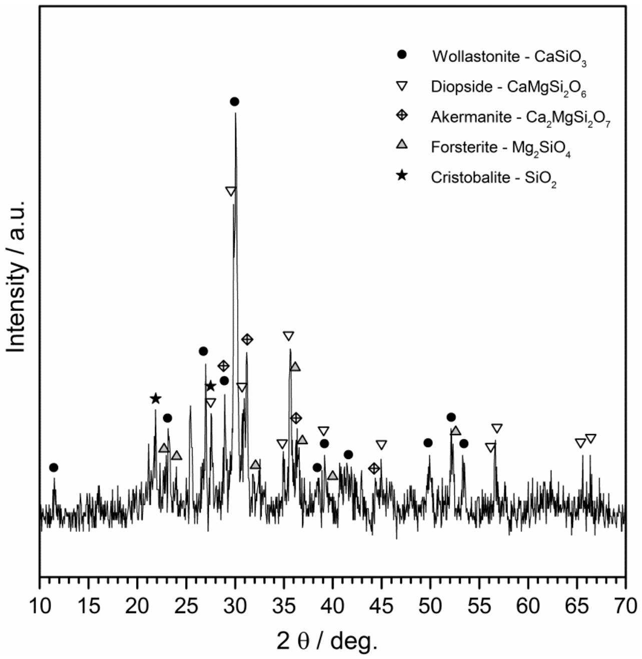

Fig. 6.6 X-Ray diffraction pattern of extruded samples after reprocessing at 350 °C and ceramization at 1100 °C in N_2.

As reported in Fig. 6.6, X-ray diffraction on a powdered sample demonstrated that W-D samples are characterized by the desired phase assemblage, comprising wollastonite ($CaSiO_3$ - PDF#42-0550) and diopside ($CaMgSi_2O_6$ – PDF#68-0932). Weak traces of akermanite ($Ca_2MgSi_2O_7$ - PDF#83-1815), forsterite (Mg_2SiO_4 – PDF#85-1346) and cristobalite (SiO_2 - PDF#85-0460 - PDF#76-0939) were also detected. The results of a quantitative phase analysis, obtained by with Rietveld method, is summarized in Tab. 6.2. Ideally, the wollastonite/diopside weight ratio (W/D) would be 0.54 in a theoretical ceramic with 50 mol% wollastonite and 50% diopside, while the obtained samples have W/D=0.91. The lack in diopside can be explained on the basis of the fact that MgO was not totally involved in the reaction leading to diopside, but partially contributed to the formation of akermanite and forsterite as well. This analysis also allowed a quantification of the amorphous phase, that exceeded the 35 wt%.

Tab. 6.2 Distribution of crystalline and amorphous phases from quantitative phase analysis of the foams ceramized in N_2 at 1100 °C, obtained by Rietveld method.

Crystalline and amorphous phases (wt%)						
Wollastonite [$CaSiO_3$]	Diopside [$CaMgSi_2O_6$]	Akermanite [$Ca_2MgSi_2O_7$]	Forsterite [Mg_2SiO_4]	Cristobalite [SiO_2]	Amorphous Phase	W/D
24.6	27.1	6.3	5.3	0.9	35.8	0.91

It has been demonstrated in previous studies by Scheffler *et al.*[29] that, throughout the pyrolysis in inert atmosphere, MK produces a Si-O-C ceramic residue with atomic proportions as follows: $Si_3O_{4.56}C_{1.92}$, or alternatively $2.3SiO_2{\cdot}0.7SiC{\cdot}1.2C$. In contrast, in the present case, Si-C bond was not detected by micro-Raman or XPS, meaning that the multi-cationic system here investigated resulted in an unedited thermal conversion of the silicone. This was probably responsible, as well, for a higher amount of oxygen incorporated in the final ceramic product, in order to form more SiO_2 in the amorphous phase, compared to the above discussed proportions suggested by Scheffler *et al.* In fact, the formation of more SiO_2 was necessary to compensate the total absence of SiC. Otherwise, a partial evaporation of Si may have occurred.

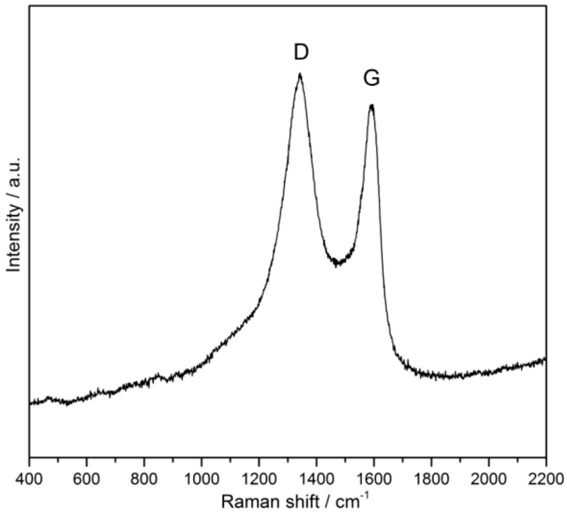

Fig. 6.7 Results of micro-Raman analysis on W-D foams ceramized in N_2, after treatment in HF.

More interestingly, graphitic carbon was detected in the final ceramic material by micro-Raman analysis, due to the presence of a pair of peaks at 1340 and 1590 cm^{-1}, assignable to the carbon D and G bands, respectively[30-31]. The micro-Raman spectrum (Fig. 6.7) was taken after immersion of a selected sample in HF for 4 weeks, to provide a selective corrosion with regard to silicates and better expose graphitic carbon and eventually SiC to the analysis. The presence of carbon is not unusual in bioceramics. In fact, many studies can be found in literature on the use of carbon nanotubes[6]. or graphene[4,5] as a reinforcement to be incorporated into materials for medical applications, aimed at enhancing the mechanical properties of the implants, without affecting the biocompatibility of the composite material. The reinforcement mechanism in ceramics consists in inhibiting the crack propagation through the matrix, that is achievable by different methods, such as deflecting crack tips, forming bridges across crack faces, absorbing energy during pull-out, and causing a redistribution of stresses in regions adjacent to crack tips[32]. For this reason, the retention of graphitic carbon in the W-D might be a further reinforcing factor in the final W-D glass-ceramics and the process proposed in this study could be exploited to fabricate C-reinforced biosilicates, without the need of incorporating carbon from an external source.

A very preliminary 7-day cell culture test *in vitro* was also carried out on W-D foams after ceramization in N_2, to have an indication of the behaviour of cells, interacting with this sort of composite material. As displayed in the SEM images reported in Fig. 6.8, cells seemed to have colonized the whole surface and the pore cavities, showing elongated profiles after 3 days (Fig. 6.8a) and forming more compact layer of cells after 7 days (Fig. 6.8b). Although more detailed biological tests are still missing to have a comprehensive overview of the applicability of these W-D foams treated in N_2 as biomedical materials, these early results are definitely encouraging.

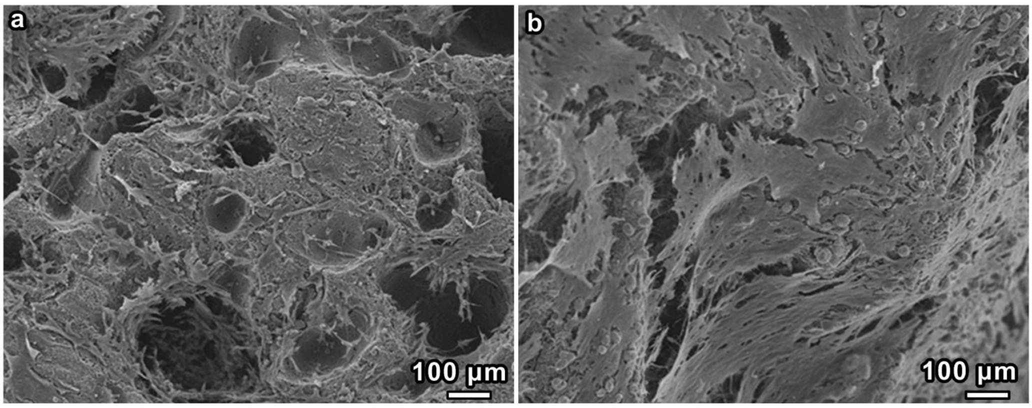

Fig. 6.8 SEM micrographs taken on W-D foams ceramized in N_2, undergoing cell culture study: a) day 3; b) day 7.

6.1.4 Conclusions

Wollastonite-diopside glass-ceramic foams were obtained from a solid silicone, incorporating inorganic micro-sized oxide precursors. The homogeneity of the powder mixture was enhanced by supercritical CO_2-assisted extrusion, which, furthermore, served as a method to dissolve CO_2 inside the polymeric chains.

A subsequent processing on extrudates, mainly consisting in grinding them and treating the powders at 350 °C, resulted in an extensive foaming. This was due to the combination of the foaming ability of the water vapour, released by hydrated fillers, and of the evaporation of CO_2, previously dissolved.

The ceramization in N_2 led to a rather unedited result in terms of final composition, obtaining, besides the desired crystalline phases, 36 wt% of amorphous, a total lack of SiC and the presence of graphitic carbon. A further consequence was the obtainment of crack-free foams, with compressive strength exceeding 20 MPa.

This method to retain graphitic carbon from the ceramic conversion of a preceramic polymer in N_2 might be exploited to fabricate C-reinforced biosilicates, with non-degraded biological properties.

6.2 Melilite solid solutions

6.2.1 Introduction

Akermanite ($CaMgSi_2O_7$), already mentioned in §4, is a silicate belonging to "melilites", a family of sorosilicates, the general formula of which is $A_2T1(T2)_2O_7$. Their structure was determined in 1930 by Warren[33] and can be described as consisting of $T2_2O_7$ dimers (T2=Si, Al, etc.) connected via T1 cations (Mg, Zn, etc.) in tetrahedra to form a sheet-like arrangement. These sheets are linked together by large cations A (Ca, Sr, Ba, etc.) occupying octahedral sites[33-35], as shown in Fig. 6.9[38].

Several silicates can be ascribed to this structure, as reported in Tab. 6.3 (Gehlenite will be further investigated in §13). By virtue of the profound analogies in their crystalline structures, solid solutions between different crystalline phases might be realized.

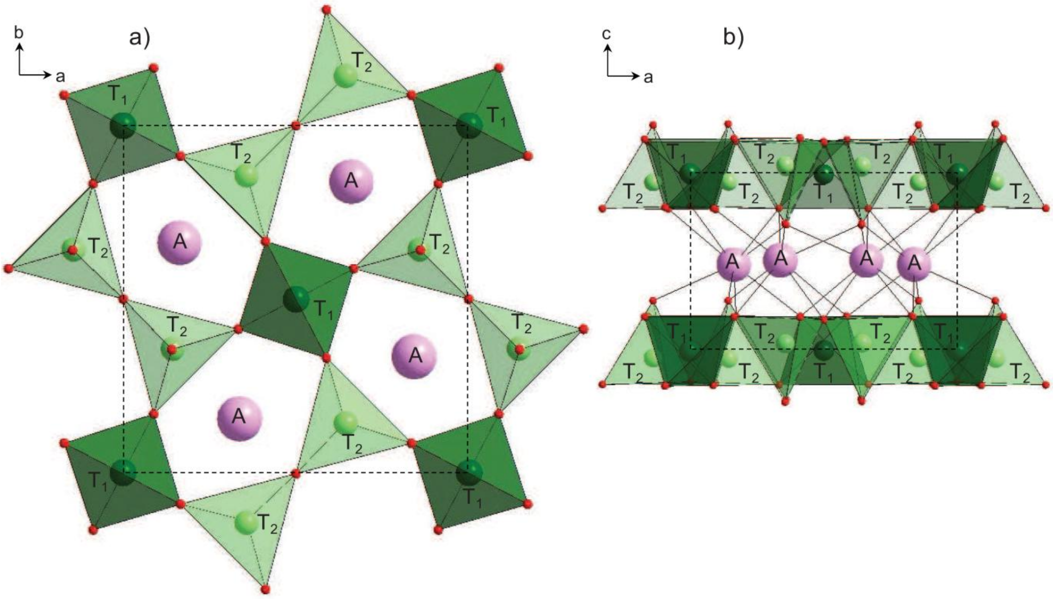

Fig. 6.9 The crystal structure of melilites[38]: a) plane (001); b) plane (010).

Tab. 6.3 Examples of silicates belonging to melilites.

	A	T1	T2	T2	
Akermanite	Ca_2	Mg	Si	Si	O_7
Hardystonite	Ca_2	Zn	Si	Si	O_7
Okayamalite	Ca_2	B	B	Si	O_7
Gehlenite	Ca_2	Al	Al	Si	O_7

An example of solid solution between akermanite and okayamalite might be realized following a molar balance akermanite:okayamalite of 0.75:0.25. The theoretical result is schematically represented by the following formula:

$$0.75 \cdot Ca_2MgSi_2O_7 + 0.25 \cdot Ca_2B_2SiO_7 \longrightarrow Ca_2Mg_{0.75}B_{0.5}Si_{1.75}O_7 \qquad \text{(Eq. 6.1)}$$

The same approach can be applied to a solid solution between hardystonite:okayamalite, as follows, replacing Mg with Zn atoms:

$$0.75 \cdot Ca_2ZnSi_2O_7 + 0.25 \cdot Ca_2B_2SiO_7 \longrightarrow Ca_2Zn_{0.75}B_{0.5}Si_{1.75}O_7 \qquad \text{(Eq. 6.2)}$$

6.2.2 Experimental

6.2.2.1 *Preparation of samples*

Solid solutions between hardystonite and okayamalite were shaped into reticulated scaffolds by means of a PowerWASP orienting extruder (Massa Lombarda, Italy), expressly equipped with a syringe to print the preceramic ink, consisting of silicone pastes incorporating fillers. The syringe of the feeding system was filled with the preceramic paste and scaffolds were later printed with conical nozzle (with a diameter of 0.41 mm, Nordson EFD, Westlake, Ohio) immersed in vegetal oil, thus preventing the premature drying of the solvent, that would have affected the viscosity of the ink. The configuration of the printing system and the final result have been reported in Fig. 4.2 in §4.2.6.

The starting materials for the realization of the printable silicone-based mixture were a solid silicon (MK, Wacker-Chemie GmbH, München, Germany), nano-sized fumed SiO_2 (Aerosil R106, Evonik Germany), $CaCO_3$ (Industrie Bitossi, Vinci, Italy), nano-sized ZnO (Sigma–Aldrich Ltd., Gillingham, UK) and colemanite ($CaB_3O_4(OH)_3 \cdot H_2O$), which was dehydrated at 420 °C for 2 hours.

Fumed silica nano-sized powders were wet mixed with MK in isopropanol (11 ml for 17 g of silica precursors) by means of a ball mill (60 min at 100 rpm, Pulverisette 7 planetary planetary ball mill, Fritsch, Idar-Oberstein, Germany). $CaCO_3$ micro-sized powders, ZnO nano-sized powders and colemanite were subsequently incorporated into the polymer and again mixed (4 h at 400 rpm), to obtain a perfectly homogenous suspension with very fine fillers and no trace of powder aggregates. The achievement of such properties was extremely necessary for the direct ink writing, due to the need to avoid clogging throughout the printing step and to have continuity in the fluid flow through the nozzle.

Following the CAD file, scaffolds were in the form of prisms with dimensions of 15 mm x 5 mm x 5 mm, as resulting from the overlapping of cylindrical rods, periodically arranged along x and y axes. The rods were in a stacking density of 11 rods/cm on the x-y plane and the distance between the longitudinal axes of adjacent rods was of 1 mm. The spacing between adjacent rods along the z axis was set at 350 µm for samples.

After removal from the oil, printed scaffolds were cross-linked at 350 °C, with a heating rate of 0.5 °C/min and dwelling time of 1 h, prior to ceramization at 950 °C.

All the experiments were done in collaboration with Mr. Mirko Sinico and Mr. Hamada Elsayed (University of Padova).

6.2.2.2 *Characterization of samples*

Microstructural characterizations were performed by scanning electron microscopy (FEI Quanta 200 ESEM, Eindhoven, The Netherlands). The crystalline phases were identified by means of X-ray diffraction on powdered samples (XRD; Bruker AXS D8 Advance, Bruker, Germany), supported by data from PDF-2 database (ICDD-International Centre for Diffraction Data, Newtown Square, PA) and Match! program package (Crystal Impact GbR, Bonn, Germany). Quantitative phase analysis (QPA), based on the Rietveld method[36], was performed by Dr. Michele Secco (University of Padova), using TOPAS software (Bruker AXS, version 4.1, Karlsruhe, Germany), starting from XRD patterns collected on glass-ceramic powders, after mixing with zincite powders, operating as internal standard. The contents of crystalline and amorphous phases were determined using the combined Rietveld–RIR method[37].

6.2.3 Results

The theoretical result shown in Eq.6.2 was dismissed and, concerning the solid solution between hardystonite and okayamalite, the resulting material was a biphasic silicate comprising hardystonite

($Ca_2ZnSi_2O_7$) and wollastonite ($CaSiO_3$), surrounded by a glass phase consisting of CaB_2O_4, as represented by the following reaction:

$$0.75\cdot Ca_2ZnSi_2O_7 + 0.25\cdot Ca_2B_2SiO_7 \longrightarrow 0.75\cdot Ca_2ZnSi_2O_7 + 0.25\cdot CaSiO_3 + 0.25\cdot CaB_2O_4 \quad \text{(Eq. 6.3)}$$

According with this reaction, the mass ratio between hardystonite and wollastonite in the final ceramic would be equal to 8, while quantitative X-ray diffraction analysis based on Rietveld method demonstrated a mass ratio of 10 (hardystonite 90 wt%, wollastonite 9 wt% and quartz 1wt%), which is illustrative of a predominance of hardystonite. This might be probably due to a partial incorporation of B atoms in the lattice of hardystonite, which is also suggested by the slight shift of the hardystonite peaks (pattern b) in comparison with the reference pattern (pattern c) of hardystonite (PDF#72-1603), as displayed in Fig. 6.10. It should be remarked that the shift is not constant for each peak, proving a deformation of the lattice due to the incorporation of B atoms and excluding a lack of precision in powders preparation prior to the analysis. Moreover, in Fig. 6.10 the pattern of a solid solution following a molar balance hardystonite:okayamalite of 0.5:0.5 is reported (pattern a). As visibile, the shift becomes even more pronounced for higher amounts of okayamalite.

A similar shift was observed by Veròn[38] regarding solid solutions between gehlenite ($Ca_2Al_2SiO_7$) and okayamalite, due to the modification of the reticular parameters of the gehlenite lattice because of the substitution of Al atoms with B atoms.

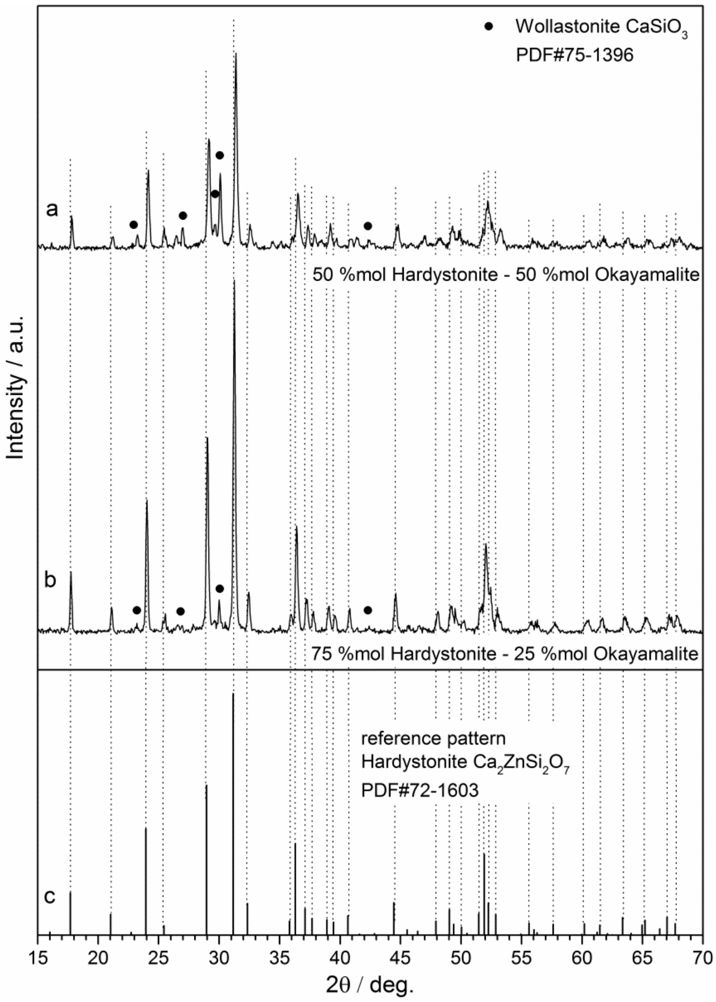

Fig. 6.10 X-ray diffraction pattern of hardystonite-okayamalite: a) 0.5:0.5 mol, b) 0.75:0.25 mol, c) hardystonite reference pattern.

Fig. 6.11 shows SEM images of hardystonite-okayamalite scaffolds following a molar balance of 0.75:0.25, in the form of 3-D printed scaffolds, after ceramization. As visible, the formulation did not exhibit viscous collapse and perfectly maintained the reticulated structure after ceramization (Fig. 6.11a-b). Moreover, a good mutual interfusion between adjacent layers of rods was observed (Fig. 6.11c), as well as an extensively porous morphology of the rods (Fig. 6.11d). Even though the scaffolds were found to suffer cracking, the result seemed to be improved in comparison with analogous samples in pure hardystonite previously developed by Mr. Hamada Elsayed (University of Padova). This might be due to a positive effect on the viscosity of the silicone-based mixture during the printing step and to the formation of liquid phase (glass phase after cooling) which could help to relax, by viscous flow or by enhancing the diffusion phenomena, the tensions related to the conversion to ceramic Further improvements of the rods morphology and the mechanical characterization of the samples are still in progress.

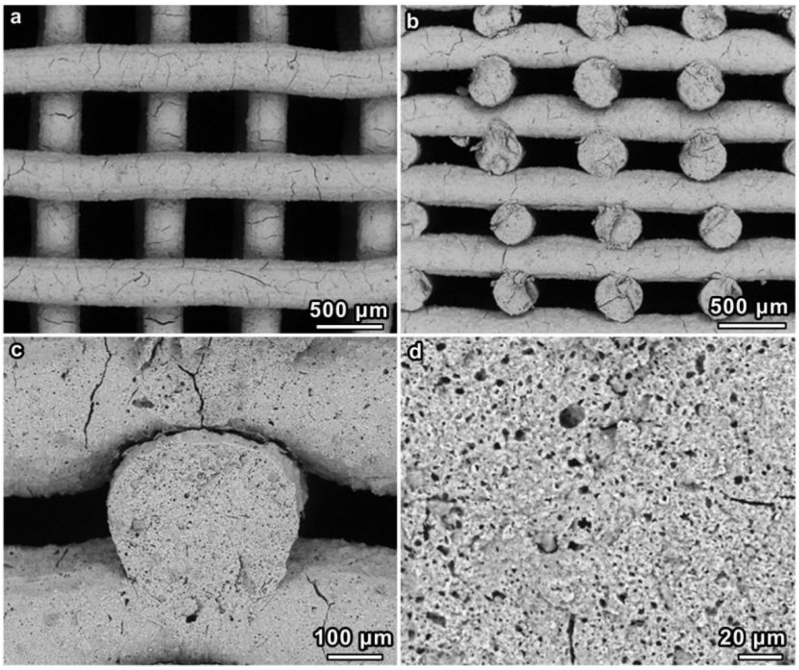

Fig. 6.11 SEM micrographs of ceramized hardystonite-okayamalite:
a) top view, b) side view, c) detail of a rod cross-section, d) higher magnification of cross-section.

6.2.4 Conclusions

A biphasic ceramic comprising hardystonite and wollastonite was fabricated starting from a molar balance of 0.75:0.25 between two melilites: a Ca-Zn melilite named hardystonite and a Ca-B melilite named okayamalite, respectively. This phase assemblage was surrounded by a Ca-borate glass phase.

The partial substitution of Zn with B atoms was suggested by the X-ray diffraction patterns, implying the potential formation of a solid solution between the two melilites.

The formulation was 3-D printed by direct ink-writing and the so-obtained reticulated structures exhibited an improved morphology in comparison with analogous scaffolds made of pure hardystonite.

The presence of cracks was slightly reduced thanks to an improved rheological behaviour of the silicone-based mixtures incorporating colemanite (as a CaO and B_2O_3 precursor) and to an enhanced stress relaxation provided by the formation of a liquid phase, later solidified in a glass phase, by viscous flow and diffusion.

References

[1] Greil P. Polymer derived engineering ceramics. Adv Eng Mater 2000;6:339–48.

[2] Colombo P, Mera G, Riedel R, Soraràù GD. Polymer-derived-ceramics: 40 years of research and innovation in advanced ceramics. J Am Ceram Soc 2010;93:1805–37.

[3] http://doktori.bme.hu/bme_palyazat/2014/honlap/Vigh_Tamas_en.htm

[4] Saha, A., Raj, R., Williamson, D. L. (2006). A Model for the Nanodomains in Polymer-Derived SiCO. Journal of the American Ceramic Society, 89(7), 2188-2195.

[5] Xie, Y., Li, H., Zhang, C., Gu, X., Zheng, X., Huang, L. (2014). Graphene-reinforced calcium silicate coatings for load-bearing implants. Biomedical Materials, 9(2), 025009.

[6] Mehrali, M., Moghaddam, E., Shirazi, S. F. S., Baradaran, S., Mehrali, M., Latibari, S. T., Osman, N. A. A. (2014). Synthesis, Mechanical Properties, and in Vitro Biocompatibility with Osteoblasts of Calcium Silicate–Reduced Graphene Oxide Composites. ACS applied materials & interfaces, 6(6), 3947-3962.

[7] Shuai C, Liu T, Gao C, Feng P, Peng S. "Mechanical Reinforcement of Diopside Bone Scaffolds with Carbon Nanotubes." International journal of molecular sciences 15.10 (2014): 19319-19329.

[8] http://www.crystecpharma.com/

[9] Eckert C, Knutson B, Debenedetti P. Supercritical fluids as solvents for chemical and materials processing. Nature 1996;383:313–83.

[10] http://doktori.bme.hu/bme_palyazat/2014/honlap/Vigh_Tamas_en.htm

[11] Nalawade SP, Picchioni F, Janssen LPBM. Supercritical carbon dioxide as a green solvent for processing polymer melts: processing aspects and applications. Prog Polym Sci 2006;31:19–43.

[12] Cooper AI. Synthesis and processing of polymers using supercritical carbon dioxide. J Mater Chem 2000;10:207–34.

[13] Tomasko DL, Li HB, Liu DH, Han XM, Wingert MJ, Lee LJ, Koelling KW. A review of CO_2 applications in the processing of polymers. Ind Eng Chem Res 2003;42:6431–56.

[14] Kazarian SC. Polymer processing with supercritical fluids. Polym Sci 2000;42:78–101.

[15] Sauceau, M., Fages, J., Common, A., Nikitine, C., Rodier, E. (2011). New challenges in polymer foaming: a review of extrusion processes assisted by supercritical carbon dioxide. Progress in Polymer Science, 36(6), 749-766.

[16] E. Bernardo, J-F. Carlotti, P. M. Dias, L. Fiocco, P. Colombo, L. Treccani, U. Hess, K. Rezwan, Novel akermanite-based bioceramics from preceramic polymers and oxide fillers, Ceram. Int 40 (2014) 1029–1035.

[17] H.M. Rietveld, A profile refinement method for nuclear and magnetic structures. Journal of Applied Crystallography 2 (1969) 65-71

[18] Gualtieri AF. Accuracy of XRPD QPA using the combined Rietveld–RIR method. Journal of Applied Crystallography (2000) 33:267–278.

[19] Bernardo, E.; Parcianello, G.; Colombo, P.; Matthews, S. Wollastonite foams from an extruded preceramic polymer mixed with $CaCO_3$ microparticles assisted by supercritical carbon dioxide. Adv. Eng. Mater. 2013, 5, 60–65

[20] R.H. Baney, M. Itoh, A. Sakakibara, and T. Suzuki, “Silsesquioxanes,” Chem. Rev., 95 [5] 1409–1430 (1995).

[21] F. Vivier, D. Santamaria, D. Pellerej, P. Buonfico, and M. Sangermano, “A Kinetic Analysis of a Thermal Curing Reaction of a Silicon Resin in Solid State”; pp. 63–72 in Charact. Miner. Met. Mater. 2014. Edited by J.S. Carpenter, C. Bai, J.-Y. Hwang, S. Ikhmayies, B. Li, S.N. Monteiro, Z. Peng and M. Zhang. John Wiley & Sons, Inc., 2014.

[22] D. Yang, W. Zhang, and B. Jiang, “Ceramization and oxidation behaviors of silicone rubber ablative composite under oxyacetylene flame,” Ceram. Int., 39 [2] 1575–1581 (2013).

[23] Colombo, P., Mera, G., Riedel, R., Sorarù, G. D. (2010). Polymer-Derived Ceramics: 40 Years of Research and Innovation in Advanced Ceramics. Journal of the American Ceramic Society, 93(7), 1805-1837.

[24] Shuai, C., Liu, T., Gao, C., Feng, P., Xiao, T., Yu, K., & Peng, S. (2016). Mechanical and structural characterization of diopside scaffolds reinforced with graphene. Journal of Alloys and Compounds, 655, 86-92.

[25] Jones, J. R., Lee, P. D., Hench, L. L. (2006). Hierarchical porous materials for tissue engineering. Philosophical Transactions of the Royal Society of London A: Mathematical, Physical and Engineering Sciences, 364(1838), 263-281.

[26] http://www.cambridge.org/us/academic/subjects/engineering/materials-science/cellular-solids-structure-and-properties-2nd-edition

[27] A. Bignon, J. Chouteau, J. Chevalier, G. Fantozzi, J.-P. Carret, P. Chavassieux, G. Boivin, M. Melin, D. Hartmann, "Effect of micro- and macroporosity of bone substitutes on their mechanical properties and cellular response," J. Mater. Sci. Mater. Med., 14 [12] 1089–1097 (2003).

[28] O. Chan, M.J. Coathup, A. Nesbitt, C.-Y. Ho, K.A. Hing, T. Buckland, C. Campion, and G.W. Blunn, "The effects of microporosity on osteoinduction of calcium phosphate bone graft substitute biomaterials," Acta Biomater., 8 [7] 2788–2794 (2012).

[29] M. Scheffler, T. Gambaryan-Roisman, T. Takahashi, J. Kaschta, H. Muenstedt, Buhler and P. Greil, "Pyrolytic decomposition of preceramic organo polysiloxanes",Innovative Processing and Synthesis of Ceramics, Glasses, and Composites IV:Ceramic Transactions, 115 239–250 (2000).

[30] Plachký, T., Lenčéš, Z., Hric, Ľ., Šajgalík, P., Baláž, P., Riedel, R., Kleebe, H. J. (2010). Processing and mechanical properties of Si_3N_4 composites employing polymer-derived SiAlOC as sintering aid. Journal of the European Ceramic Society, 30(3), 759-767.

[31] Renlund, G. M., Prochazka, S., Doremus, R. H. (1991). Silicon oxycarbide glasses: Part II. Structure and properties. Journal of Materials Research, 6(12), 2723-2734.

[32] White, A. A., Best, S. M., & Kinloch, I. A. (2007). Hydroxyapatite–carbon nanotube composites for biomedical applications: a review. International Journal of Applied Ceramic Technology, 4(1), 1-13.

[33] Warren, B. E. (1930). Zeitschrift Fur Kristallographie, 74, 131.

[34] Burzo, E. (2005). Melilites and related silicates. Magnetic Properties of Non-Metallic Inorganic Compounds

[35] Chihara, H., Koike, C., Tsuchiyama, A. (2007). Compositional dependence of infrared absorption spectra of crystalline silicates-III. Melilite solid solution.Astronomy & Astrophysics, 464(1), 229-234.

[36] H.M. Rietveld, A profile refinement method for nuclear and magnetic structures. Journal of Applied Crystallography 2 (1969) 65-71

[37] Gualtieri AF. Accuracy of XRPD QPA using the combined Rietveld–RIR method. Journal of Applied Crystallography (2000) 33:267–278.

[38] Véron, E. (2011). Synthèse et étude structurale de la gehlénite au bore Ca_2Al_2-xBxSiO_7: mécanisme de substitution B/Al et ordre local (Doctoral dissertation, Université d'Orléans).

7 Novel wollastonite-apatite composite

7.1 Introduction

Wollastonite-apatite glass-ceramics are widely recognized as highly efficient biomaterials[1-3]. The usual approach for their synthesis is based on conventional vitrification followed by controlled crystallization, with two main disadvantages: a complex thermal treatment is normally required and the apatite phase corresponds more specifically to fluorapatite, rather than to natural apatite[4-6].

An alternative and more recent route for the fabrication of A-W ceramics is offered by preceramic polymers. This strategy involves the use of a silicone resin as silica source, filled with active and passive fillers. Calcium carbonate, as active filler, decomposes to CaO, in turn reacting with the silica derived from the oxidative decomposition of silicones; hydroxyapatite powders remain practically inert (passive), but contribute positively to both structural integrity and biocompatibility of the final ceramic[7]. The approach based on preceramic polymers not only allows for highly phase pure ceramics, despite low processing temperatures, but has the fundamental advantage of combining synthesis and shaping.

$CaCO_3$ is not only a valid CaO precursor for polymer-derived wollastonite, but also can be considered by itself as the major phase in biomaterials, in form of foams and microspheres, in turn referring to various polymorphs (calcite, aragonite, vaterite)[8-10]. Calcite-based ceramics can be transformed into carbonate apatite ceramics by a phosphatization treatment, i.e. by immersion in a Na_2HPO_4 aqueous solution. Carbonate apatite is actually more similar to natural apatite[1] favoring integration with bone, but several problems still remain. First, obtaining calcite-based materials is quite complicated, considering the low decomposition temperature (e.g. foams are obtained by infiltration of PU foams with calcium hydroxide, later subjected to carbonation)[8,9]; second, the mechanical properties of these particular ceramics are quite low (e.g. the compressive strength of foams is in the order of kPa)[8]. Stronger materials can be obtained only using very specific firing conditions (e.g. CO_2 atmosphere)[11].

Here, the aim was to fabricate a material with the mechanical properties of porous wollastonite, to improve on the mechanical strength of previous foam-like 3-D scaffolds, while maintaining bioactivity and interconnected pore network for cell and tissue ingrowth. The route chosen was to develop a composite material through polymer-derived-ceramic methodology for synthesizing and shaping the scaffolds and a novel phosphatization treatment for developing an hydroxyapatite coating, prior to ceramization.

Part of this work was carried out at Imperial College London under the supervision of Prof. J. R. Jones, during a 6-months student exchange program in 2014. The results were submitted for publication in 2015 by Fiocco *et al.*

7.2 Experimental

7.2.1 Preparation of foams

A commercially available liquid silicone, H62C (Wacker-Chemie GmbH, Munich, Germany), was used as silica source. The polymer was first dissolved in isopropanol (10 g in 15 ml) and then mixed with the fillers, which consisted of micro-sized powders. CaO was provided by $CaCO_3$, in form of microparticles (<10 µm, Industrie Bitossi, Vinci, Italy). Dicarbamoylhydrazine (DCH, Alfa Aesar GmbH, Germany) was added to act as the foaming agent (2 wt% in overall ceramic residue), being subjected to decomposition at approximately 250 °C.

All the other chemicals and reagents were purchased from Invitrogen/ Life Technologies Ltd. (Paisley, UK) and Sigma-Aldrich (Gillingham, UK).

Concerning the foam synthesis, the balance between the two main constituents (CaO precursor:silicon) was fixed at the stoichiometric CaO:SiO_2 molar ratio equal to 0.8 and 1.6 (the specific ratio for wollastonite is CaO:SiO_2=1). The mixing was performed by magnetic stirring and ultrasonication for one hour in total, which resulted in stable and homogeneous dispersions. The preceramic mixture was later cast in large glass containers and left to dry overnight at 60 °C.

After drying, the H62C-based mixtures were in the form of pastes, fluid enough to be poured into cylindrical Al moulds, where they were subjected to a foaming treatment at 350 °C in air (samples were placed directly in oven, for 30 min). Cylindrical foam samples (approximately 15 mm in diameter and 30 mm in height) were obtained upon foaming. Smaller samples (10 mm diameter and 10 mm height) were cut from bigger ones and manually polished with abrasive paper.

The foams were thermally treated at 700 °C for 1 h, using a heating rate of 5 °C/min. The ceramized samples were later immersed in a 1 mol/L Na_2HPO_4 phosphatizing solution at 60 °C for 14 days, in order to have some of the outer $CaCO_3$ phosphatized[8,9]. Finally, the samples were subjected to a reactive ceramization up to 900 °C for 1 h, using a heating rate of 1 °C/min.

7.2.2 Characterization of foams

The bulk density of the foams was determined using a caliper and a digital balance. The skeletal density was measured on foams, using a He gas pycnometer (Micromeritics AccuPyc 1330, Norcross, GA).The percentage of porosity was then calculated using the following equation: $\%P=1-(\rho_b/\rho_s)$; where ρ_b was the bulk density and ρ_s was the skeletal density.

Mercury intrusion porosimetry (PoreMaster 33, Quantachrome UK) was used to determine the pore interconnect size distribution.

Optical stereomicroscopy (AxioCam ERc 5s Microscope Camera, Carl Zeiss Microscopy, Thornwood, New York, US) on foams and scanning electron microscopy (JSM 6010 L, JEOL USA; LEO GEMINI 1525 FESEM, LEO electron microscopy, Thornwood, New York, USA) on gold-coated specimens were used to examine the morphological and textural features of the samples.

The phase identification was performed by means of X-ray diffraction (XRD; Bruker AXS D8 Advance, Bruker, Germany – CuKα radiation, 0.15418 nm, 40 kV-40 mA, 2θ=15-70°, step size=0.05°, 2s counting time), supported by data from PDF-2 database (ICDD-International Centre for Diffraction Data, Newtown Square, PA) and Match! programme package (Crystal Impact GbR, Bonn, Germany).

The compressive strength of foams was measured at room temperature, using an Instron 1121 UTM (Instron Danvers, MA), equipped with a 10 kN load cell, with a crosshead speed of 1 mm/min. The mean value of five to ten samples was used for each data point.

7.2.3 Bioactivity test

Foams with weight of 37.5 mg were immersed in 25 ml of simulated body fluid (SBF) at 37 °C and 120 rpm for 1, 2, 4, 8, 24, 72, 168, 336, 504 h[12]. At each time point, the pH was measured and samples of 1 ml of the medium were taken and refreshed. After dilution with 9 ml of 2M HNO_3, the reacted medium was analyzed by inductive coupled plasma (ICP) spectroscopy for Si, Ca, P concentration in solution. All the experiments were done in triplicate.

At the end of the test, the foams were washed in distilled water, dried and analyzed by attenuated reflectance Fourier transform infrared spectroscopy (ATR-FTIR) at room temperature, to monitor the growth of the HCA layer, using a wavenumber resolution of 4 cm^{-1} for 32 scans from 4000 to 600 cm^{-1}. Samples were also imaged under scanning electron microscopy (SEM).

7.2.4 Cell culture test

MC3T3 osteoblast precursor cells were culture expanded to confluence in monolayer cultures in basal media (α-MEM supplemented with 10% (v/v) FCS, 100 unit/ml penicillin, 100 μg/ml streptomycin). Cultures were maintained in humidified atmosphere at 37 °C, 5% CO_2 and 21% O_2. Foams were cut to 37.5 mg of weight (the size was approximately 5×5×5 mm^3) and sterilised with 70% EtoH, then washed with PBS and then plain α-MEM. MC3T3 cells were harvested at confluence from monolayer cultures and suspended in basal media at a concentration of 1×10^6 cells in 25 ml. 25 ml of cell suspension was added to each sterile 50 ml Falcon tube containing one foam 3-D scaffold. The tubes were placed in an incubator (humidified atmosphere at 37 °C, 5% CO_2 and 21% O_2) for 2 h with gentle agitation every 30 minutes to allow diffused cell adhesion. The solution was then replaced with osteogenic media (basal α-MEM supplemented with 100 μM ascorbate-2-phosphate, 10 nM dexamethasone and 10 mM of β-glycerophosphate). Cell-seeded foams were cultured in humidified atmosphere at 37 °C, 5% CO_2 and 21% O_2 for 21 days with media changes every 3-4 days. 1 ml of culture medium was collected prior to each media change for ICP analysis of Si, Ca and P concentrations for dissolution study in cell culture medium.

Cell viability of MC3T3 cells cultured in the 3-D foams was determined by colorimetric WST-1 assay, which is based on the cleavage of the water-soluble tetrazolium salt WST-1 to formazan by mitochondrial dehydrogenases in metabolically active cells. Three day-3 cell-seeded foams were collected and each submerged in 5 ml of WST-1 reagent (1:10 dilution in α-MEM, Roche Diagnostic, West Sussex, UK). 100 μl was aspirated in triplicate from each sample following 2 and 4 hours incubation and, the optical density was measured spectrophotometrically at 440 nm using a SpectraMax M5 microplate reader. The mean optical densities values (n=3) of the solution were calculated at 2 and 4 hours time points and compared using Mann-Whitney U test with b Bonferroni correction. Cells were deemed viable if an increase in optical density of the solution was observed.

Cell-seeded foams were fixed with 4% (w/v) paraformaldehyde (PFA) and used for immunohistochemical analysis of cell attachment (day-3 samples) and osteogenic differentiation (day-21 samples). After permeabilisation with buffered 0.5% (v/v) Triton X-100 in PBS (300 mM sucrose, 50 mM NaCl, 3 mM $MgCl_2$, 20 mM Hepes and pH 7.2) and blocking with 10 mg/ml BSA in PBS, samples were incubated with relevant primary antisera (diluted appropriately using 10 mg/ml BSA in PBS) at 4 °C overnight. This was followed by hour-long incubation with Alexa Fluor® 488-conjugated secondary antibody. Negative controls (omission of the primary antisera) were performed in all immunohistochemistry procedures. No staining was observed in the samples used as negative controls.

The anti-Vimentin antibody (rabbit polyclonal, IgG, Abcam, Cambridge, UK), anti-Collagen Type I antibody (rabbit polyclonal, IgG, Abcam, Cambridge, UK), anti-Osteopontin antibody (rabbit polyclonal, IgG, Merck Millipore, Watford, UK) and anti-Osteocalcin antibody (rabbit polyclonal, IgG, Merck Millipore, Watford, UK) were used at dilutions of 1:500, 1:1000, 1:500 and 1:50 respectively. Alexa Fluor® 488-conjugated secondary antibody (goat anti-rabbit, IgG, Abcam, Cambridge, UK) was used at a dilution of 1:1000.

F-actin was labelled using CytoPainter F-actin staining kit (Abcam, Cambridge, UK) following the manufacture's instruction. Briefly, Alexa Fluor® 568-conjugated phalloidin (1:1000 dilution in labelling buffer) was added simultaneously with the secondary antibody during the incubation period. All samples were counter-stained with DAPI (0.1 μg ml^{-1} in PBS).

The samples were imaged under confocal microscopy. The same samples were then dehydrated using an ascending series of ethanol and hexamethyldisilazane (HDMS) prior to sputter coating with gold and observation under scanning electron microscopy.

Cell culture studies were performed by Dr. S. Li (Imperial College London).

7.3 Results

7.3.1 Characterization of samples

The molar ratio of CaO:SiO_2 was at first kept lower than that used for previous investigations on polymer-derived bioceramics based on wollastonite[8,13-14], in order to achieve dispersions with higher homogeneity and lower viscosity. Fig. 7.1a shows that the molar ratio of CaO:SiO_2=0.8 samples (F1) led to foams with very uniform pore size (mean diameter of 500 µm) and good interconnectivity (well defined openings are visible between adjacent cells). The porosity was provided by the thermal decomposition of the hydrazine additive below 350 °C. At this temperature, the cross-linking of the same polymer hindered any viscous collapse of the pore structure, which was finally stabilized by the ceramization at 700 °C. The samples from the mixture corresponding to a higher CaO:SiO_2 molar ratio (CaO:SiO_2=1.6 samples, F2) were much less uniform (Fig. 7.1b). For bone tissue engineering applications, the porosity, pore size and pore interconnectivity are critical parameters: in general, interconnected pores with a mean diameter of 100 µm or greater and open porosity higher than 50% are considered to be the minimum requirements to allow cell penetration, tissue ingrowth and eventually vascularisation[15]. The graph in Fig. 7.1c shows that the obtained foams had modal interconnect diameters of 161 µm (F1) and 135 µm (F2), matching the above mentioned constraints: for both formulations, most of the interconnected pores had diameters greater than 100 µm, as required for cell penetration and vascularisation.

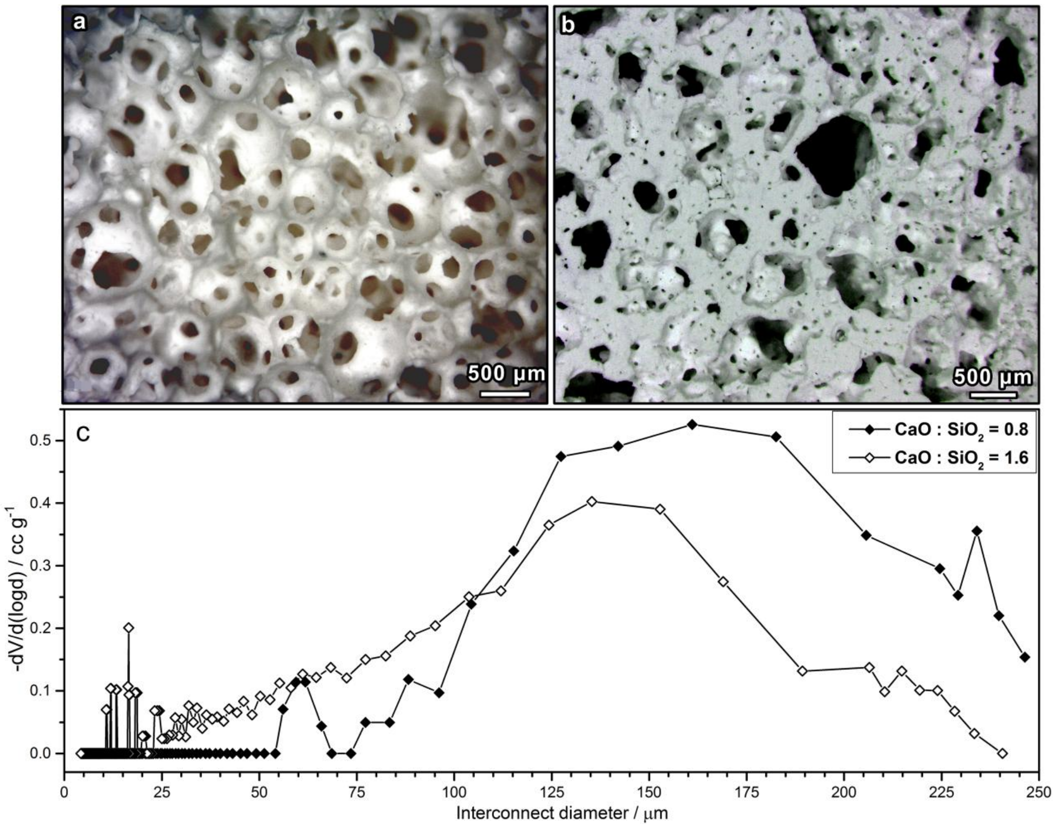

Fig. 7.1 Stereomicroscopy of scaffolds after phosphatization and pyrolysis at 900 °C in air of F1 (a) and F2 (b) samples, with details of interconnect size distribution (c).

Fig. 7.2 shows the phase evolution upon the three processing steps by XRD. After the first non-reactive ceramization at 700 °C, as expected, calcium carbonate did not decompose ($CaCO_3$ - PDF 86-2334) and the selected thermal treatment only caused the formation of an amorphous silica-rich matrix derived from the thermal decomposition of the preceramic polymer, for both formulations (see Fig. 7.2a and Fig. 7.2b). After phosphatization, calcium carbonate was partially transformed, again for both formulations. Weak peaks, in positions consistent with those of hydroxycarbonate apatite (HCA - PDF#04-0697), were visible, while the calcite peaks decreased in intensity. The weakness of the apatite peaks is reasonable, owing to the probable confinement of transformation at the calcite particle present at the surface of cell walls. The high width-to-height ratio of the apatite peaks, in addition, is reasonably due to the limited crystal size.

After the reactive ceramization at 900 °C, the weak peaks attributed to apatite content did not change, while calcium carbonate underwent complete decomposition and reacted with the surrounding silica-rich matrix, with formation of mixed calcium silicates (β-wollastonite, β-$CaSiO_3$ - PDF#420547; di-calcium silicate, β-Ca_2SiO_4 - PDF#83-0460) for both the formulations. Anyway, the balance between the two phases was different, with more peaks related to β-$CaSiO_3$ in F1 samples (Fig. 7.2a) and more related to β-Ca_2SiO_4 in F2 samples (Fig. 7.2b). Some cristobalite (SiO_2 - PDF#76-0936) traces were also visible in the two spectra at 900 °C, but the samples from CaO-poor formulation (Fig. 7.2a) showed a higher content.

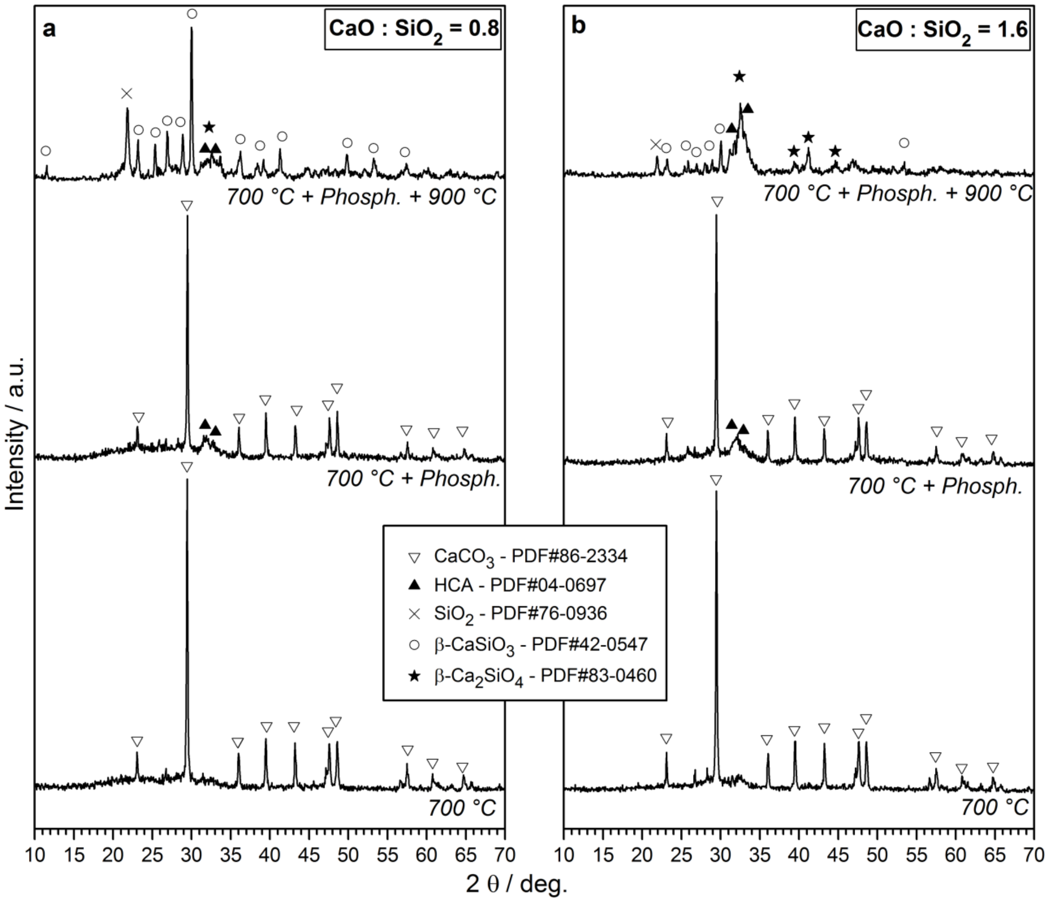

Fig. 7.2 XRD patterns of F1 (a) and F2 (b) scaffolds.

Further evidence of transformation of calcite into apatite as a consequence of the phosphatization treatment, is provided by a SEM micrograph reported in Fig. 7.3a (taken on a F1 sample that subjected to the complete 3-step treatment), which emphasized the formation of flower-like precipitates, a common morphology for hydroxyapatite. The EDS spectrum on the precipitates is reported in Fig. 7.3b and exhibited high P and Ca contents. The peak corresponding to Na was reasonably due to the presence of Na^+ ions in the phosphatizing solution, while the peaks associated with Au were the effect of the gold-sputter coating carried out before SEM imaging.

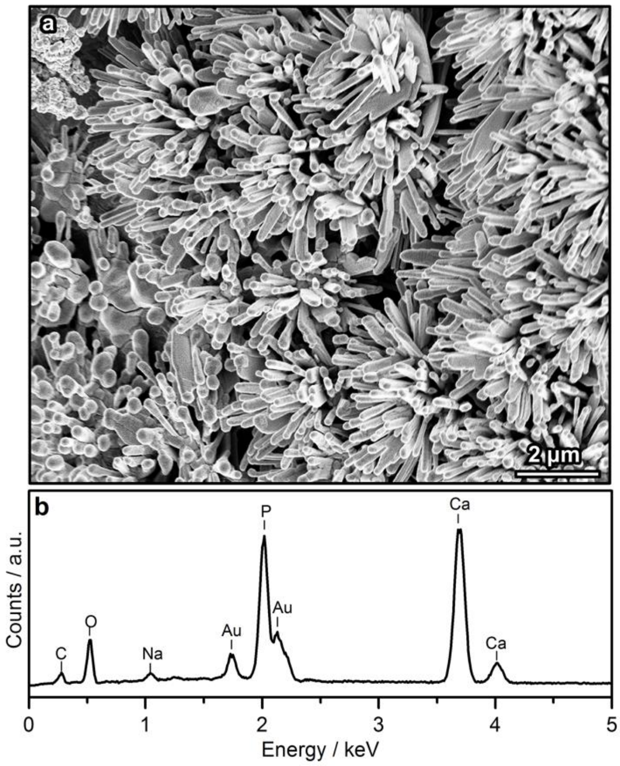

Fig. 7.3 SEM Micrograph of F1 foam scaffolds after the complete synthesis cycle (a) with EDS spectrum on the apatite formed on the scaffold surface (b).

Tab. 7.1 Physical and mechanical properties of foams at different steps of the synthesis cycle.

Foam formulation	ρ_{bulk} (g/cm^3)	$\rho_{skeletal}$ (g/cm^3)	P_{open} (%)	σ_{comp} (MPa)
$CaO:SiO_2$=0.8 [F1] 700 °C	0.34 ± 0.09	2.54 ± 0.01	87	1.6 ± 0.2
$CaO:SiO_2$=0.8 700 °C + Phosph.	0.37 ± 0.07	2.31 ± 0.02	84	3.6 ± 0.8
$CaO:SiO_2$=0.8 700 °C + Phosph. + 900 °C	0.27 ± 0.02	2.85 ± 0.07	91	2.9 ± 0.5
$CaO:SiO_2$=1.6 [F2] 700 °C	0.68 ± 0.06	2.96 ± 0.05	64	1.5 ± 0.7
$CaO:SiO_2$=1.6 700 °C + Phosph.	0.80 ± 0.04	2.52 ± 0.01	68	1.0 ± 0.7
$CaO:SiO_2$=1.6 700 °C + Phosph. + 900 °C	0.96 ± 0.06	2.68 ± 0.01	77	1.6 ± 0.2

Tab. 7.1 summarises the mechanical and physical properties of the foams after each step of the treatment process, including the compressive strength σ_{comp}, the ρ_{bulk} density, the $\rho_{skeletal}$ and the open porosity P_{open}.

The differences in homogeneity, already observed with Fig. 7.1, had a significant impact on mechanical properties. F1 samples exhibited a compressive strength of 2.9 ± 0.5 MPa, despite the high porosity of 90 %. The compressive strength for F2 samples did not exceed 1.6 MPa, even if their porosity was lower at 77%. This compares to 2.4 MPa for sol-gel bioactive glass foams (porosity of 82 %, modal interconnect diameter of 98 μm)[16] and 1.9 MPa for melt-derived bioactive gel-cast foams (79 % porosity, modal interconnect size of 144 μm)[17].

7.3.2 Bioactivity test

The behaviour of the foam scaffolds in SBF was investigated in order to monitor the surface reactions of the material, the dissolution profiles and the pH change as a function of time. Fig. 7.4 shows the elemental concentrations (from ICP) of calcium (Fig. 7.4a), silicon (Fig. 7.4b) and phosphorous (Fig. 7.4c) in SBF, as a function of immersion time for the scaffolds, with a control of pure SBF. The error bars are standard deviations from the mean calculated from triplicate results. The pH change as a function of time is shown in Fig. 7.4d. Soluble silica and calcium ions were released from the scaffolds and phosphate deposited on the scaffolds over time.

SBF contains approximately 80 μg ml^{-1} of calcium ions. The calcium content of the control SBF was constant concentration at around 72 μg ml^{-1}. Concerning the release profile of Ca^{2+} ions from the foams (Fig. 7.4a), the concentration of Ca in SBF increased and reached plateau at saturation concentration of 249 μg ml^{-1} after 7 days. The Ca concentrations, however, decreased slightly as the soaking time increased from 7 days to 21 days, reaching 225 μg ml^{-1} after 21 days. This was likely caused by calcium phosphate deposition on the scaffold surface after 7 days immersion.

SBF does not contain Si, as proven by the control (Fig. 7.4b). After immersion of F1 samples in SBF for 24 h, the Si species increased to 57 μg ml^{-1}. From 24 h to 72 h, the concentration of Si species increased to 72 μg ml^{-1}, but with a slower rate of Si release, as the solution neared saturation. From 72 h to 21 days, the amount of Si found in SBF was maintained at approximately 70 μg ml^{-1}.

With respect to phosphorous (Fig. 7.4c), SBF contains around 30 μg ml^{-1}. The control SBF showed levels of P between 28 and 24 μg ml^{-1} up to 21 days immersion. In contrast, when foams were immersed in SBF, the P concentration rapidly decreased to 2 μg ml^{-1} after 72 h. Phosphorous was expected to be released by foams due to the phosphatising step of the synthesis cycle. The formation of a HCA layer on the scaffolds surface, as shown by FTIR spectra (Fig. 7.5), was likely the reason for decreased P concentration in SBF (coupled with the decrease in Ca content).

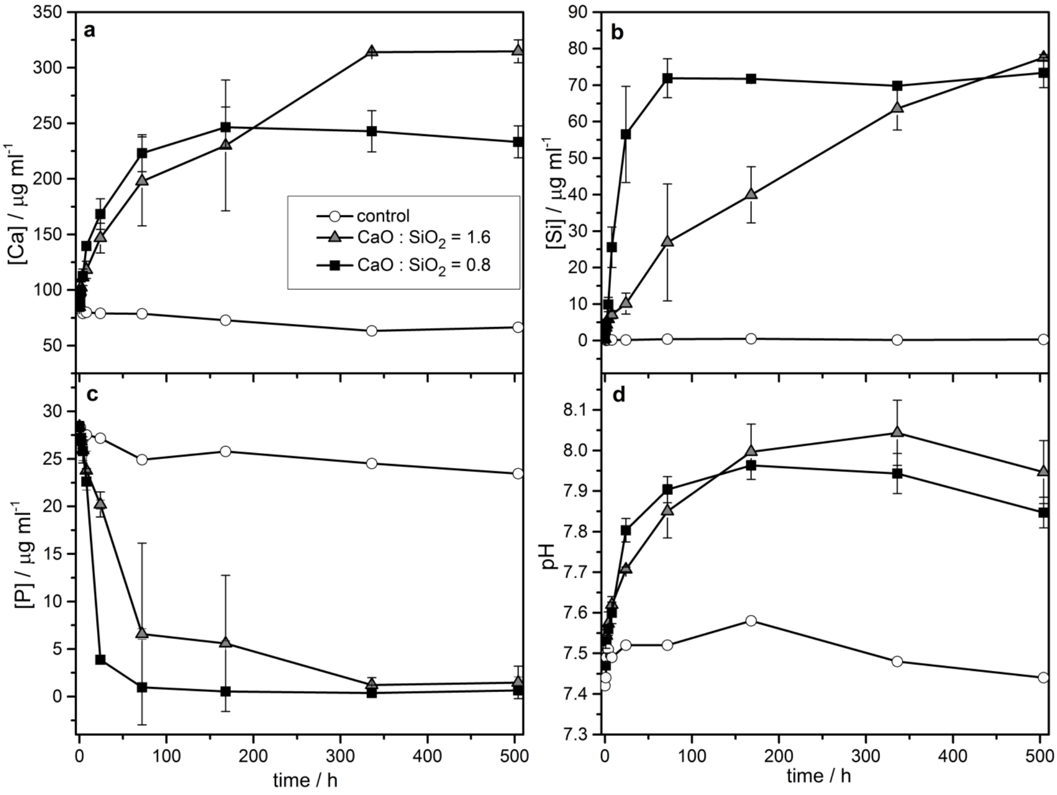

Fig. 7.4 Dissolution profiles (a: Ca; b: Si; c: P) and pH (d) as a function of time for foams after soaking in SBF for 21 days [results are presented as mean ± SD, n=3 per each time point].

The dissolution of the foams caused the pH of the medium to increase from 7.42 to 7.75 over 1 week, as shown in Fig. 7.4d. Then it increased to 7.85 between 1 week and 3 weeks.

For F2 samples, the trend of Ca, P, Si content of the SBF as a function of time was similar, but with some differences in the µg ml^{-1} levels and in the dissolution rate. The amount of Ca species released was higher, reaching 320 µg ml^{-1} after 2 weeks (see Fig. 7.4a). The release rate for Si species was slower in comparison to the previous material and the rate was almost linear from 72 h to 3 weeks, finally reaching 75 µg ml^{-1} (Fig. 7.4b). The precipitation rate of P species was also slower, however P was mostly removed by 2 weeks (Fig. 7.4c). The pH trend was similar to that for F1 samples. The highest value of 8 was reached after 2 weeks, after which the pH decreased to 7.95 between 2 weeks and 3 weeks. The initial rapid dissolution did not appear detrimental, since the pH fluctuation was within the buffering capability of culture medium.

Fig. 7.5 compares FTIR (Fig. 7.5a) spectra and XRD (Fig. 7.5b) patterns of the samples before and after 3 week immersion in SBF. For unreacted samples of both formulations, the FTIR spectra contained vibration bands at 510, 900 and 1010 cm^{-1} which can be reasonably associated with wollastonite ($CaSiO_3$).[18] The same peaks were not detected in the FTIR spectra for the samples after soaking in SBF, meaning that wollastonite was progressively subjected to decomposition in SBF, in agreement with the calcium release (Fig. 7.5). This is also confirmed by the XRD patterns (Fig. 7.5b), which showed silica, HAp, HCA, Ca_2SiO_4 peaks for the samples after soaking in SBF (Ca_2SiO_4 only for F2 samples), but no wollastonite.

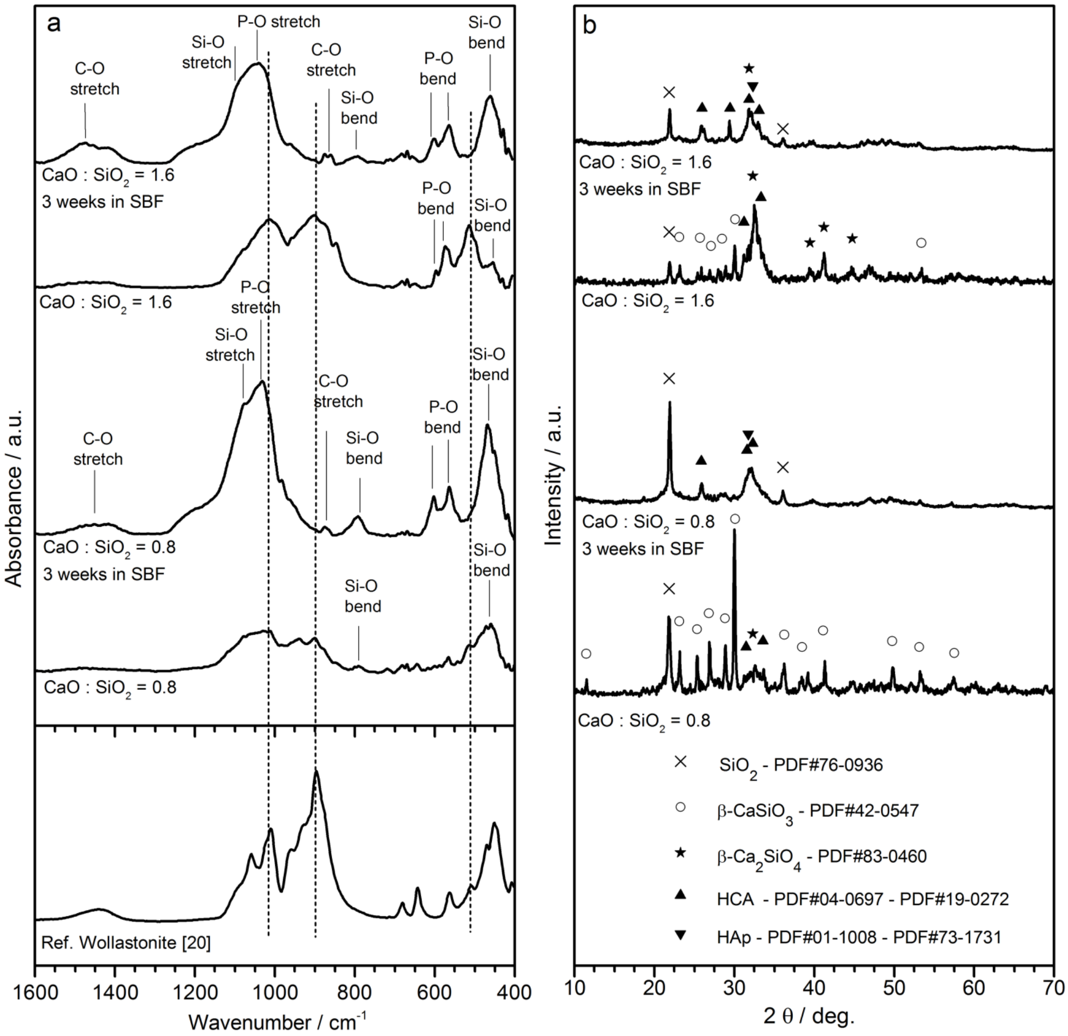

Fig. 7.5 FTIR and XRD spectra of ceramic foams before and after soaking in SBF for 21 days.

For ceramics of both compositions, the FTIR spectra contained vibrational bands at 567 and 603 cm^{-1}, corresponding to the P-O υ_4 bending vibrations, and at 1040 cm^{-1}, corresponding to the P-O υ_3 stretching vibrations. Vibrational bands were also observed for carbonate ions at 1400-1600 cm^{-1}, corresponding to the carbonate υ_3 vibrational mode, and at 873 cm^{-1}, corresponding to υ_2. All of them can be associated with the presence of crystalline HCA[19-21], which can also be correlated with the peaks in the XRD patterns.

Si-O absorption bands were observed in the FTIR spectra at 1080, corresponding to the stretching vibrations, and at and 800 and 460 cm^{-1}, corresponding to the bending vibrations[16,22]. In particular, the peak at 800 cm^{-1} is present before and after soaking for F1 samples, but only after soaking for F2 samples, while the peak at 460 cm^{-1} and at 1080 cm^{-1} increased in intensity for both the formulations after soaking. All these peaks are probably related to the presence of silica: in fact, considering the XRD patterns, SiO_2 is present in all the samples and, in particular, the intensity of its peaks is even higher after soaking, but it is notably lower for F2 unreacted samples.

These results are likely in agreement with Siriphannon *et al.*[20]: the mechanism of HAp formation on $CaSiO_3$ was hypothesized to involve its initiation from a rapidly-formed silica-rich interlayer, followed by the formation of an amorphous calcium phosphate layer resembling HAp, by reaction of Ca^{2+} with PO_4^{3-} and OH^- ions from the SBF solution. After the prolonged soaking, the amorphous layer grows and crystallizes to HAp[20] with partial incorporation of CO_3^{2-}.

7.3.3 Cell culture study

After 3 days and 21 days of cell culture, the attachment of the cells to the scaffolds surface, the cell morphology and the formation of cell matrix were investigated by SEM imaging. After 3 days (Fig. 7.6a) the cells spread across the 3-D surface, formed a compact layer and colonized the pores, following the architecture of the pores, whereas after 21 days (Fig. 7.6b) the cells appeared to have formed mineralized bone nodules, in the form of white globular precipitates.

The CaO-rich samples (F2) seemed to enhance the cellular response, compared to F1 samples . After 3 days, the cells were spread across the surface and the interconnections demonstrating elongated profiles, as shown in Fig. 7.6d, even if they did not form compact layers of cells as in Fig. 7.6a. However, after 21 days of culture (Fig. 7.6e) they seemed to have more mineralized bone nodules. One explanation for this discrepancy in the cell morphology could be the higher content of calcium.

The EDS spectra in Fig. 7.6c (F1) and Fig. 7.6f (F2) were taken on the apparent bone nodules formed by the cells and on the scaffold surface adjacent to the cell groups (samples were previously coated with gold). The spectra on the cellular deposits show that calcium and phosphorous were present, confirming that mineralization occurred; the spectra on the scaffold surfaces adjacent to the cell groups shows that phosphorous and calcium content was much lower when compared with silicon.

Following 3 days of culture, WST-1 cell proliferation assay was used as a quantitative indication of total cell viability. The assay demonstrated a significant increase ($p<0.05$) in mean absorbance (i.e. optical density) for WST-1 solution mixed with both cell-seeded F1 and F2 constructs from 2 to 4 hours of incubation, suggesting excellent ongoing cell survival and growth (Fig. 7.7). Excessive mitochondrial Ca^{2+} uptake and accumulation can result in a switch from a useful physiological regulatory mechanism to a potentially harmful pathological pathway[23]. In this study, there was no significant difference in optical densities observed between the two material compositions at either the 2 or 4 h time point of the assay. Doubling the Ca^{2+} ions in F2 foams, therefore, did not raise concerns regarding the cellular toxicity. One possible explanation is the likely precipitation of calcium in the form of calcium phosphates, limiting the Ca^{2+} ions in cell culture media.

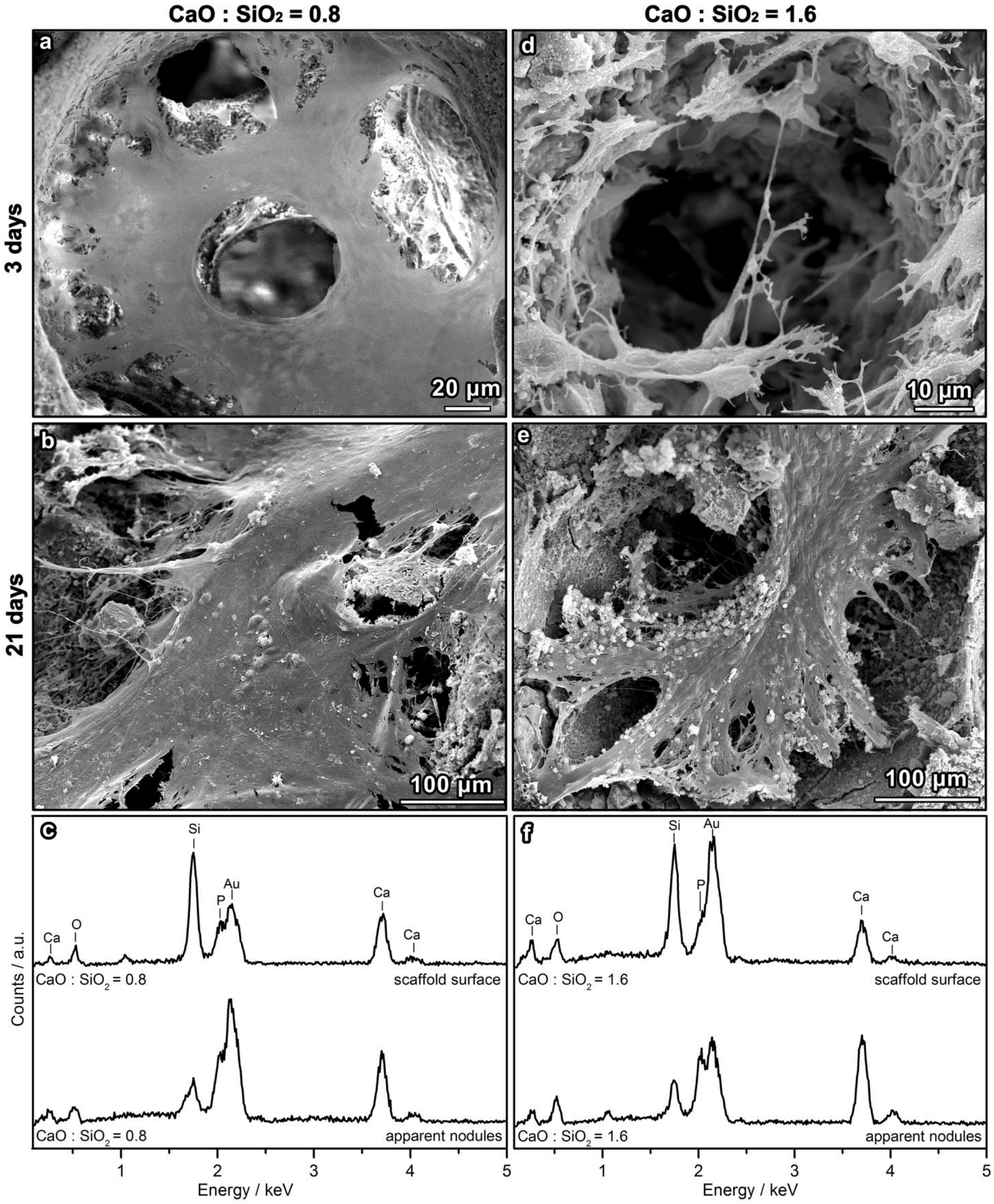

Fig. 7.6 SEM micrographs of MC3T3 cells following culture on the scaffolds with details of EDS spectra on surfaces adjacent to the cells and on apparent bone nodules: a-c) F1; d-f) F2.

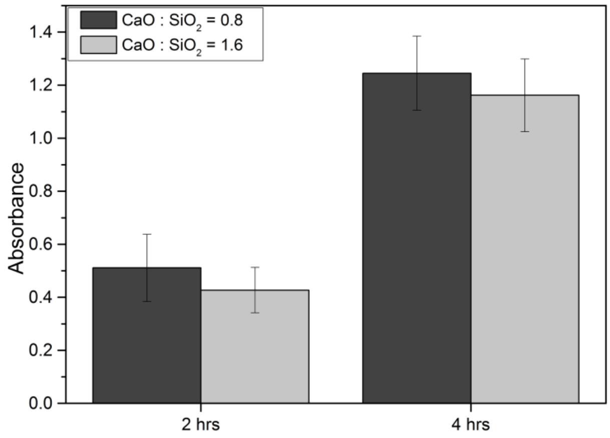

Fig. 7.7 Total cell viability of day-3 cell-seeded constructs determined by WST-1 assay [values expressed as mean ± SD, n=3 in each group].

Cell adhesion on a scaffold is essential for the development of anchorage-dependent cells in tissue engineering applications. HCA is chemically similar to the mineral component of bones in mammals and, its innate capacity to adsorb serum proteins plays a vital role in providing the matrix for cell attachment and the subsequent cellular events[24]. The formation of HCA on the surface of the 3-D foam scaffolds allowed excellent cell attachment. As shown in Fig. 7.8, the expression of the vimentin and actin cytoskeletal proteins was evident in MC3T3 cells seeded on both F1 and F2 foams following 3 days of culture. The expression of these cytoskeletal proteins was previously shown in osteoblasts cultured on matrix protein (e.g. Collagen Type I) coated glass coverslips[25]. It should be noted, however, that the organisation of the actin cytoskeleton appeared to be more advanced with extensive vimentin throughout the cytoplasm on cell-seeded F2 constructs.

For analysis of osteogenic differentiation, day-21 cell-seeded constructs were immunostained with antibodies against phenotypic osteogenic proteins (Fig. 7.8). The osteoblastic activity of both cell-seeded F1 and F2 constructs was evidently supported by the positive immunolocalisation of Collagen Type I, a commonly used extracellular matrix marker for early bone matrix deposition. Interestingly, the Collagen Type I appeared more organised in F2 constructs. Similarly, robust expression of Osteopontin, an early marker of osteogenic differentiation, was observed in F2 constructs in comparison to F1 constructs. The expression of late osteogenic marker Osteocalcin by MC3T3 cells on F1 foams was negligible. In contrast, the expression of Osteocalcin was noticeably upregulated in F2 constructs by day 21. The upregulated expression of Osteocalcin can be partially related to the enhanced deposition of Collagen Type I on F2 samples. The events of osteogenesis take place in the presence of a collagenous matrix[26]. The binding of MC3T3 cells to this collagenous matrix is mediated by $\alpha2\beta1$ integrin, the binding of which at the cell membrane induces the expression mitogen-activated protein kinases (MAPK). It has been shown that the phosphorylation of these MAPK activates Alkaline Phosphatase and Runx2, which in turn promote the downstream expression of Osteocalcin[26].

The observation from immunohistochemical analyses suggests a material preference to MC3T3 osteoblast precursor cells for F2 foams as a substratum during osteogenic differentiation *in vitro*. The dissolution products of the bioactive foams likely had a significant impact on osteogenic differentiation of MC3T3 cells. In the complex field of biomaterials design, in fact, the simple inclusion of an ion generally induces important changes in gene expression, metabolic pathways and the membrane composition of osteoprogenitor cells[27]. The enhanced osteogenic response of MC3T3 cells in the presence of F2 foams can be partly explained due to the increase Ca^{2+} concentration in culture media. The role of Ca^{2+} in osteoblast activity is well established. While moderate Ca^{2+} concentration (2-4 mM) was suitable for proliferation and survival of osteoblasts, higher Ca^{2+} concentration (6-8 mM) can favour osteogenic differentiation and matrix mineralisation in both monolayer and 3-D cultures of murine primary osteoblasts[28]. Extracellular calcium receptors were reported to be involved in the mechanism in which MC3T3 respond to Ca^{2+} in media[29,30].

Studies have also reported that silicon deficiency in chicks and rats led to defective bone and cartilage tissue, both of which were restored with the addition of soluble Si to their diet[31-32]. Si therefore also play an important role in skeletal tissue development. Indeed, soluble silica has been shown to stimulate Collagen Type I production and Alkaline Phosphatase activity by human osteoblast cells at a concentration of 10-20 mmol[33].

Numerous studies have reported on the osteogenic effects of bioactive silicate glasses and their dissolution products, which release both Ca^{2+} and soluble silica. Xynos *et al.* demonstrated that genes that play a role in metabolism, proliferation and cell-cell and cell-matrix interaction were significantly up-regulated when human osteoblastic cells were cultured in bioactive glass dissolution products[34-36]. The effect of bioactive glass dissolution products on osteogenic differentiation has been found to be dose-dependent, with the highest gene expression observed at about 20 µg ml^{-1} of soluble silica, accompanied by 60–90 µg ml^{-1} of calcium ions[37]. A similar response was observed for human foetal osteoblasts, with 15–20 µg ml^{-1} of soluble silica promoting highest metabolic activity, with expression of the core-binding factor alpha 1 (Cbfa1) and enhanced formation of mineralised bone nodules[38]. The concentrations of Ca (~300 µg ml^{-1}) and Si (~70 µg ml^{-1}) released by the wollastonite-apatite were notably higher in comparison to conventional bioactive glass used in the aforementioned previously published studies. A direct comparison between the effects of wollastonite-apatite and bioactive glass on osteogenesis will therefore need to be investigated in future studies.

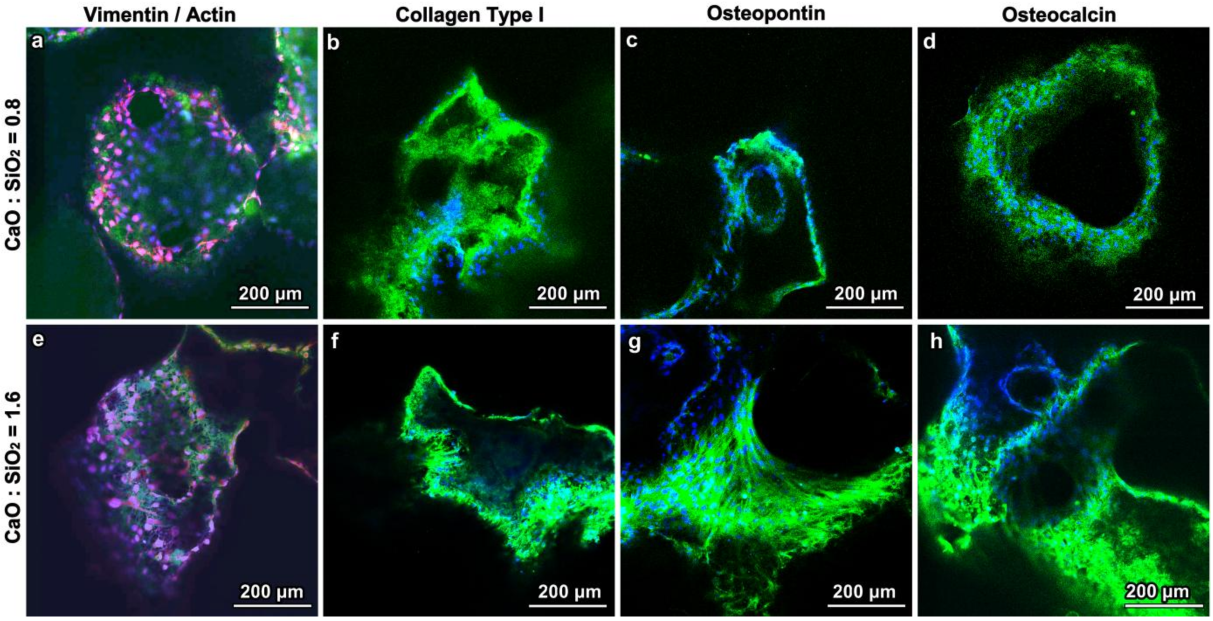

Fig. 7.8 a-b) Expression of vimentin and actin cytoskeletal proteins by MC3T3 cells in F1 and F2 samples following 3 days of cell culture; c-h) Immunohistochemical examination.

7.3.4 Direct 3-D printing

A preceramic mixture of the same composition as the foams was directly 3-D printed using a robotic deposition device (Robocad 3.0, 3-D Inks, Stillwater, OK). The diameter of the printing nozzles controlling the diameter of the scaffold rods was 250 µm (EFD precision tips, EFD, East Providence, RI). The width between rods and the layer height were fixed at 560 and 190 µm, respectively. As printed, the geometry of the scaffolds was 10x10x2 mm.

Concerning the viscosity of the preceramic ink, a substitution of the polymer was required: liquid H62C was replaced with solid MK, which was dissolved in isopropyl alcohol and mixed with $CaCO_3$ powders. Before being printable, the ink was left overnight to dry at room temperature. The amount of MK was calculated according to the different silica yield (84 wt%) compared to H62C (58 wt%).

After printing, the 3-D structures were subjected to the same treatment cycle as the foams:

- non reactive ceramization at 700 °C, only providing the polymer-to-ceramic conversion (Fig. 7.9a,b,c);
- phospatization by immersion for 14 days at 60 °C in 1 mol/L Na_2HPO_4, to convert the outer shell of $CaCO_3$ in hydroxyapatite (Fig. 7.9d);
- reactive ceramization at 900 °C, promoting the formation of wollastonite and maintaining hydroxyapatite.

The images presented in Fig. 7.9a,b were taken after ceramization at 700 °C and testify that no viscous collapse of the polymer took place after printing, so that the 3-D structure and the shape of the rods were maintained quite regular even after ceramization. SEM micrographs at a higher magnification reported in Fig. 7.9b show that actually the ceramization treatment at 700 °C produced a lot of cracks in the rods, probably because of the gas release occurring during the thermal treatment, but it was not completely clarified if it was caused by the decomposition of the polymer or of the $CaCO_3$ filler.

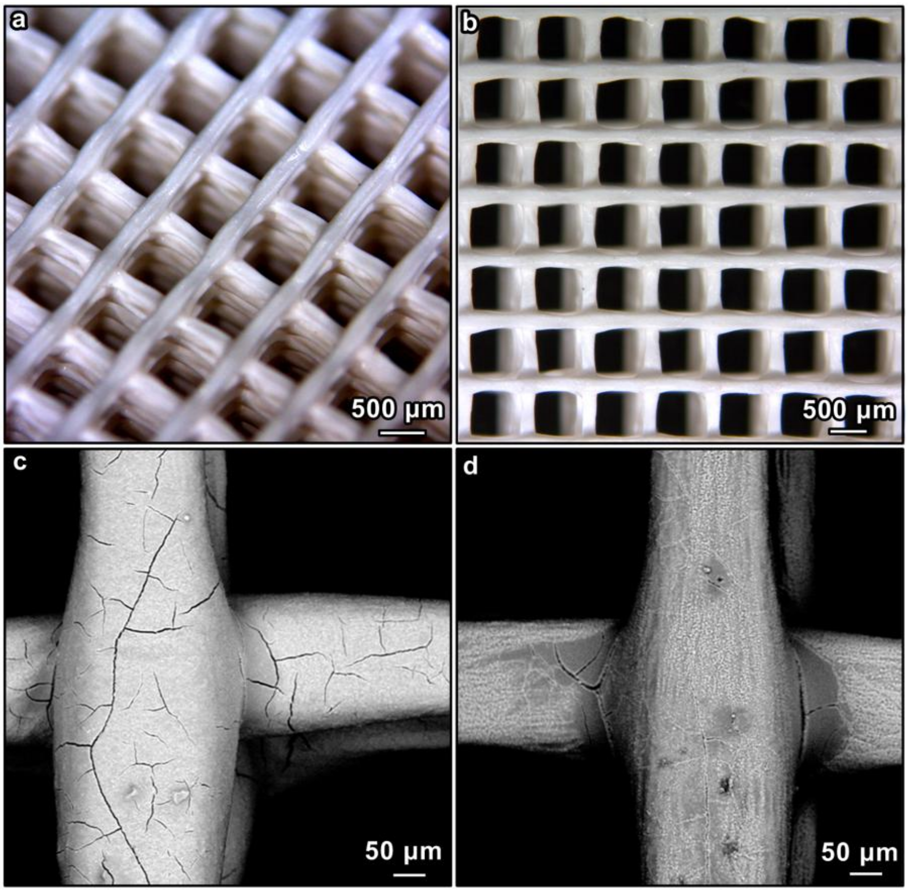

Fig. 7.9 Images of 3-D printed scaffolds – top view: a,b) stereomicroscopy after ceramization at 700 °C, c) SEM micrograph after ceramization at 700 °C, d) SEM micrograph after ceramization at 700°C and phosphatization.

This might be investigated by changing the CaO/SiO_2 ratio and comparing the extent of the cracking among samples with different composition. By this way, a preferable precursors ratio might be selected to minimise the cracking. Alternatively, the amount of material subjected to decomposition with gas release might be reduced by incorporating in the preceramic mixture of some powdered pre-ceramized wollastonite (still derived from preceramic polymers). Ultimately, a further option might be the addition of a glass filler to promote the viscous flow during heating, thus helping the crack relaxation and, possibly, the crack filling.

Fig. 7.10 presents the phase evolution upon the three processing steps by XRD. After the first ceramization at 700 °C, even if at this temperature no reaction between Si and Ca was expected, the XRD pattern showed the presence of some silica (PDF#82-1567 – PDF#76-0940) and of a silicate ($CaSi_3O_5$ – PDF#73-0599 – PDF#75-1400), besides $CaCO_3$ in form of calcite (PDF#86-0714) and vaterite (PDF#33-0268). This means that the SiO_2 formed by the conversion of the preceramic polymer started to crystallise and react with Ca. This might depend on the different reactivity of the preceramic polymer used for the ink. After phosphatization, the formation of Hap (PDF#86-0740 – PDF#76-0694 – PDF#73-0294) was observed, thanks to the exposure of $CaCO_3$ to P ions of the phosphatizing solutions. With the last step, the scaffolds were ceramized at 900 °C, in order to convert $CaCO_3$ into $CaSiO_3$ (PDF#84-0655) by reaction with SiO_2, maintaining the Hap coating.

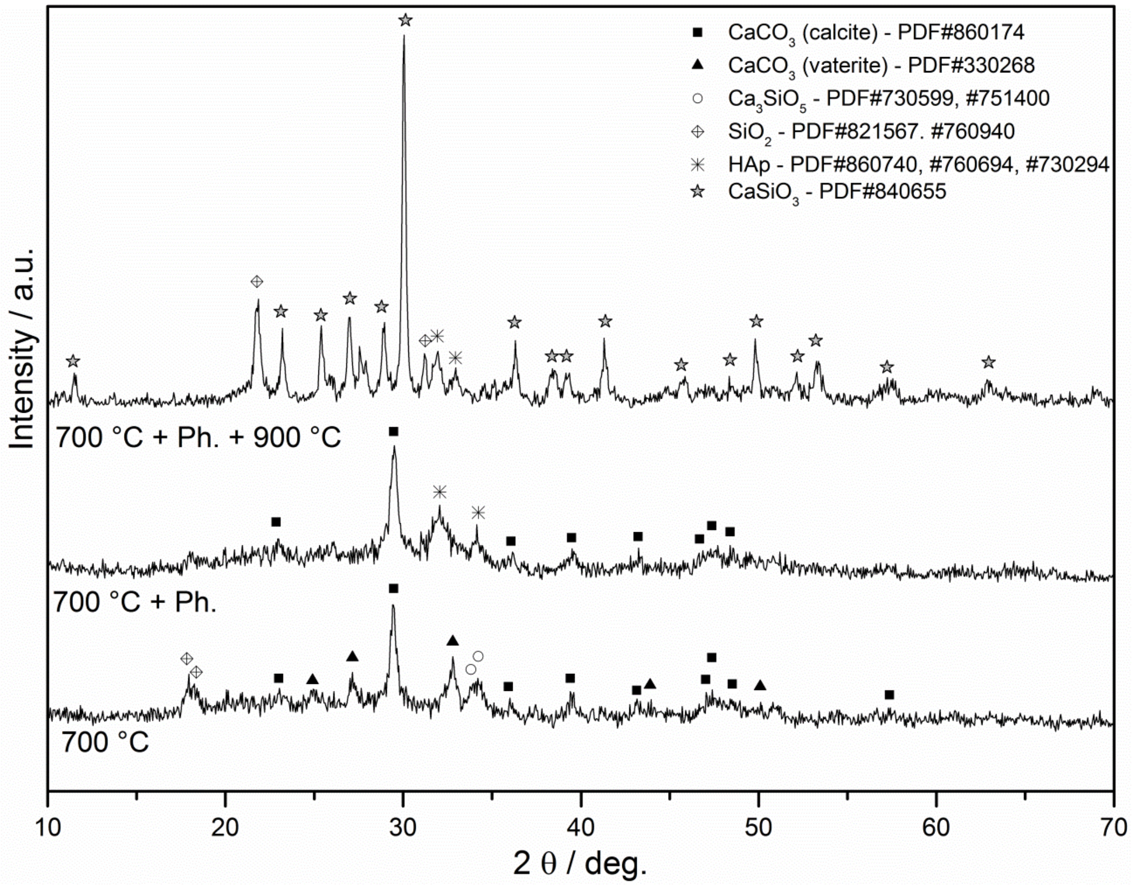

Fig. 7.10 XRD patterns of samples at different steps of the synthesis cycle.

Tab. 7.2 Summary of physical and mechanical properties of 3-D printed scaffolds at different steps of the synthesis cycle.

Sample type	ρ_{bulk} (g/cm^3)	σ_{comp} (MPa)	Specific σ_{comp} (MPa·cm^3/g)
700 °C	0.58 ± 0.09	0.78 ± 0.15	1.35
700 °C + Ph	0.69 ± 0.12	0.84 ± 0.24	1.22
700 °C + Ph + 900°C	0.60 ± 0.06	0.93 ± 0.26	1.56

The mechanical behaviour of the 3-D structures was evaluated by mechanical tests in compression mode. The compressive strength (σ_{comp}) was measured at room temperature, as the mean value of four samples and it is summarized Tab. 7.2. Values were between 780 and 930 kPa, but considering the bulk density of the scaffolds (ρ_{bulk}), the specific compressive strength was calculated to be between 1.35 and 1.56 MPa. The weakness is reasonably due to the extensive cracking suffered by the samples during the ceramization treatment; therefore, the improvement of the mechanical properties go hand in hand with the minimization of defects, which might be achieved by following the strategies above explained. This is confirmed by the trend of σ_{comp}, which slightly increased moving from the samples just ceramized at 700 °C to the samples also phosphatised (Tab. 7.2). In fact, it is remarkable that the phosphatization step was somehow very helpful in filling and coating the cracks, as clearly visible in Fig. 7.9d, thus enabling a sort of recovering of the structural integrity, even if only partially.

7.4 Conclusions

In this study, highly porous wollastonite-apatite composite ceramics were synthesized and shaped from preceramic polymers filled with calcium oxide precursor. This demonstrated the possibility to obtain high phase purity components, having a strong control over the final composition of the material just playing on the amount of precursors.

The idea of combining these two crystal phases was born as a solution to the issue concerning the mechanical weakness hydroxyapatite. Therefore, the new material was thought to couple the strong bioactivity of an outer shell of hydroxyapatite with a mechanically stronger open foamed wollastonite core. The resulting component might be used for bone tissue ingrowth applications.

A novel method was chosen to develop the hydroxyapatite coating on the wollastonite-based scaffolds. Pre-ceramized foams made of SiO_2 and $CaCO_3$ were immersed in a controlled phosphatizing solution, specifically prepared in order to provide P^{5+} and H^+ ions for the reaction with Ca^{2+} from the samples surface. Then the phosphatized foams were thermally treated to at 900 °C to enable the formation of wollastonite from the reaction between SiO_2 and $CaCO_3$.

Concerning the pore structure and mechanical properties, the samples fulfilled the requirements for being promising scaffolds for bone tissue engineering applications, exhibiting a compressive strength around 3 MPa, a porosity of 90 % and a modal interconnect pore diameter of approximately 130-160 µm.

The obtained foams (in particular those with enhanced calcium content) demonstrated excellent bioactivity, biocompatibility, as well as osteogenic potential when MC3T3 cells were cultured on the scaffolds *in vitro*.

Concerning the direct 3-D printing, it can be concluded that a silicone-based mixture incorporating fillers is printable, but the process needs to be further improved in order to solve the issue related to the cracking of the rods. Moreover, the viscosity and, more generally, the rheological behaviour of the preceramic ink should be better analysed and corrected, in order to optimize the morphology of the scaffolds and increase their height.

References

[1] Hench L L 1991 Bioceramics: From Concept to Clinic J. Am. Ceram. Soc. 74 1487-1510

[2] Kokubo T 1991 Bioactive glass ceramics: properties and applications Biomaterials. 12 155–163

[3] Zhang H, Ye X J, Li J S 2009 Preparation and biocompatibility evaluation of apatite/wollastonite-derived porous bioactive glass ceramic scaffolds Biomed. Mater. 4 045007.

[4] Nakamura T, Yamamuro T, Higashi S, Kokubo T, Itoo S 1985 A New Glass-Ceramic for Bone Replacement: Evaluation of its Bonding to Bone Tissue J. Biomed. Mater. Res. 19 685-698

[5] Kokubo T, Ito S, Sakka S, Yamamuro T 1986 Formation of a High-Streght Bioactive Glass-Ceramic in the System MgO-CaO-SiO_2-P_2O_5 J. Mater. Sci. 21 536-540

[6] Kitsugi T, Yamamuro T, Kokubo T 1989 Bonding Behavior of a Glass-Ceramic Containing Apatite and Wollastonite in Segmental Replacement of the Rabbit Tibia Under Load-Bearing Conditions J. Bone Joint Surg. Am. 71 264-272

[7] Bernardo E, Colombo P, Cacciotti I, Bianco A, Bedini R, Pecci R, Pardun K, Treccani L, Rezwan K 2012 Porous wollastonite-hydroxylapatite bioceramics from preceramic polymer and micro- or nano-sized fillers J. Eur. Ceram. Soc. 32 399–408

[8] Maruta M, Matsuya S, Nakamura S, Ishikawa K 2011Fabrication of low-crystalline carbonate apatite foam bone replacement based on phase transformation of calcite foam Dent. Mater. J. 30 14-20

[9] Senouchi K, Tsuru K, Maruta M, Kawachi G, Matsuya S, Terada Y, Ishikawa K 2012 Fabrication of solid and low-crystalline carbonate apatite microspheres as bone substitutes using calcite microspheres as a precursor Dent. Mater. J. 31 549-557

[10] Maeda H, Maquet V, Kasuga T, Chen Q Z, Roether J A, Boccaccini A R 2007 Vaterite deposition on biodegradable polymer foam scaffolds for inducing bone-like hydroxycarbonate apatite coatings J. Mater. Sci: Mat. in Med.18 2269-2273.

[11] Monchau F, Hivart P, Genestie B, Chai F, Descamps M, Hildebrand N F 2013 Calcite as a bone substitute. Comparison with hydroxyapatite and tricalcium phosphate with regard to the osteoblastic activity Mater. Sci. and Eng. C. 33 490–498

[12] Maçon ALB et al 2015 A unified in vitro evaluation for apatite-forming ability of bioactive glasses and their variants 2015 J. Mater. Sci.: Mat. in Med. 26 Article published online: 11 February 2015 | DOI 10.1007/s10856-015-5403-9

[13] Bernardo E, Parcianello G, Colombo P, Matthews S 2013 Wollastonite foams from an extruded preceramic polymer mixed with $CaCO_3$ microparticles assisted by supercritical carbon dioxide Adv. Eng. Mater. 15 60–65

[14] Bernardo E, Colombo P, Dainese E, Lucchetta G, Bariani P F 2012 Novel 3D wollastonite-based scaffolds from preceramic polymers containing micro- and nano-sized reactive particles Adv. Eng. Mat. 14 269–274

[15] Rahaman M N, Day D E, Bal B S, Fu Q, Jung S B, Bonewald L F, Tomsia A P 2011 Bioactive glass in tissue engineering Acta Biomater. 7 2355–73

[16] Jones J R, Ehrenfried L M, Hench L L 2006 Optimising bioactive glass scaffolds for bone tissue engineering Biomaterials 27 964-973

[17] Wu Z Y, Hill R G, Yue S, Nightingale D, Lee P D, Jones J R 2011 Melt-derived bioactive glass scaffolds by gel-cast foaming technique Acta Biomater. 7 1807-1816

[18] Downs R T 2006 The RRUFF Project: an integrated study of the chemistry, crystallography, Raman and infrared spectroscopy of minerals. Program and Abstracts of the 19th General Meeting of the International Mineralogical Association in Kobe, Japan. O03-13 (spectrum ID R040131).

[19] Rehman I, Bonfield W 1997 Characterization of hydroxylapatite and carbonated apatite by photo acoustic FTIR spectroscopy J. Mater. Sci.: Mat. in Med. 8 1-4

[20] Siriphannon P, Kameshima Y, Yasumori A, Okada K., S. Hayashi 2012 Formation of hydroxyapatite on $CaSiO_3$ powders in simulated body fluid J. Eur. Ceram. Soc. 22 511-520

[21] Jones J R, Tsigkoua O, Coates E E, Stevens M M, Polak J M, Hench L L 2007 Extracellular matrix formation and mineralization on a phosphate-free porous bioactive glass scaffold using primary human osteoblast (HOB) cells Biomaterials 28 1653–1663

[22] Serra J, Gonzalez P, Liste S, Serra C, Chiussi S, Leon B, Perez-Amor M, Ylanen H O, Hupa M 2003 FTIR and XPS studies of bioactive silica based glasses J. Non-Cryst. Sol. 332 20–27

[23] Duchen M R 2000 Mitochondria and calcium: from cell signalling to cell death J. Physiol. 529 57-68

[24] Wang K, Zhou C, Hong Y, Zhang X 2012 A review of protein adsorption on bioceramics Interface focus. 2 259-277

[25] Demais V, Audrain C, Mabilleau G, Chappard D, Baslé M F 2014 Diversity of bone matrix adhesion proteins modulates osteoblast attachment and organization of actin cytoskeleton Morphology. 98 53-64

[26] Xiao G, Gopalakrishnan R, Jiang D, Reith E, Benson M D, Franceschi R T 2002 Bone morphogenetic proteins, extracellular matrix, and mitogen-activated protein kinase signaling pathways are required for osteoblast-specific gene expression and differentiation in MC3T3-E1 cells J. Bone Miner. Res. 17 101-110

[27] Autefage H, Gentleman E, Littmann E, Hedegaard M A B, Von Erlach T, O'Donnell M, Burden F R, Winkler D A, Stevens M M 2015 Sparse feature selection methods identify unexpected global cellular response to strontium-containing materials PNAS 112 4280-4285

[28] Maeno S, Niki Y, Matsumoto H, Morioka H, Yatabe T, Funayama A, Toyama Y, Taguchi T, Tanaka J 2005 The effect of calcium ion concentration on osteoblast viability, proliferation and differentiation in monolayer and 3-D culture Biomaterials 26 4847-4855

[29] Takaoka S, Yamaguchi T, Yano S, Yamauchi M, Sugimoto T 2010 The Calcium-sensing Receptor (CaR) is involved in strontium ranelate-induced osteoblast differentiation and mineralization Horm. Metab. Res. 42 627-631

[30] Yamauchi M, Yamaguchi T, Kaji H, Sugimoto T, Chihara K 2005 Involvement of calcium-sensing receptor in osteoblastic differentiation of mouse MC3T3-E1 cells Am. J. Physiol. Endocrinol. Metab. 288 608-616

[31] Carlisle E M 1972 Silicon: an essential element for the chick Science 178 619-621

[32] Schwarz K, Milne D B 1972 Growth promoting effects of silicon in rats Nature 239 333-334

[33] Reffitt D M, Ogston N, Jugdaohsingh R, Cheung H F J, Evans B A J, Thompson R P H, Powell J J, Hampson G N 2003 Orthosilicic acid stimulates collagen type 1 synthesis and osteoblastic differentiation in human osteoblast-like cells in vitro Bone 32 127-135

[34] Xynos I D, Edgar A J, Buttery L D K, Hench L L, Polak J M 2001 Gene-expression profiling of human osteoblasts following treatment with the ionic products of Bioglass® 45S5 dissolution J. Biomed. Mater. Res. 55 151-157

[35] Xynos ID, Edgar AJ, Buttery LDK, Hench LL, Polak JM 2000 Ionic products of bioactive glass dissolution increase proliferation of human osteoblasts and induce insulin-like growth factor II mRNA expression and protein synthesis Biochem. Biophys. Res. Commun. 276 461-465

[36] Xynos ID, Hukkanen MVJ, Batten JJ, Buttery LD, Hench LL, Polak JM 2000 Bioglass® 45S5 stimulates osteoblast turnover and enhances bone formation in vitro: Implications and applications for bone tissue engineering Calcified Tissue Int. 67 321-329

[37] Hench L L 2009 Genetic design of bioactive glass J. Eur. Ceram. Soc. 29 1257-1265

[38] Tsigkou O, Jones J R, Polak J M, Stevens M M 2009 Differentiation of fetal osteoblasts and formation of mineralized bone nodules by 45S5 Bioglass® conditioned medium in the absence of osteogenic supplements Biomaterials 30 3542-3550

8 Silica-bonded apatite ceramics

8.1 Introduction

Natural bone, like any other connective tissue, consists of an extracellular matrix (ECM) and cells. Among the various specific types of cells, osteoblasts, osteoclasts, stomal fibroblasts, adipocytes, endothelial and hematopoietic cells are present. The ECM is here specifically mineralized, so it is made of 35% organic and 65% minerals. The organic matrix is proteic, being composed of mainly collagen-1 and fibronectin. Concerning the inorganic fraction, the most abundant mineral is hydroxyapatite ($Ca_{10}(PO_4)_6(OH)_2$), a calcium phosphate that is found within and between the length of collagen fibers, where it is needed to resist bending and compression[1]. Hence, hydroxyapatite ceramics have been successfully implemented in clinical applications for bone repairing, by virtue of excellent osteconductive properties.

Even if the inorganic phase of bone has been idealized as hydroxyapatite (HAp), studies on biological apatites demonstrated that the bone mineral contains 4-8 % of carbonate in its apatitic structure[2], thus the inorganic component of bone should be referred to as carbonate apatite (HCA), in which CO_3^{2-} ion substitutes PO_4^{3-} or OH^- ion. It has also been demonstrated that there is a strong relationship between carbonate substitution in apatitic structures and solubility of apatite in weak acid conditions (the environment produced by osteoclasts to dissolve the bone minerals has a pH of about 3-5)[3]. Specifically, the solubility of apatite increases with the increase in carbonate content of apatite, so, while HAp cannot be totally resorbed by osteoclasts, HCA has a high solubility and it can be completely replaced by new natural bone, through the remodelling cycle of the bone tissue[4]. Therefore, HCA would be a preferable choice as a bone substitute biomaterial than pure HAp.

The issue concerning the synthesis of dense HCA deals with its lack of thermal stability at the high temperatures that are required for the sintering process, due to the decomposition of the material and the subsequent release of CO_2[5,6]. However, a dense structure is not the best candidate for replacing bone, whereas a HCA scaffold would better mimic the typical morphology of cancellous bone when shaped in an interconnected porous structure, thus promoting rapid cell penetration and revascularization.

Sunouchi *et al.*[4] reported a novel method to obtain solid and hollow HCA microsphere, which could be packed giving a 3-D interconnected porous structure. Calcite ($CaCO_3$), calcium hydroxide ($Ca(OH)_2$) and sodium chloride (NaCl) cores were covered with a further layer of $Ca(OH)_2$ and then treated with CO_2 for two weeks to obtain the conversion to $CaCO_3$ by carbonation. The obtained spheres were later phosphatised in a Na_2HPO_4 solution for two weeks, successfully converting $CaCO_3$ into HCA by dissolution-precipitation reactions. Maruta *et al.*[7] applied the same approach to convert $CaCO_3$ foams into HCA foams. In this case, cellular materials were obtained by negative replica, using polyurethane (PU) sponges as templates and dipping them in a slurry consisting of $Ca(OH)_2$ dispersed in distilled water. After drying the slurry and burning out the PU substrate, the foams were converted to $CaCO_3$ (again by carbonation) and later phosphatised (by immersion in the same Na_2HPO_4 solution).

A similar approach was already followed in § 7 to convert calcite into apatite[8], demonstrating the possibility of fabricating wollastonite-apatite foams from direct foaming of a slurry consisting in a liquid preceramic polymer mixed with fillers. After synthesising calcite foams, they were first phosphatised to obtain a partial $CaCO_3$-to-Ap conversion and later ceramized at 1100 °C to allow the reaction between the remaining calcite and silica left from the silicone-to-ceramic conversion, thus obtaining wollastonite-apatite composite foams.

In the present study, which was submitted for publication in 2015 by Fiocco *et al.*, an easy method is proposed to fabricate silica-bonded apatite porous structure by negative replica, starting from PLA

3-D printed sacrificial templates. Here, the goal was to obtain a high conversion of calcite into apatite. Liquid preceramic polymers mixed with powdered $CaCO_3$ fillers were used as a slurry to infiltrate PLA foams and they were cross-linked at room temperature prior to burning out the PLA. After ceramization at 600 °C, particularly low compared to the temperatures adopted for other silicone-derived ceramics[9], the ceramic scaffolds were phosphatised by immersion in a Na_2HPO_4 bath, following the same procedure as Sunouchi *et al.*[4] and Maruta *et al.*[7]. The $CaCO_3$-to-Ap conversion was even more successful when $CaCO_3$ was replaced with a biological one, derived from eggshell waste, due to its natural impurities facilitating the interdiffusion phenomena.

8.2 Experimental

8.2.1 Preparation of samples

Two commercial liquid silicones, RTV90700 (Siliconi Padova, Italy) and RTV960 (Angeloni, Italy) constituted the reference materials for the silica binder. The two bi-component polymers feature a silica yield of 72.5 % and 58 wt%, respectively, and can cross-link at room temperature, by a polyaddition mechanism, when mixed with their specific cross-linking agents. RTV90700 and RTV960 were used to obtain 67 and 33 wt% of the total silica content, respectively, so that the polymers were used in the weight ratio of RTV90700/RTV960=1.6. Two different types of micro-sized calcite ($CaCO_3$) were used: i) commercial calcite (<10 µm, Industrie Bitossi, Vinci, Italy - later referred to as "BIT"); ii) calcite from eggshell waste, after a heating cycle up to 450 °C, for 4 hours, with a heating rate of 5 °/min 17 µm, - later referred to as "ESW"). The $CaCO_3/SiO_2$ weight ratio was kept constant at 70/30.

The egg shells were obtained from Lecoque Eggs (Tongeren, Belgium). The resulting BET of the ESW powder was 4-6 m^2/g. The inorganic fractions consisted of 98 wt% $CaCO_3$, with traces of $MgCO_3$. From TGA measurements, it was deducted that 2 – 5 wt% of organic material was still present from the egg shell membrane.

RTV90700 and RTV960 were homogeneously mixed by mechanical stirring, then the $CaCO_3$ powders were incorporated. Only for the filler derived from eggshell waste, a small amount of solvent (isopropyl alcohol) was added (1 ml for 10 g of final ceramic), because the viscosity of the slurry tended to increase rapidly as the powders were incorporated. At last, the curing agents for the two polymers were added and the resulting mixtures were further subjected to mechanical stirring, in order to obtain homogeneous pastes.

Before the occurrence of curing reactions, silicone/calcite slurries were used to infiltrate, by immersion, 3-D printed reticulated polylactic acid (PLA) scaffolds, in turn obtained by means of a Power WASP orienting extruder (Massa Lombarda, Italy). The PLA scaffolds were placed at the bottom of a plastic container and left immersed in the slurries for 12 h, until the silicone/calcite pastes became rubbery. At this stage, the excess paste was removed from the PLA scaffold by means of a cutter.

The infiltrated PLA scaffolds were thermally treated at 350 °C, with a heating rate of 0.5 °C/min, for 1 hour. This step led to the decomposition of PLA, obtaining reticulated structures (replicas) made of cross-linked silicones and $CaCO_3$. The replicas were later subjected to a ceramization treatment at 600 °C, with a heating rate of 2 °C/min, for 2 hours, in order to transform the silicones into amorphous silica SiO_2, while maintaining $CaCO_3$ unreacted.

After ceramization, the scaffolds were subjected to a phosphatization treatment by immersion in a 1 mol/L Na_2HPO_4 solution at 60 °C for 14 days, resulting in silica-bonded apatite ceramics.

8.2.2 Characterization of samples

Micro-structural characterizations were performed by optical stereomicroscopy (AxioCam ERc 5s Microscope Camera, Carl Zeiss Microscopy, Thornwood, New York, US), scanning electron microscopy (FEI Quanta 200 ESEM, Eindhoven, The Netherlands) equipped with EDS and X-ray diffraction (XRD; Bruker AXS D8 Advance, Bruker, Germany - CuKα radiation, 0.15418 nm, 40 kV-40 mA, 2θ=15-70°, step size=0.05°, 2s counting time). The Match! software package (Crystal Impact GbR, Bonn, Germany) was used for phase identification, supported by data from PDF-2 database (ICDD-International Centre for Diffraction Data, Newtown Square, PA, USA) and Crystallography Open Database (COD) database.

The bulk density (ρ_b) of the foams was determined using a caliper and a digital balance. The skeletal density (ρ_s) was measured on foams, using a He gas pycnometer (Micromeritics AccuPyc 1330, Norcross, GA). The percentage of porosity was then calculated using the following equation:
$\%P=1-(\rho_b/\rho_s)$.

Samples were analyzed by attenuated reflectance Fourier transform infrared spectroscopy (ATR-FTIR, Thermo Scientiic Nicolet iS10) at room temperature, to monitor the growth of the hydroxycarbonate apatite layer, using a wavenumber resolution of 4 cm^{-1} for 32 scans from 4000 to 600 cm^{-1}. Selected scaffold structures were subjected to mechanical characterization in compression mode at room temperature, using an Instron 1121 UTM (Instron Danvers, MA, USA) with a cross-head speed of 1 mm/min, on samples in the as-ceramized form and after phosphatization. Each data point is presented as the mean value of five to ten samples

All the experiments were performed in collaboration with Ms. Isabella Pezzetta (University of Padova).

8.3 Results

Fig. 8.1 reports the micrographs obtained by optical stereomicroscopy of the samples BIT (Fig. 8.1a,b) and ESW Fig. 8.1c,d). As previously mentioned, the ceramic scaffolds were replicas of the original PLA scaffolds, so that the accuracy of the shape was directly related to the quality of the original PLA structure. The geometrical defects which can be observed in Fig. 8.1 are mostly due to some irregularities in the 3-D printed PLA sacrificial scaffolds. Concerning the small holes randomly distributed across the filaments, they might be due to the incorporation of some air during the infiltration of PLA with the preceramic slurry, considering that the preceramic mixture had the viscosity of a paste.

The presence of a geometrically distributed open porosity, left by the PLA by thermal volatilization, was clearly visible in three dimensions for both samples. At the same time, the thermal decomposition of PLA had, as a negative consequence, the formation of some cracks: in fact, this step was responsible for local increase in pressure inside the material, because of the formation of gases and their migration from the core to the external layers. The difference in coloration was due to the type of $CaCO_3$ employed for fabricating the samples (samples from natural $CaCO_3$ were darker).

In Fig. 8.2, the X-ray diffraction patterns of the two types of samples, BIT (Fig. 8.2a) and ESW (Fig. 8.2b), are presented. Concerning the spectra before phosphatization, which are reported in the lower part of the two panels, both BIT and ESW samples featured the presence of unreacted calcite ($CaCO_3$ - PDF#72-1650) after the ceramization at 600 °C, accompanied by weak trace of cristobalite (PDF#75-0923), attributable to colloidal silica present in the starting polymers[10].

The upper patterns, instead, show the evolution of the material due to the phosphatization treatment. As desired, it can be observed that the immersion in the phosphatising solution caused a significant conversion of $CaCO_3$ into apatite (Ap – PDF#86-0740 – COD#96-900-3553), thanks to the exposure of the samples to the P ions provided by the solution. This is evident from two observations: first, apatite peaks are well visible in the upper patterns; second, the intensity of the $CaCO_3$ main peak, at $2\theta \approx 30$ °, had a substantial decrease, even more significant for the ESW samples (panel b, upper pattern).

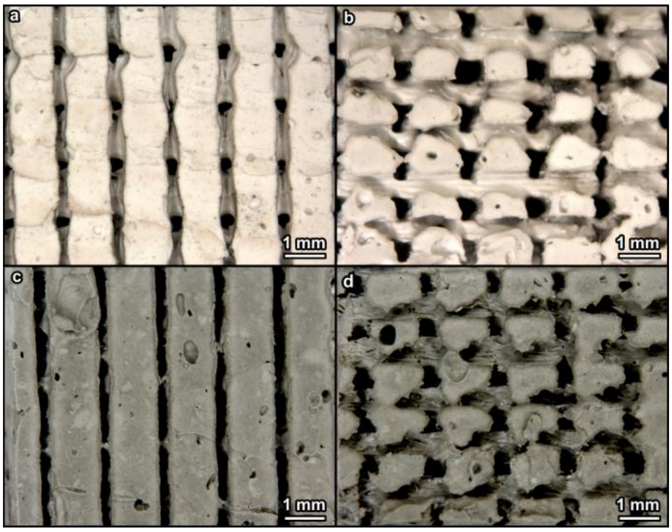

Fig. 8.1 Stereomicroscopy images of samples ceramized at 600 °C:
a) BIT (top view), b) BIT (side view), c) ESW (top view), d) ESW (side view).

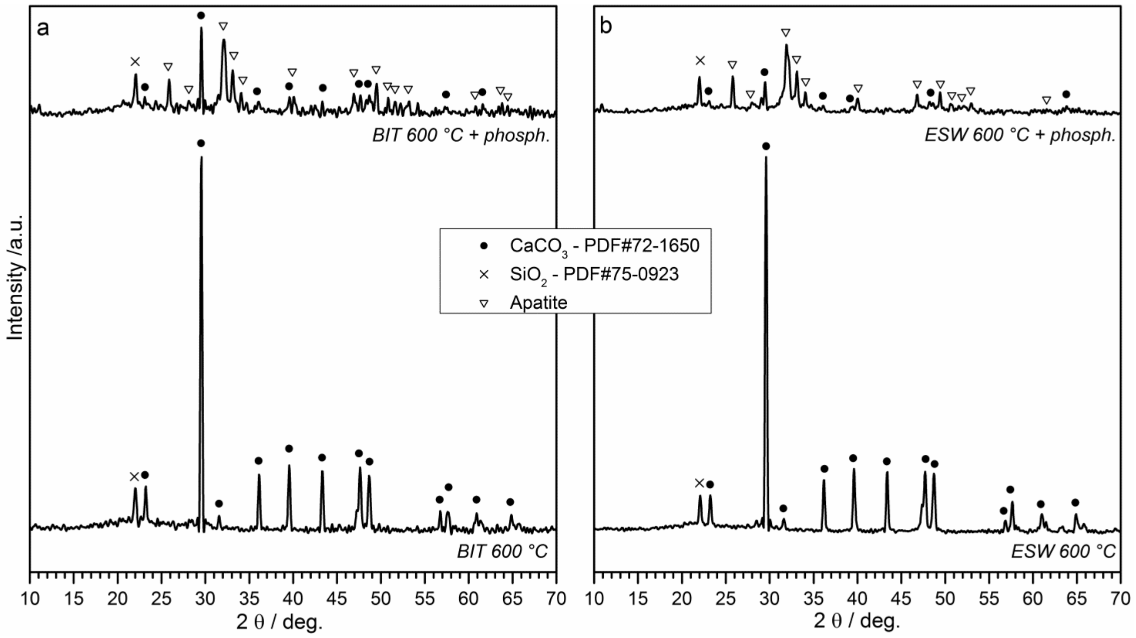

Fig. 8.2 X-ray diffraction patterns of ceramized samples before (lower patterns) and after (upper patterns) phosphatization: a) BIT samples; b) ESW samples.

From our analysis, the peaks of apatitic phase actually consisted of two different contributions, as reported in detail in Fig. 8.3. Focusing on the $CaCO_3$ peak at $2\theta=29.5°$, the spectra of BIT and ESW samples were perfectly aligned; on the contrary, the apatite peaks differ and do not exactly match with the previously cited reference pattern of apatite, in the form of hydroxyapatite (HAp). For both experimental patterns, the main peaks are placed between those of HAp and carbonate apatite

(HCA). The apatite obtained by phosphatisation could be seen, as a consequence, as a kind of solid solution with an intermediate composition between those of the hydroxyapatite and carbonate-substituted apatite references.

A comment should be made about the extent of the $CaCO_3$-to-Ap conversion. From XRD patterns, as previously observed, the decrease in intensity of the calcite peaks, which is directly correlated with the decrease in the amount of calcite, looked more pronounced for ESW samples, the ones derived from natural $CaCO_3$. This can be explained, as a first step, with a different reactivity of the two types of $CaCO_3$, but a further contribution might be given by the different purity. Indeed, interdiffusion phenomena, which are responsible for the ionic migration, are well known to be simplified in solid solutions rather than in pure phases and natural $CaCO_3$ is characterized by having trace elements in its composition, such as Mg[11]. Hence, it can be assumed that the conversion to Ap was facilitated in ESW samples.

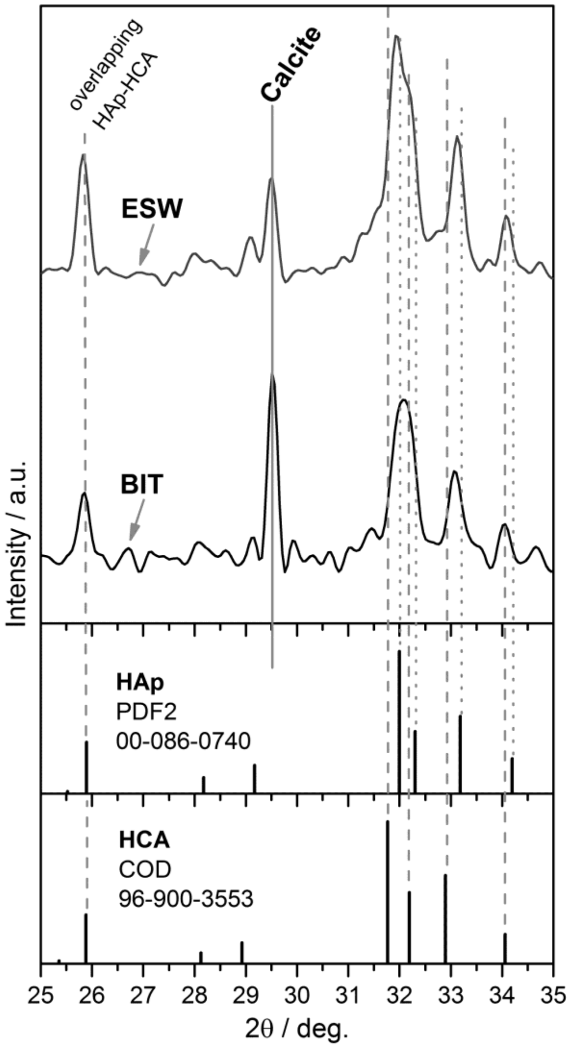

Fig. 8.3 Detail of X-ray diffraction patterns of ceramized BIT and ESW samples in comparison with reference patterns of HAp and HCA.

Tab. 8.1 summarizes the results of physical and mechanical characterizations performed on the two types of samples, as ceramized at 600 °C and even phosphatised. The difference in bulk density (ρ_{bulk}) between BIT and ESW samples is reasonably due to the different flow of silicone-based pastes infiltration, considering the different size of commercial calcite and ESW: in particular, in our opinion, finer ESW particles could lead to more viscous pastes, so that they could not pack very well, but form a sort of solid network. A similar behaviour was already discussed in literature and confirmed by recent experiments with colloidal silica[12-13]. An extensive rheological characterization would be needed to clarify this point, but it is beyond the aims of the present work.

Tab. 8.1 Summary of physical and mechanical properties of ceramized samples BIT and ESW, before and after phosphatization.

Type of sample	ρ_{bulk} (g/cm^3)	$\rho_{skeleton}$ (g/cm^3)	P_{open} (%)	σ_{comp} (MPa)
BIT	1.08 ± 0.13	2.51 ± 0.02	57	13.0 ± 2.1
BIT + Ph.	1.11 ± 0.03	2.56 ± 0.02	57	15.9 ± 2.4
ESW	0.78 ± 0.03	2.49 ± 0.01	69	15.2 ± 2.7
ESW + Ph.	0.92 ± 0.08	2.54 ± 0.01	64	16.7 ± 4.7

Interestingly, the compressive strength (σ_{comp}) was not degraded by the transformation of $CaCO_3$, occurring during the 2-week immersion in the phosphatising bath. In fact, BIT samples passed from approximately 13 to 16 MPa and ESW samples from 15 to 17 MPa with the phosphatisation. The differences, however, are not significant, considering the relatively large values of the standard deviations, in turn due to defects in the scaffolds geometry (intrinsically derived from the method applied, as already discussed). In their comparative study, Monchau *et al.*[14] reported a compressive strength from 10 to 16 MPa for HAp and β-TCP macroporous materials, with total pore volume of 70 %, whereas they showed a significantly lower compressive strength for calcite, from 4 to 9 MPa. BIT and ESW samples are perfectly in line with the values found in literature and with the compressive strength of natural trabecular bones, which is reported to be in the range 2-12 MPa[15].

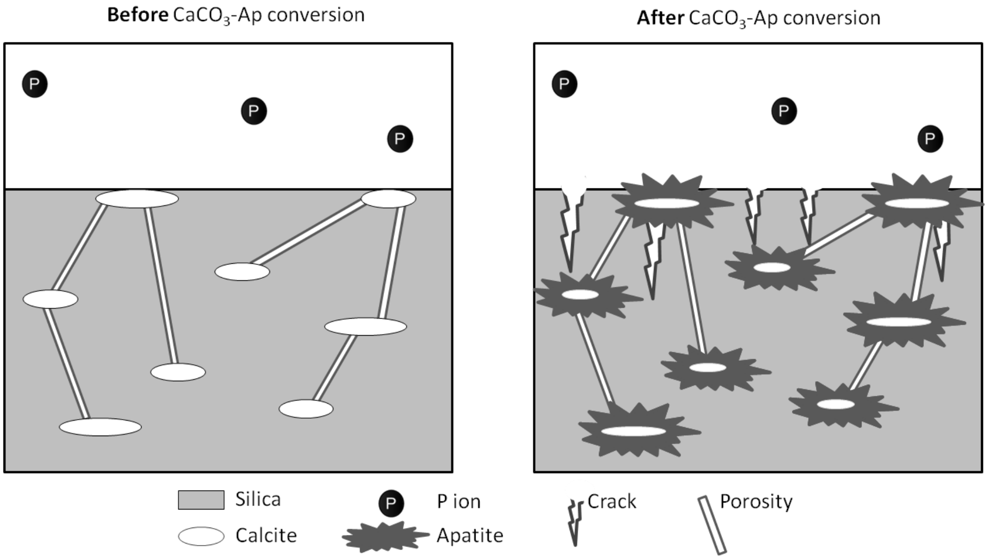

Fig. 8.4 Scheme of extensive phosphatization.

Concerning the porosity data, the values were between 57 and 69%, particularly high considering the voids in the reticulated structures, as illustrated by Fig. 8.1. This means that the samples were very permeable: besides the desired open spaces between the filaments of the scaffolds, which are a specific feature of the selected shape, and the cracks due to the thermal volatilization of PLA, the struts were probably characterized themselves by a very extended system of micro-sized, interconnected pores. This secondary porosity might be also responsible for the massive conversion of $CaCO_3$ into Ap, which not only concerned the surface, with the formation of an Ap coating, but managed to reach more internal layers, with conversion to Ap of deeper $CaCO_3$ agglomerates. Fig. 8.4 reports a scheme of hypothetical mechanism.

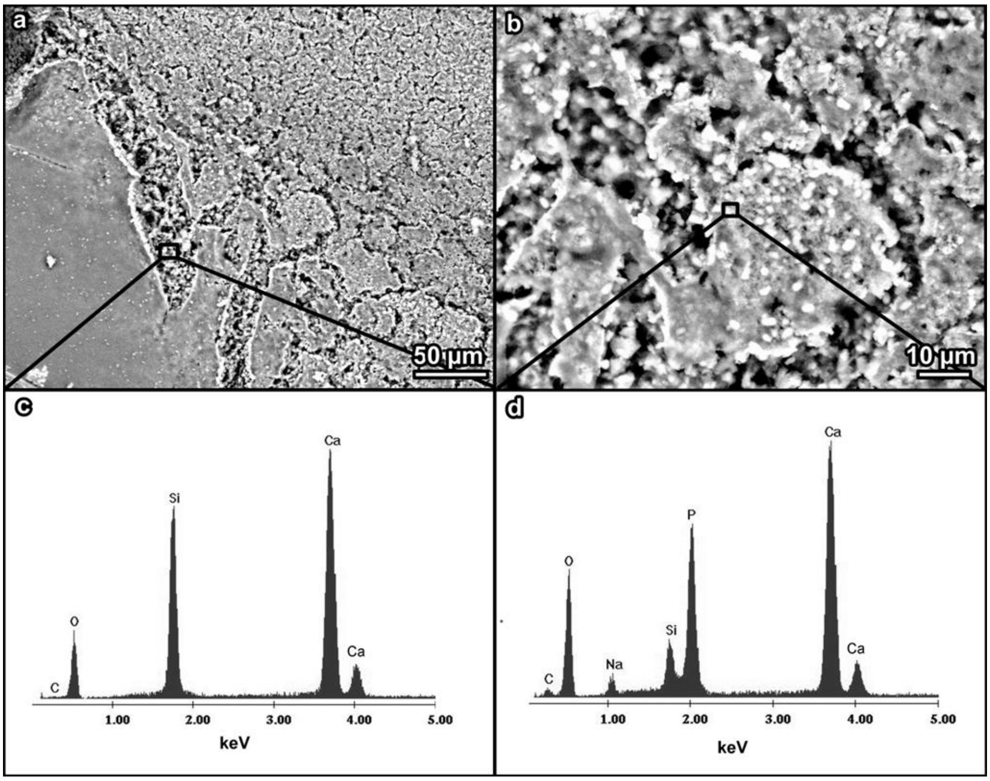

Fig. 8.5 SEM micrographs of BIT sample after ceramization and phospatization: a) Ap layer on micro-porous calcite, b) higher magnification detail,d) EDS spectrum taken on silica-bonded calcite, e) EDS spectrum of the surface.

The mechanism illustrated can also be deduced from the SEM micrographs shown in Fig. 8.5, where an extensive cracking of the Ap surface layer is visible: due to the micro-sized porosity of the struts, P ions were able to reach the internal layers of silica-bonded calcite, causing the nucleation and volumetric expansion of Ap in the inner core of the material and thus causing the cracking (Fig. 8.5a-b) of the layers above. The same comments can be done for both types of samples, but for the sake of brevity only BIT sample is represented.

Fig. 8.5 presents the EDS spectra taken on the SiO_2-bonded calcite (Fig. 8.5c) and on the Ap coating (Fig. 8.5d). In the spectrum of Ap layer (Fig. 8.5d), the peak of P is visible, confirming the phosphatization. The presence of a weak peak related to Na was possibly due to the exposure to the phosphatising solution, prepared starting from a sodium phosphate salt.

Fig. 8.6 reports the FTIR spectra of BIT (panel a) and ESW (panel b) samples, which were taken to analyze the material evolution undergone by the scaffolds with the phosphatization. Peaks at 1425 (CO_3^{2-} asymmetric stretching), 870 (CO_3^{2-} out-of-plane bending) and 710 (CO_3^{2-} in-plane bending) cm^{-1} are related to calcite[16] and are all visible in the two spectra before phosphatization (lower patterns). After phosphatization (upper patterns), the two peaks at 1425 and 870 cm^{-1} were still present, but they showed a significant decrease in intensity. All the other peaks in the lower patterns are attributable to silica[17-18], in particular 1080 (Si-O stretching), 800 and 460 (Si-O bending) cm^{-1} and they are maintained in the upper patterns after phosphatization. The formation of Ap was confirmed by the presence of phosphate vibrational bands[19-21] at 1040 (P-O stretching), 567 and 603 (P-O bending) cm^{-1}, as visible in both the upper patterns.

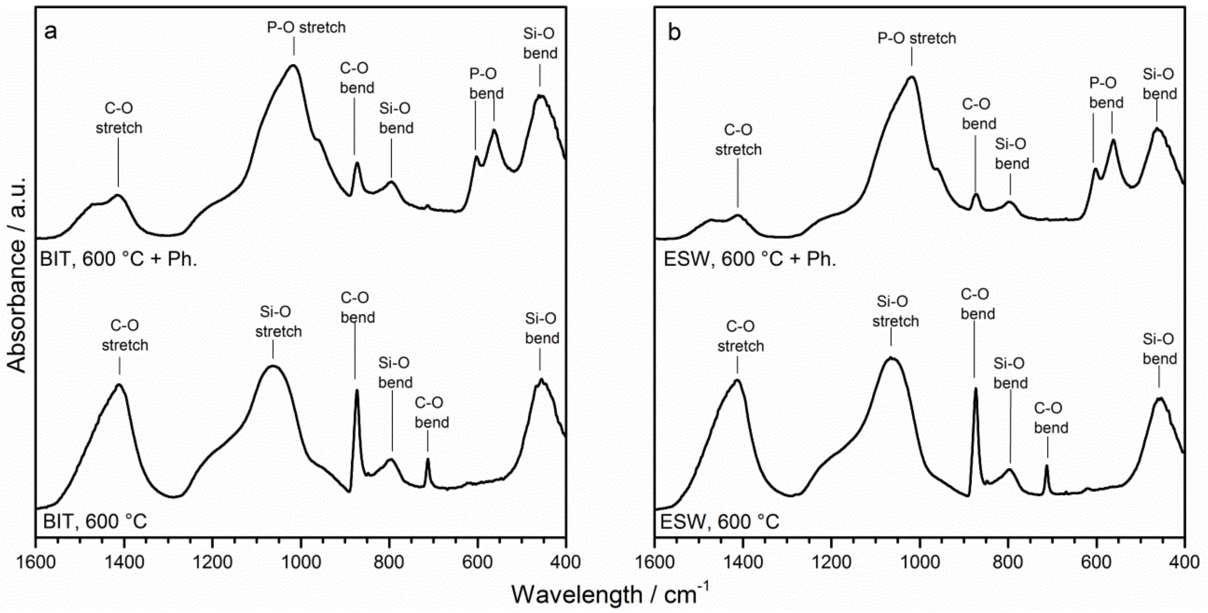

Fig. 8.6 FTIR spectra of ceramized BIT (a) and ESW (b) samples before and after phosphatization.

All the FTIR observations are in agreement with the expected $CaCO_3$-to-Ap conversion, taking place during the phosphatization treatment, but the spectra cannot shed light on the presence of HCA. In fact, while in the unphosphatized samples the peaks are definitely due to $CaCO_3$, in the phosphatized ones CO_3^{2-} vibrational bands can obviously been associated with the presence of both $CaCO_3$ and HCA and the two contributions cannot be distinguished.

8.4 Conclusions

Silica-bonded apatite was successfully fabricated by negative replica, starting from preceramic polymers incorporating powdered calcite.

The selection and application of a mixture of two commercial liquid silicones gave the desired rheological properties to the slurry, making it suitable to be used for impregnation of sacrificial PLA scaffolds, obtained by direct 3-D printing.

A treatment at a very low temperature (600 °C), compared to those used for many silicone-based ceramics, caused the transformation of polymers into silica, maintaining $CaCO_3$ unreacted. The resulting material was a kind of silica-bonded calcite.

$CaCO_3$ was later converted into apatite, by immersion of ceramized samples in a phosphatising bath, providing the reaction of $CaCO_3$ with the P ions. The conversion reached massively the core of the filaments, thanks to the high permeability of the material itself, due to the highly porous structure of the silica-bonded calcite.

The decomposition of calcite was maximized replacing mineral calcite with biological material (eggshell waste).

Defects in the geometry of the final scaffolds were directly related to quality of the sacrificial PLA templates; however, both silica-bonded calcite and silica-bonded apatite samples exhibited an excellent compressive strength, well exceeding 10 MPa.

Further investigations will be undoubtedly dedicated to biological tests, to assess the actual biocompatibility of the material and to explain if the use of biological $CaCO_3$ can positively affect it.

References

[1] B. Baroli, From natural bone grafts to tissue engineering therapeutics: brainstorming on pharmaceutical formulative requirements and challenges. Journal of pharmaceutical sciences, *98*(4) (2009) 1317-1375.

[2] K. de Groot, Bioceramics of calcium phosphate. CRC Press, Boca Raton, FL, 1983.

[3] R.Z. LeGeros, M.S. Tung, Chemical stability of carbonate-and fluoride-containing apatites, Caries Research. 17(5) (1983) 419-429.

[4] K. Sunouchi, K. Tsuru, M. Maruta, G. Kawachi, S. Matsuya, Y. Terada, K. Ishikawa, Fabrication of solid and hollow carbonate apatite microspheres as bone substitutes using calcite microspheres as a precursor, Dental materials journal. 31(4) (2012) 549-557.

[5] Y.D.T Koda, N. Wakamatsu, T. Goto, H. Kamemizu, Y. Moriwaki, M. Adachi, Y. Suwa, Influence of carbonate on sintering of apatites, Journal of dental research. 72(9) (1993) 1279-1284.

[6] J. Barralet, J.C. Knowles, S. Best, W. Bonfield, Thermal decomposition of synthesised carbonate hydroxyapatite, Journal of Materials Science: Materials in Medicine. 13(6) (2002) 529-533.

[7] M. Maruta,S. Matsuya, S. Nakamura, K. Ishikawa, Fabrication of low-crystalline carbonate apatite foam bone replacement based on phase transformation of calcite foam. Dental materials journal. 30(1) (2011) 14-20.

[8] L. Fiocco, S. Li, E. Bernardo, M.M. Stevens, J.R. Jones, Highly porous polymer-derived Wollastonite-Hydroxyapatite ceramics for bone regeneration. Submitted to Biomed. Mater. (2015).

[9] E. Bernardo, L. Fiocco, G. Parcianello, E. Storti, P. Colombo, Advanced ceramics from preceramic polymers modified at the nano-scale: A review, Materials. 7(3) (2014) 1927-1956.

[10] A. Pouchelon, M. Quemin, F. Lafaysse, U.S. Patent No. 7,642,331. Washington, DC: U.S. Patent and Trademark Office (2010).

[11] I. Abdulrahman, H.I. Tijani, B.A. Mohammed, H. Saidu, H. Yusuf, M. Ndejiko Jibrin, S. Mohammed. From Garbage to Biomaterials: An Overview on Egg Shell Based Hydroxyapatite. Journal of Materials, 2014 (2014).

[12] A. Zocca, G. Franchin, H. Elsayed, E. Gioffredi, E. Bernardo, P. Colombo, Direct ink writing of a preceramic polymer and fillers to produce hardystonite $Ca_2ZnSi_2O_7$ bioceramic scaffolds. Submitted to JACS (2015).

[13] I.-J. Paquien, J. Galy, J.-F. Gérard, A. Pouchelon, Rheological studies of fumed-silica-polydimethylsiloxane suspensions, Colloids and Surfaces A: Physicochem. Eng. Asp. 260(1) (2005) 165-172.

[14] F. Monchau, P. Hivart, B. Genestie, F. Chai, M. Descamps, H. F. Hildebrand, Calcite as a bone substitute. Comparison with hydroxyapatite and tricalcium phosphate with regard to the osteoblastic activity, Materials Science and Engineering: C. 33(1) (2013) 490-498.

[15] M.N. Rahaman, X. Liu, T.S. Huang, Bioactive glass scaffolds for the repair of load-bearing bones, in R. Narayan and P. Colombo, Advances in Bioceramics and Porous Ceramics, John Wiley & Sons, 32 (2009) pp. 65-78.

[16] R.A. Nyquist, C.L. Putzig, M.A. Leugers, M. A, The Handbook of Infrared and Raman Spectra of Inorganic Compounds and Organic Salts, Four Volume Set, Journal of the American Chemical Society. 119 (1997) 12422-12422.

[17] J.R. Jones, L.M. Ehrenfried, L.L. Hench, Optimising bioactive glass scaffolds for bone tissue engineering, Biomaterials. 27 (2006) 964-973.

[18] J. Serra, P. Gonzalez, S. Liste, C. Serra, S. Chiussi, B. Leon, M. Perez-Amor, H. O. Ylanen, M. Hupa, FTIR and XPS studies of bioactive silica based glasses, J. Non-Cryst. Sol. 332 (2003) 20–27.

[19] I. Rehman, W. Bonfield, Characterization of hydroxylapatite and carbonated apatite by photo acoustic FTIR spectroscopy, J. Mater. Sci.: Mat. in Med. 8 (1997) 1-4.

[20] P. Siriphannon, Y. Kameshima, A. Yasumori, K. Okada, S. Hayashi, Formation of hydroxyapatite on $CaSiO_3$ powders in simulated body fluid, J. Eur. Ceram. Soc. 22 (2012) 511-520.

[21] J. R. Jones, O. Tsigkoua, E. E. Coates, M. M. Stevens, J. M. Polak, L. L. Hench, Extracellular matrix formation and mineralization on a phosphate-free porous bioactive glass scaffold using primary human osteoblast (HOB) cells, Biomaterials. 28 (2007)1653–1663.

9 Silica-bonded calcite ceramics

9.1 Introduction

Calcium carbonate ($CaCO_3$) is a well-established material for implantation purposes, due to its high biocompatibility and bioactivity. Marine corals (99% $CaCO_3$, aragonite polymorph – 1% organic) have been used as bone graft substitutes since the 80s and 90s[1-4], owing to the distinctive three-dimensional macro-porous framework, naturally mimicking cancellous bone and promoting cell penetration and vascular invasion[4]. From experimental and clinical data, they feature excellent vascularisation, resorbability, biocompatibility and osteoconductivity, so that they can be seen as an interesting alternative to bone grafts[1,2]. It has been also proven that the bone forming response of calcium carbonate is comparable to that of hydroxyapatite[3] (HAp) and that it is able to present rapid carbonated apatite formation[4].

Nowadays, implants of natural origin (such as coral) are no longer accepted in orthopaedics, due to serious drawbacks, such as supply difficulties, biological variability, risks of viral or bacterial contamination[5]. Therefore, synthetic ceramic biomaterials, chemically and morphologically mimicking natural bone tissue, have received a growing interest in the last years. Several studies have been proposed on synthetic $CaCO_3$ and its polymorphs (calcite, aragonite, vaterite)[5-10]. Monchau *et al.*[5] compared the biological properties of synthetic $CaCO_3$ with those of hydroxyapatite and tricalcium phosphate (β-TCP), commonly used as substitutes or filling materials in bone surgery, and demonstrated that synthetic $CaCO_3$ can be shaped into a bone substitute scaffold by slip-casting. The obtained material is non-cytotoxic and facilitates cell proliferation. Similar results were achieved by Lemos and Ferreira[7], who fabricated macroporous $CaCO_3$ by starch consolidation and assessed its accentuated bioactivity. Porous $CaCO_3$ microparticles were also used by Sukhorukov *et al.*[10] as a template for encapsulation of bioactive compounds, exploiting the complete biodegradability of $CaCO_3$. Moreover, Fujita *et al.*[9] performed *in vivo* tests in rabbit tibiae to assess the $CaCO_3$ bone bonding ability, showing an adequate strength of bonding. So, $CaCO_3$ is an interesting alternative not only to natural coralline aragonite, but also to calcium phosphate ceramics in general.

Further experiences are reported in literature about the synthesis of porous calcite microspheres. For instance, hollow $CaCO_3$ microspheres have been produced starting from water-soluble NaCl cores, covered with $Ca(OH)_2$ by granulation[11]. The external shell was later converted from $Ca(OH)_2$ to $CaCO_3$ by carbonation through a stream of CO_2 saturated with water vapour, whereas the cores were solubilised. Otherwise, hierarchically porous $CaCO_3$ microspheres have been fabricated by a precipitation reaction of $CaCO_3$ in the presence of polystyrene-alt-maleic acid (PSMA) as a crystal modifier, starting from a solution of Na_2CO_3 and $CaCl_2$[12].

Considering that cancellous bone has a fully interconnected porous structure, a good bone substitute needs a specific morphology, besides a suitable composition. Therefore, porous materials are of course preferable. Calcite foams have already been fabricated by replica, starting from polyurethane (PU) templates dipped into a slurry of $Ca(OH)_2$ and distilled water[13]. Once infiltrated, the foams have been thermally treated to burn out PU and they have been subsequently exposed to a CO_2 atmosphere to get the carbonation of $Ca(OH)_2$ in $CaCO_3$. Though effective, this method could be simplified using a slurry directly containing calcite, instead of starting with a calcite precursor and then converting it into calcite; anyway, the authors reported to have failed using a calcite slurry, because the foams could not keep their structure after sintering.

In the present study, a technologically advanced method is proposed to fabricate calcite scaffolds with highly ordered open porosity. In particular, we refer to the robocasting of a preceramic paste. This technique relies on direct-writing a continuous ink filament in a layer-by-layer build sequence. The 3-D printable ink was obtained from a solid preceramic polymer (giving SiO_2 in an amount of 35 wt% of the final ceramic), dissolved in isopropanol and mixed with powdered $CaCO_3$ (65 wt%). The polymer-derived-ceramic approach easily allowed the realization of a material which can be considered as a sort of "silica-bonded calcite", in the sense that $CaCO_3$ is bound by amorphous silica, originated by the thermo-oxidative decomposition of the polymer[14] at a particularly low temperature (600 °C). At the same time, this synthesis methodology was successfully coupled with the most revolutionary building technique developed in the last years, i.e. the direct 3-D printing. Scaffolds showed a good mechanical behaviour in compression mode and an extensive open porosity, besides extremely pronounced biological properties, being able to stimulate the cells proliferation when cultured with bone marrow stromal cells for 2 weeks. The results will be submitted soon for publication.

9.2 Experimental

9.2.1 Preparation of scaffolds

A commercial polymethylsiloxane, SILRES® MK (Wacker-Chemie GmbH, München, Germany), known to have a silica yield of 84 wt% after thermal decomposition in air[15], was used for the fabrication of the preceramic ink. The required amount of silica (35 wt% of the final ceramic) was obtained from two contributions, that is 10 wt% from nano-sized silica (fumed silica, Aerosil R106, Evonik Germany) and 90 wt% from the above silicone, in order to positively modify the rheological properties of the slurry[16,17]. All the 3-D printing operations were carried out in collaboration with Mr. Hamada Elsayed (University of Padova).

Fumed silica powders were wet mixed with MK in isopropanol (8 ml for 16 g of silica precursors) by means of a ball mill (60 min at 100 rpm, Pulverisette 7 planetary planetary ball mill, Fritsch, Idar-Oberstein, Germany). $CaCO_3$ micro-sized powders (<10 µm, Industrie Bitossi, Italy) were subsequently incorporated into the polymer and again mixed (4 h at 400 rpm), to obtain a perfectly homogenous suspension with very fine fillers and no trace of powder aggregates. The achievement of such properties was strictly necessary for the direct ink writing, due to the need to avoid clogging throughout the printing step and to have continuity in the fluid flow through the nozzle.

A Power WASP orienting extruder (Massa Lombarda, Italy), expressly equipped with a syringe to print silicones pastes incorporating fillers, was used to print the preceramic ink. The syringe of the feeding system was filled with the preceramic paste and scaffolds were later printed with conical nozzle (with a diameter of 0.41 mm, Nordson EFD, Westlake, Ohio) immersed in vegetal oil, thus preventing the premature drying of the solvent, that would have affected the viscosity of the ink. The configuration of the printing system and the final result have been reported in Fig. 4.2 in §4.2.6.

Following the CAD file, scaffolds were in the form of prisms with dimensions 15 mm x 5 mm x 5 mm, as resulting from the overlapping of cylindrical rod, periodically arranged along x and y axes. The rods were in a stacking density of 11 rod/cm on the x-y plane, and the distance between the longitudinal axes of adjacent rods was of 1 mm. Two different designs were considered for the scaffolds, with a distinction regarding the spacing between adjacent rods along the z axis: the spacing was set at 350 µm for samples later referred to as "t-1" design and 300 µm for "t-2" design.

After removal from the oil, printed scaffolds were cross-linked at 350 °C, with a heating rate of 0.5 °C/min and dwelling time of 1 h, prior to ceramization at 600 °C (same heating rate and dwelling time as the cross-linking treatment). This relatively low temperature was selected with the aim of getting the thermo-oxidative decomposition of silicone into amorphous silica[14], without affecting the stability of calcite.

9.2.2 Characterization of scaffolds

Micro-structural characterizations were performed by optical stereomicroscopy (AxioCam ERc 5s Microscope Camera, Carl Zeiss Microscopy, Thornwood, New York, US), scanning electron microscopy (FEI Quanta 200 ESEM, Eindhoven, The Netherlands) equipped with EDS and X-ray diffraction (XRD; Bruker AXS D8 Advance, Bruker, Germany - CuKα radiation, 0.15418 nm, 40 kV-40 mA, 2θ=20-70 °, step size=0.05 °, 2s counting time). The Match! software package (Crystal Impact GbR, Bonn, Germany) was used for phase identification, supported by data from PDF-2 database (ICDD-International Centre for Diffraction Data, Newtown Square, PA, USA).

The bulk density (ρ_b) of the foams was determined using a caliper and a digital balance. The skeletal density (ρ_s) was measured on foams, using a He gas pycnometer (Micromeritics AccuPyc 1330, Norcross, GA), while the true density (ρ_t) of the material was measured on very finely ground powders of scaffolds. The percentage of porosity (%P) was then calculated using the following equation: $\%P=1-(\rho_b/\rho_s)$.

Selected scaffold structures were subjected to mechanical characterization in compression mode at room temperature, using an Instron 1121 UTM (Instron Danvers, MA, USA) with a cross-head speed of 1 mm/min. Each data point is presented as the mean value of five to ten samples.

9.2.3 Biological tests

Scaffolds of 100 mg were immersed in 25 ml of simulated body fluid (SBF) and maintained in a controlled environmental chamber at at 37 °C. The solution was refreshed every 2 days and the pH of the SBF was measured to monitor the pH variation induced by the samples. All the experiments were done in triplicate.

After 1, 3, 7 and 14 days, the samples were removed from the solution, immediately rinsed with distilled water and then dried at room temperature for 24 hours, before being characterized by SEM imaging (Quanta 2000; FEI Co., Eindhoven, the Netherlands). In addition, a local chemical analysis was carried out by X-ray Energy Dispersion Spectroscopy (Inca; Oxford Instruments, Buckinghamshire, U.K.). The chemical nature of the precipitated HCA was also investigated by means of Micro-Raman spectroscopy (Horiba Jobin-Yvon, Villeneuve d'Ascq, France). A 632.8 nm diode laser with an output power of 20 mW without any filter was employed. The laser was focused on the scaffolds' surface by means of 50x and 100x objectives.

Samples of around 200 mg were also seeded with bone marrow stromal cells for 14 days and cultivated in α-MEM supplemented with 50 mg/ml ascorbic acid, 100 nM dexamethasone and 10 mM b-glycerophosphate for osteogenic stimulation. Cells were suspended in basal media at a concentration of 100.000 cells/ml before being seeded.

The biological tests were performed thanks to a collaboration with Prof. V. Cannillo's group (University of Modena and Reggio Emilia, Italy) and with Prof. A. Boccaccini's group (University of Erlangen-Nuremberg, Germany).

9.3 Results

9.3.1 Characterization of scaffolds

The morphological structure of 3-D printed samples was highly regular, as visible in Fig. 9.1. The open porosity was geometrically ordered and interconnected in all 3 dimensions (Fig. 9.1a-c). Although the diameter of the nozzle was of 410 μm, the rods were approximately 450 μm in diameter as printed. This was obviously due to the radial expansion of the extrudate occurring when the material leaves the nozzle, caused by the abrupt drop of temperature and pressure. Anyway, after ceramization, the diameter of the rods decreased to approximately 400 µm, due to the shrinkage which usually accompanies the polymer-to-ceramic conversion of preceramic polymers[14].

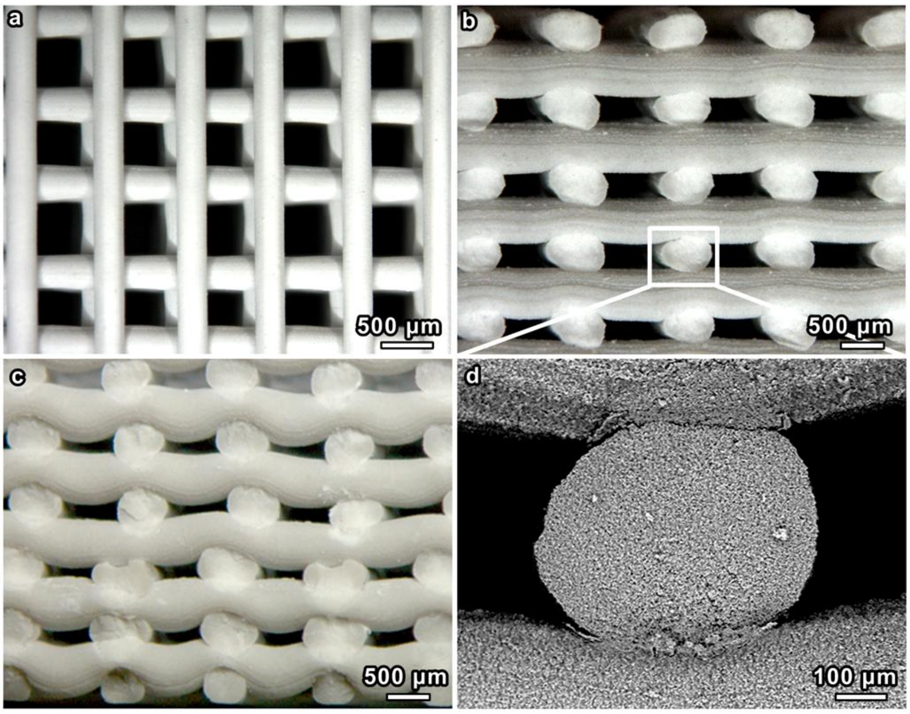

Fig. 9.1 Morphology of 3-D printed scaffolds after ceramization: a) t-1 top view; b) t-1 side view; c) t-2 side view; d) high magnification detail of a rod fracture surface.

For t-1 and t-2 designs, the overall morphology was identical, except for the spacing along the z axis (Fig. 9.1b-c). As previously mentioned, the spaces between adjacent rods were of 350 µm along the z axis for t-1 design and 300 µm for t-2 design. The reduction of the space along the z axes resulted in a higher mutual interfusion between adjacent layers of rods in t-2 samples, with an increase in the contact area at the joints. Furthermore, in t-2 samples the rods were affected by structural sagging, in comparison to perfectly linear rod deposition observed for t-1 samples (Fig. 9.1b-c).

The final spacing between adjacent rods on the x-y plane was of approximately 500 µm. This pore size fits well with the requirements for a scaffold for bone tissue engineering. Hulbert *et al.*[18], in fact, recommended a minimum pore diameter of 100 µm in their early work, but more recent studies have shown better osteogenesis for implants with pores greater than 300 µm[19-21].

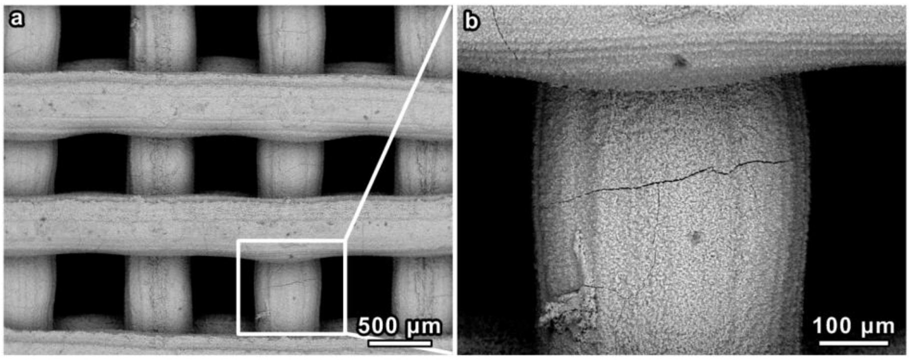

Fig. 9.2 SEM images of t-1 scaffolds after ceramization: a) top view, b) higher magnification detail.

The higher magnification detail in Fig. 9.1d reveals that the cross-section of the rods did not contain defects; on the contrary, some microcracks were present on the surface of rods, as shown by Fig. 9.2a-b, for both designs. The cracks might be reasonably correlated with both the shrinkage of the material and the release of gaseous products throughout the thermo-oxidative decomposition of the silicone, while converting into a ceramic material. Crack generation is typically observed especially in dense polymer-derived-ceramic components, since the elimination of gases can cause local pressure accumulation phenomena[14].

Tab. 9.1 Summary of physical and mechanical properties of printed scaffolds after ceramization.

Type of geometry	ρ_{bulk} (g/cm^3)	$\rho_{skeleton}$ (g/cm^3)	ρ_{true} (g/cm^3)	P_{open} (%)	σ_{comp} (MPa)
t-1	0.93 ± 0.04	2.56 ± 0.01	2.57 ± 0.01	64	2.9 ± 0.7
t-2	1.07 ± 0.02	2.43 ± 0.04	2.57 ± 0.01	56	5.5 ± 0.3

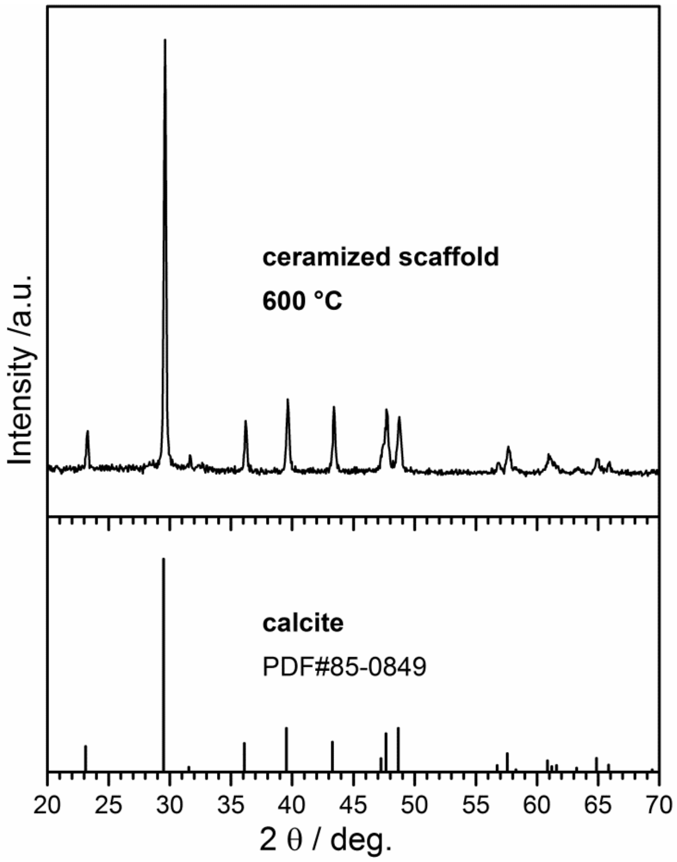

Fig. 9.3 X-ray diffraction patterns of printed scaffolds, after ceramization at 600 °C.

The fact that the cracks were not visible in the cross-section, but only on the surface, suggests that the mechanical properties of the printed scaffolds could not be considerably degraded. This is confirmed by Tab. 9.1, where it is reported a compressive strength (σ_{comp}) of about 2.9 ± 0.7 MPa for t-1 samples and 5.5 ± 0.3 MPa for t-2 ones. These values are in line with the compressive strength of natural trabecular bone, which is reported to be in the 2-12 MPa[22] range. In particular, for t-2 samples, the standard deviation is quite low, as a proof of high sample reproducibility and more reliable values. The increase in σ_{comp} for t-2 samples compared to t-1 might be explained by several factors. First, it could be correlated with the decrease in open porosity (P_{open}), which was calculated to be 64 % for t-1 and 56 % for t-2. Then, as already highlighted, rods in t-2 samples had a higher contact area at the joints, due to a higher mutual interfusion between adjacent layers of rods. Finally, the reduced voids in the cross-section could limit buckling phenomena. A summary of density and porosity values is also presented in Tab. 9.1. The similarity between skeleton and true density ($\rho_{skeleton}$ and ρ_{true} respectively) is an indicator of a total lack of closed porosity.

The X-ray diffraction patterns presented in Fig. 9.3 demonstrate that the thermal treatment at 600 °C of silicone mixed with powdered $CaCO_3$ was effective in maintaining calcite unreacted, while the polymer transformed into silica. In fact, a perfect overlapping between the experimental and the reference pattern of calcite ($CaCO_3$ – PDF#85-0849) can be observed, and no other peak appears.

Silica (SiO_2), resulting from the polymer-to-ceramic conversion of silicone, is obviously not visible in the pattern, due to its amorphous nature[14]. As a final remark on the microstructure, Fig. 9.4 demonstrates that both calcium (Ca) and silicon (Si) concentration were practically uniform along the cross-section of rods, so that the calcite filler can be considered to be homogeneously distributed.

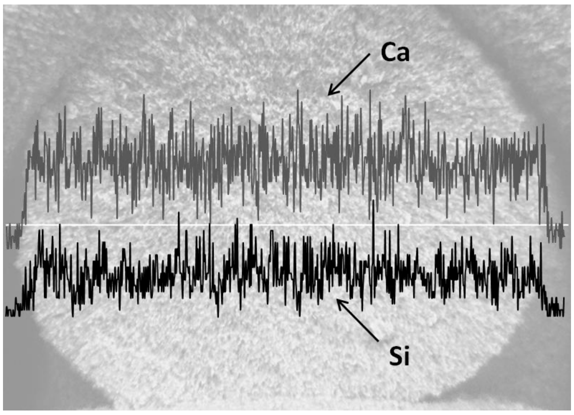

Fig. 9.4 Semi-quantitative SEM-EDS: Ca and Si concentration profiles along the line in a rod cross-section.

9.3.2 Bioactivity tests

One of the main features of bioactive materials is the ability to form an hydroxyapatite-like layer on their surfaces when in contact with physiological fluids *in vivo* or with simulated body fluids (SBF) *in vitro*, i.e. an acellular solution with inorganic ion concentrations similar to those of the human extracellular fluid. This hydroxyapatite layer appears to be associated with bioactivity and it is considered as responsible for the bonding of bioactive ceramics to the host bone. Thereby, the *in vitro* bioactivity, is considered as a fundamental prerequisite for an in vivo biointegration of the implant. However, such tests should be considered with great caution. In fact *in vitro* assays are too simple to simulate the real physiological context, which is intrinsically dynamic and includes vitamins, proteins and in particular growth factors, lipids, cells and so forth; so, SBF tests are rather intended to offer a relatively cheap and easy tool to mimic the inorganic reactions which are expected to take place after the implantation of the material. For these reasons, although the apatite formation in SBF is usually considered as an important prerequisite for the subsequent *in vivo* osseointegration, however the assessment of the biological responsiveness needs further experimental steps, such as cytotoxicity and genotoxicity assays[23].

After 7 days in SBF it was possible to locally identify, on the samples surface, several globular precipitates with the typical HAp morphology. The precipitation of a HAp film can be easily confirmed by means of Raman spectroscopy, due to the high intensity of the Raman peaks related to P–O vibration modes, when apatite nucleation begins. Moreover, since the C–O vibrational modes, which are associate to a carbonate group, are expected to be very active in Raman spectroscopy, it is possible to study in greater detail the nature of the *in vitro* grown HA, which is usually carbonated.

Raman spectra were acquired on samples immersed in SBF for different times are reported in Fig. 9.5a. The spectra seemed to evolve with increasing soaking times and become similar to that of HAp, apart from local fluctuations.

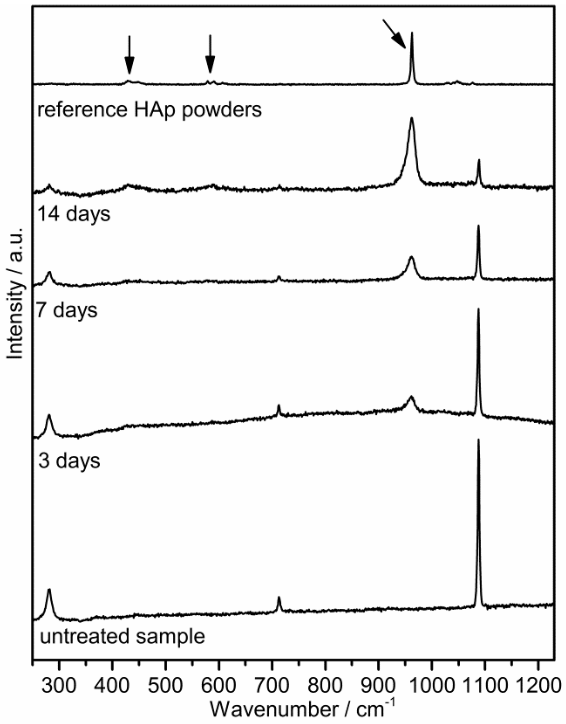

Fig. 9.5 Raman spectra of samples immersed in SBF for different times, in comparison with HAp powders taken as a reference (upper pattern).

The strong peak at 950 cm^{-1} corresponds to the symmetric stretching of the $(PO_4)^{3-}$ groups of HAp, as well as the two peaks at about 430 cm^{-1} and 590 cm^{-1}, which can be ascribed to the ν_2 (bend, asymmetric stretch) and ν_4 (bend, asymmetric stretch) modes of the $(PO_4)^{3-}$ groups of HAp[24,25]. These peaks (arrows in Fig. 9.5b) were found to become stronger for increasing times of immersion, confirming the precipitation of an increased amount of HAp with time.

Concerning the intense sharp Raman band at about 1085 cm^{-1}, it can be assigned to the ν_1 $(CO_3)^{2-}$ symmetric stretching vibration. Obviously, this cannot be a selective indication of the presence of carbonate apatite (HCA), in fact carbonate groups could belong to both $CaCO_3$ and HCA. Other relatively strong Raman bands at about 713 cm^{-1} and 280 cm^{-1} can be assigned to calcite as well[26-27].

The produced scaffolds look rather promising in terms of pH variation induced in SBF. In this sense, the pH value was between 7.4 and 7.6 throughout the process, thus indicating a slow ion leaching. Values between 7.4 and 8 can be considered optimal for osteoblast adhesion and proliferation.

9.3.3 Cell culture test

After 14 days of cell culture, the attachment of the cells to the scaffolds, the cell morphology and the formation of cell matrix were investigated by SEM imaging. The images are reported in Fig. 9.6a,b,c. Cells spread across the surface of the struts, exhibiting elongated profiles, and colonized the 3-D architecture of the scaffolds. Cells were also found to form Ca-phosphates precipitates, confirming that mineralization occurred.

The same conclusions can be drawn from the fluorescence staining reported in Fig. 9.6d, showing the homogeneous cell growth on the samples.

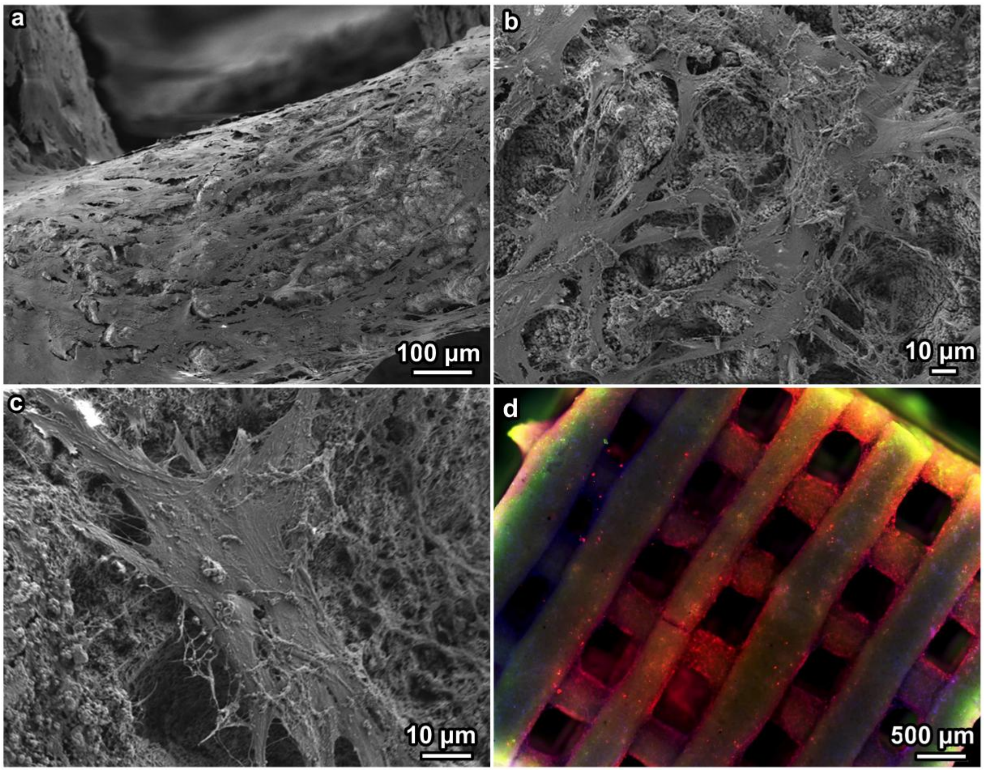

Fig. 9.6 SEM micrographs of MC3T3 cells following culture on the scaffolds for 14 days: a) detail of a strut; b-c) higher magnification; d) live/dead fluorescence staining (red=cytoskeleton, blue=nuclei; green=mineralization).

9.4 Conclusions

Silica-bonded calcite has been successfully fabricated by direct 3D printing of silicone/calcite pastes. The printed scaffolds were cross-linked prior to ceramization, resulting in ceramic components made of calcite surrounded by binding phase of amorphous silica.

The decomposition of calcite was prevented by the adoption of a temperature of polymer-to-ceramic conversion far lower than usual for silicone-derived ceramics.

The samples exhibited a highly ordered and interconnected porosity of 56-64 % and a good mechanical behaviour, with a compressive strength of 2.9-5.5 MPa, in good agreements with the requirements of porosity and mechanical strength for scaffold to be used in actual tissue engineering experiments.

Concerning the biological properties, the printed samples were subjected to dissolution study in SBF and cell culture study with bone marrow stromal cells. They showed good bioactivity and very pronounced ability to stimulate cell adhesion and proliferation on the scaffolds surface.

In the light of these encouraging results, 3D printed silica-bonded calcite samples derived from preceramic polymers and fillers are expected to be suitable candidates for bone tissue engineering applications.

Further biological analyses will certainly be performed to assess if the scaffolds can also stimulate cell differentiation and gene expression.

References

[1] Guillemin, G., Patat, J. L., Fournie, J., Chetail, M. (1987). The use of coral as a bone graft substitute. Journal of biomedical materials research, 21(5), 557-567

[2] Guillemin, G., Meunier, A., Dallant, P., Christel, P., Pouliquen, J. C., Sedel, L. (1989). Comparison of coral resorption and bone apposition with two natural corals of different porosities. Journal of biomedical materials research, 23(7), 765-779

[3] Ohgushi, H., Okumura, M., Yoshikawa, T., Inboue, K., Senpuku, N., Tamai, S., Shors, E. C. (1992). Bone formation process in porous calcium carbonate and hydroxyapatite. Journal of biomedical materials research, 26(7), 885-895

[4] Ohgushi, H. (1997, September). Coral Derived Porous Framework Having Different Chemical Compositions as a Scaffold for Osteoblastic Differentitation. In Materials Science Forum (Vol. 250, pp. 209-220).

[5] Monchau, F., Hivart, P., Genestie, B., Chai, F., Descamps, M., Hildebrand, H. F. (2013). Calcite as a bone substitute. Comparison with hydroxyapatite and tricalcium phosphate with regard to the osteoblastic activity. Materials Science and Engineering: C, 33(1), 490-498.

[6] Maeda, H., Maquet, V., Kasuga, T., Chen, Q. Z., Roether, J. A., Boccaccini, A. R. (2007). Vaterite deposition on biodegradable polymer foam scaffolds for inducing bone-like hydroxycarbonate apatite coatings. Journal of Materials Science: Materials in Medicine, 18(12), 2269-2273.

[7] Lemos, A. F., Ferreira, J. M. F. (2000). Porous bioactive calcium carbonate implants processed by starch consolidation. Materials Science and Engineering: C, 11(1), 35-40.

[8] Lucas, A., Gaudé, J., Carel, C., Michel, J. F., Cathelineau, G. (2001). A synthetic aragonite-based ceramic as a bone graft substitute and substrate for antibiotics. International Journal of Inorganic Materials, 3(1), 87-94.

[9] Fujita, Y., Yamamuro, T., Nakamura, T., Kotani, S., Ohtsuki, C., Kokubo, T. (1991). The bonding behavior of calcite to bone. Journal of biomedical materials research, 25(8), 991-1003.

[10] Sukhorukov, G. B., Volodkin, D. V., Günther, A. M., Petrov, A. I., Shenoy, D. B., Möhwald, H. (2004). Porous calcium carbonate microparticles as templates for encapsulation of bioactive compounds. Journal of Materials Chemistry, 14(14), 2073-2081.

[11] Sunouchi, K., Tsuru, K., Maruta, M., Kawachi, G., Matsuya, S., Terada, Y., Ishikawa, K. (2012). Fabrication of solid and hollow carbonate apatite microspheres as bone substitutes using calcite microspheres as a precursor. Dental materials journal, 31(4), 549-557.

[12] Yu, J., Jimmy, C. Y., Zhang, L., Wang, X., Wu, L. (2004). Facile fabrication and characterization of hierarchically porous calcium carbonate microspheres. Chemical communications, (21), 2414-2415.

[13] Maruta, M., Matsuya, S., Nakamura, S., Ishikawa, K. (2011). Fabrication of low-crystalline carbonate apatite foam bone replacement based on phase transformation of calcite foam. Dental materials journal, 30(1), 14-20.

[14] Colombo, P., Mera, G., Riedel, R., Sorarù, G. D. (2010). Polymer-Derived Ceramics: 40 Years of Research and Innovation in Advanced Ceramics.Journal of the American Ceramic Society, 93(7), 1805-1837.

[15] Bernardo, E., Colombo, P., Dainese, E., Lucchetta, G., Bariani, P. F. (2012). Novel 3-D wollastonite-based scaffolds from preceramic polymers containing micro-and nano-sized reactive particles. Advanced Engineering Materials, 14(4), 269-274.

[16] Zocca A, Franchin G, Elsayed H, Gioffredi E, Bernardo E, Colombo P. Direct ink writing of a preceramic polymer and fillers to produce hardystonite $Ca_2ZnSi_2O_7$ bioceramic scaffolds. Submitted to JACS 2015

[17] Paquien I-J, Galy J, Gérard J-F, Pouchelon A. Rheological studies of fumed-silica-polydimethylsiloxane suspensions. Colloids surf. Physicochem. Eng. Asp. 260, 165-172 (2005)

[18] Hulbert, S. F., Young, F. A., Mathews, R. S., Klawitter, J. J., Talbert, C. D., Stelling, F. H. (1970). Potential of ceramic materials as permanently implantable skeletal prostheses. Journal of biomedical materials research, 4(3), 433-456.

[19] Kuboki, Y., Jin, Q., Takita, H. (2001). Geometry of carriers controlling phenotypic expression in BMP-induced osteogenesis and chondrogenesis. The Journal of Bone & Joint Surgery, 83(1 suppl 2), S105-S115.

[20] Tsuruga, E., Takita, H., Itoh, H., Wakisaka, Y., Kuboki, Y. (1997). Pore size of porous hydroxyapatite as the cell-substratum controls BMP-induced osteogenesis. Journal of Biochemistry, 121(2), 317-324.

[21] Götz, H. E., Müller, M., Emmel, A., Holzwarth, U., Erben, R. G., Stangl, R. (2004). Effect of surface finish on the osseointegration of laser-treated titanium alloy implants. Biomaterials, 25(18), 4057-4064.

[22] M.N. Rahaman, X. Liu, T.S. Huang, Bioactive glass scaffolds for the repair of load-bearing bones, in R. Narayan and P. Colombo, Advances in Bioceramics and Porous Ceramics, John Wiley & Sons, 32 (2009) pp. 65-78.

[23] Bohner, M., Lemaitre, J. (2009) Can bioactivity be tested in vitro with SBF solution? Biomaterials, 30, 2175-2179

[24] Grossin D, Rollin-Martinet S, Estournès C, Rossignol F, Champion E, Combes C et al. Biomimetic apatite sintered at very low temperature by spark plasma sintering: Physico-chemistry and microstructure aspects. Acta Biomater 2010;6:577-585.

[25] Bellucci D, Sola A, Cannillo V. Low temperature sintering of innovative bioactive glasses. J Am Ceram Soc 2012;95:1313-1319.

[26] Sun, J., Wu, Z., Cheng, H., Zhang, Z., Frost, R. L. (2014). A Raman spectroscopic comparison of calcite and dolomite. Spectrochimica Acta Part A: Molecular and Biomolecular Spectroscopy, 117, 158-162.

[27] Gunasekaran, S., Anbalagan, G., Pandi, S. (2006). Raman and infrared spectra of carbonates of calcite structure. Journal of Raman Spectroscopy, 37(9), 892-899.

Part II

Functional ceramics from preceramic polymers and reactive fillers

Introduction

The deep knowledge and expertise gained in the silicone/fillers systems could also be applied for synthesizing further silicate formulations for different applications, in the lights of the following observations:

- multifunctionality of silicates;
- analogies in the crystalline structure;
- analogies in synthesis process;
- multifunctionality of fillers.

First, one of the most peculiar characteristics of specific silicates, such as forsterite (Mg_2SiO_4) or hardystonite ($Ca_2ZnSi_2O_7$), is that they are multifunctional. In fact, besides pronounced biological properties which make them suitable as biomaterials, as reported in literature[1,2], they also exhibit other properties. In particular, forsterite is known to be a dielectric material, whereas hardystonite may be used as a phosphor (bluish-violet emission).

The biocompatibility of a polymer-derived forsterite coating on hydroxyapatite foams was assessed in 2012 (in the framework of "Progetto Vigoni") with preliminary investigations, but the tests did not succeed, possibly due to the presence of residual MgO agglomerates in the material, negatively affecting the pH when immersing forsterite in Millipore water. For this reason, biomedical applications of polymer-derived forsterite were abandoned in favour of its dielectric applications. In this case, MgO residual phase was suppressed by means of the incorporation of TiO_2: when using micro-sized TiO_2, it reacted with MgO giving Mg-titanates; when using nano-sized TiO_2, it reacted with pure forsterite, which transformed into a forsterite solid solution with Ti^{4+} replacing Si^{4+} ions. Forsterite and its above-mentioned modifications showed interesting dielectric properties[3], especially in terms of low dielectric losses, and they will be shown in §10.

A second connection between the applications of silicates in bone replacing and in other fields is offered by the analogy in the crystalline structure of silicates belonging to the same family. For instance, akermanite ($Ca_2MgSi_2O_7$), hardystonite and gehlenite ($Ca_2Al(AiSi)O_7$) are all classified as melilites, which are sorosilicates. Melilites are not only good biosilicates, as in the case of akermanite and hardystonite, but they also are interesting host matrices for rare-earth ions (RE).

Their general formula is $X_2T1(T2)_2O_7$, possessing a structure that can be described as consisting of $T2_2O_7$ dimers (T2=Si, Al, etc.) connected via T1 cations (Mg, Zn, etc.) in tetrahedra to form a sheet-like arrangement[4]. These sheets are linked together by large cations X (Ca, Sr, Ba, etc.) occupying octahedral sites, as already explained in §6.2.

RE have been widely studied due to the distinctive optical properties of the materials in which they are inserted as dopants (in fact the size of RE ions is similar to that of alkali earth metals). On the one hand, akermanite and hardystonite might be doped with bivalent phosphor activators, such as Eu^{2+}, which are difficult to achieve by reduction of Eu^{3+} upon high temperature synthesis processes. On the other hand, trivalent ions could be hosted in their crystalline structure, but the charge variation induced would be compensated by the creation of vacancies, with a dramatic decrease of luminescence, because of the non-radiative nature of the transitions to a vacancy. Instead, we can refer to a "compensable system", such as the crystal structure of gehlenite. Gehlenite ($Ca_2Al(AiSi)O_7$) has a stechiometry of T2 sites of 50 % Al – 50 % Si, being Al ions accommodated in all the T1 sites and in half of the T2 sites. Therefore, gehlenite can easily incorporate trivalent ions when partially replacing Si^{4+} with Al^{3+} ions, thus adopting a formulation allowing charge compensation ($Ca_{2-2x}Eu_{2x}(Al_{1+2x}Si_{1-2x})O_7$ with x=0.07)[5]. Eu-doped polymer-derived gehlenite ceramics[6] exhibiting strong optical properties will be shown in §13.

A third aspect which can connect silicates for different applications is the analogy in the synthesis process, which enable the transfer of the approach for the synthesis of biosilicates to other formulations. For instance, it has been shown in §5.1 that sodium borate ($Na_2B_4O_7{\cdot}10H_2O$) can be incorporated in the silicone-based mixtures in low amount as a foaming agent, but also as a mineralizing filler. In fact, it provides a borate liquid phase upon firing, thus promoting the ionic interdiffusion and facilitating the formation of the desired silicate phases, and then, after cooling at room temperature, it remains as a glass phase. By this way, the crystal phases are surrounded by an intergranular glass matrix, resulting in a glass-ceramic product.

The same approach has been used for synthesizing a Eu-doped polymer-derived glass-ceramic with luminescent properties[7], incorporating a B_2O_3 precursor (boric acid) in a higher amount than in the previous experiences. In this case, B_2O_3 was not intended to represent simply a flux, but it was specifically designed to react with lanthanum oxide (La_2O_3), thus forming one of the host crystalline phases for Eu ions, besides its participation in the surrounding glass matrix. These results will be discussed in depth in §12.

Finally, the same fillers already discussed in the previous section can still be used by virtue of their multifunctionality, such as magnesium hydroxide ($Mg(OH)_2$), sodium phosphate dibasic heptahydrate ($Na_2HPO_4{\cdot}7H_2O$), sodium borate ($Na_2B_4O_7{\cdot}10H_2O$). They have been extensively shown to be helpful in the fillers/silicones mixtures as foaming agents, thanks to their water release upon heating, and as oxide precursors. This feature has also been exploited for the synthesis of porous cordierite ($Mg_2Al_4Si_5O_{18}$), starting from silicone-based mixtures incorporating alumina (Al_2O_3) and $Mg(OH)_2$. Cordierite is an appreciated silicate in the field of catalytic converters and particulate filters for diesel engines and, in general, for components subjected to severe thermal gradients. Polymer-derived cordierite ceramics[8] have shown mechanical and physical properties in good agreement with those reported in literature and will be discussed in §11.

References

[1] Wu, C., Chang, J., Zhai, W. (2005). A novel hardystonite bioceramic: preparation and characteristics. Ceramics international, 31(1), 27-31.

[2] Tavangarian, F., Emadi, R. (2011). Nanostructure effects on the bioactivity of forsterite bioceramic. Materials Letters, 65(4), 740-743.

[3] Bernardo, E., Fiocco, L., Giffin, G. A., Di Noto, V., Colombo, P. (2014). Microstructure Development and Dielectric Characterization of Forsterite-Based Ceramics from Silicone Resins and Oxide Fillers. Advanced Engineering Materials, 16(6), 806-813.

[4] Burzo, E. (2005). Melilites and related silicates. Magnetic Properties of Non-Metallic Inorganic Compounds Based on Transition Elements: Sorosilicates, Landolt-Börnstein–Group III Condensed Matter, 27.

[5] Zhang, Q., Wang, J., Zhang, M., Ding, W., Su, Q. (2007). Enhanced photoluminescence of Ca2Al2SiO7: Eu^{3+} by charge compensation method. Applied Physics A, 88(4), 805-809.

[6] Bernardo, E., Fiocco, L., Prnová, A., Klement, R., Galusek, D. (2014). Gehlenite: Eu^{3+} phosphors from a silicone resin and nano-sized fillers. Optical Materials, 36(7), 1243-1249.

[7] Fiocco L., Babakhanova Z., Bernardo E. Facile obtainment of luminescent glass-ceramics by direct firing of a preceramic polymer and oxide fillers. Ceram. Int. (Accepted for publication in January 2016 – DOI: 10.1016/j.ceramint.2016.01.052)

[8] Fiocco L., Bernardo E. (2015). Novel cordierite foams from preceramic polymers and reactive oxide fillers. Materials Letters, 159, 98-101.

10 Forsterite ceramics

10.1 Introduction

The present chapter aims at exploring the production of forsterite, Mg_2SiO_4 (or $2MgO{\cdot}SiO_2$), from preceramic polymers incorporating MgO nanoparticles. This silicate is particularly appreciated for submillimetric-wave applications (telecommunication and radar systems, from ultra-high speed LAN to car anti-collision devices, dielectric resonators and filters), due to its low dielectric losses when operating with high-frequency electromagnetic waves[1-3].

The technology of "oxide-filled silicones" is intended for many applications, both structural (e.g. refractory components, thermal barrier coatings)[4,5] and functional (bioactive scaffolds, inorganic phosphors)[5,6]. Except for mullite, well-known to be an excellent substrate material in high-performance packaging applications[7], no specific investigation has been so far dedicated to silicate dielectrics produced by this approach. Dielectric applications, however, can benefit from the distinctive advantage of preceramic polymers, that is the possibility to shape components in the polymeric form using plastic forming technologies, such as warm pressing, extrusion, injection molding, foaming, machining, fused deposition and 3-D printing, before ceramic conversion[4].

According to this approach, nano-sized particles act as active fillers, directly reacting with the amorphous silica, deriving from the oxidative decomposition of the silicone resins. The contribution of micro-sized particles is less straightforward, since they are much less reactive. It should be noted, however, that also passive (i.e. not reactive) fillers could be useful because they dilute the preceramic polymer, as secondary unreactive phases, and consequently decrease the amount of gas evolved and the associated shrinkage that generates during the polymer-to-ceramic transformation, in turn favoring the manufacturing of samples free from macroscopic cracks[4].

Forsterite possesses a poor solid-state sinterability[2], in analogy with mullite, but with additional difficulties associated to the possible presence of impurities, such as unreacted MgO and Mg-silicates with different MgO/SiO_2 molar ratio, e.g. polymorphic variants of enstatite ($MgSiO_3$, or $MgO{\cdot}SiO_2$), known to affect negatively both sinterability and dielectric losses[3]. The control of impurities, in forsterite ceramics, relies basically on the adoption of non-stoichiometric formulations, e.g. associated to MgO/SiO_2 molar ratios higher than 2, or on the introduction of further components, such as TiO_2, leading to forsterite solid solutions (Ti^{4+} ions replacing Si^{4+} ions, according to the general formula $Mg_2Si_{1-x}Ti_xO_4$)[3,8]. Titania, when not incorporated in forsterite or in further compounds (Mg-titanates),[8] is useful also for modifying the dielectric properties of forsterite-based ceramics, with forsterite/rutile composites typically exhibiting an improved temperature coefficient of resonant frequency (τ_f)[1].

The multiform impact of TiO_2 on forsterite ceramics was considered as a great challenge for the polymer-based approach, with micro-sized powders (passive) introduced as secondary phase or with nano-sized powders (reactive) added to form solid solutions.

Although densification of forsterite-based ceramics was not optimized in this work, mainly due to the very low temperatures adopted (not exceeding 1100 °C), the polymer-based approach was effective in controlling the phase development and leading to materials with very promising dielectric properties.

The results of this investigation were published in 2014 by Bernardo *et al.*[9].

10.2 Experimental

10.2.1 Preparation of samples

A commercially available solid silicone resin, Silres® MK (Wacker-Chemie GmbH, Munich, Germany), was used as silica source. The polymer was first dissolved in isopropanol and then mixed with MgO nanoparticles (Inframat Advanced Materials, Manchester, CT, USA, 30 nm). The weight balance among constituents followed the stoichiometric SiO_2/MgO molar proportions of forsterite (i.e. SiO_2/MgO=1/2), considering the ceramic yield of MK (84 %, i.e. 84 g of silica are obtained from 100 g of polymer after heating in air to high temperature)[6]. Selected additional formulations were moreover tested, comprising also a different liquid preceramic polymer, Silres® H62C (Wacker-Chemie GmbH, Munich, Germany) and secondary fillers. The second polymer was used to replace 50% of the total silica content deriving from the MK polymer (considering the lower ceramic yield of H62C, equal to 0.58, the two polymers were used in the weight ratio of H62C/MK=0.84/0.58=~1.45). The secondary fillers consisted of TiO_2, in form of both micro- and nano- sized particles (m-TiO_2, 0.8 µm mean particle size, Industrie Bitossi, Vinci, Italy, and n-TiO_2, 13 nm mean particle size, VP P90, Evonik Industries AG, respectively). Isopropanol was used as solvent/dispersant, in an amount of 20 ml for for 10 g of starting materials.

The mixing was performed under magnetic stirring, followed by sonication for 10 min, which allowed to obtain stable and homogeneous dispersions, later cast in large glass containers and left to dry overnight at 80 °C in air. The mixtures comprising the H62C silicone were additionally heated also at 250 °C for 30 min, in order to favour the cross-linking of the polymer, in analogy with previous experiences[10]. The resulting silicone/filler composites were then manually ground into fine powders by pestle and mortar, subsequently cold-pressed in a cylindrical steel die (40 MPa for 2 min), without using any binder. Disc specimens with a diameter of 20 mm and thickness of approximately 1 mm were obtained and heat treated at 800-1100 °C for 1-3 h, with a heating rate of 2 °C/min.

10.2.2 Characterization of samples

The bulk density of the discs was determined by means of the Archimedes' method, using water as the buoyancy medium.

Microstructural characterizations were performed by scanning electron microscopy (FEI Quanta 200 ESEM, Eindhoven, The Netherlands) equipped with EDS and by X-ray diffraction (Bruker AXS D8 Advance, Karlsruhe, Germany), supported by data from PDF-2 database (ICDD-International Centre for Diffraction Data, Newtown Square, PA) and Match! program package (Crystal Impact GbR, Bonn, Germany).

Dielectric spectra of selected samples were obtained by Prof. V. Di Noto's group (Department of Chemical Sciences, University of Padova). Spectra were collected from 0.01 to 10^7 Hz using an Alpha-A analyser (Novocontrol Technologies GmbH, Hundsangen, Germany) and from 10^3 Hz to 2×10^{10} Hz with a E5071C network analyser and a high temperature coaxial probe coupled with an electronic calibration module (ECal) (Agilent Technologies Inc., Santa Clara CA, USA) as described elsewhere[11].

10.3 Results

Fig. 10.1 illustrates the phase evolution of MK/nano-MgO mixtures. We can observe that, operating with a constant holding time of 1h (Fig. 10.1a), the mixtures were particularly reactive: the desired phase (Mg_2SiO_4, PDF#87-0061) is well recognizable at 900°C, with traces already visible even for firing at a lower temperature (800 °C), i.e. just above the temperatures at which silicones finish undergoing the thermal polymer-to-ceramic conversion (for clarity, the symbols for forsterite are reported only on the patterns of samples fired at 800 °C and 1100 °C). 800 °C can be actually considered as the onset of forsterite formation, on the basis of Fig. 10.1b: indeed, the intensity of forsterite peaks, weak for 1 h, had a dramatic increase for 3 h at the same temperature. Fig. 10.1c reports the data for a sample optimized in terms of phase purity: the diffraction peaks are well aligned to those of the reference forsterite pattern, except for minor traces attributed to unreacted MgO (periclase, PDF#87-0653) and enstatite ($MgSiO_3$, PDF#19-0768).

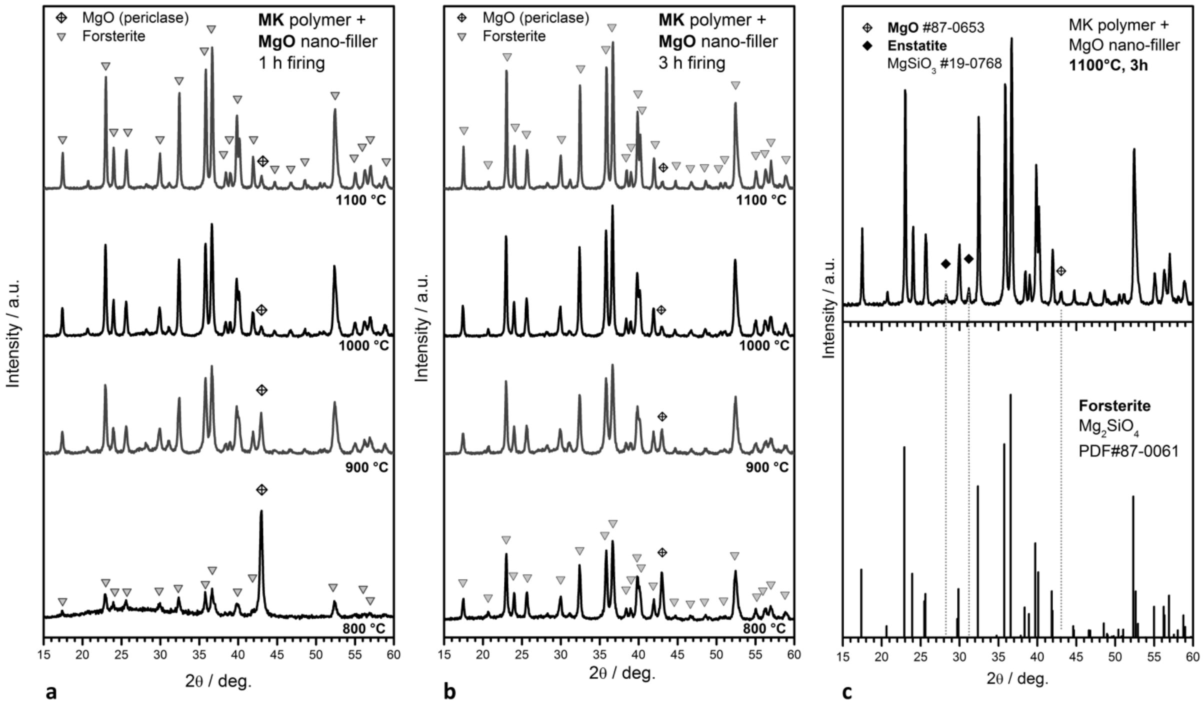

Fig. 10.1 Phase evolution of ceramics from MK/nano-sized MgO mixtures fired at different temperatures: a) 1 h holding time, b) 3 h holding time, c) phase identification for the sample with optimized phase purity (3 h - 1100 °C).

Fig. 10.2a provides a further evidence of the presence of un-reacted MgO, as a function of both firing temperature and holding time. The most significant decreases in intensity of the main diffraction peak (expressed in total counts), a rough index of the quantity of MgO, occurred passing from 800 to 900 °C, for a holding time of 1 h, i.e. at the onset of forsterite formation. The intensity was always decreasing, with increasing temperature and time, as a proof of the progressive, but not complete, dissolution of MgO. A possible explanation could be the same observed high reactivity of constituents. Forsterite, formed at low temperature, likely delayed further dissolution due to the characteristic poor interdiffusion of silicates[12]. This poor interdiffusion could also be the cause of the presence of a minor enstatite contamination, deriving from local fluctuations of the MgO/SiO_2 ratio.

The density of MK-derived forsterite ceramics had a quite peculiar evolution, as shown in Fig. 10.2b. For a holding time of 1 h, the density was almost stationary, up to 1000 °C, then exhibited a significant increase. For longer thermal treatments, there is an almost linear increase of density, with increasing temperature. The large data scatter does not allow the application of any reasonable model; we can only observe that the maximum values are far below the theoretical density of forsterite (~3.2 g/cm^3)[13].

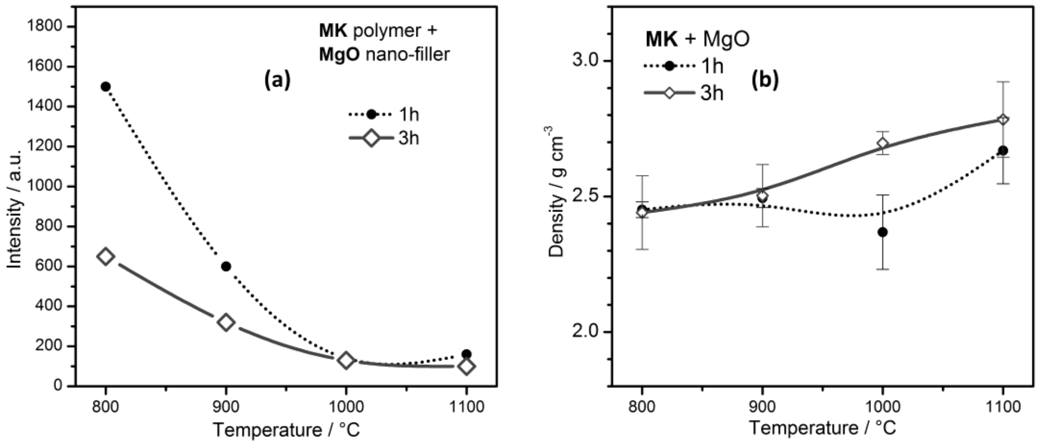

Fig. 10.2 Evolution of the intensity of the main diffraction peak for MgO (a) and of the bulk density (b), for silicone/nano-sized MgO mixtures, with increasing firing temperature and different holding time.

Fig. 10.3 provides some microstructural details about the ceramic sample exhibiting the highest phase purity, i.e. that fired at 1100 °C, for 3 h. We can observe, in Fig. 10.3a, a number of macrocracks around dense fragments, that could justify the large scatter of density data (evaluated by means of the Archimedes' method, i.e. by immersion in water, that could penetrate in the cracks). The higher magnification view, Fig. 10.3b, shows that the fragments were not actually dense, but contained a lot of submicron pores (dark dots); forsterite crystals (lighter zones) were sub-micrometric as well. The cracks could be due, in our opinion, to the intensive crystallization occurring already at low temperature; since no viscous flow could be provided by the ceramic residue of silicone oxidation (pure amorphous silica), the volumetric changes associated to both ceramic conversion and forsterite crystallization could not be accommodated, with the development of internal stresses and residual porosity.

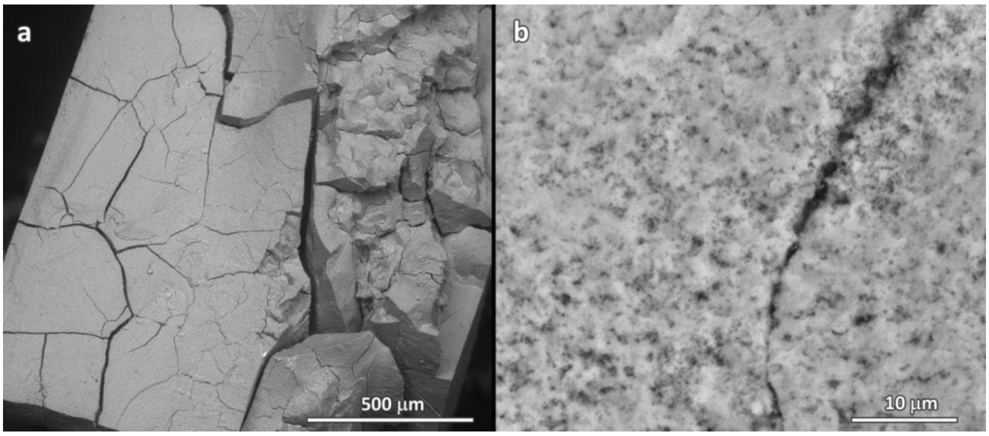

Fig. 10.3 Microstructural details (fracture surfaces) of a ceramic sample from MK polymer (firing at 1100 °C, for 3h).

The cracking of forsterite monoliths and the presence of some residual undesirable phases, such as MgO and enstatite, led us to produce a second generation of samples (see Tab. 10.1), derived from MK mixed with H62C and also with additional fillers. As pointed out for recently presented polymer-derived cordierite ceramics[10], several factors may justify the increase of compactness obtained when substituting part of MK by H62C; they include the reduction of the gas release during polymer cross-linking, due to different cross-linking reactions occurring in the two polymers; the application of a cross-linking step (30 min at 250 °C) before powder compaction, which involves a certain degree of shrinkage that is consequently absent in the subsequent pyrolysis; the different molecular structure of the polymeric precursors, which could generate a silica matrix with different features, e.g. network connectivity and number of defects, and thus with a different ability to relax structural rearrangements and eliminate gases during the pyrolysis step, without local pressure accumulation phenomena.

Tab. 10.1 Summary of formulations for refined forsterite-based ceramics (fired at 1100 °C, for 3h).

Samples	**Components**					**Density**
	MK	H62C	n-MgO	m-TiO_2	n-TiO_2	**(g/cm^3)**
Pure forsterite, polymer mix (F)	x	x	x			2.76 ± 0.03
Composite (FT)	x	x	x	x[25 wt%]		2.93 ± 0.03
Forsterite solid solution (FSS)	x	x	x		x	2.78 ± 0.03

Un-cracked samples were indeed obtained from mixtures in which 50% of the silica was provided by the oxidation of each polymer, MK and H62C. However, as shown by the diffraction pattern in Fig. 10.4 (lower spectrum), this improvement had a major drawback in the enhanced intensity of the peaks of unwanted phases, such as periclase and enstatite. The presence of MgO is quite surprising, since H62C, known for its linear polymer chains[14], was expected to provide relatively shorter siloxanic fragments upon thermal decomposition, compared to MK, possessing a much more complicated network structure[15]. Such shorter fragments were thought to react easily with nano-sized MgO, favoring its dissolution, contrary to what experimentally found. A possible explanation could be the possible formation of MgO-defective forsterite instead of stoichiometric forsterite, at low temperature.

Periclase was eliminated by the introduction of m-TiO_2 used, as in the highly efficient dielectrics presented by Ohsato *et al.*[1], in an amount of 25 wt% (referred to the weight of the ceramic product). Micro-sized titania, as testified by Fig. 10.4 (central spectrum), was not actually an inert filler. In fact, we could detect the presence of rutile (PDF#21-1276), i.e. pure titania (m-TiO_2 was in the anatase form, known to transform into rutile upon heating), as well as Mg-titanates, due to the reaction between fillers. The main titanate phase corresponded to a Mg-Ti spinel ($MgTi_2O_5$, PDF#82-1125), with $MgTiO_3$ (PDF#79-0831) in minor traces. Enstatite was still present, reasonably favored by the decrease of the MgO/SiO_2 ratio associated with the MgO-TiO_2 interaction. Some microstructural details concerning this forsterite/titania composite (FT sample) are shown in Fig. 10.5. In analogy with the sample without TiO_2 (not shown for the sake of brevity), there was no evidence of macro-cracks (see Fig. 10.5). As shown by the high magnification detail of a polished surface (Fig. 10.5b), there are some micropores (black spots) – consistent with a still limited density value (2.93 g/cm^3) – surrounded by a multitude of micro-crystals. The lighter dots are associated to concentrations of Ti (the heaviest element, associated to a light color in backscattered imaging), in rutile and titanate crystals. The darkest areas, on the contrary, were found to be rich in Mg (from EDS analysis). This particular distribution is thought to be developed upon drying of polymer suspensions: a precipitation of heavier filler particles (titania micro-filler) could occur, leading to the formation of silicone powders in which the filler content is not homogeneous. A similar problem occurred with wollastonite ceramics, when developed from MK and micro-sized $CaCO_3$[4], and it has been recently solved by adopting melt mixing, i.e. mixing MK and fillers in a polymer extruder, assisted by supercritical carbon dioxide[16]. This refined mixing strategy will then be applied also to forsterite ceramics in future investigations.

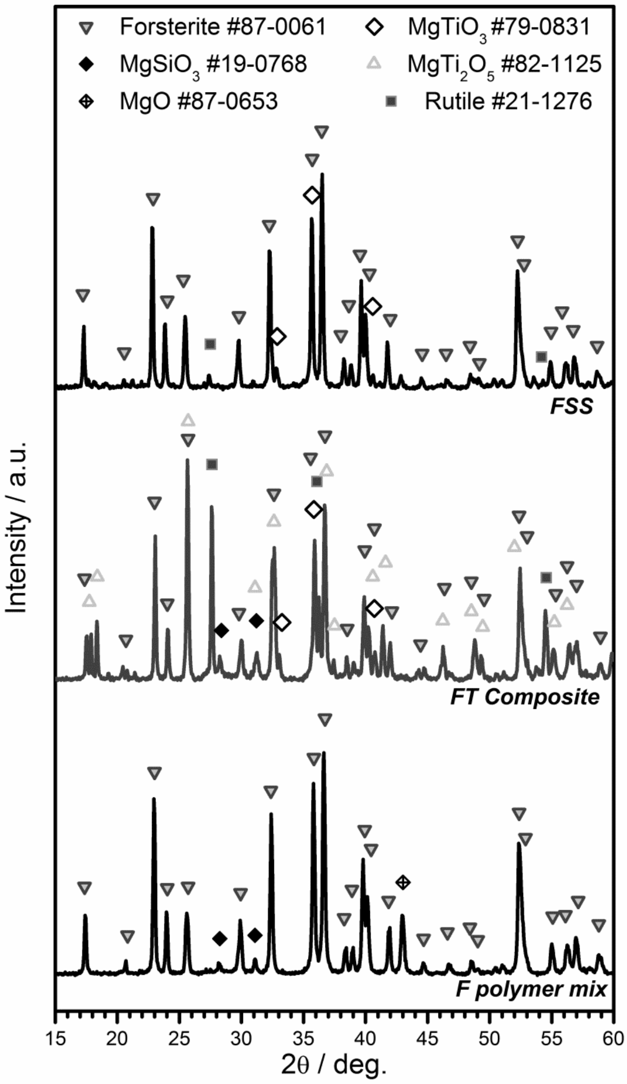

Fig. 10.4 X-ray diffraction patterns of refined polymer-derived forsterite-based ceramics (fired at 1100°C, for 3 h).

A further development was associated to the use of nano-sized titania (n- TiO_2) in order to form a forsterite solid solution, with TiO_2 partially replacing SiO_2 (10% mol., expressed by the formula $Mg_2Si_{0.9}Ti_{0.1}O_4$). Contrary to the addition of m-TiO_2, the addition was obviously accompanied by changes in the MgO/SiO_2 molar ratio (from $MgO/SiO_2=2$ to $MgO/(SiO_2+TiO_2)=2$). In Fig. 10.4 (upper spectrum, sample FSS) the peaks associated to forsterite are accompanied only by weak traces of rutile (PDF#87-0710), from unreacted titania, and $MgTiO_3$. Both undesirable phases, enstatite and periclase, were not detected.

The improvements in the phase assemblage were accompanied by a high microstructural homogeneity, as shown in Fig. 10.5c (polished surface); the porosity, still of about 15% (see Tab. 10.1), is evidently distributed on a sub-micrometric scale. The fine distribution of crystals and pores is further confirmed by Fig. 10.5d (granules, attributable to forsterite crystals, well below 1 μm).

Forsterite ($\sigma_{EP}=8.6\times10^{-11}$ S/cm) exhibited a slightly lower conductivity than the composite materials ($\sigma_{EP}=2.8\times10^{-10}$and 1.5×10^{-10} S/cm are for FT and FSS respectively). However, the here investigated ceramics had relatively low ε_r values ($\varepsilon_{r,forsterite}=4.6$, $\varepsilon_{r,FT}=5.6$ and $\varepsilon_{r,FSS}=6.2$). Other relevant fit parameters can be found in Tab. 10.2.

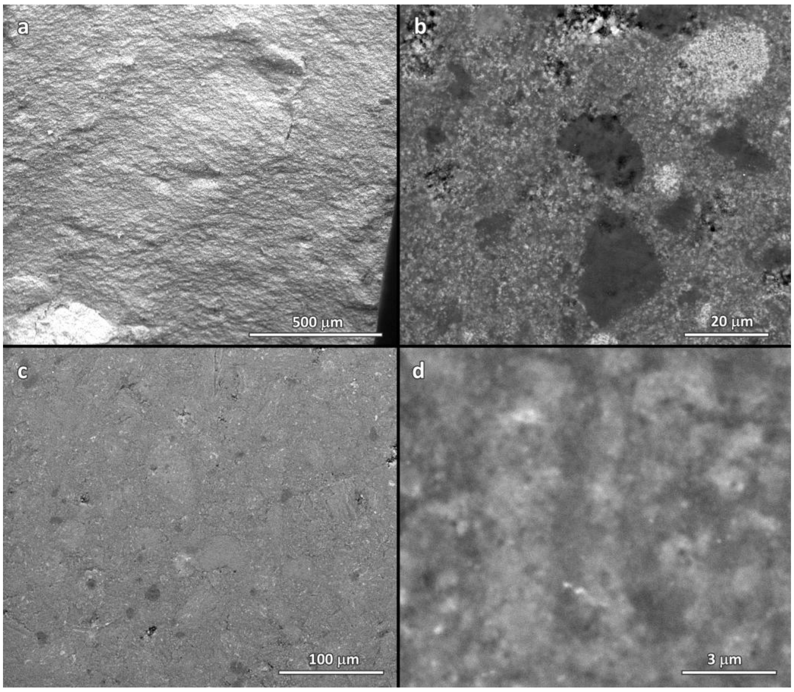

Fig. 10.5 Microstructural details of refined polymer-derived forsterite-based ceramics: a,b) FT composite; c,d) F solid solution.

Tab. 10.2 Parameters derived from fitting of BDS data (measured at 20 °C).

	σ_{EP} (S/cm)	τ (s)	ε_r	*Q·f* (GHz) at 10 GHz
Forsterite (F)	8.6×10^{-11}	5.7×10^{-3}	4.6	330000
Composite (FT)	2.8×10^{-10}	2.6×10^{-3}	5.6	79000
Forsterite ss (FSS)	1.5×10^{-10}	5.6×10^{-4}	6.2	145000

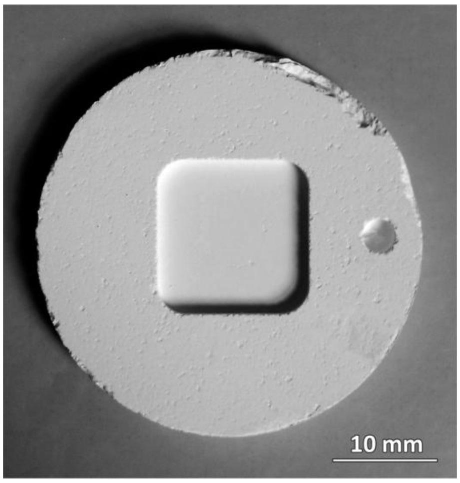

Fig. 10.6 Machining of a composite block, resulting from warm pressing of a MK/MgO/TiO_2 mixture

Materials that are used in millimeter-wave applications are generally characterized by high values of $Q\cdot f$ and low values of ε_r[1,17]. The quality factor Q is the inverse of the dielectric loss tanδ and is typically reported as the product $Q\cdot f$ in GHz. Previously published work on forsterite has shown values of $Q\cdot f$=270000 and ε_r=6.8.[1] In this work, even lower values of ε_r and higher values of $Q\cdot f$ were found for the forsterite (F) sample. The composite material exhibited properties that were less favourable than those of the forsterite sample, but were comparable to previously published values[1].

The present results are still somewhat preliminary, but the proposed approach has a great potential for the fabrication of dielectric components. Fig. 10.6, as an example, shows the easy machining of a composite (silicone/MgO/TiO_2) block (warm pressed at 250 °C): the presence of fillers helps in reducing the crack propagation during machining and in limiting the surface damage.

Improvements in the densification are expected from treatments at higher temperatures (e.g. above 1200 °C), in analogy to the sintering treatments presented in the literature. It should be noted, however, that the densest forsterite ceramics were not prepared by a single step treatment, like the one applied here, but by a double step treatment (calcination and sintering) [2-8,18-20]. The relative density of our samples, at 1100°C (85%), compares favorably with the value reported by Ni *et al.*[18] (at 1450 °C, for 3 h), starting from pre-calcined (at 1200 °C) sol-gel derived forsterite powders.

10.4 Conclusions

Commercial silicone resins containing nano-sized MgO fillers were easily converted into forsterite ceramics, upon heat treatment in air at relatively low temperature (starting from 800 °C). A combination of silicones was found to favour the structural integrity of the polymer-derived ceramic components, in analogy with other previously investigated silicate and alumino-silicate systems.

The presence of secondary undesired phases, such as MgO (from unreacted filler particles) and enstatite, could be controlled by introducing TiO_2 in form of both micro- and nano-sized particles.

TiO_2 micro-particles did not actually behave as passive fillers, in fact MgO/TiO_2 interactions led to the formation of Mg-titanates. The addition of TiO_2 micro-particles, though effective in suppressing the MgO contamination, had no practical effect on the formation of enstatite. The distribution of micro-particles remains an open issue: a more intensive mixing is probably required to limit the observed local fluctuations in the concentration of TiO_2 and MgO.

TiO_2 nano-particles were effective as secondary active filler; in particular, pure forsterite, from silicone/MgO interaction, transformed into a forsterite solid solution, with Ti^{4+} ions replacing Si^{4+} ions.

Despite residual (sub micrometric) porosity (~15 %, after firing at 1100 °C), selected polymer-derived forsterite ceramics exhibited interesting dielectric properties, especially in terms of low dielectric losses.

A final remark concerns the multifunctionality of forsterite ceramics. Applications in biomaterials, in fact, have been recently proposed, besides in dielectrics, for both forsterite monoliths[18,20] and coatings (on hydroxyapatite ceramics)[21,22], due to the observed biocompatibility and bioactivity of this specific Mg-silicate.

References

[1] Ohsato, H., Tsunooka, T., Sugiyama, T., Kakimoto, K. I., Ogawa, H. (2006). Forsterite ceramics for millimeterwave dielectrics. Journal of electroceramics, 17(2-4), 445-450.

[2] Sano, S., Saito, N., Matsuda, S. I., Ohashi, N., Haneda, H., Arita, Y., Takemoto, M. (2006). Synthesis of High Density and Transparent Forsterite Ceramics Using Nano-Sized Precursors and Their Dielectric Properties. Journal of the American Ceramic Society, 89(2), 568-574.

[3] Song, K. X., Chen, X. M., Fan, X. C. (2007). Effects of Mg/Si ratio on microwave dielectric characteristics of forsterite ceramics. Journal of the American Ceramic Society, 90(6), 1808-1811.

[4] Colombo, P., Bernardo, E., Parcianello, G. (2013). Multifunctional advanced ceramics from preceramic polymers and nano-sized active fillers. Journal of the European Ceramic Society, 33(3), 453-469.

[5] Bernardo, E., Parcianello, G., Colombo, P. (2012). Novel synthesis and applications of yttrium silicates from a silicone resin containing oxide nano-particle fillers. Ceramics International, 38(7), 5469-5474.

[6] Bernardo, E., Colombo, P., Dainese, E., Lucchetta, G., Bariani, P. F. (2012). Novel 3D wollastonite-based scaffolds from preceramic polymers containing micro-and nano-sized reactive particles. Advanced Engineering Materials, 14(4), 269-274.

[7] Aksay, I. A., Dabbs, D. M., Sarikaya, M. (1991). Mullite for structural, electronic, and optical applications. Journal of the American Ceramic Society, 74(10), 2343-2358.

[8] Song, K. X., Chen, X. M. (2008). Phase evolution and microwave dielectric characteristics of Ti-substituted Mg_2SiO_4 forsterite ceramics. Materials Letters, 62(3), 520-522.Phase evolution and microwave dielectric characteristics of Ti-substituted Mg_2SiO_4 forsterite ceramics

[9] Bernardo, E., Fiocco, L., Giffin, G. A., Di Noto, V., & Colombo, P. (2014). Microstructure Development and Dielectric Characterization of Forsterite-Based Ceramics from Silicone Resins and Oxide Fillers. Advanced Engineering Materials, 16(6), 806-813.

[10] Parcianello, G., Bernardo, E., Colombo, P. (2013). Cordierite ceramics from silicone resins containing nano-sized oxide particle fillers. Ceramics International, 39(8), 8893-8899.

[11] Piccolo, M., Giffin, G. A., Vezzù, K., Bertasi, F., Alotto, P., Guarnieri, M., Di Noto, V. (2013). Molecular relaxations in magnesium polymer electrolytes via GHz broadband electrical spectroscopy. ChemSusChem, 6(11), 2157-2160.

[12] Long, L. H., Chen, L. D., Chang, J. (2006). Low temperature fabrication and characterizations of β-$CaSiO_3$ ceramics. Ceramics international, 32(4), 457-460.

[13] Yoder, H. S., Generation of Basaltic Magma, National Academy of Sciences, Washington, USA 1976.p.95

[14] Goerke, O., Feike, E., Heine, T., Trampert, A., Schubert, H. (2004). Ceramic coatings processed by spraying of siloxane precursors (polymer-spraying). Journal of the European Ceramic Society, 24(7), 2141-2147.

[15] Riedel, R., Toma, L., Fasel, C., Miehe, G. (2009). Polymer-derived mullite-SiC-based nanocomposites. Journal of the European Ceramic Society, 29(14), 3079-3090.

[16] Bernardo, E., Parcianello, G., Colombo, P., Matthews, S. (2013). Wollastonite foams from an extruded preceramic polymer mixed with $CaCO_3$ microparticles assisted by supercritical carbon dioxide. Advanced Engineering Materials, 15(1-2), 60-65.

[17] Ohsato, H., Tsunooka, T., Kan, A., Ohishi, Y., Miyauchi, Y., Tohdo, Y., Ogawa, H. (2004, July). Microwave-millimeterwave dielectric materials. In Key Engineering Materials (Vol. 269, pp. 195-198).

[18] Ni, S., Chou, L., Chang, J. (2007). Preparation and characterization of forsterite (Mg_2SiO_4) bioceramics. Ceramics International, 33(1), 83-88.

[19] Tsunooka, T., Androu, M., Higashida, Y., Sugiura, H., Ohsato, H. (2003). Effects of TiO_2 on sinterability and dielectric properties of high-Q forsterite ceramics. Journal of the European Ceramic Society, 23(14), 2573-2578.

[20] Ramesh, S., Yaghoubi, A., Lee, K. S., Chin, K. C., Purbolaksono, J., Hamdi, M., Hassan, M. A. (2013). Nanocrystalline forsterite for biomedical applications: Synthesis, microstructure and mechanical properties. journal of the mechanical behavior of biomedical materials, 25, 63-69. Nanocrystalline forsterite for biomedical applications: synthesis, microstructure and mechanical properties.

[21] Emadi, R., Tavangarian, F., Esfahani, S. I. R., Sheikhhosseini, A., Kharaziha, M. (2010). Nanostructured forsterite coating strengthens porous hydroxyapatite for bone tissue engineering. Journal of the American Ceramic Society, 93(9), 2679-2683.Nanostructured Forsterite Coating Strengthens Porous Hydroxyapatite for Bone Tissue Engineering

[22] Sebdani, M. M., Fathi, M. H. (2011). Novel hydroxyapatite-forsterite-bioglass nanocomposite coatings with improved mechanical properties. Journal of Alloys and Compounds, 509(5), 2273-2276.Novel hydroxyapatite-forsterite-bioglass nanocomposite coatings with improved mechanical properties

11 Cordierite ceramics

11.1 Introduction

Porous ceramics based on cordierite ($2MgO\cdot2Al_2O_3\cdot5SiO_2$ or $Mg_2Al_4Si_5O_{18}$) are particularly appreciated in the field of catalytic converters and particulate filters for diesel engines[1-3] and, in general, for components subjected to severe thermal gradients (for a maximum temperature generally not exceeding 1250 °C)[4]. This is due to the characteristic combination of properties, such as low CTE (coefficient of thermal expansion, equal to $\sim1.5\cdot10^{-6}$ /K), good thermal stability, corrosion resistance and generally low price.

In the present work, cordierite ceramics are fabricated starting from silicone resins, filled with oxide particles. According to this approach, the fillers directly react with the product of oxidative decomposition of the resins, consisting of amorphous silica, possessing a particularly defective network and consequently prone to very favorable reaction kinetics[5]. A previous paper[6] has already been dedicated to cordierite ceramics, from silicones combined with MgO and γ-Al_2O_3, in form of nano-sized particles. Cordierite is feasible in conditions of high microstructural homogeneity and phase purity, comparable to those provided by the sol-gel route[7,8], and the distinctive possibility of shaping in the polymeric state, for preceramic polymers, can be exploited for the development of particularly strong and homogeneous foams. However, nano-sized particles and the methods for obtaining a uniform porosity remain as open issues, in the view of large scale industrial applications. In particular, toxicological effects associated with human exposure to nanoparticles are still unknown [9,10] and the formation of pores by burn-out of sacrificial polymeric beads, as proposed by Parcianello *et al.*[6], poses some difficulties in terms of costs and control of gaseous emissions.

The present investigation, published by Fiocco and Bernardo in 2015[11], is based on a revision of the approach of silicone resins filled with oxide particles: firstly, high purity and relatively low processing temperature are maintained, despite the use of micro-sized fillers; secondly, the fabrication of highly porous components relies on the use of a "double role" filler, both reacting with polymer-derived silica to yield the desired crystalline phase and acting as foaming agent. More precisely, as observed in the development of akermanite ($2CaO\cdot MgO\cdot2SiO_2$) porous ceramics, the double role is provided by magnesium hydroxide ($Mg(OH)_2$), decomposing, with release of water vapour, at very low temperature (300-350 °C). Since the release occurs in a silicone below the temperature of ceramic conversion (> 500 °C), i.e. in a viscous mass, the developed (harmless) gas may lead to an extensive foaming, with no need for additives; the residue (MgO) is obviously incorporated in cordierite.

The commercially available silicone polymers are actually quite numerous; a protocol for the development of cordierite-based porous ceramics, based on a specific silicone, could have a limited impact. We will show, on the contrary, that the "double role" filler approach may be applied to silicone of different nature. The key constraint of the availability of a viscous mass, upon decomposition of $Mg(OH)_2$, will be fulfilled operating with different mixing strategies, operating with liquid or solid silicones.

11.2 Experimental

11.2.1 Preparation of samples

Two commercially available silicones, Silres® MK and Silres® H62C (Wacker-Chemie GmbH, Munich, Germany) were used as silica sources. MK is a solid methyl polysilsesquioxane resin with a 84 wt% SiO_2 yield after pyrolysis in air[12]. It is characterized by the presence of OH functional groups inside its chemical structure, which allow the cross-linking mechanism to occur by condensation. H62C instead is a highly viscous liquid polysiloxane resin with a 58 wt% silica yield[12], which can cross-link without the release of gaseous products, thanks to the presence of vinyl groups.

As MgO and Al_2O_3 precursors, we considered $Mg(OH)_2$ microparticles (< 10 µm, Industrie Bitossi, Vinci, Italy) and transition Al_2O_3 microparticles (Puralox UF 5/230, < 11 µm, Sasol, Brunsbüttel, Germany). The balance among the most important constituents (silicones/MgO precursor/Al_2O_3 precursor) followed the stoichiometric $MgO/Al_2O_3/SiO_2$ molar proportions of cordierite (i.e. $MgO/Al_2O_3/SiO_2$ =2/2/5 by mol.). Considering the different silica yields, the amount of polymer, with the same amount of fillers, obviously changed ($Mg(OH)_2/Al_2O_3$/H62C=0.23/0.39/1 and $Mg(OH)_2/Al_2O_3$/MK=0.32/0.57/1 by weight).

Foams from liquid polymer were prepared by dissolving H62C in isopropanol (15 ml for 10 g of final ceramic) and adding the fillers under magnetic stirring. Further sonication for 10 minutes provided a stable and homogeneous dispersion. The mixture was subsequently poured into a large glass container and dried at 60 °C overnight. After drying, the preceramic mixture was in form of a thick paste, which was manually transferred into cylindrical Al molds and thermally treated at 300 °C for 30 minutes. Cylindrical samples, 10 mm in diameter and 20 mm in height, were obtained by polishing the foams with abrasive paper.

Foams from solid polymer were obtained by mixing MK with Al_2O_3, $Mg(OH)_2$ microparticles and paraffin (13 wt% of the total preceramic formulation). The components were first homogenized by means of a shaker-mixer (Turbula T2F, WAB, Switzerland), then inserted in a twin-screw co-rotating extruder (Prism TSE 24 HC, 24 mm screw diameter, length/diameter ratio equal to 40:1, Thermo Prism Ltd, Stone, United Kingdom) operating at 75 °C at the die. The extrudates, which were in form of cylindrical fragments, were later subjected to secondary processing, including manual grinding, sieving to a dimension below 300 µm, pouring in Al molds and thermal treating at 300 °C for 30 minutes. Extrusions were performed at SCF Processing Ltd. (Drogheda, Ireland) during a 3-month student exchange in 2013.

All the foams obtained from both liquid and solid silicone resins have been subjected to ceramization at 1350 °C for 3 hours, with a heating rate of 10 °/min.

11.2.2 Characterization of samples

The bulk density (ρ_b) of the foams was determined from the weight-to-volume ratio, using a caliper and a digital balance. The skeletal density (ρ_s) was measured on foams, using a He gas pycnometer (Micromeritics AccuPyc 1330, Norcross, GA). The percentage of open porosity was then calculated using the following equation: % Open Porosity = 1 - (ρ_b / ρ_s); where ρ_b was the bulk density and ρ_s was the skeletal density.

Microstructural characterizations were performed by optical stereomicroscopy (AxioCam ERc 5s Microscope Camera, Carl Zeiss Microscopy, Thornwood, New York, US) and scanning electron microscopy (FEI Quanta 200 ESEM, Eindhoven, The Netherlands) equipped with EDS.

The crystalline phases were identified by means of X-ray diffraction on powdered samples (XRD; Bruker AXS D8 Advance, Bruker, Germany), supported by data from PDF-2 database (ICDD-International Centre for Diffraction Data, Newtown Square, PA) and Match! program package (Crystal Impact GbR, Bonn, Germany).

The crushing strength of foams was measured at room temperature, by means of an Instron 1121 UTM (Instron Danvers, MA) operating with a cross-head speed of 1 mm/min. Each data point represents the average value of 5 to 10 individual tests.

11.3 Results

11.3.1 Pure cordierite

The ability of $Mg(OH)_2$ to act as a foaming agent by releasing water vapour is shown in Fig. 11.1. Using both the solid and the liquid silicones as a polymeric matrix for the shaping and as source of silica in the final composition, a highly porous structure was achieved by foaming at 300 °C for 30 minutes, even though the foams obtained from liquid H62C exhibited a more pronounced homogeneity in the distribution and mean diameter of the pores. The mean diameter can be estimated from Fig. 11.1a-b between 500 µm and 1 mm for both the samples.

Concerning the use of MK for the extrusions, the foaming on secondary heating is an evidence that the relatively rapid thermal cycle operated by extrusion did not cause its cross-linking. Anyway, samples were found to exhibit some cracks, as shown in Fig. 11.1b.

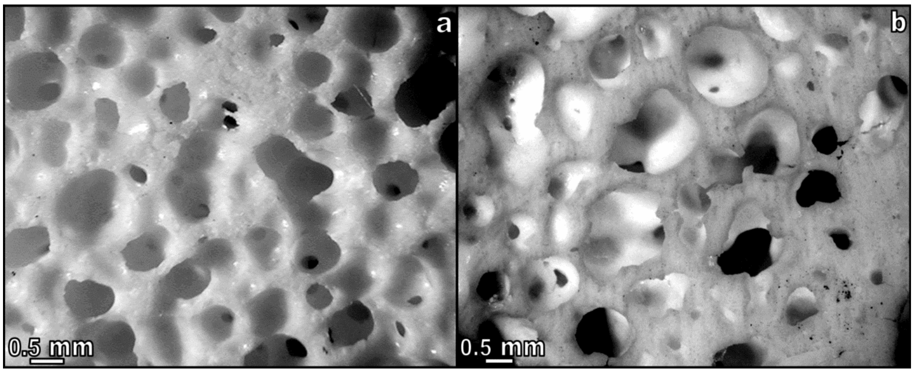

Fig. 11.1 Microstructural details of cordierite foams after ceramization at 1350 °C: a) from H62C; b) from MK.

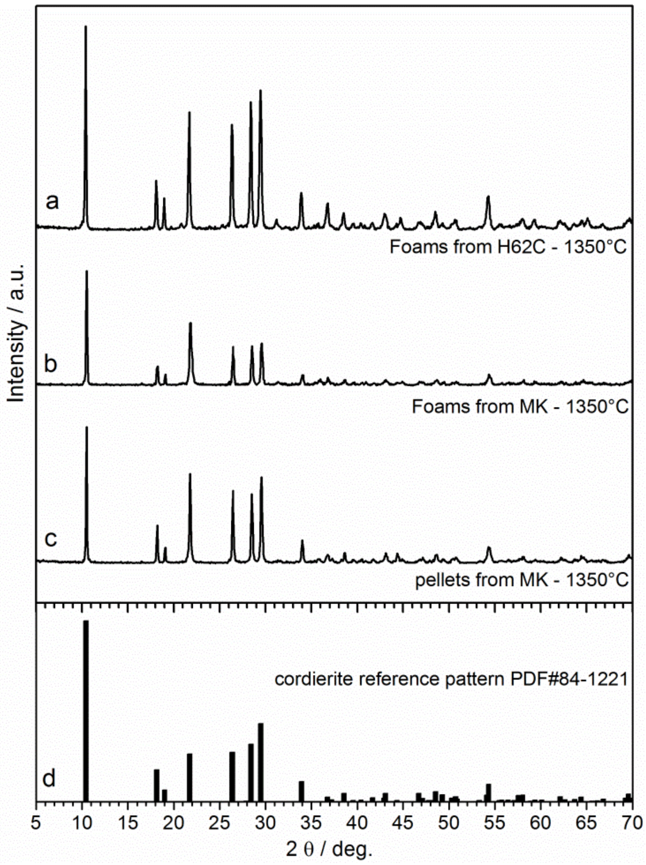

Fig. 11.2 Qualitative X-ray diffraction patterns of cordierite after ceramization at 1350 °C: a) foams from H62C; b) foams from MK; c) dense sample from MK; d) reference pattern.

In Fig. 11.2 the XRD patterns for both the samples (a-b) are reported and compared with the pattern exhibited by dense cordierite (c), obtained from MK by Parcianello *et al.*[6], and with a reference pattern for pure cordierite (d). All the samples, which were thermally treated at 1350 °C with a heating rate of 10 °/min, are characterized by high phase purity, with not even weak traces of secondary crystalline phases. This result also shows that the substitution of MK with H62C and the use of different mixing processes did not affect the crystal phase assemblage and purity of the final ceramic product.

Tab. 11.1 summarizes the physical and mechanical properties of the foams. As previously noticed for the morphology of the foams, there is again a strong similarity between the samples derived from H62C and MK, but data for compressive strength highlighted a significant difference in terms of reproducibility of the samples. Concerning the samples derived from MK, the variability in compressive strength is probably due to the previously observed cracks. In any case, the strength-to-density ratio compares favourably with that of commercial cordierite foams. It should be noticed that cellular cordierite with open porosity (P_{open}) around 80 % and a mean bulk density (ρ_{bulk}) of approximately 0.5 g/cm^3 possesses a compressive strength (σ_{comp}) of 1.3 MPa and a strength-to-density ratio of 2.6 MPa·cm^3/g, which perfectly matches the data summarized in Tab. 11.1[13].

Tab. 11.1 Summary of physical and mechanical properties of ceramized cordierite foams.

Sample	ρ_{bulk} (g/cm^3)	$\rho_{skeleton}$ (g/cm^3)	P_{open} (%)	σ_{comp} (MPa)	Specific σ_{comp} (MPa·cm^3/g)
Foams from H62C	0.91 ± 0.01	2.56 ± 0.01	64	2.3 ± 0.2	2.6
Foams from MK	0.93 ± 0.04	2.54 ± 0.01	64	2.3 ± 0.8	2.4

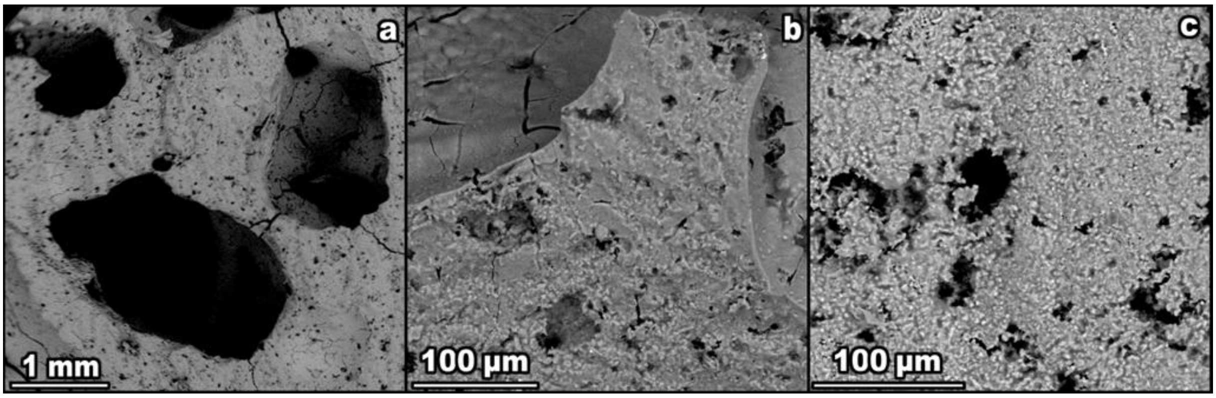

Fig. 11.3 High magnification details of cordierite foams from MK after ceramization at 1350 °C.

SEM imaging was performed on the samples derived from extruded MK, to have a clearer overview of the crack development inside the samples. Fig. 11.3 testifies not only the presence of cracks (a), but also a very homogenously distributed microporosity inside the struts of the open cells (b-c), likely originated by the paraffin additive. The negative impact of macrocracks is somewhat compensated by the microporosity, offering an improved stress distribution upon loading[14].

The cracks could be ascribed to the peculiar nature of MK. As reported by Parcianello *et al.*[6], cordierite MK-based monoliths were not crack-free; a substantial improvement was offered by the partial replacement of MK, as silica source, with H62C. As the authors assumed, this could be due to the same molecular structure of the second polymer: since H62C does not include the release of gaseous products in the cross-linking reactions, the formation of cracks is minimized. In addition, the different chemical characteristics of the two silicones could reasonably lead to different features in the polymer-derived silica matrix, such as the network connectivity or the number of defects, thus giving a different ability in the relaxation of internal stresses arising from the volumetrical changes which occur during the pyrolysis. The crack-free samples from H62C may be seen as a confirmation.

Future investigation will be likely dedicated to the use of MK/H62C mixtures also for extrusion. A further improvement could be due to the application of super-critical CO_2-assisted extrusion, that would allow the elimination of paraffin, used as a plasticizer. The release of CO_2 dissolved in the polymer has a great potential for enhancing the microporosity and reducing the stresses arising from ceramization, as previously shown for wollastonite foams[15].

11.3.2 B-substituted polymer-derived cordierite ceramics

B-substituted polymer-derived cordierite ceramics were synthesized by replacing Al^{3+} with B^{3+}, using boric acid ($B(OH)_3$) as a boron source. The experiments were done by Mr. Lucas S.M. Kodaira (University of São Paulo, Brazil).

Boric acid loses all its water and transforms into boron oxide (B_2O_3) above 150 °C, thus being exploitable as a foaming agent for silicone-based mixture, as well as $Mg(OH)_2$. Then, if crystalline, it has a melting point of 450 °C, while, if amorphous, it does not have a specific melting temperature, but starts to soften at 325 °C and becomes fluid at 500 °C[16]. Therefore, boric acid was added with the aim of forming a liquid phase upon heat treatment, enhancing the diffusion and promoting the crystallization of cordierite.

Moreover, the formation of a glass matrix by cooling would improve the thermal properties by further reducing the thermal expansion coefficient (CTE), that is of $1.5 \cdot 10^{-6}$ K^{-1} for pure cordierite[17].

Three different formulations were compared:

- original cordierite, 0 mol% of Al_2O_3 replaced with B_2O_3 ($5SiO_2 \cdot 2MgO \cdot 2Al_2O_3$);
- 12.5 mol% of Al_2O_3 replaced with B_2O_3 ($5SiO_2 \cdot 2MgO \cdot 1.75Al_2O_3 \cdot 0.25B_2O_3$);
- 25 mol% of Al_2O_3 replaced with B_2O_3 ($5SiO_2 \cdot 2MgO \cdot 1.5Al_2O_3 \cdot 0.5B_2O_3$).

For original cordierite, silicone-based mixtures were prepared using the same precursors as described in §11.2. In the case of B-modified cordierite, alumina (Al_2O_3) was partially replaced with $B(OH)_3$ (Sigma-Aldrich Chem., MO, USA), following the stoichiometric $SiO_2/MgO/Al_2O_3/B_2O_3$ molar proportions above reported (i.e. 5/2/2/0 for pure cordierite; 5/2/1.75/0.25 and 5/2/1.5/0.5 for the modified one).

Once studied the foaming potential of boric acid at 300-350 °C, the water release from $Mg(OH)_2$ was suppress by using nano-sized MgO, in order to have a greater control on foaming and a more homogenous pore distribution when using $B(OH)_3$. Foams were later ceramized at 1350 °C for 3 hours, with a heating rate of 10 °C/min.

X-ray diffraction patterns are reported for the three formulations in Fig. 11.4. As shown, cordierite phase purity increased with B_2O_3 content. In fact, samples with no B (pattern b) and samples with 0.25 mol of B_2O_3 (pattern c) presented traces of a secondary phase, consisting of mullite ($3Al_2O_3 \cdot 2SiO_2$ – PDF#12-0776), beside cordierite peaks (PDF#84-1221); while samples with higher content of B (0.5 mol of B_2O_3 – pattern d) exhibited exclusively pure cordierite (PDF#84-1221), with peaks perfectly matching those of the reference cordierite phase of pattern a.

The incorporation of B in the cordierite crystals should have resulted in a shift of the cordierite peaks along the x axis, while the participation of B in a glass phase should have caused the emergence of an "amorphous halo". Neither of these observations can be much appreciated from the patterns reported, possibly due to the very small amount of B incorporated in the formulations. Anyway, it seems reasonable to suppose that some of the B content entered the cordierite lattice and the remaining B participated in the formation of a glass phase.

The formation of glass phase might be supported by a further remark on the porosity values reported in Fig. 11.4.

The samples containing less B exhibited a higher open porosity (50%) than original cordierite (41%), but samples with more B exhibited a smaller porosity (45%) than those with less B. This was surprising, because a higher B content should have resulted in a higher open porosity. This can be explained with the presence of glass, which could have occupied the pores, thus reducing the open porosity. Moreover, the connections between pores could have been filled, so the close porosity increased with the B content.

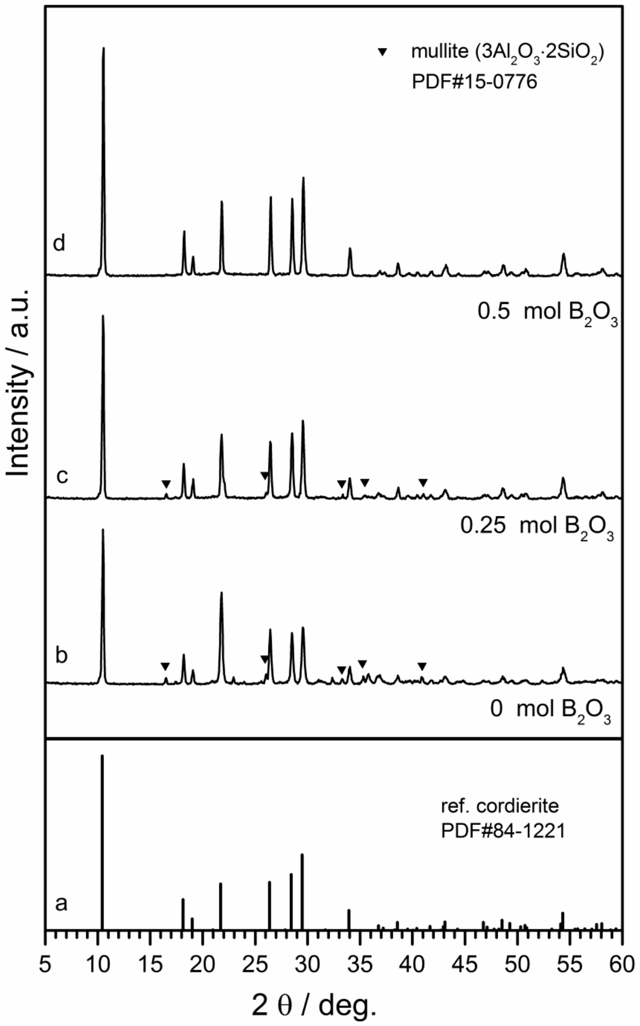

Fig. 11.4 X-ray diffraction patterns of original and B-modified cordierite foams.

Tab. 11.2 Summary of porosity values of original and B-modified cordierite foams.

B_2O_3 content	P_{open} (%)	P_{closed} (%)
0 mol of B_2O_3	40.6	0.3
0.25 mol of B_2O_3	50.4	1.0
0.5 mol of B_2O_3	45.3	2.6

Finally, the evolution of the CTE was assessed for foams and for dense samples, these obtained simply by replacing the liquid silicone H62C with a solid one (MK, Wacker-Chemie GmbH, Munich, Germany), in order to avoid the eventual influence of porosity. Dilatometric curves are reported in Fig. 11.5. Interestingly, the transition present in the curve of 0.5 mol% B_2O_3 sample is typical of glasses, but the material did not flow: this indicates the presence of an amorphous phase well restrained by the ceramic crystals. Concerning the CTE values (Tab. 11.3), they were relatively high for original cordierite samples, if compared to the value found in the literature ($1.5 \cdot 10^{-6}$ K^{-1}). Nevertheless, it is remarkable the influence of B in the material: foams and dense samples incorporating B displayed lower CTE values than samples without B.

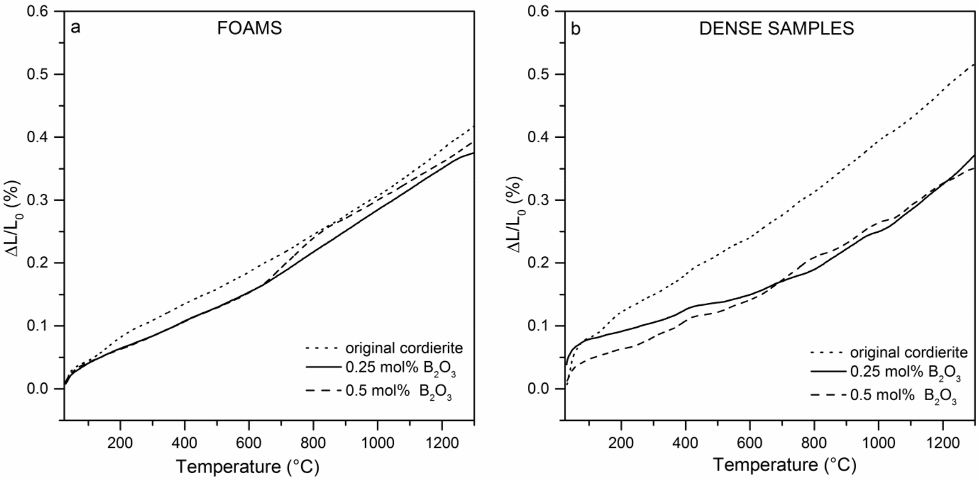

Fig. 11.5 Dilatometric curves for original and B-modified cordierite for foams (a) and dense samples (b).

Tab. 11.3 Summary of CTE for original and B-modified cordierite foams and dense samples.

		Dense samples	**Porous samples**
CTE at 400 °C (10^{-6} K^{-1})	0 mol% of B_2O_3	2.96	3.38
	0.25 mol% of B_2O_3	2.33	2.33
	0.5 mol% of B_2O_3	2.19	2.08
CTE at 1300 °C (10^{-6} K^{-1})	0 mol% of B_2O_3	3.09	3.63
	0.25 mol% of B_2O_3	2.92	2.44
	0.5 mol% of B_2O_3	2.80	2.54

11.4 Conclusions

Silicone-based mixtures comprising micro-sized fillers effectively led to cordierite with high phase purity, comparable to the one achieved from nano-sized fillers, after ceramization at 1350 °C.

The foaming of the samples was achieved by exploiting the release of water vapour from Mg hydroxide, obtained by heat treatment at 300 °C. The foams exhibited a homogenously distributed porosity, especially when operating with liquid polymer-based formulations.

A similar shaping step was applied to silicone/fillers mixtures based on a solid polymer. Prior to foaming, in this case, extrusion was applied as a mixing technique. Although samples from extrusion processing are still to be optimized, the possible use of different polymers and the simplicity of foaming reaction are thought to positively contribute to the industrial transfer of the approach.

The mechanical and physical properties are in good agreement with those of cordierite foams for technical application in the field of ceramic filters, with open porosity of 64 % and compressive strength exceeding 2 MPa.

Boric acid can be used as a further foaming agent. Boron can partially replace the aluminum content in cordierite, forming a liquid phase upon thermal treatment, which enhances significantly the final purity.

Some boron can also enter the cordierite crystal structure, reducing the CTE. A glass phase is still present after the ceramization and is responsible for the increased closed porosity, but it might be eliminated via acidic attack.

References

[1] Adler J. Ceramic diesel particulate filters. Int J Appl Cer Tech 2005; 2:429-439.

[2] Park JK, Park JH, Park JW, Kim HS, Y.I. Preparation and characterization of porous cordierite pellets and use as a diesel particulate filter. Sep Pur Tech 2007;55:321-326.

[3] Yao Y, Ochiai T, Ishiguro H, Nakano R, Kubota Y. Antibacterial performance of a novel photocatalytic-coated cordierite foam for use in air cleaners. Appl Catal B-Environ 2011;106:592-599.

[4] Grohol D, Han C, Pyzik AJ, Goss JM, Todd CS. Acicular mullite-cordierite composites with controllable CTE values, J Am Ceram Soc 2010;93:3600-3603.

[5] Colombo P, Bernardo E, Parcianello G. Multifunctional advanced ceramics from preceramic polymers and nano-sized active fillers. J Eur Ceram Soc 2013;33:453-469.

[6] Parcianello G, Bernardo E, Colombo P. Cordierite ceramics from silicone resins containing nano-sized oxide particle fillers. Cer Int 2013;39:8893-8898.

[7] Menchi AM, Scian AN. Mechanism of cordierite formation obtained by the sol–gel technique. Mater Lett 2005;59:2664-2667.

[8] Radev L, Samuneva B, Mihailova I, Pavlova L, Kashchieva E. Sol-gel synthesis and structure of cordierite/tialite glass-ceramics. Proc Appl Ceram 2009; 3:125-130.

[9] Oberdörster G, Oberdörster E, Oberdörster J. Nanotoxicology: an emerging discipline evolving from studies of ultrafine particles. Environ Health Persp 2005;113:823-839.

[10] Yah CS, Simate GS, Iyuke SE. Nanoparticles toxicity and their routes of exposures. Pak J Pharm Sci 2012;25:477-491.

[11] Fiocco, L., Bernardo, E. (2015). Novel cordierite foams from preceramic polymers and reactive oxide fillers. Materials Letters, 159, 98-101.

[12] Bernardo E, Colombo P, Dainese E, Lucchetta G, Bariani P. Novel 3D wollastonite-based scaffolds from preceramic polymers containing micro- and nano-sized reactive particles. Adv Eng Mat 2012;4:269-274

[13] Database of the software Granta CES EduPack 2013.

[14] Colombo P, Bernardo B. Cellular Structures, in Riedel R, Chen I-W. Ceramics Science and Technology, Volume 1, Structures. KGaA,Weinheim:WILEY-VCH Verlag GmbH &Co; 2005.

[15] Bernardo E, Parcianello G, Colombo P, Matthews S. Wollastonite foams from an extruded preceramic polymer mixed with $CaCO_3$ microparticles assisted by supercritical carbon dioxide. Adv Eng Mat 2013;15:60-65.

[16] Sevim, F., F. Demir, M. Bilen and H. Okur (2006). "Kinetic analysis of thermal decomposition of boric acid from thermogravimetric data." Korean Journal of Chemical Engineering 23(5): 736-740.

[17] Camerucci, M. A., Urretavizcaya, G., Castro, M. S., & Cavalieri, A. L. (2001). Electrical properties and thermal expansion of cordierite and cordierite-mullite materials. *Journal of the European Ceramic Society*, *21*(16), 2917-2923.

12 Polymer-derived luminescent glass-ceramics

12.1 Introduction

Rare-earth (RE) ions have been widely studied over the last few decades, due to the distinctive optical properties of the materials in which they are inserted as dopants. The main applications are in solid state lighting, sensors, lasers, displays, optical amplifiers, etc[1]. Among the different RE elements, europium (Eu) has been extensively used in phosphors, in different oxidation states. The electronic configuration of Eu is [Xe] $4f^7 5d^0 6s^2$, so that there are possibilities of transitions from D and F shells[2]. When incorporated in oxide matrices as divalent or trivalent ions, it is responsible for red (Eu^{3+}) or bluish (Eu^{2+}) photoemission. Exploiting coexisting emissions of Eu^{2+} and Eu^{3+}, tunable phosphors can be obtained.

It is well known that, in the case of Eu^{2+}, the emission generally originates from the transition $4f^6 5d \rightarrow 4f^7$, typically exhibiting broad bands and being strongly field-dependent. The emission of Eu^{3+} ions, instead, shows a series of narrow bands, corresponding to ${}^5D_0 \rightarrow F_{0\text{-}4}$ transitions, which are nearly independent of ligand field strength[3-5].

As reported in a recent paper by Gao *et al.*[6], a mixed-valence Eu-doped silicate glass-ceramic can be achieved by annealing at 800-950 °C an alumino-boro-silicate glass (SABBL), in turns obtained by conventional melting of specific reagents at 1600 °C. This procedure, summarized in Fig. 12.1, led to the crystallization of hexacelsian ($BaAl_2Si_2O_8$) and lanthanum orthoborate ($LaBO_3$). La^{3+} sites in $LaBO_3$ crystallites are known to host Eu^{3+} ions, whereas the Ba^{2+} sites, in hexacelsian (barium feldspar), can incorporate Eu^{2+} ions, allowing simultaneous photoemission from Eu^{2+} (bluish) as well as Eu^{3+} centers (red).

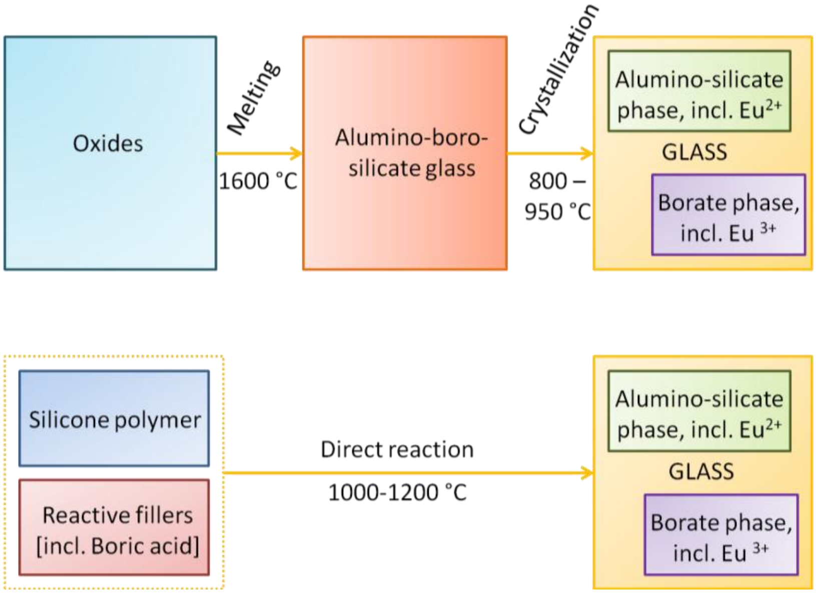

Fig. 12.1 Scheme for the obtainment of Eu-doped glass-ceramics according to the reaction between silicones and fillers and to conventional crystallization of an alumino-boro-silicate glass (SABBL).

In this study, which was edited by Fiocco *et al.*[7] and accepted for publication in 2016, an alternative approach is proposed in order to obtain alumino-boro-silicate glass-ceramics, with final phase assemblage (comprising distribution of Eu ions) resembling that of SABBL, starting from a preceramic polymer incorporating micro- and nano-sized reactive fillers. This methodology, again schematized in Fig. 12.1, only requires a direct reaction at 1000-1200 °C of the ceramic precursors, thanks to the high reactivity of this system, consisting of a silicone polymer and several inorganic fillers. Indeed the fillers directly react with the amorphous silica provided by oxidative decomposition of the silicone, which exhibits a particularly defective network, being consequently prone to very favourable reaction kinetics[8]. The use of boric acid ($B(OH)_3$), as one of the fillers, is aimed at forming a borate liquid phase upon firing, in turn enhancing the interdiffusion phenomena. This has been already shown for the development of polymer-derived wollastonite-diopside glass-ceramics, to be applied as biomaterials, with a small amount of borax (sodium borate) among fillers[9]. In the present case, however, the boron compound is not intended to represent simply a flux, providing a liquid phase later remaining as intergranular glass phase, after cooling; it is specifically designed to react with lanthanum oxide (La_2O_3), leading to $LaBO_3$, besides its participation in the surrounding glass matrix.

The flexibility of the polymer-based approach was assessed, on a preliminary basis, by developing glass-ceramics with modified composition, owing to the replacement of Ba^{2+} with Sr^{2+} ions (SABSL). The luminescence characteristics of the SASBL glass-ceramics support the hypothesis of Eu ions distributed in a feldspar phase (Sr-hexacelsian), as Eu^{2+}, and in La borate, as Eu^{3+}.

12.2 Experimental

12.2.1 Preparation of samples

A commercial silicone resin, MK (Wacker-Chemie GmbH, Munich, Germany), solid at room temperature, was considered as the silica source, with a yield of 84 wt%[8]. The polymer was added with fillers, provided in form of nano- or micro-sized particle: γ-Al_2O_3 (Evonik Ind. AG, Germany, 13 nm), Eu_2O_3 (Cometox, Italy, < 60 nm), $B(OH)_3$ (micro-sized, VWR Normapur Int.), $BaCO_3$ (micro-sized, Sigma-Aldrich Chem., MO, USA), $SrCO_3$(micro-sized, Bitossi, Italy), La_2O_3 (micro-sized, Sigma-Aldrich Chem., MO, USA). Two different formulations were prepared, as reported in Tab. 12.1. SABSL samples came from a modification of the SABBL composition, obtained by replacing BaO with SrO.

Tab. 12.1 Nominal composition of SABBL and SABSL samples.

	Sample composition (mol%)						
Sample type	SiO_2	Al_2O_3	Eu_2O_3	B_2O_3	La_2O_3	BaO	SrO
SAB**B**L	33.3	10	0.2	16.7	5	35	0
SAB**S**L	33.3	10	0.2	16.7	5	0	35

MK was first dissolved in isopropanol (20 ml for 10 g of final ceramic) and then mixed with the fillers. The mixing was performed by casting calibrated amounts of each filler in the solution of MK under magnetic stirring, followed by sonication for 10 min, thus obtaining stable and homogeneous dispersions. The mixtures were poured into large PTFE containers and dried at 60°C overnight.

After drying, the silicone-based mixtures were in the form of solid fragments, later converted into fine powders by manual grinding with pestle and mortar. The powders were cold pressed in a cylindrical steel die applying a pressure of 40 MPa for 40 sec, without any additive. Disk specimens with diameter of 13 mm in diameter and approximately 3-3.5 mm in thickness were obtained and later fired in air at 1000-1100-1200 °C for 2 hours, with a heating rate of 5 °C/min.

The preparation of SABSL samples was carried out by Dr. Zebo Babakhanova (Tashkent Institute of Chemical Technology, Uzbekistan).

12.2.2 Characterization of samples

The crystalline phases were identified by means of X-ray diffraction on powdered samples (XRD; Bruker AXS D8 Advance, Bruker, Germany – CuKα radiation, 0.15418 nm, 40 kV-40 mA, 2θ=10-70°, step size=0.05°, 2s counting time), supported by data from PDF-2 database (ICDD-International Centre for Diffraction Data, Newtown Square, PA) and Match! program package (Crystal Impact GbR, Bonn, Germany).

Photoluminescence was studied with a spectrofluorometer (FP-6300, JASCO) equipped with a Xe lamp. The emission was monitored at 612 nm and 450 nm, while the excitation wavelength was set at 250, 350, 390 nm. Luminescence spectra were collected between 280 and 800 nm.

12.3 Results

12.3.1 Phase development and evolution

Fig. 12.2 reports the X-ray diffraction patterns of SABBL samples fired in air at 1000-1100-1200 °C. The lower pattern, referring to the treatment at 1000 °C, illustrates the formation of hexacelsian ($BaAl_2Si_2O_8$ – PDF#12-0725), belonging to Ba-feldspars, and La-orthoborate ($LaBO_3$ – PDF#12-0762). The specific Ba-feldspar polymorph and the borate phase exactly match the crystal phases found by Gao *et al.*[6], after annealing of SABBL glass. As reported by Gao *et al.*[6], the borate phase might be the result of lattice distortions (from monoclinic to orthorhombic polymorph) associated with the incorporation of dopants, namely Eu^{3+}. Some additional phases, such as a secondary La-borate phase ($La(BO_2)_3$ – PDF#23-1140) and quartz (SiO_2 – PDF#85-0794), were actually detected, but they were not expected to degrade the luminescence of the material.

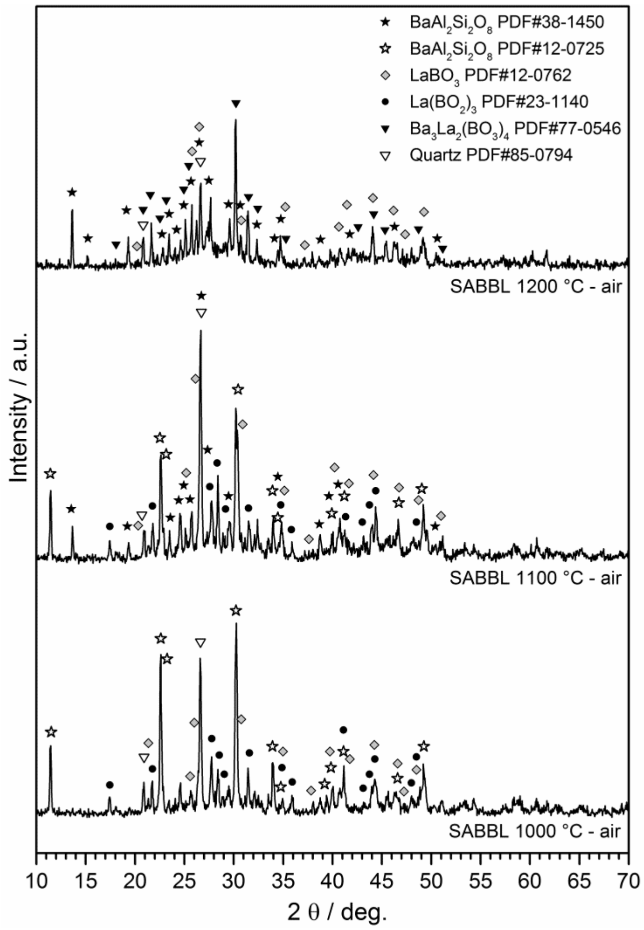

Fig. 12.2 X-ray diffraction patterns of SABBL samples fired in air at different temperatures.

The sample treated at 1200 °C (upper pattern) exhibited, besides the desired La-orthoborate phase, the formation of a different Ba-feldspar polymorph. More precisely, the main crystal phase consists of monoclinic celsian ($BaAl_2Si_2O_8$ – PDF#38-1350), also known to host Eu^{2+} ions[10]. The phase composition after treatment at 1200 °C is actually much complicated: besides the two "extra-phases" observed after treatment at 1000 °C (quartz and La-borate), we could detect Ba-La borate ($Ba_3La_2(BO_3)_4$ - PDF#77-0546). Also in this case, the new phase is known to accommodate RE ions (Eu^{3+} ions, like in the case of La-orthoborate)[11].

Concerning the sample treated at 1100 °C (central pattern), it may be seen as a "transition sample" between those developed at 1000 and 1200 °C, possessing intermediate characteristics. In fact, both hexagonal and monoclinic celsians can be detected, as well as La-orthoborate, secondary La-borate and quartz.

12.3.2 Photoluminescence properties

Fig. 12.3a reports a room temperature excitation spectra of Eu^{3+}, monitoring the photoemission at 612 nm, in SABBL samples. The multiple excitation peaks are related to the Eu^{3+} transitions from the ground state $^7F_0$ to the indicated excited levels[12]. The most intense peak lies at approximately 393 nm, corresponding to the $^7F_0 \rightarrow {}^5L_6$ transition.

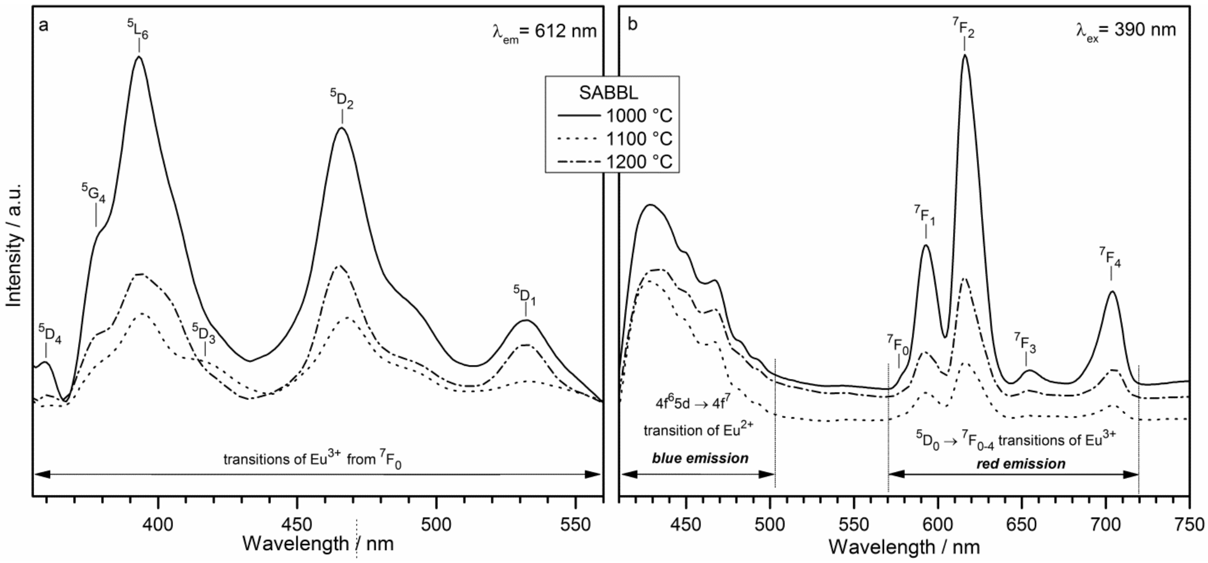

Fig. 12.3 Eu^{3+} excitation (a) and emission (b) spectra of SABBL samples treated at different temperatures.

The wavelength of maximum absorption, 393 nm, was selected for recording Eu^{3+} emission spectra, reported in Fig. 12.3b. In analogy with the findings concerning the SABBL glass-ceramics from conventional vitrification and annealing[6], the peaks between 570 and 720 nm are due to the relaxation $^5D_0 \rightarrow {}^7F_{0\text{-}4}$ (red emission). Among them, $^5D_0 \rightarrow {}^7F_2$ transition is electric-dipole allowed and the intensity of the corresponding photoemission depends strongly on the symmetry of the environment in which Eu^{3+} is hosted, whereas $^5D_0 \rightarrow {}^7F_1$ transition is magnetic-dipole allowed and the intensity is independent of local symmetry[13]. The broad emission bands appearing between 410 and 500 nm can be reasonably assigned to the transition $4f^65d \rightarrow 4f^7$ of Eu^{2+} ions (bluish emission)[14].

Considering the evolution of the spectra at different heat treatment, the emission bands are more intense and sharper for SABBL sample treated at 1000 °C, indicating optimized red and bluish luminescence. The luminescence effects at 1200 °C, however, are quite interesting, especially concerning the blue emission. The stabilization of Eu^{2+} at high temperature is mostly allowed in reducing atmosphere, while the samples in this study were treated in air. Passing from 1000 °C to higher temperatures in oxidizing atmosphere, the bands of the blue emission would be expected to decrease; on the contrary, the red emission should increase, because of the oxidation of Eu^{2+} to Eu^{3+}.

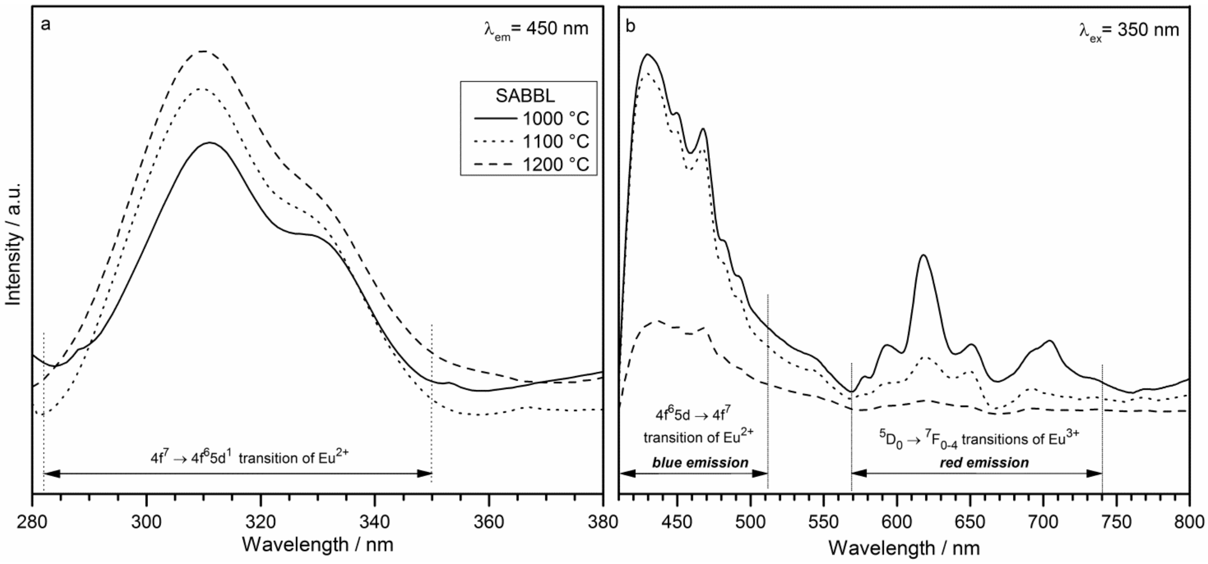

Fig. 12.4 Eu^{2+} excitation (a) and emission (b) spectra of SABBL samples treated at different temperatures.

The quite anomalous spectra in Fig. 12.3b, in our opinion, could be ascribed to the particular chemical environment associated with the ceramic conversion of the silicone polymers embedding the fillers, Eu_2O_3 particles included. The thermo-oxidative reactions occurring in the silicone upon firing imply the release of carbon-based moieties that could provide a reducing environment locally, favoring the presence of both Eu^{2+} and Eu^{3+} species. Anyway, transition from Eu^{3+} to Eu^{2+} with increasing T are also reported in the literature due to several mechanisms.[2,15] The actual mechanism of transition between different valence states would need a specific investigation, also considering that the sample fired at 1100°C, "intermediate" in the sense of crystal phases developed, did not provide an intermediate optical behaviour. This investigation, however, is beyond the aim of the present work.

The excitation spectra of SABBL samples corresponding to a secondary monitoring wavelength, i.e. 450 nm, are reported in Fig. 12.4a. The strong excitation band between 280 and 350 nm is assigned to the $4f^7 \rightarrow 4f^6 5d$ transition of Eu^{2+}.[14] The corresponding emission spectra, for samples excited at 350 nm, are shown in Fig. 12.4b. In this case, the bluish photoluminescence is dominant; anyway, emission peaks related to red emission are still clearly present. Again, as observed for exciting at 390 nm, the photoluminescence of SABBL samples is optimized at 1000 °C.

12.3.3 Extension to Sr-substituted boro-alumino-silicate glass-ceramic

As previously mentioned, a Sr-La boro-alumino-silicate formulation (SABSL, molar composition in Tab. 12.1) was considered in order to test the flexibility of our polymer-based approach. The X-ray diffraction patterns of SABSL samples are presented inFig. 12.5. Differently from SABBL, the treatment at 1200 °C caused vitrification of samples (see the upper pattern, typical for a glass). The samples treated at 1000 and 1100 °C remained crystalline (lower and central pattern, respectively) and exhibited the same phase assemblage. In particular, two phases detected for SABSL samples resemble some of those developed for SABBL samples: La-orthoborate ($LaBO_3$ - PDF#12-0762) exactly matches the phase in SABBL, while Sr-feldspar ($SrAl_2Si_2O_8$ – PDF#70-1862) is isomorphous to monoclinic Ba-celsian. Again, some extra-phases appeared, in the form of Sr-melilite ($SrAl_2SiO_7$ – PDF#38-1333), La-silicate ($La_{9.31}(Si_{1.04}O_4)_6O_2$ – PDF#76-0340) and secondary La-borate phase (La_3BO_6 – PDF#50-1379).

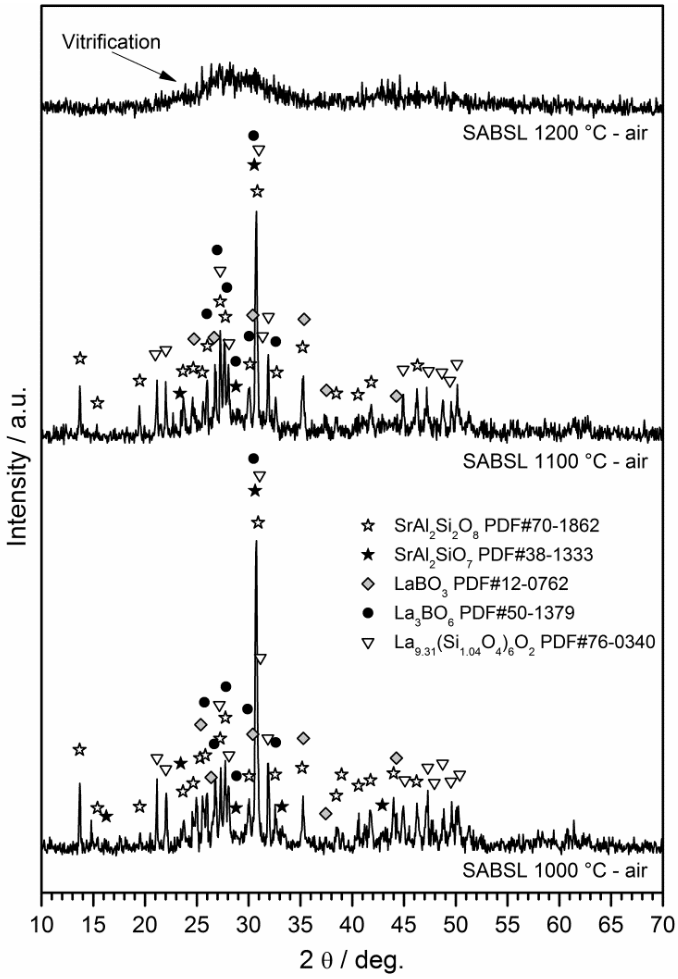

Fig. 12.5 X-ray diffraction patterns of SABSL samples fired in air at different temperatures.

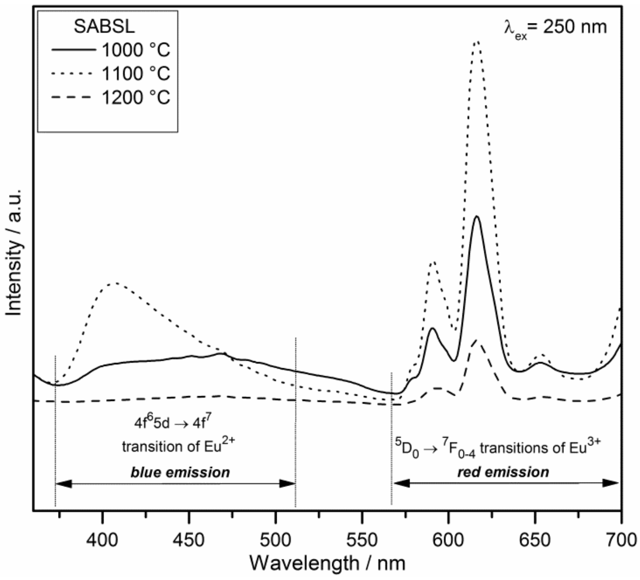

Fig. 12.6 Emission spectra of SABSL samples treated at different temperatures (excited at 250 nm).

Regarding the photoluminescence of SABSL samples after direct treatment at different temperatures, both red and blue emissions were expected, thanks to the incorporation of Eu^{3+} in La-based compounds (red) and Eu^{2+} in Sr-feldspar phase (blue). The reduction of Eu^{3+} to Eu^{2+} with increasing temperature was allowed again, thanks to locally reducing conditions upon polymer-to-ceramic conversion, as already explained for SABBL samples.

In Fig. 12.6, we can observe the emission spectra of SABSL samples when excited at 250 nm. The emission peaks between 560 and 700 nm are compatible with red photoluminescence, while the broad band close to 400 nm is consistent with blue emission. While red emission is clearly identified at each temperature treatment, due to the Eu^{3+} incorporation, the blue emission is not present at 1200 °C. The blue emission is actually optimized turning to 1100 °C, being very weak at 1000 °C. Again, the mechanism of Eu reduction/oxidation probably needs further clarification, and will constitute the focus of future investigations.

12.4 Conclusions

A “dual phase” Eu-doped glass-ceramic (alumino-silicate phase coupled with a borate phase) was successfully synthesized by direct thermal treatment of mixtures based on a silicone and ractive fillers, at 1000-1200 °C. The phase assemblage resembled that of a glass-ceramic obtained by conventional process (melting at 1600 °C and subsequent annealing), starting from the same oxide system (SABBL).

The same polymer-based approach was extended to a Eu-doped Sr-containing glass-ceramic formulation (SABSL), by simple replacing of the filler acting as BaO precursor with one providing SrO. This proved the high flexibility of the PDC approach. The phase assemblage of the Sr-containing glass-ceramics was similar to that of Ba-containing ones.

Spectroscopic data indicated both red and blue photoluminescence, as a consequence of the incorporation of both Eu^{2+} and Eu^{3+} species, in Ba/Sr-feldspar phases and in La-borate phases respectively. The reduction of Eu^{3+} to Eu^{2+} at high temperatures in oxidizing atmosphere was possibly favored by the reducing conditions, locally caused by the polymer-to-ceramic conversion of the silicone matrix.

Secondary phases detected in the SABBL/SABSL samples need to be individually investigated for clarifying their potential contribution to luminescence. Further experiments could also include the use of nano-sized fillers, which are thought to promote higher homogeneity in the silicone-based mixtures, and some changes in dopants oxides/doping concentrations.

In the light of these observations, the PDC approach is definitely confirmed to be suitable as an alternative method for synthesizing glass-ceramic phosphors by direct treatment at lower temperatures.

References

[1] C.R. Ronda, Luminescence: from theory to applications, John Wiley & Sons, 2007.

[2] J. Chen, Y. Liu, H. Liu, H. Ding, M. Fang, Z. Huang, Tunable $SrAl_2Si_2O_8$: Eu phosphor prepared in air via valence state-controlled means, Opt. Mater. 42 (2015) 80-86.

[3] K.K. Mahato, S.B. Rai, A. Rai, Optical studies of Eu^{3+} doped oxyfuloroborate glass, Spectrochim. Acta A Mol. Biomol. Spectrosc. 60 (2004) 979–985.

[4] S.S. Babu, K. Jang, E.J. Cho, H. Lee, C.K. Jayasankar, Thermal, structural and optical properties of Eu^{3+}-doped zinc-tellurite glasses, J. Phys. D Appl. Phys. 40 (2007) 5767.

[5] S. Balaji, P.A. Azeem, R.R. Reddy, Absorption and emission properties of Eu^{3+} ions in Sodium fluoroborate glasses, Physica B 394 (2007) 62–68.

[6] G. Gao, N. Da, S. Reibstein, L. Wondraczek, Enhanced photoluminescence from mixed-valence Eu-doped nanocrystalline silicate glass ceramics, Optics express. 18 (2010) A575-A583.

[7] L. Fiocco, Z. Babakhanova, E. Bernardo, Facile obtainment of luminescent glass-ceramics by direct firing of a preceramic polymer and oxide fillers, Ceramics International. (Accepted for publication in January 2016 – DOI: 10.1016/j.ceramint.2016.01.052)

[8] P. Colombo, E. Bernardo, G. Parcianello, Multifunctional advanced ceramics from preceramic polymers and nano-sized active fillers, J. Eur. Ceram. Soc. 33 (2013) 453-469.

[9] L. Fiocco, H. Elsayed, J.K.M.F. Daguano, V.O. Soares, E. Bernardo. Silicone resins mixed with active oxide fillers and Ca–Mg Silicate glass as alternative/integrative precursors for wollastonite–diopside glass-ceramic foams. J. Non-Cryst. Solids 416 (2015) 44-49.

[10] W.B. Im, Y.I. Kim, D.Y. Jeon, Thermal stability study of $BaAl_2Si_2O_8$: Eu^{2+} phosphor using its polymorphism for plasma display panel application, Chem. Mat. 18 (2006) 1190-95.

[11] P. Dorembos, The Eu^{3+} charge transfer energy and the relation with the band gap of compounds, J. Lumin. 111 (2005) 89-104.

[12] Q. Zhang, Enhanced photoluminescence of $Ca_2Al_2SiO_7$:Eu^{3+} by charge compensation method, Appl. Phys. A 88 (2007) 805-09.

[13] K. Driesen, V.K. Tikhomirov, C. Görller-Walrand, Eu^{3+} as a probe for rare-earth dopant site structure in nano-glass-ceramics. Journal of Applied Physics, 102 (2007) 4312.

[14] F. Clabau, A. Garcia, P. Bonville, D. Gonbeau, T. Le Mercier, P. Deniard, S. Jobic, Fluorescence and phosphorescence properties of the low temperature forms of the $MAl_2Si_2O_8$: Eu^{2+}(M= Ca, Sr, Ba) compounds, J. Solid State Chem. 181 (2008) 1456-1461.

[15] C. Zhang, J. Yang, C. Lin, C. Li, J. Lin, Reduction of Eu^{3+} to Eu^{2+} in $MAl_2Si_2O_8$ (M= Ca, Sr, Ba) in air condition. J. Solid State Chem. 182 (2009) 1673-1678.

13 Polymer-derived gehlenite phosphors

13.1 Introduction

The present chapter aims at exploring the potential of nano-filled silicones for the preparation of luminescent powders based on gehlenite ($Ca_2Al_2SiO_7$ or $2CaO{\cdot}Al_2O_3{\cdot}SiO_2$).

Gehlenite belongs to a quite complex system and implies the introduction, in a silicone polymer, of more than one main oxide fillers, i.e. both CaO and Al_2O_3 precursors. If, on one hand, the possible interaction between fillers may complicate the reaction with polymer-derived silica (as recently found for cordierite, $2MgO{\cdot}2Al_2O_3{\cdot}5SiO_2$, in which the formation of Mg-Al spinel, $MgO{\cdot}Al_2O_3$, was found to precede the development of the desired alumino-silicate[1]), the chosen phase, on the other, is known for its flexibility, that could promote the ionic interdiffusion. In fact, gehlenite is well-known to form solid solutions with other phases, such as akermanite ($Ca_2MgSi_2O_7$), sharing its melilite-type crystal structure: 2 Al^{3+} ions in tetrahedral coordination, as an example, may be exchanged with a Mg^{2+}/Si^{4+} couple ($Ca_2Al^{3+}(Al^{3+},Si^{4+})O_7$ turns into $Ca_2Mg^{2+}(Si^{4+},Si^{4+})O_7$)[2].

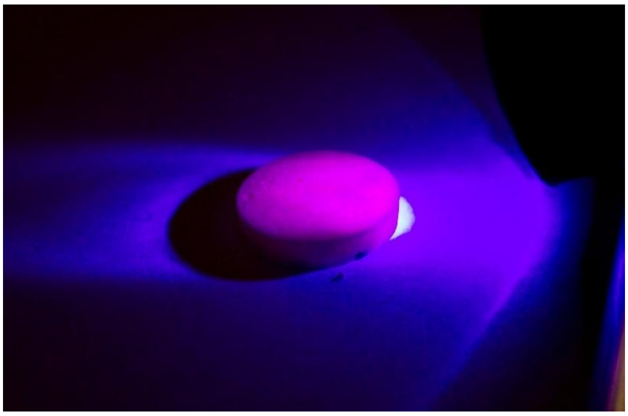

Fig. 13.1 Red-emitting Eu-doped polymer-derived gehlenite ceramic.

Melilites have been increasingly considered as reference phases for luminescent materials[3-8], based on the introduction of rare-earth ions in the relatively large octahedral sites (sandwiched between layers of interconnected coordination tetrahedra, e.g. $Al_2SiO_7^{4-}$ for gehlenite or $MgSi_2O_7^{4-}$ for akermanite) normally occupied by Ca^{2+} ions.

The PDC approach, here presented, is intended to provide an easy way for extensive industrial production, with the help of conventional firing or un-conventional treatments, such as flame synthesis, the latter representing feasible and low-cost method for preparation of a wide range of various materials. The method is based on feeding a solid (polycrystalline or amorphous) powder precursor directly into high temperature H_2/O_2 or CH_4/O_2 flame. The powder particles melt and the molten droplets are quenched by spraying them with deionized water, forming microspheres of desired composition. According to this method, high cooling rates (up to 1000 $K{\cdot}s^{-1}$) can be achieved, and even systems with high melting temperature and high tendency to crystallization can be prepared in glassy state. The method was successfully applied for the preparation of hardly meltable rare earth aluminates such as Al_2O_3-Y_2O_3 [9,10], Al_2O_3-La_2O_3 [9,11], Al_2O_3-Gd_2O_3 [9], aluminozirconates Al_2O_3-La_2O_3-ZrO_2, Al_2O_3-Gd_2O_3-ZrO_2, Al_2O_3-Y_2O_3-ZrO_2 [9], and aluminosilicates (e.g.), Al_2O_3-Y_2O_3-SiO_2 [12]. Such amorphous structures can contain much higher level of homogeneously distributed optically active dopants, in comparison to their single crystal, or polycrystalline counterparts, representing promising laser materials or phosphors for energy saving lighting appliances. Luminescent properties of Er^{3+} and Nd^{3+}-doped amorphous yttrium aluminosilicates have been reported[12].

The present work, published in 2014 by Bernardo *et al.*[13], reports on a novel approach in preparation of glasses with gehlenite matrix, doped with an optically active additive (Eu). The method combines the preparation of a precursor powder from nano-filled silicones, with the application of flame synthesis to glasses of gehlenite composition. The glasses are characterized from the point of view of their luminescence properties and compared to their polycrystalline counterparts. A sample of the red-emitting Eu-doped gehlenite ceramic obtained is reported in Fig. 13.1.

13.2 Experimental

13.2.1 Preparation of samples

A commercially available silicone powder, MK (Wacker-Chemie GmbH, Munich, Germany) was used as silica source. The polymer was first dissolved in isopropanol and then mixed with nano-sized fillers, in amounts corresponding to stoichiometric gehlenite. CaO was provided by $CaCO_3$ nanoparticles (PlasmaChem, Berlin, Germany, 90 nm), whereas Al_2O_3 came from γ-Al_2O_3 nanoparticles (Evonik Industries AG, Essen, Germany, 13 nm). Given the silica yield of MK (84 wt%) and the CaO yield of $CaCO_3$ (56 wt%), we referred to the silicone/Al_2O_3/$CaCO_3$ weight proportion of 1/1.43/1.57. For the preparation of luminescent powders, Ca^{2+} ions were partially replaced by Eu^{3+} ions, provided by Eu_2O_3 nanoparticles (purity >99.9%, diameter 45-58 nm, Cometox Srl, Milan, Italy), for an amount of 7 mol%; the adjustment of the Al/Si ratio, necessary for charge compensation, gave the final composition of $Ca_{1.86}Eu_{0.14}Al(Al_{1.14}Si_{0.86}O_7)$ instead of $Ca_2Al_2SiO_7$ [8].

The mixing was performed under magnetic stirring, followed by ultrasonication for 10 min, which allowed the preparation of stable and homogeneous dispersions, later cast in large glass containers and left to dry overnight at 80 °C.

After the evaporation of the solvent, the material obtained was first finely ground with mortar and pestle, to a size of about 100 µm, then put on alumina trays and subjected to thermal treatment in air ("conventional firing"), with target temperatures varying from 1100 to 1300 °C, with holding time of 1-3 h and heating rate of 10 °C/min. As an alternative (tested for Eu-doped composition), fine powders of silicone/filler mixture were sprayed into a modified glass-melting burner with methane-oxygen flame ("unconventional firing"). In order to avoid undercooling of the flame methane was used as a carrier gas. The temperature of the flame was estimated on the basis of the ability to melt the glass with the melting temperature exceeding 1900 °C, as determined from the phase diagram. The temperature in the center of the flame was thus estimated to be approx. 2200 °C. The powders were sprayed axially through the center of the burner. After passing the hot zone of the flame the stream of combustion gases carrying molten droplets was sprayed with deionized water in order to ensure rapid cooling of the product and to prevent its crystallization. The product was collected in a sedimentation vessel, and after sedimentation water was drained out. The sediment was thoroughly rinsed with acetone and dried.

13.2.2 Characterization of samples

The crystalline phase identification in powders from conventional firing was performed by means of X-ray diffraction (XRD; Bruker AXS D8 Advance, Bruker, Germany, operating with CuKα radiation with the wavelength of 1.5418 Å), supported by data from PDF-2 database (ICDD-International Centre for Diffraction Data, Newtown Square, PA) and Match! program package (Crystal Impact GbR, Bonn, Germany).

The product of flame synthesis, in the form of microspheres with diameters ranging from 1 to approx 40 μm, was first examined by optical microscope to make sure that the input powder was thoroughly melted and glass microspheres were formed. The amorphous nature of the product was verified by X-ray powder diffraction (Panalytical Empyrean equipped with the PixCEL® detector, and with CuKα radiation with the wavelength of 1.5405 Å).

The density of microspheres was determined by helium pycnometry (Quantachrome Ultrapyc 1200e). The morphology of amorphous microspheres has been examined by scanning electron microscopy (JEOL 7600 F) at the accelerating voltage 15 kV. Before the measurement the microspheres were dried in laboratory oven for 24 h at 50 °C, mixed with isopropanol, and the suspension was deposited on sample holder. After drying the microspheres were sputtered with gold in order to prevent charging of the surface during measurement.

Preliminary optical characterization was conducted by means of a spectrofluorometer (FP-6300, JASCO Ltd, Great Dunmow, UK), on powders of crystalline gehlenite ground and sieved to a maximum diameter of 2 μm, dispersed in distilled water. The photoluminescence spectra were recorded by Fluorolog FL3-21 spectrometer (Horiba Jobin Yvon) using Xe (400 W) arc lamp as an excitation source. All the presented photoluminescence spectra were obtained by Prof. D. Galusek's group (Joint Glass Centre of the IIC SAS, TnUAD and RONA, University of Trencin, Slovak Republic).

13.3 Results

13.3.1 Synthesis of Eu-doped gehlenite ceramic

The high reactivity of preceramic polymers mixed with nano-sized oxide powders is confirmed by the X-ray diffraction patterns in Fig. 13.2a. The $CaCO_3$/Al_2O_3/silicone mixture transformed into gehlenite (PDF#74-1607) even at only 1100 °C, for 1h; the polymer approach is evidently close to the efficiency of sol-gel processing (gehlenite achievable at 1000 °C, see Chaui *et al.* [14]). However, traces of Ca-monoaluminate ($CaAl_2O_4$ or $CaO{\cdot}Al_2O_3$, PDF#70-0134) were detected, and were persistent even with increasing firing temperature and holding time (1300°C, 3h). The characteristic main peak of Ca-monoaluminate is well visible at $2\theta \sim 30°$, whereas the minor ones are hidden by the ones of gehlenite. The formation of this phase is likely due to the direct reaction between the oxides provided by the nano-sized fillers, in analogy to what found for cordierite synthesis (formation of Mg-Al spinel, $MgAl_2O_4$ [1]); the difficult dissolution could be ascribed to the high thermal stability (the melting point of $CaAl_2O_4$ is 1600 °C, approximately[15]).

The formation of Ca-monoaluminate was practically suppressed for Eu-doped gehlenite, as testified by Fig. 13.2b. The lattice distortion associated to the formation of a solid solution, with nominal composition of $Ca_{1.86}Eu_{0.14}Al(Al_{1.14}Si_{0.86}O_7)$ (with Al^{3+} ions substituting Si^{4+} ions as a compensation of the partial replacement of Ca^{2+} ions with Eu^{3+} ions), instead of normal gehlenite, probably favoured the ionic interdiffusion, even for only 1 h at 1300 °C. This result is quite significant, since analogous charge-compensated gehlenite solid solutions[8] were prepared with a more severe firing (1350 °C, for 4 h), in the presence of fluxes, such as boric acid (H_3BO_3, evidently aimed at providing some liquid phase, and thus enhance interdiffusion). The formation of gehlenite solid solution simply from silicone-based powders could be seen as a further confirmation of the high reactivity of silicones combined with nano-sized fillers and of the good homogeneity achievable starting from suspensions of nano-particles in silicone solutions.

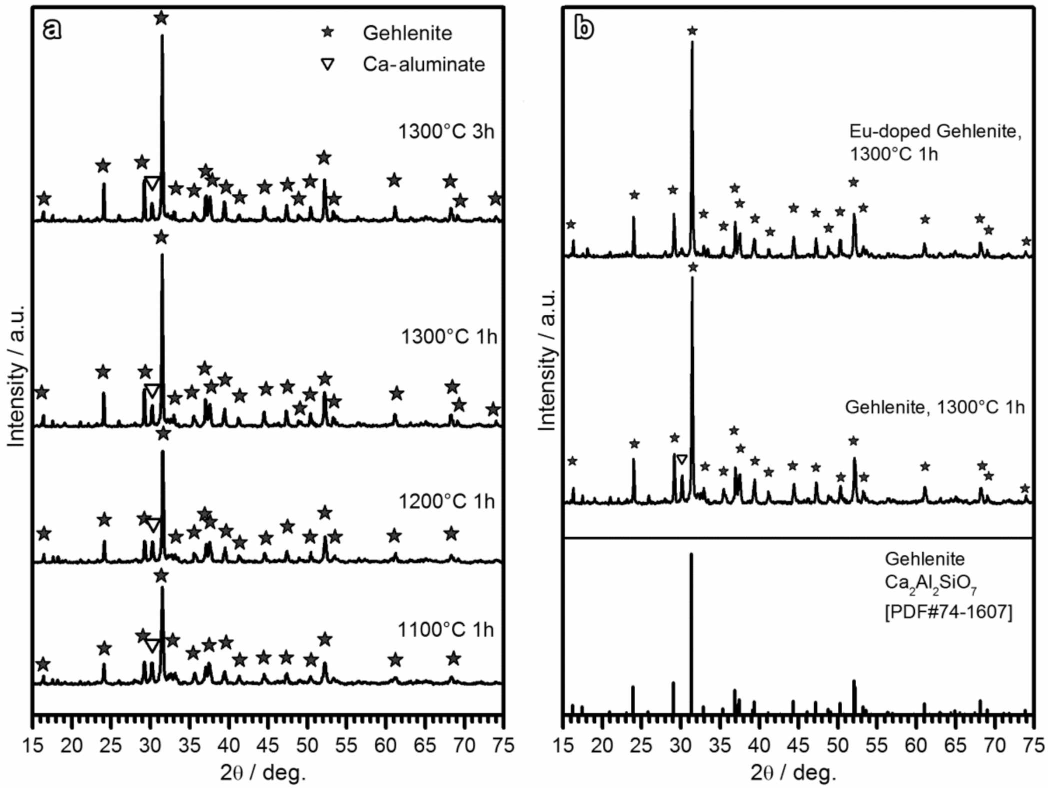

**Fig. 13.2 a) Phase evolution of the $CaCO_3/Al_2O_3$/silicone mixture for stoichiometric gehlenite;
b) Comparison between stoichiometric and "charge-compensated" Eu-doped gehlenite ceramized at 1300 °C.**

13.3.2 Synthesis of Eu-doped gehlenite glass

The precursor powder used for preparation of polycrystalline gehlenite by conventional heating was used also for preparation of glass of identical composition by flame synthesis. As mentioned above, the precursor powder comprised nanocrystalline calcium carbonate mixed with alumina, and embedded in a polymer silicon matrix. The X-ray diffraction confirmed calcium carbonate (in the form of mineral calcite) was the main crystalline phase present in the precursor powder (Fig. 13.3).

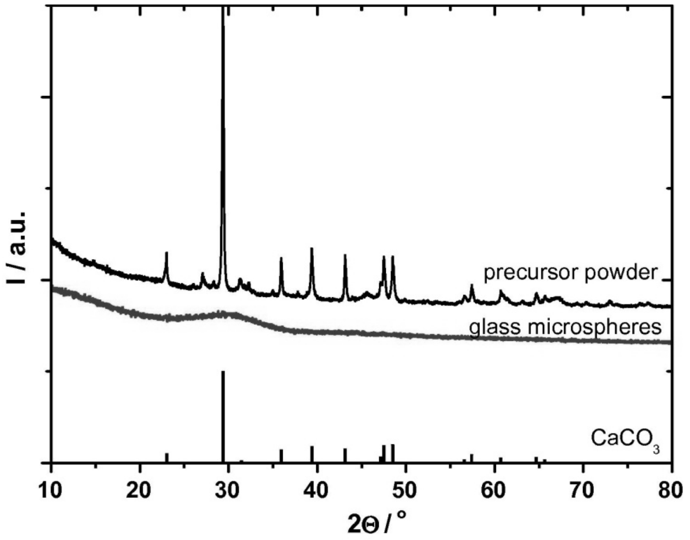

**Fig. 13.3 Fig. 2: X-ray diffraction patterns of precursor powder and glass microspheres after flame synthesis.
The bars at the bottom of the graph represent diffraction pattern of $CaCO_3$ (calcite).**

The powder was fed into methane-oxygen flame with an estimated temperature of 2200 °C, where the calcium carbonate and silicon resin decomposed to yield CaO and SiO_2. The oxide fused and melted, creating calcium aluminosilicate melt in the form of micrometer-sized droplets. These were quenched by spraying them with de-ionized water yielding glass microspheres. The amorphous nature of microspheres was confirmed by X-ray powder diffraction (Fig. 13.3). The pattern contains no distinct diffraction maxima, only a broad hump in the 2θ range 20 - 40°, characteristic for silicate and aluminosilicate glasses. The measured density of glass was 3.044 ± 0.006 g/cm^3, which was virtually identical with the density of mineral gehlenite (3.04 g.cm^{-3})[16].

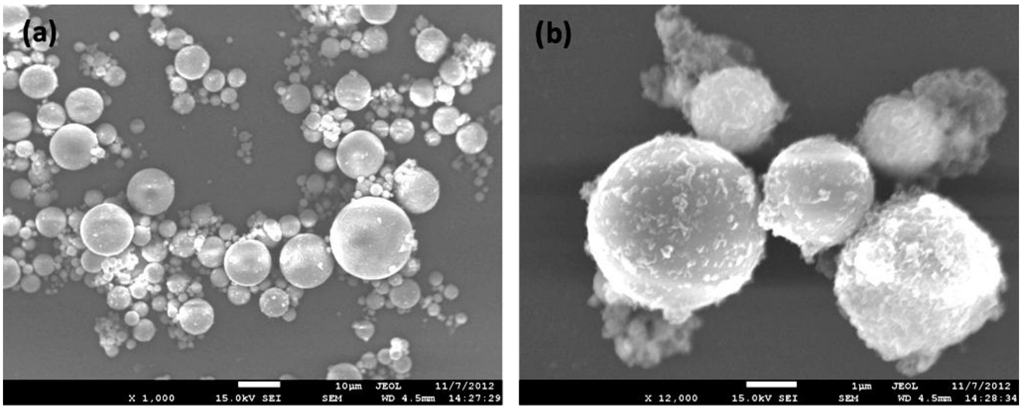

Fig. 13.4 SEM micrographs of gehlenite glass microspheres demonstrating polydispersity of the system (a), and a detailed view showing irregular features at the surfaces of microspheres (b).

The SEM examination of the flame synthesis product revealed a polydisperse system with diameters of gehlenite glass microspheres ranging between 1 and approximately 15 µm (Fig. 13.4a). The shape of microbeads, close to ideal spheres, confirms thorough melting of precursor powder particles. More detailed examination at higher examination revealed the presence of irregularly shaped protrusions on the microspheres, which appear to be firmly attached to their surface. Their origin is not clear at present, but they might comprise hydrated amorphous or crystalline aluminosilicates created by reaction of glass with water in the course of quenching, or partial dissolution of microspheres with subsequent re-precipitation of hydrated products during separation of microspheres in sedimentation tank. However, their content was below the detection limit of X-ray diffraction.

13.3.3 Characterization of crystalline and amorphous Eu-doped gehlenite

The excitation-emission matrix for the studied Eu^{3+}-doped gehlenite glass and its crystallized counterpart is shown in Fig. 13.5. Several excitation regions can be clearly seen in the range of 360–400 nm and 460–470 nm, with emissions approximately at 620 and 700 nm. The maximum of emission intensity was observed for excitations at about 395 nm and 465 nm, respectively. For Eu^{3+}-doped gehlenite glass, the emission intensity at 620 nm is comparable for both excitation wavelengths (395 and 465 nm), while for crystalline sample the maximum emission intensity has been observed when sample was excited at about 395 nm. The glassy character of the Eu^{3+}-doped gehlenite glass sample is reflected in broader excitation-emission regions compared to the crystalline sample.

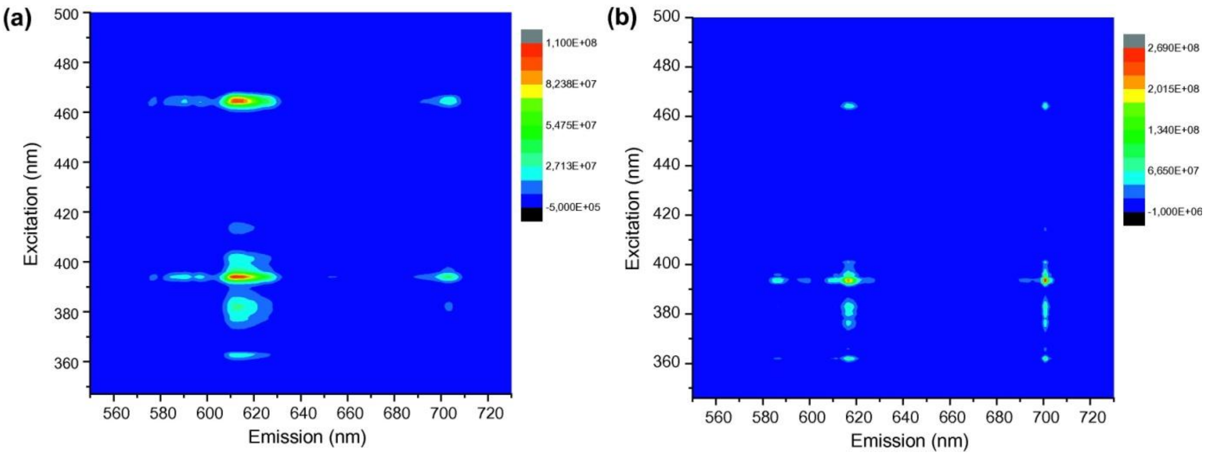

Fig. 13.5 Excitation-emission matrix of Eu^{3+}-doped gehlenite glass microspheres (a) and of polycrystalline Eu^{3+}-doped gehlenite (b).

The more detailed excitation spectra for both samples measured in the wavelength range of 225–560 nm by monitoring the intense red emission located at 613 nm are shown in Fig. 13.6. All excitation as well as emission spectra were recorded at room temperature. The broad band (assigned as CTB) extending from 240–340 nm is associated with charge-transfer (CT) transition in the Eu^{3+}–O^{2-} species and corresponds to the electronic transition from 2p orbital of O^{2-} ions to the empty 4f orbitals of Eu^{3+} ions. For crystalline sample CTB is shifted toward the lower energy side (red shift) compared to the glass sample. The sharp lines in the longer wavelength region are assigned to the intra-configurational 4f–4f forbidden transitions of Eu^{3+} ions. The excitation spectra consist of two intense bands at 394 and 464 nm in addition to other relatively weak bands peaking at about 320, 362, 365, 376, 382, 400, 413, 526 and 532 nm. The two strong excitation lines at 394 and 464 nm are attributed to the $^7F_0 \rightarrow {}^5L_6$ and $^7F_0 \rightarrow {}^5D_2$ transitions, respectively. The bands peaking around 320, 362, 376, 526 nm are assigned to transitions from the $^7F_0$ level to the $^5H_4$, $^5D_4$, $^5G_2$, $^5D_2$, and $^5G_1$ levels. On the other hand, the bands peaking around 365, 382, 400, 413 and 532 nm are assigned to the transitions from the thermally populated $^7F_1$ level to the $^5L_7$, $^5L_6$, $^5D_3$, $^5D_3$ and $^5D_1$ levels of Eu^{3+} ions, respectively.

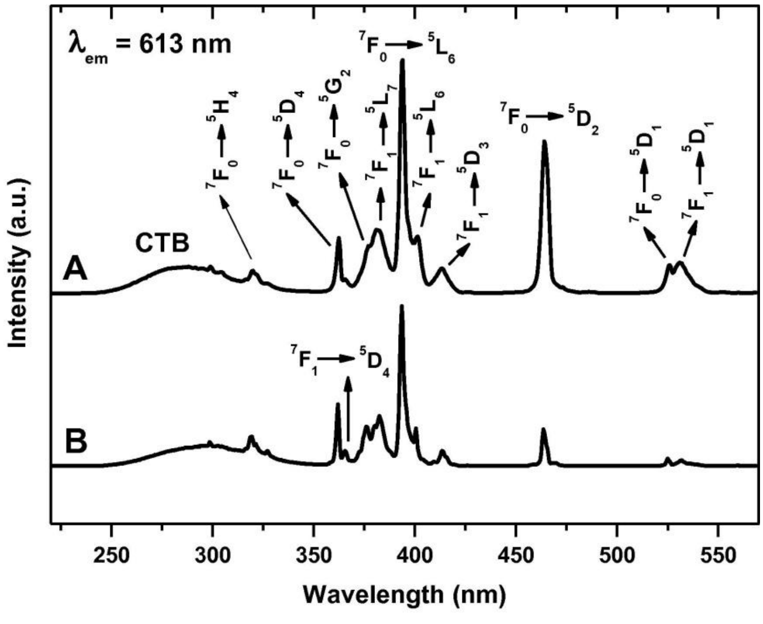

Fig. 13.6 Excitation spectra (λ_{em} = 613 nm) of Eu^{3+}-doped gehlenite glass microspheres (A) and of polycrystalline Eu^{3+}-doped gehlenite (B).

The emission photoluminescence (PL) spectra of the studied samples recorded in the 550–750 nm spectral range at both excitation wavelength (394 and 464 nm) are shown in Fig. 13.7. After excitation into the $^5L_6$ excited level, appreciable radiative emissions occur from the $^5D_0$ metastable state to ^7F_J (J = 0, 1, 2, 3, 4) states in the range of 550–750 nm. When any other levels above $^5D_0$ are excited, there is fast non-radiative relaxation to the $^5D_0$ level due to the small energy gaps between them and consequently the same emission spectrum is obtained. The PL spectra of the studied samples show five major emission lines at 577 (yellow), 587 (orange), 617 (red), 655 (deep-red) and 701 nm (deep-red) corresponding to the $^5D_0 \rightarrow {}^7F_J$ (J = 0, 1, 2, 3, 4) transitions, respectively. The transitions $^5D_0 \rightarrow {}^7F_J$ with J = 5 and 6 were not observed due to their low transition probabilities. The $^5D_0 \rightarrow {}^7F_J$ (J = 2, 4 and 6) transitions are electric dipole transitions; the existence of electric dipole transitions is due to the absence of the centre of symmetry and the mixing of 4f orbitals with orbitals of opposite parity. The appearance of narrow emission bands in the spectra is due to the shielding effect of $4f^6$ electrons by 5s and 5p electrons in outer shells in the Eu^{3+} ion. Among the five observed emission bands, the transition $^5D_0 \rightarrow {}^7F_2$ (617 nm; red emission) is the one of the most intense transition, and is considered as hypersensitive transition (very sensitive to the site symmetry of Eu^{3+} ions) that follows the selection rule $\Delta J = 2$. The transition $^5D_0 \rightarrow {}^7F_1$ (587 nm; orange emission) allowed by the selection rule $\Delta J = 1$ is magnetic dipole transition and is independent of the crystal field strength around Eu^{3+} ion[17]. The emission due to $^5D_0 \rightarrow {}^7F_0$ transition at 577 nm is normally forbidden. However, in the present hosts, it is observed with moderate emission intensity. The existence of $^5D_0 \rightarrow {}^7F_0$ transition with a moderate intensity substantiates the presence of strong crystal field in the vicinity of rare earth ion causing Stark splitting in electric dipole ($^5D_0 \rightarrow {}^7F_2$) and magnetic dipole ($^5D_0 \rightarrow {}^7F_1$) transitions. As found from the de-convolution of the emission spectra (not shown in Fig. 13.7), the latter transition at 587 nm clearly shows three Stark components while the former at 617 nm exhibits five components due to the influence of the crystal-field. This indicates total removal of the crystal-field degeneracy. Based on the selection rules, the observed number of three and five Stark components for magnetic and electric dipole transitions of Eu^{3+} ions as well as appearance of $^5D_0 \rightarrow {}^7F_0$ transition indicates the fact that the symmetry at Eu^{3+} ion site is low. Due to the presence of high energy phonons in host matrix (e.g. aluminosilicate glasses), the emissions starting from the excited levels ^5D_J (J = 1, 2 and 3) are suppressed i.e., there is a fast non-radiative relaxation to the $^5D_0$ level when the Eu^{3+} ions are excited to any level above the $^5D_0$.

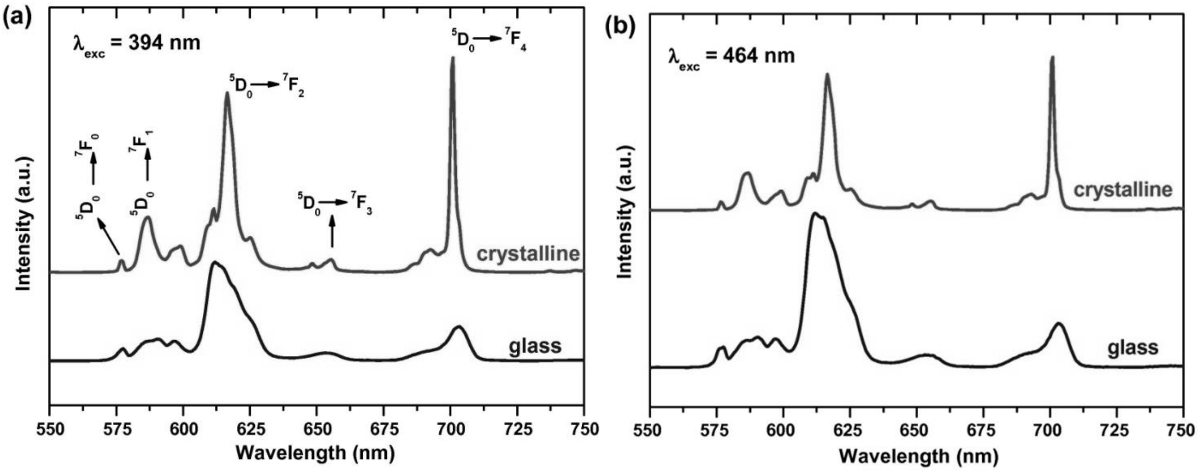

Fig. 13.7 Emission spectra of Eu^{3+}-doped gehlenite glass microspheres and polycrystalline gehlenite excited at λ_{exc} = 394 nm (a) and λ_{exc} = 464 nm (b), respectively.

The hypersensitivity ratio R (ration between integrated intensities of $^5D_0 \rightarrow {}^7F_2$ and $^5D_0 \rightarrow {}^7F_1$ transitions), known as the asymmetric ratio, allows one to estimate the covalent nature and polarization of the surrounding of the Eu^{3+} ions by short range effects and centrosymmetry distortion of Eu^{3+} ion site. The higher the value R, the lower the symmetry around the Eu^{3+} ions, and the higher the Eu–O covalence, and vice versa[18-20]. The R values for the studied systems were found to be 4.28 for gehlenite glass and 2.57 for crystalline sample, respectively. This suggests the presence of lower symmetry around the Eu^{3+} ions and possibly higher covalency of the Eu–O bond in the gehlenite glass, compared to crystalline Eu^{3+}-doped $Ca_2Al_2SiO_7$ sample.

As to the comparison of the emission spectra of gehlenite glass and of the crystalline sample, the emission peaks are broadened in the glass sample and intensities of the emissions (especially red emissions) are lower compared to the crystalline sample when excited at 394 nm (NUV). However, when the samples are excited at 464 nm (blue light) the intensities of the red emission at about 617 nm are comparable for both glass and crystalline samples. The computation of chromaticity is based on the procedure made available by Commission Internationale de L´Eclairage (CIE), France. When excited at 394 nm the CIE chromaticity coordinates of both the gehlenite glass and polycrystalline gehlenite were found to be (x = 0.65, y = 0.35), indicating that both systems are suitable candidates for red light emitting phosphors. The emission spectra of the crystalline Eu^{3+}-doped $Ca_2Al_2SiO_7$ sample are comparable with the Eu^{3+}-doped $Ca_2Al_2SiO_7$ systems prepared by other methods[8,14,21].

The room-temperature decay curves of Eu^{3+} ions in glass and polycrystalline gehlenite for the emission transition $^5D_0 \rightarrow {}^7F_2$ monitored at 617 nm with an excitation at 394 nm are shown in Fig. 13.8. The decay curves of both samples can be well fitted by a single exponential decay function, $I(t) = I_0(t)\ exp(-t/\tau)$, where I and I_0 are luminescence intensities, t is the time, and τ is the decay time, respectively (correlation coefficient R_2 ~ 0.999). The decay time for Eu^{3+} doped gehlenite glass (1.59 ms) was found to be smaller than for the crystalline gehlenite sample (2.30 ms). The increased lifetime in polycrystalline gehlenite proves higher symmetry around the Eu^{3+} ions and thus better crystal environment for Eu^{3+} ions in the doped $Ca_2Al_2SiO_7$ phase, compared to the disordered glass host structure.

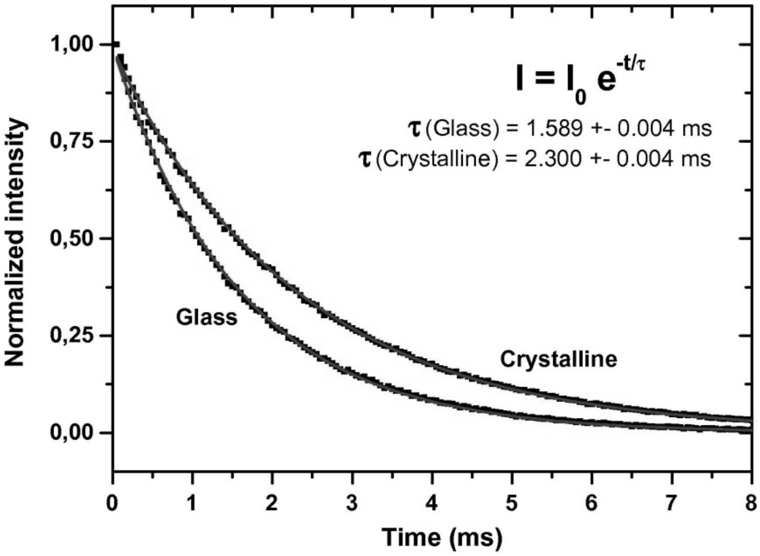

Fig. 13.8 Decay curves for the $^5D_0 \rightarrow 7F_2$ emission transition of Eu^{3+} ion monitored at 617 nm under excitation at 394 nm of polycrystalline gehlenite and gehlenite glass microspheres.

13.4 Conclusions

Gehlenite ($Ca_2Al_2SiO_7$) ceramics were successfully prepared by the heat treatment in oxidative atmosphere of a silicone resin embedding CaO and Al_2O_3 precursors, in the form of nano-sized particles which acted as reactive fillers. Luminescence was due to the use of nano-sized Eu_2O_3 as secondary additive, adopting a charge compensation formulation ($Ca_{2-2x}Eu_{2x}Al(Al_{1+2x}Si_{1-2x}O_7)$), with x=0.07.

Conventional firing at only 1300 °C in oxidative atmosphere for 1 h led to a practically single phase Eu-containing gehlenite solid solution, as an evidence of the good homogeneity achievable starting from suspensions of nano-particles in silicone solutions.

The homogenous distribution of components was further testified by the formation of Eu-doped alumino-silicate glass, using an alternative thermal treatment, i.e. flame synthesis.

Crystalline and amorphous powders, with the same oxide composition, i.e. corresponding to Eu-doped gehlenite $Ca_{1.86}Eu_{0.14}Al(Al_{1.14}Si_{0.86}O_7)$, produced by conventional firing and flame synthesis, respectively, could be seen as efficient inorganic phosphors, to be activated in the near-UV range. The different structure was associated to different emission characteristics (red luminescence dominant for crystalline powders, orange for amorphous powders).

An increased lifetime for $^5D_0 \rightarrow ^7F_2$ transition was observed for polycrystalline gehlenite (2.30 ms) compared to gehlenite glass (1.59 ms).

References

[1] Parcianello, G., Bernardo, E., Colombo, P. (2013). Cordierite ceramics from silicone resins containing nano-sized oxide particle fillers. Ceram. Int. 39(8), 8893-8899.

[2] Swainson, I. P., Dove, M. T., Schmahl, W. W., Putnis, A. (1992). Neutron powder diffraction study of the akermanite-gehlenite solid solution series. Physics and Chemistry of Minerals, 19(3), 185-195.

[3] Kodama, N., Takahashi, T., Yamaga, M., Tanii, Y., Qiu, J., Hirao, K. (1999). Long-lasting phosphorescence in Ce^{3+}-doped $Ca_2Al_2SiO_7$ and $CaYAl_3O_7$ crystals. Applied physics letters, 75(12), 1715-1717.

[4] Kodama, N., Tanii, Y., Yamaga, M. (2000). Optical properties of long-lasting phosphorescent crystals Ce^{3+}-doped $Ca_2Al_2SiO_7$ and $CaYAl_3O_7$. Journal of luminescence, 87, 1076-1078.

[5] Kodama, N., Sasaki, N., Yamaga, M., Masui, Y. (2001). Long-lasting phosphorescence of Eu^{2+} in melilite. Journal of luminescence, 94, 19-22.

[6] Yamaga, M., Tanii, Y., Kodama, N., Takahashi, T., Honda, M. (2002). Mechanism of long-lasting phosphorescence process of Ce^{3+}-doped $Ca_2Al_2SiO_7$ melilite crystals. Physical Review B, 65(23), 235108.

[7] He, D., Shi, Y., Zhou, D., Hou, T. (2007). Photoluminescence properties of $M_2MgSi_2O_7:Re^{2+}$(M=Ba, Sr, Ca). Journal of luminescence, 122, 158-161.

[8] Zhang, Q., Wang, J., Zhang, M., Ding, W., Su, Q. (2007). Enhanced photoluminescence of $Ca_2Al_2SiO_7:Eu^{3+}$ by charge compensation method. Applied Physics A, 88(4), 805-809.

[9] Rosenflanz, A., Frey, M., Endres, B., Anderson, T., Richards, E., Schardt, C. (2004). Bulk glasses and ultrahard nanoceramics based on alumina and rare-earth oxides. Nature, 430(7001), 761-764.

[10] Prnova, A., Karell, R., Galusek, D. (2008). The preparation of binary Al_2O_3-Y_2O_3 glass microspheres by flame synthesis from powder oxide precursors. Ceramics-Silikáty, 52(2), 109-114.

[11] Haliaková, A., Prnová, A., Klement, R., Galusek, D., Tuan, W. H. (2012). Flame-spraying synthesis of aluminate glasses in the Al_2O_3-La_2O_3 system. Ceramics International, 38(7), 5543-5549.

[12] Prnová, A., Domanická, A., Klement, R., Kraxner, J., Polovka, M., Pentrák, M., Galusek, D., Simurka, P., Kozánková, J. (2011). Er-and Nd-doped yttrium aluminosilicate glasses: Preparation and characterization. Optical Materials, 33(12), 1872-1878.

[13] Bernardo, E., Fiocco, L., Prnová, A., Klement, R., Galusek, D. (2014). Gehlenite: Eu^{3+} phosphors from a silicone resin and nano-sized fillers. Optical Materials, 36(7), 1243-1249.

[14] Chuai, X. H., Zhang, H. J., Li, F. S., Chou, K. C. (2004). The luminescence of Eu^{3+} ion in $Ca_2Al_2SiO_7$. Optical Materials, 25(3), 301-305.

[15] Zawrah, M. F., Khalil, N. M. (2007). Synthesis and characterization of calcium aluminate nanoceramics for new applications. Ceramics International, 33(8), 1419-1425.

[16] http://webmineral.com/data/Gehlenite.shtml#.UkUqvH-Ge8U

[17] Blasse, G., Bril, A., Nieuwpoort, W. C. (1966). On the Eu^{3+} fluorescence in mixed metal oxides: Part I-The crystal structure sensitivity of the intensity ratio of electric and magnetic dipole emission. Journal of Physics and Chemistry of Solids, 27(10), 1587-1592.

[18] Reisfeld, R., Zigansky, E., Gaft, M. (2004). Europium probe for estimation of site symmetry in glass films, glasses and crystals. Molecular Physics, 102(11-12), 1319-1330.

[19] Babu, P., Jayasankar, C. K. (2000). Optical spectroscopy of Eu^{3+} ions in lithium borate and lithium fluoroborate glasses. Physica B: Condensed Matter, 279(4), 262-281.

[20] Patra, A., Sominska, E., Ramesh, S., Koltypin, Y., Zhong, Z., Minti, H., Gedanken, A. (1999). Sonochemical preparation and characterization of Eu_2O_3 and Tb_2O_3 doped in and coated on silica and alumina nanoparticles. The Journal of Physical Chemistry B, 103(17), 3361-3365.

[21] Jiao, H. Y., Wang, Y. (2012). A potential red-emitting phosphor $CaSrAl_2SiO_7:Eu^{3+}$ for near-ultraviolet light-emitting diodes. Physica B: Condensed Matter, 407(14), 2729-2733.

Concluding remarks and future perspectives

The research activity presented in this thesis involved the synthesis, the characterization and the optimization of silicate ceramics of various formulations, obtained through the thermal conversion into ceramics, mainly conducted in air, of silicone-based mixtures. The synthesis route, based on polymer-derived ceramics, was proposed as an alternative to conventional techniques, such as the ceramic powder processing technology, undoubtedly providing a series of advantages: the wide variety and availability of precursors, their low cost and easy-handling, the relatively low synthesis temperatures and the possibility to apply the conventional plastic shaping techniques.

In this work, the main novelty lies in the incorporation of fillers in the silicone resins to serve as oxide precursors, rather than to dilute the transforming mass or to compensate the shrinkage. In fact, here the fillers were intended to decompose into oxides and fully react only with the ceramic residue of the polymeric precursors, in order to obtain the formation of specific crystalline phases with the composition of silicates, that are generally not directly achievable by the simple pyrolysis of a preceramic polymer. By this way, the above-listed advantages related to preceramic polymers were exploited for the fabrication of ceramics at relatively low temperatures (below 1200 °C), by means of easy plastic forming techniques, in particular direct foaming and direct 3-D printing of preceramic slurries filled with reactive fillers. The fillers incorporated in the preceramic mixtures were also exploited, in some cases, as foaming agents or liquid phase formers, thus helping respectively the direct shaping of porous bodies or the obtainment of glass-ceramic components.

The type of fillers was conveniently selected according to the desired final composition; therefore, a wide variety of ceramic systems was achieved, simply by changing the proportions and composition of the starting polymers and fillers.

The work was logically divided into two main macro-areas: the first one regarding the realization of peculiar silicate formulations known for their pronounced biological properties, aimed at the fabrication of scaffolds for bone regeneration implants, and the second one regarding other silicate formulations specifically designed for further functional applications.

Concerning the first part, devoted to bioceramic compositions, the starting point was the realization of silicates resembling the composition of two famous bioglasses, 45S5 (SiO_2-CaO-Na_2O-P_2O_5 oxides system) and 58S (SiO_2-CaO-P_2O_5 oxides system). The materials obtained exhibited good bioactivity, although the use of preceramic polymers and fillers did not lead to amorphous products, like the original bioglasses, but to only partially amorphous components. A further observation regarded the double role of sodium phosphate dibasic heptahydrate ($Na_2HPO_4 \cdot 7H_2O$), which was used as an oxide precursor for Na_2O and P_2O_5 and, at the same time, as a foaming agent, due to the water release from its thermal decomposition. Future investigations concerning the realization of amorphous ceramics might involve the application of flame synthesis to solid preceramic mixtures: in fact, according to this method, high cooling rates (up to 1000 $K \cdot s^{-1}$) can be achieved and even systems with high melting temperature and high tendency to crystallization can be prepared in glassy state.

A second topic involved the modification of calcium silicates by incorporation of magnesium. Ca-silicates have received a growing interest in the last decades, but have a main drawbacks related to the low mechanical strength of porous bodies and the high degradation rate, which may lead to high pH values with detrimental effects on cells. Therefore, ion modifications of Ca-silicates have been proposed in literature with the aim of tailoring both mechanical and biomedical properties and, in this framework, significant attention has been given to the CaO-MgO-SiO_2 oxides system. In particular, two Ca-Mg silicates were developed in this thesis: one, akermanite ($Ca_2MgSi_2O_7$), as the the only crystal phase; the other, diopside ($CaMgSi_2O_6$), coupled with wollastonite ($CaSiO_3$). Both formulations exhibited good bioactivity and great potential as bone tissue engineering materials, as demonstrated by the excellent cellular response of MC3T3 osteoblast precursors cells cultured on polymer-derived samples, besides a compressive strength in the range of 1-2 MPa. In this case, samples were first obtained by direct foaming of preceramic slurries, due to the water release from the thermal decomposition of $Mg(OH)_2$ and to the decomposition of hydrazine, added as a foaming agent.

Especially for the wollastonite-diopside composite, further experiments involved the incorporation of sodium borate decahydrate ($Na_2B_4O_7 \cdot 10H_2O$) and sodium phosphate dibasic heptahydrate ($Na_2HPO_4 \cdot 7H_2O$) as "mineralizing" fillers, aimed at forming a liquid phase upon firing, then remaining as an intergranular glass phase, surrounding the two main crystalline phases. This liquid phase was expected, on the one hand, to promote the ionic interdiffusion, thus obtaining high phase purity; on the other hand, instead, it was expected to promote a viscous flow, thus helping the relaxation of stresses arising from the ceramization. These effects were also enhanced by the direct incorporation of a glass filler, reaching a final compressive strength of 6 MPa. Again, the multifunctionality of specific fillers was exploited: in fact $Na_2B_4O_7 \cdot 10H_2O$ and $Na_2HPO_4 \cdot 7H_2O$ acted as foaming agents, as well as a mineralizing fillers, allowing an extensively foaming of the silicone-based mixtures by water release from thermal decomposition.

Still regarding wollastonite-diopside, other shaping techniques were experimented, besides the direct foaming. In particular, direct ink writing was applied to silicone-based pastes for the realization of reticulated structures reaching 3 MPa in compression, while supercritical CO_2-assisted extrusions were applied to solid preceramic mixtures, avoiding, in the latter case, the use of solvents and reaching 4 MPa in compression mode. These two processing options, made possible by the presence of a polymeric phase in the preceramic mixtures, showed a way to make industrial application of the preceramic polymers and might be further optimized in future.

Concerning only the extruded materials, a heat treatment in inert atmosphere was carried out to prevent the removal of carbon in the form of gaseous products, as usually occurring in air, leading to the formation of a carbon phase. This was thought to be an interesting strategy for biomedical applications, given the recent developments concerning bioceramics incorporating carbon structures as reinforcement. From a mechanical point of view, the samples exceeded 20 MPa in compression mode, demonstrating their suitability for the realization of bone scaffolds. Nevertheless, the biological properties of products pyrolyzed in inert atmosphere have not been fully tested yet and further dissolution/cell culture studies are planned.

Another novel formulation developed in this research work was a wollastonite-apatite composite, realized by a multistep synthesis process. The idea of combining these two crystal phases was born as a solution to the issue concerning the mechanical weakness of porous hydroxyapatite. Therefore, the new material was thought to couple the strong bioactivity of an outer shell of hydroxyapatite with a mechanically stronger open foamed wollastonite core. The route chosen was to develop a composite material starting from calcite ($CaCO_3$) foams, obtained from preceramic polymers and fillers, treated by immersion in a phosphatising bath to obtain a partial $CaCO_3$-to-apatite conversion and later ceramized to allow the reaction between the remaining calcite and silica left from the silicone-to-ceramic conversion. The final result was a wollastonite-apatite composite foamed material, that demonstrated excellent biocompatibility, bioactivity and osteogenic potential when MC3T3 cells were cultured on it, besides a compressive strength of 3 MPa. The same scaffolds were also fabricated by direct 3-D printing, obtaining an encouraging result, but the printing process still needs to be improved.

A similar approach was followed to fabricate silica-bonded apatite porous structures, but by negative replica, which exhibited a compressive strength between 13 and 17 MPa. Here, the goal was to obtain a high $CaCO_3$-to-apatite conversion, to realize a final ceramic mainly consisting of apatite.

One last composite material was represented by directly 3-D printed silica-bonded calcite, being $CaCO_3$ a well-established material for implantation purposes. The compressive strength of the 3-D printed scaffolds was between 3 and 5 MPa.

An interesting future development of some of the most attractive bioceramics realized in this PhD program might be the functionalization of the samples surfaces with biomolecules, mimicking the organic structure of natural bones and thus promoting the cell viability on the scaffolds after implantation. Moreover, osteoblast adhesion and proliferation might be promoted by the incorporation of specific adhesive sequences, in order to enhance the interactions between the implant and the living cells, so that to further increase the osseointegration.

Another useful improvement, in this case concerning the shaping and synthesis method, would be a more extensive use of robocasting techniques for the samples production on an industrial scale.

The second part of the present thesis, as already mentioned, regarded the fabrication of other silicate formulations for further functional applications. The technology transfer to other compositions was enabled by virtue of the high flexibility of the PDCs approach, besides a series of analogies in the fabrication process and in the crystal structures, as well as the multifunctionality of some fillers and of final silicates.

A first example was represented by apolymer-derived forsterite ceramic (Mg_2SiO_4), a Mg-silicate which can serve as a biomedical material for its biocompatibility and bioactivity, but can also be considered a valid dielectric material, since it exhibits very low dielectric losses. For this reason, this silicate is much appreciated in telecommunications and in radar systems, from ultra-high speed LAN to car anti-collision devices, dielectric resonators and filters.

Another composition developed in this research work was a polymer-derived cordierite ($Mg_2Al_4Si_5O_{18}$) ceramic, a Mg-Al silicate with applications in in the field of catalytic converters and particulate filters for diesel engines and, more generally, for components subjected to severe thermal gradients. Cordierite ceramics were shaped into highly porous bodies, exploiting, as already described for some biosilicates, the water release from dehydration of $Mg(OH)_2$, that was used as a MgO precursor, for the realization of the final composition of cordierite, but also as a foaming agent, thanks to its multifunctionality.

A “dual-phase” Eu-doped glass-ceramic with luminescent properties was also synthesized by direct reaction of a preceramic mixture, through a heat treatment at 1000-1200 °C in air. The final result was an alumino-boro-silicate glass-ceramic, with final phase assemblage (comprising distribution of Eu ions) resembling that of SABBL glass, that is usually obtained by melting at 1600 °C and crystallization at 900 °C. As described for some biomedical compositions, glass-ceramics can be fabricated from preceramic polymers incorporating some fillers, like boron compounds, that act as a flux, providing a liquid phase later remaining as intergranular glass phase, after cooling. However, if incorporated in higher amounts, the same filler, besides forming the surrounding glass matrix, could participate in the formation of a borate phase, that could host Eu^{3+} ions. Moreover, Eu^{2+} species were incorporated in an Al-silicate phase, thus giving both red and blue luminescence photoemission. The reduction of Eu^{3+} to Eu^{2+} at high temperatures in oxidizing atmosphere was possibly favoured by the reducing conditions, locally caused by the polymer-to-ceramic conversion of the silicone matrix.

Eu species were also exploited as dopants for polymer-derived gehlenite ($Ca_2Al_2SiO_7$) phosphor, a Ca-Al silicate exhibiting the same crystal structure as akermanite ($Ca_2MgSi_2O_7$), in which RE ions can easily replace alkali earth metals due to the similarity in their size. Eu-doped gehlenite ceramics showed strong optical properties as well.

Curriculum vitae

Education

- **Ph.D. Industrial Engineering** *(January 2013 - December 2015)*
  University of Padova, Dpt. of Industrial Engineering, Padova (Italy)
  Thesis title: *Silicate ceramics from preceramic polymers and fillers*
  Advisor: Prof. Enrico Bernardo

- **M.Sc. Materials Engineering** *(October 2010 - October 2012)*
  University of Padova, Padova (Italy)
  110 / 110 magna cum laude
  Thesis title: *Bioceramics from preceramic polymers and fillers*

- **B.Sc. Materials Engineering** *(October 2007 - July 2010)*
  University of Padova, Padova (Italy)
  109 / 110
  Thesis title: *NBR-HNBR diaphragms and gaskets characterization: lifetime prediction using Arrhenius and Williams-Landel-Ferry models and damage modelling*

Experiences abroad

- **Visiting Ph.D. researcher** *(May 2015 - June 2015)*
  Imperial College London, Dpt. of Materials, London (UK)
  Project title: *Synthesis and in vitro biological characterization of highly porous bioceramics for bone regeneration implants*
  Advisor: Prof. Julian R. Jones

- **Recipient of 6-month student travel scholarship** *(February 2014 – August 2014)*
  financed by "Fondazione Ing. Aldo Gini", Padova, Italy
  Imperial College London, Department of Materials, London (UK)
  Project title: *Synthesis and in vitro biological characterization of highly porous bioceramics for bone regeneration implants.*
  Advisor: Prof. Julian R. Jones

- **Recipient of 3-month student travel scholarship** *(September 2013 – December 2013)*
  cofinanced by MIUR in the framework of the Eu program LLP/Erasmus
  Topic: *Supercritical CO_2-assisted extrusion of alumina-silicone and alumina-magnesium hydroxide-silicone mixtures, as precursors for mullite and cordierite ceramics*
  Company: SCF Processing Ltd, Drogheda (Ireland)

- **Visiting Ph.D. researcher** *(May and July 2013)*
  Advanced Ceramics Group, University of Bremen (Germany)
  Project title: *Novel monolithic and cellular bioactive silicate-based ceramics from preceramic polymers and nano-sized fillers*
  Advisor: Dr. Laura Treccani

Publications in Journals

- Fiocco L., Babakhanova Z., Bernardo E. *Facile obtainment of luminescent glass-ceramics by direct firing of a preceramic polymer and oxide fillers.*
  CERAMICS INTERNATIONAL (Accepted in January 2016 – DOI: 10.1016/j.ceramint.2016.01.052)

- Fiocco L., Ferroni L., Gardin C., Zavan B., Secco M., Matthews S., Bernardo E. *Wollastonite-diopside glass-ceramic foams from supercritical carbon dioxide-assisted extrusion of a silicone resin and inorganic fillers.*
  Submitted to JOURNAL OF NON-CRYSTALLINE SOLIDS (January 2016)

- Fiocco L., Michielsen B., Bernardo E. *Silica-bonded apatite scaffolds from calcite-filled preceramic polymers.*
  Submitted to JOURNAL OF EUROPEAN CERAMIC SOCIETY (December 2015)

- Fiocco L., Li S., Bernardo E., Stevens M.M., Jones J.R. *Highly porous polymer-derived wollastonite-apatite ceramics for bone regeneration*.
  Submitted to BIOMEDICAL MATERIALS (August 2015)

- Fiocco L., Bernardo E. *Novel Cordierite foams from preceramic polymers and reactive oxide fillers.*
  MATERIALS LETTERS 159 98-101 (2015)

- Fiocco L., Elsayed H., Bernardo E., Ferroni L., Gardin C., Zavan B. *Bioactive wollastonite-diopside foams from preceramic polymers mixed with active oxide fillers.*
  MATERIALS. 8 (5) 2480-2494 (2015)

- Fiocco L., Elsayed H., Daguano J.K.M.F., Soares V.O., Bernardo E. *Silicone resins mixed with active oxide fillers and Ca-Mg Silicate glass as alternative/integrative precursors for wollastonite-diopside glass-ceramic foams.*
  JOURNAL OF NON-CRYSTALLINE SOLIDS. 415 44-49 (2015)

- Bernardo E., Fiocco L., Parcianello G., Storti E., Colombo P. *Advanced ceramics from preceramic polymers modified at the nano-scale: A review.*
  MATERIALS. 7 (3) 1927-1956 (2014)

- Bernardo E., Fiocco L., Prnová A., Klement R., Galusek D. *Gehlenite: Eu*$^{3+}$ *phosphors from a silicone resin and nano-sized fillers.*
  OPTICAL MATERIALS. 36 (7) 1243-1249 (2014)

- Bernardo E., Fiocco L., Giffin G.A., Di Noto V., Colombo P. *Microstructure development and dielectric characterization of forsterite-based ceramics from silicone resins and oxide fillers.*
  ADVANCED ENGINEERING MATERIALS. 16 (6) 806–813 (2014)

- Bernardo E., Carlotti J.F., Dias P.M., Fiocco L., Colombo P., Treccani L., Hess U., Rezwan K. *Novel akermanite-based bioceramics from preceramic polymers and oxide fillers.*
  CERAMICS INTERNATIONAL. 20 1029-35 (2014)

- Fiocco L., Bernardo E., Colombo P., Cacciotti I., Bianco A., Bellucci D., Sola A., Cannillo V. *Novel processing of bioglass ceramics from silicone resins containing micro- and nano-sized oxide particle fillers.*
  JOURNAL OF BIOMEDICAL MATERIALS RESEARCH. 40 (1) Part A, 1029–1035 (2014)

Presentations at Conferences

- 39th International Conference and Exposition on Advanced Ceramics and Composites
  Daytona Beach, Florida, USA, 25-30 January 2015
  Highly porous wollastonite-hydroxyapatite scaffolds for bone ingrowth from preceramic polymers.

- CIMTEC 2014 – 13th International Ceramic Congress
  Montecatini Terme, Italy, 8-13 June 2014
  Highly porous wollastonite-diopside and wollastonite-apatite ceramic foams from low temperature foaming and reactive ceramization of silicone-based mixtures.

- ECerS XIII - 13th International Conference of the European Ceramic Society
  Limoges, France, 23-27 June 2013
  Porous bioactive glass-ceramics from preceramic polymers and fillers.